Investigation of membrane-active peptides and proteins by vibrational spectroscopy

vorgelegt von
Diplom-Humanbiologe
Enrico Forbrig
geboren in Berlin

von der Fakultät II – Mathematik und Naturwissenschaften
der Technischen Universität Berlin
zur Erlangung des akademischen Grades

Doktor der Naturwissenschaften

– Dr. rer. nat. –

genehmigte Dissertation

Promotionsausschuss:

Vorsitzender: Prof. Dr. Nediljko Budisa
Berichter: Prof. Dr. Peter Hildebrandt
Berichter: Prof. Dr. Thomas Gutsmann
Berichter: Prof. Dr. Peter Hegemann

Tag der wissenschaftlichen Aussprache: 17.04.2018

Berlin 2018

ABSTRACT

The plasma membrane acts as the barrier and interface between the intracellular compartment and the extracellular environment. There are a variety of physical and chemical stimuli that are transmitted over the plasma membrane by means of integrated biomolecules, e.g. membrane proteins and peptides.

To elucidate such processes in more detail, the development of artificial biomimetic membrane systems has been a focus during the last decades. In this work, the multiple mechanisms of interactions between peptides and proteins with membranes have been investigated by utilizing a previously established tethered bilayer lipid membrane (tBLM) system. This tBLM was assembled on a nanostructured gold electrode and surface-enhanced infrared (SEIRA) spectroscopy was applied under control of electrical potentials to mimic the transmembrane potential.

Antimicrobial peptides (AMPs), synthesized by a wide range of organisms, target and disrupt the negatively charged bacterial cell membrane due to their positive charge. However, the exact mode of action of AMPs still remains elusive. The development of resistances against antibiotics becomes a major issue in the clinical treatment of bacterial infections, making AMPs interesting targets of study.

The human AMP LL-37 as well as its mutated fragments LL-32 and LL-20 were analysed using a tBLM comprised of 1-palmitoyl-2-oleoyl-sn-glycero-3-phosphocholine (POPC) and 1-palmitoyl-2oleoyl-sn-glycero-3-phospho-(1'-rac-glycerol) (POPG). To obtain information about the secondary structure of these peptides in solution IR measurements were conducted. The analysis of the peptide backbone amide modes revealed an α-helical structure of all peptides. The same result was obtained by molecular dynamics (MD) simulations of the peptides in solution. Based on the surface-selection rules and the distance dependence of SEIRA, the orientation and location of the peptides within the tBLM was determined. These measurements revealed that LL-37 incorporates horizontally with its N-terminus into the hydrophobic core of the membrane, whereas LL-32 adsorbs horizontally onto the hydrophilic headgroups and LL-20 does not interact with the system. The same conclusion was drawn from MD simulations of 300 ns, in agreement with the previously described importance of the amino acid residues 17 - 29 for the peptide function, since LL-20 lacks this region.

The AMP alamethicin (ALM), comprised of a N-terminal α-helix and C-terminal 3_{10}-helix, interacts with bacterial membranes in response to the transmembrane potential. The conducted voltage-dependent SEIRA study, using a tBLM composed of POPC:POPG, was combined with density functional theory (DFT) calculations resulting in the development of a kinetic integration model of ALM. After its adsorption on the bilayer surface the peptide incorporates via its N-terminus. This leads to a reorientation with respect to the surface normal, between 78° - 69° in the horizontally adsorbed state to 21° in the transmembrane-incorporated state.

The bacterial Complex I (CpI) couples the electron transfer between nicotinamide adenine dinucleotide (NADH) and ubiquinone resulting in their respective oxidation and reduction. This process allows the transmembrane translocation of protons, making CpI an essential membrane protein in the energy production of bacterial cells. CpI was incorporated into a supported lipid membrane system based on a (de)protonable 4-aminothiophenol (4-ATP) SAM, POPC:POPA phospholipids and a quinone. 4-ATP serves not only as linker molecule to a nanostructured gold-surface but also as pH sensor, as indicated by concomitant DFT calculations. In this way, the transmembrane proton translocation was observable via the protonation state of 4-ATP depending on the net orientation of CpI molecules induced by two complementary approaches. An associated change of the amide I/amide II band intensity ratio indicates conformational modifications upon catalysis which may involve movements of transmembrane helices or other secondary structural elements as suggested in literature.

ZUSAMMENFASSUNG

Die Plasmamembran fungiert als äußere Grenzschicht und Schnittstelle zwischen dem intrazellulären Kompartiment und der extrazellulären Umgebung. Integrierte Biomoleküle, wie z.B. Proteine und Peptide, übertragen unterschiedliche physikalische und chemische Reize an der Plasmamembran. Die Entwicklung künstlicher biomimetischer Membransysteme ermöglicht die Aufklärung dieser Prozesse. In dieser Arbeit werden trägerfixierte Lipiddoppelschichtmembranen (tethered bilayer lipid membrane – tBLM) genutzt, um die Interaktionsmechanismen von Peptiden sowie Proteinen mit Membranen zu untersuchen. Es wurde eine tBLM auf einer nanostrukturierten Goldelektrode aufgebaut und die oberflächenverstärkte Infrarot-Spektroskopie (surface-enhanced irfrared absorption - SEIRA) wurde unter Kontrolle des elektrischen Potentials zur Nachbildung des Transmembranpotentials angewendet.

Die rasante Entwicklung antibiotikaresistenter Bakterienstämme stellt eine wachsende Herausforderung für die Behandlung von Infektionen dar. Antimikrobielle Peptide (AMP), hergestellt durch eine Vielzahl an Organismen, wirken aufgrund ihrer positiven Ladung destruktiv auf die negativ geladene Bakterienmembran, wobei der genaue Wirkmechanismus nicht abschließend geklärt ist.

Das humane AMP LL-37 und dessen synthetisch hergestellte Fragmente LL-32 und LL-20 wurden mit Hilfe einer tBLM, welche aus 1-palmitoyl-2-oleoyl-sn-glycero-3-phosphocholine (POPC) und 1-palmitoyl-2oleoyl-sn-glycero-3-phospho-(1'-rac-glycerol) (POPG) besteht, analysiert. Mit Hilfe von IR-Messungen wurde die Sekundärstruktur in Lösung ermittelt. Die Analyse der Amid-Banden des Peptidrückgrats ergab für alle Peptide eine α-helikale Struktur. Moleklulardynamische (MD) Simulationen der Peptide in Lösung bestätigten dieses Ergebnis. Auf Grundlage der Oberflächenauswahlregeln und Abstandsabhängigkeit von SEIRA wurde die Orientierung und Lage der Peptide innerhalb der tBLM bestimmt. LL-37 inkorporierte horizontal mit dem N-Terminus in den hydrophoben Membranteil, LL-32 adsorbierte horizontal auf der hydrophilen Membranaußenseite, während LL-20 nicht mit dem System interagierte. Dieselbe Schlussfolgerung wurde aus MD Simulationen (300ns) gezogen, welche die zuvor beschriebene Bedeutung der Aminosäurereste 17-29 für die antimikrobielle Aktivität des LL-37 bestätigen. Diese Sequenz ist im Fall von LL-20 nicht intakt.

Das AMP Alamethicin (ALM), aufgebaut aus einem α-helikalen N-Terminus und einer C-terminalen 3_{10}-Helix, interagiert in Abhängigkeit des Transmembranpotentials mit Bakterienmembranen. Unter Nutzung einer tBLM (POPC:POPG) wurde eine potentialabhängige SEIRA-Studie mit Dichtefunktionstheorie (DFT) Rechnungen kombiniert, um ein kinetisches Model der Integration von ALM in Membranen zu beschreiben. Das Peptid inkorporiert nach Adsorption mit Hilfe des N-Terminus in die Doppelmembran. Dies führt zu einer Reorientierung bezüglich der Oberflächennormalen von einem Winkel von 78° - 69° in der horizontal adsobierten Form hin zu 21° im inkorporierten Zustand.

Als Teil der Atmungskette koppelt der bakterielle Complex I (CpI) den Elektronentransfer zwischen Nicotinamidadenindinukleotid (NADH) und Ubichinon resultierend in einer Oxidation bzw. Reduktion. Die darauf folgende Protonenübertragung über die Bakterienmembran hat eine wichtige Funktion für die Energiebereitstellung der Bakterienzelle. CpI wurde in ein Lipidmembransystem inkorporiert, das auf einer selbstassemblierten Monolage aus (de)protonierbarem 4-Aminothiophenol (4-ATP), einem POPC:POPA Lipidgemisch und Ubichinon zusammengesetzt ist. Neben seiner Funktion als Linker-Molekül, dient 4-ATP ebenso als pH Sensor, wie ergänzende DFT Rechnungen bestätigten. Somit wurde die Protonentranslokation über die Membran mittels des Protonierungsgrades von 4-ATP in zwei komplementären Ansätzen abhängig von der Proteinorientierung ermittelt. Die induzierte Änderung des Quotienten der Amid I/Amid II Bandenintensität zeigte katalytische Konformationsänderungen, die eine mögliche Bewegung von Transmembranhelices oder anderer Sekundärstrukturelemente einschließen.

PUBLICATIONS

Parts of this thesis are published in the following articles:

Reproduced with permission from **Forbrig, E.**; Staffa, JK.; Salewski, J.; Mroginski MA.; Hildebrandt P.; Kozuch, J. Monitoring the Orientational Changes of Alamethicin Incorporating into Bilayer Lipid Membranes. *Langmuir* 2018 *34* (6), pp 2373–2385 doi: 10.1021/acs.langmuir.7b04265 (chapter 4.2.3, 5.2.1, 5.4, 6.3 and 8.1)

Reproduced with permission from *Gutiérrez-Sanz, O.; ***Forbrig, E**.; Batista AP.; Pereira MM.; Salewski, J.; Mroginski MA.; Götz, R.; De Lacey, AL.; Kozuch, J.; Zebger, I. Catalytic Activity and Proton Translocation of Reconstituted Respiratory Complex I monitored by Surface-enhanced Infrared Absorption Spectroscopy. *Langmuir* 2018 *34* (20), pp 5703-5711 (*These authors contributed equally.) doi: 10.1021/acs.langmuir.7b04057 (chapter 4.3, 5.1.4, 5.2.2, 5.6, 6.4, 8.2)

Other publications in peer-reviewed Journals:

*Wiebalck, S.; *Kozuch, J.; **Forbrig, E**.; Tzschucke, CC.; Jeuken, LJ; Hildebrandt, P. Monitoring the Transmembrane Proton Gradient Generated by Cytochrome bo3 in Tethered Bilayer Lipid Membranes Using SEIRA Spectroscopy. *J Phys Chem B* 2016, 120(9), 2249-2256. (*These authors contributed equally.) doi: 10.1021/acs.jpcb.6b01435

Oral presentations:

- *"Combined Spectroscopic and Computational Study of Human Cathelicidin LL-37 and its Fragments LL-32 and LL-20",* ICAVS9 - 9th International Conference on Advanced Vibrational Spectroscopy, June 11th - 16th, 2017, Victoria (Canada)

Poster presentations:

- SES 2014 - Surface Enhanced Spectroscopies, August 7th – 10th, 2014, Chemnitz (Germany)
- 5th BSRT PhD Symposium - Berlin School of Regenerative Therapies, December 3rd – 5th, 2014, Berlin (Germany)
- AMP2016 - Antimicrobial Peptide Symposium, June 6th – 8th, 2016, Montpellier (France)
- IMAP 2016 - 6th International Meeting on Antimicrobial Peptides, August 31th – September 3rd, Leipzig (Germany)
- ICAVS8 - 8th International Conference on Advanced Vibrational Spectroscopy, July 12th - 17th, 2015, Vienna (Austria)

TABLE OF CONTENTS

ABBREVIATIONS

4-ATP	4-aminothiophenol
6MH	6-mercaptohexanol
Aib	2-aminoisobutyric acid
ALM	alamethicin
ADP	adenosine diphosphate
AMP	antimicrobial peptide
ATP	adenosine triphosphate
ATR	attenuated total reflectance
CHARMM	Chemistry HARvard Molecular Mechanics
CL	cardiolipin
COM	center of mass
CPE	constant phase element
CpI	bacterial complex I (NADH:quinone oxidoreductase)
DAG	diacylglycerol backbone
DDM	n-dodecyl β-D-maltoside
DFT	density functional theory
DMN	2,3-dimethyl-1,4-naphthoquinone
$DMNH_2$	2,3-dimethyl-1,4-naphthoquinol
DPTL	2,3-di-O-phytanyl-sn-glycerol-1-tetraethylene glycol-d,l-alpha-lipoic acid
EDTA	ethylenediaminetetraacetic acid
EIS	electrochemical impedance spectroscopy
EM	electromagnetic
FF	force field
F-MMM	Fluid-Mosaic Membrane Model
FMN	flavin mononucleotide
FT	Fourier transform
FT-IR	Fourier transform infrared
GUI	graphical user interface
hCAP18	human 18-kDa cationic antibacterial protein
IE	interaction energy
IM	inner membrane
IR	infrared
IRE	internal reflection element
LPS	lipopolysaccharide
LTA	lipoteichoic acid
MD	molecular dynamics
MM	molecular mechanics
MUA	11-mercaptoundecanoic acid
MUOL	11-mercaptoundecanol
NAD^+	nicotinamide adenine dinucleotide
NADH	nicotinamide adenine dinucleotide
NAMD	Nanoscale Molecular Dynamics

OCP	open circuit potential
OM	outer membrane
PA	phosphatidic acid
PBC	periodic boundary conditions
PBS	phosphate-buffered saline
PDB	protein data bank
PE	phosphatidylethanolamine
PGN	peptidoglycan
PG	phosphatidylglycerol
Pheol	phenylalaninol
PI	phosphatidylinositol
PMSF	phenylmethylsulfonyl fluoride
PS	phosphatidylserine
POPA	1-palmitoyl-2-oleoyl-sn-glycero-3-phosphate
POPC	1-palmitoyl-2-oleyl-sn-glycero-3-phosphocholine
POPG	1-palmitoyl-2oleoyl-sn-glycero-3-phospho-(1'-rac-glycerol)
PZC	potential of zero charge
RDF	radial distribution function
RMSD	root mean square deviation
RMSF	root mean square fluctuation
RR	resonance Raman
SAM	self-assembled monolayer
SEIRA	surface-enhanced infrared absorption
SERS	surface-enhanced Raman scattering
SLM	supported lipid membrane
tBLM	tethered bilayer lipid membrane
tHLM	tethered hybrid lipid membrane
TdCM	time-dependent contact map
TDC	transition dipole moment coupling
TDM	transition dipole moment
WK3SH	[(β-cholestanoxy)ethoxy)ethoxy)ethanethiol]

1 INTRODUCTION AND MOTIVATION

The plasma membrane is of fundamental importance as barrier and interface between the extracellular environment and intracellular cytosol. In this role it provides the necessary stability as well as flexibility, due to the amphipathic character of phospholipids and their property to assemble energetically favorable structures. Moreover, it protects the cell from chemical and physical stimuli that are toxic in high dosages, e.g. reactive oxygen species or UV radiation.

Due to the fast adaptation of pathogens to changed environmental conditions, resistance mechanisms against conventional antibiotics, discovered for the first time in 1928,[1] appeared already after a short time of use in clinics. Currently, different man-made factors, e.g. misuse of antibiotics in the treatment of patients and agriculture, accelerate this process leading to a precarious worldwide health threat. The lack of effective antibiotics causes high economical costs and the spread of multiple drug resistant microbes. Thus, there is a general demand for substances using alternative antimicrobial mechanisms. Besides their effectiveness, a rational design of antibiotics needs to consider the requirement of a high specificity by inhibiting pathogens, while protecting commensal bacteria and preventing lysis of host cells.[2]

Antimicrobial peptides (AMPs), which are constituted by 10 - 100 amino acid residues, interact with different bacterial cell wall components, e.g. lipopolysaccharide and especially the plasma membrane. In general, AMPs are evolutionary conserved in a multitude of organisms and have been isolated from bacteria, fungi, plants amphibians and mammals. The physicochemical properties of these molecules are defined by the amino acid composition, resulting in specific functional properties. AMPs are mostly cationic and contain a high percentage of hydrophobic amino acids (> 30%).[3] This allows the formation of diverse amphipathic secondary structures.

This leads to a variety of modes of action on the basis of electrostatic and hydrophobic interactions which are often related to the target cell's transmembrane potential.[4] That allows protecting the host from pathogenic infections at micromolar concentrations.

Simultaneously, the plasma membrane is the site of signal transduction, ion transport and energy production facilitated by integrated membrane proteins, which are interconnected and concentrated in microdomains named lipid rafts.[5,6] In case of the electron transport chain, an assembly of respirasomes or supercomplexes suggests the direct interaction of the involved respiratory proteins.[7]

These examples illustrate the potential of and the need for biophysical investigations on lipid bilayer properties in relation to membrane-interacting molecules. Probing such processes demands reproducible platforms that ensure a high stability over a time range of hours or even days. Metal electrodes coated by membrane models represent such platforms since they mimic essential features of natural membranes but are sufficiently simplified in their composition to allow for structural analyses. Specifically such devices offer the possibility to combine electrochemistry with vibrational spectroscopy, surface plasmon resonance, sum-frequency vibrational spectroscopy Raman and IR spectroscopy.

Such biomimetic membrane systems provide the opportunity to study the AMP-membrane interaction and enable the incorporation of membrane proteins *in-situ* in an environment that stabilizes the peptide structure. In this approach that was employed in the present thesis, a nanostructured Au surface was functionalized by a variety of self-assembled monolayer (SAM) compositions and three different biomimetic membrane systems were assembled. Such devices

allow employing surface-enhanced infrared absorption (SEIRA) spectroscopy under electrochemical control.

The tethered bilayer lipid membrane (tBLM) was based on a mixed SAM comprised of the linker [(β-cholestanoxy)ethoxy)ethoxy)ethanethiol] (WK3SH)[8] and the spacer 6-mercaptohexanol (6MH). The adsorption of POPC:POPG phospholipids led to an assembly of lipid bilayer compartments covering an aqueous reservoir alternating with lipid monolayer islands. In contrast, a lipid monolayer was assembled using a pure WK3SH-SAM coating, corresponding to the tethered hybrid lipid membrane (tHLM). The supported lipid membrane (SLM), however, required the pH sensor 4-aminothiophenol (4-ATP) SAM and the addition of POPC:POPA vesicles including the quinone 2,3-dimethyl-1,4-naphthoquinone (DMN).[9]

The present study focuses on two AMPs. First, the α-helical human AMP LL-37, a member of the cathelicidin family, exhibits pleiotropic functions with respect to immune modulation, e.g. regulation of chemotaxis, apoptosis and wound healing processes, but also interacts with cellular membranes. Interestingly, a variant of LL-37 comprising the residues 17-29 was defined as peptide core owing to a high antibacterial activity[10] and the C-terminal residues 32-27 were described to be unstructured.[11] These hypotheses were tested by means of two C-terminally mutated fragments LL-32 and LL-20, which were compared to LL-37 regarding their relation between structure and function. A previous study revealed decisive differences in the secondary structure in solution, where LL-32 and LL-20 were unstructured in bulk water.[12] Furthermore, LL-32 exhibited a higher antibacterial activity compared to LL-37 while LL-20 did not show any antibacterial activity. The interactions of these peptides with membranes are, however, not yet understood on a molecular level.

The second AMP, alamethicin (ALM), is an amphipathic peptide, which was shown to form ion channels in bacterial membranes consisting of 4-12 monomers. The assembly is controlled by the transmembrane potential and barrel-stave model of integration was proposed. An interaction of the hydrophobic membrane core with the hydrophobic side of ALM was observed, whereas the hydrophilic patch pointed to the inside enabling a water-filled pore.[13,14] However, the kinetics and exact mechanism of the voltage-dependent integration process still remains elusive.

The first objective of this work is, therefore, to contribute to a better understanding of the molecular processes associated with the interactions of these AMPs with membranes. To achieve this goal, primarily vibrational spectroscopic methods combined with electrochemical techniques were employed, complemented by theoretical methods carried out by collaboration partners. This integral approach was also applied to elucidate a second biophysical problem, i.e., the molecular mechanism of the redox-linked proton transfer of the membrane-bound bacterial complex CpI. The protein was immobilized on membrane models to probe simultaneously proton translocation and redox transitions by SEIRA spectroscopy and electrochemistry, respectively.

2 THEORETICAL BACKGROUND

2.1 Vibrational Spectroscopy

The discovery of infrared (IR) radiation in the electromagnetic spectrum of the sun by William Herschel two centuries ago was the prerequisite for the development of vibrational spectroscopy as one of the oldest spectroscopic methods. In early studies the focus laid on the interaction of electromagnetic radiation with matter and first vibrational spectra were obtained. In 1928, the Indian scientist Chandrasekhara V. Raman set the foundation for the widely used Raman spectroscopy by discovering the Raman effect. In the beginning, these two spectroscopic methods were used to investigate inorganic materials and small molecules due to limitations regarding the sensitivity of the instruments.[15] Technical innovations during the second half of the 20th century led to the development of lasers, interferometers as well as methods to purify biological compounds enabling life scientists to apply vibrational spectroscopy in studies of highly complex biomolecules.[16]

Today, vibrational modes of single bonds of molecular structures can be analyzed by use of the resonance Raman (RR) effect and the difference mode in IR spectroscopy in high resolution. In particular time-resolved measurements allow to study dynamic biological processes even in a femtosecond time scale.[17,18] Furthermore, vibrational spectroscopy is progressively applied to solubilized, crystallized and especially immobilized molecules. Surface-sensitive techniques, namely surface-enhanced Raman (SER) and surface-enhanced infrared absorption (SEIRA) spectroscopy proved to be highly suitable techniques to study adsorbed macromolecules at metal surfaces, which utilize the surface-enhancement effect and serve as electrodes at the same time.[19,20]

The present work describes a spectroelectrochemical approach linking SEIRA spectroscopy with electrochemistry to investigate the interaction between peptides and proteins with model membrane systems.

2.1.1 Theory of Vibrational Spectroscopy

The interaction of electromagnetic radiation with matter which induces transitions between different vibrational modes of molecules provides the basis of vibrational spectroscopy. These transitions rely on inelastic scattering or resonant absorption of IR radiation ($10 - 12500$ cm^{-1}). The latter takes place when the energy of a photon hv_{IR} of the polychromatic IR radiation matches the energy difference between an initial and final vibrational state (hv_i and hv_f, respectively) and is the basis of IR spectroscopy:

$$hv_{\mathrm{IR}} = hv_f - hv_i \tag{2.1}$$

On the other hand, Raman spectroscopy is characterized by inelastic scattering induced by monochromatic light. The photon scattering leads to an energy difference between scattered photons hv_R and incident photons hv_0, which is attributed to transitions of vibrational states:

$$hv_0 - hv_R = hv_f - hv_i \tag{2.2}$$

These characteristics might be related to rotational transitions that appear as a fine structure of the vibrational transition which are observable only in high-resolution spectra in the gas phase showing no relevance for investigations in a biomolecular context. IR absorption and Raman scattering differ regarding their fundamental mechanisms and thus exhibit, to a certain extent, complementary information. Vibrational transitions are IR-active, if the excited vibrational mode goes along with a change of the dipole moment and Raman-active due to a change of the polarizability. On that account, the relative band intensities of IR and Raman spectral contributions are generally different.

Molecular Vibrations

An eligible model to specify molecular vibrations is the harmonic oscillator where atoms are treated as point masses connected by mass-less springs.[21] The simplest case is the vibration of a diatomic molecule with its masses m_1 and m_2. The displacement along the x-axis from their equilibrium position by Δx induces a restoring force described by Hooke's law

$$F_x = -f\Delta x. \tag{2.3}$$

where the force constant f represents the strength of the bond. This assumption results in the potential energy V of the vibrational movement

$$V = \frac{1}{2}f\Delta x^2 \ . \tag{2.4}$$

Considering the reduced mass μ of the atoms

$$\mu = \frac{m_1 \cdot m_2}{m_1 + m_2} \tag{2.5}$$

and the motion velocity $d\Delta x/dt$ the kinetic energy T is obtained

$$T = \frac{1}{2}\mu\left(\frac{d\Delta x}{dt}\right)^2 \ . \tag{2.6}$$

The model of a harmonic oscillator presumes that the energy of an undamped vibration is conserved. Therefore, the sum of the derivatives of the potential and kinetic energy is equal to zero

$$0 = \frac{dV}{dt} + \frac{dT}{dt} = f\Delta x + \mu\frac{d^2\Delta x}{dt^2} \tag{2.7}$$

which leads to the Newton equation of motion

$$0 = \frac{f}{\mu}\Delta x + \frac{d^2\Delta x}{dt^2} \ . \tag{2.8}$$

The solution of equation (2.8) requires the application of a cosine function

$$\Delta x = A \cdot \cos(\omega t + \theta) \tag{2.9}$$

where A denotes the amplitude, ω the circular frequency and θ the phase of the vibrational motion. Introducing equation (2.9) into (2.8) results in the following description of the circular frequency

$$\omega = \sqrt{\frac{f}{\mu}}.$$
(2.10)

The commonly used expression of the circular frequency in wavenumbers (cm^{-1}) is obtained by dividing equation (2.10) by $2\pi c$, where the velocity of light is represented by c

$$\tilde{v} = \frac{1}{2\pi c}\sqrt{\frac{f}{\mu}}.$$
(2.11)

Equation (2.11) shows that the wavenumber (or frequency) of a vibration increases with a higher bond strength and decreasing mass of the corresponding atoms.

Normal Modes

The extension of the model to molecules that consist of more than two atoms requires a more complex mathematical treatment. A molecule with N atoms possesses 3N degrees of freedom in a Cartesian coordinate system, as each atom can be displaced in x-, y- and z-direction. Translational and rotational displacements, however, do not contribute to vibrational degrees reducing the total number by 6 degrees of freedom in case of nonlinear molecules (3N-6). The number of vibrational degrees of freedom of linear molecules is 3N-5 due to their limited rotation along two axes.

To estimate the frequencies of these vibrations, termed normal modes, the displacement of the Cartesian coordinates of each atom of the molecule has to be contemplated and the kinetic energy is obtained by:

$$T = \frac{1}{2}\sum_{\alpha=1}^{N} m_\alpha \left[\left(\frac{d\Delta x_\alpha}{dt}\right)^2 + \left(\frac{d\Delta y_\alpha}{dt}\right)^2 + \left(\frac{d\Delta z_\alpha}{dt}\right)^2\right]$$
(2.12)

Here, the use of mass-weighted Cartesian displacement coordinates are required that are given as

$$q_i = \sqrt{m_i}\Delta x_i, \qquad q_{i+1} = \sqrt{m_i}\Delta y_i, \qquad q_{i+2} = \sqrt{m_i}\Delta z_i \quad (for\ each\ atom\ \alpha = i).$$
(2.13)

that leads to the following description of the kinetic energy:

$$T = \frac{1}{2}\sum_{i=1}^{3N}\left(\frac{dq_i}{dt}\right)^2.$$
(2.14)

The term for the potential energy V implies the consideration of all possible interactions between individual atoms of a molecule, i.e. covalent bonding, as well as electrostatic and van-der-Waals interactions and can be represented as a Taylor series:

$$V = V_0 \sum_{i=0}^{3N} \left(\frac{\partial V}{\partial q_i}\right)_0 q_i + \frac{1}{2} \sum_{i,j=1}^{3N} \left(\frac{\partial^2 V}{\partial q_i \partial q_j}\right)_0 q_{ij} + \cdots \tag{2.15}$$

Since solely changes of the vibrational potential energy due to displacement of atoms need to be taken into account, the potential energy at the equilibrium, represented by the first term, equals zero. The same applies to the second term expressing infinitesimal changes of q_i from the equilibrium position which do not lead to changes of V.

In case of small displacements q_i within the harmonic approximation, higher order terms do not affect the potential energy and can be neglected, thus V denotes as

$$V \cong \frac{1}{2} \sum_{i,j=1}^{3N} \left(\frac{\partial^2 V}{\partial q_i \partial q_j}\right)_0 q_i q_j = \frac{1}{2} \sum_{i,j=1}^{3N} f_{ij} q_i q_j \,. \tag{2.16}$$

The derivative of the kinetic and potential energy results in Newton´s equation[16] of motion (analog to equation (2.8)

$$0 = \frac{\mathrm{d}^2 q_j}{\mathrm{d}t^2} + \sum_{i=1}^{3N} f_{ij} q_i \tag{2.17}$$

comprised of $3N$ linear second order differential equations and its general solution

$$q_i = A_i \cos\left(\sqrt{\lambda} t + \theta\right). \tag{2.18}$$

This system of differential equations has $3N$ solutions for λ that illustrate $3N$ frequencies $\lambda^{\frac{1}{2}}$, whereas 6 solutions (or 5 in case of linear molecules; see above) are equal to zero as they are attributed to translational and rotational motions of the molecule. Hence, there are 3N-6 (or 3N-5, respectively) non-zero values for λ yielding the frequencies of the normal modes. The information about all frequencies allows to calculate the amplitude of the displacement of each atom A_i for every normal mode. Thus, a normal mode describes an in-phase-oscillation of an entire molecule with a given frequency, however certain segments of the molecule exhibit significantly different amplitudes. In this approximation it appears useful to reduce the normal modes to the part of the molecule with distinct motions, e.g. specific group vibrations with dominant coordinates. The representation of the probability of vibrational transitions can be simplified by conversion of the mass-weighted Cartesian coordinates q_i into normal coordinates Q_k (for k normal modes) using an orthogonal transformation

$$Q_k = \sum_{i=1}^{3N} l_{ik} q_i. \tag{2.19}$$

The transformation coefficient l_{ik} is chosen in such a way that T and V take the shape of equations (2.14) and (2.15). The potential energy does not depend on the cross products $Q_k \times Q_{k'}$ ($k \neq k'$) resulting in the following solution of the Newton equation:

$$Q_k = K_k \cdot \cos\left(\sqrt{\lambda} t + \theta_k\right). \tag{2.20}$$

Infrared Absorption

The extent of the IR absorption is depicted as the absorbance A (in OD = optical density) by the use of the Lambert-Beer law:

$$A = -lg\left(\frac{I}{I_0}\right) = \varepsilon \cdot [J] \cdot l. \tag{2.21}$$

In this relation the IR radiation after passing through an analyte solution is represented by I and the reference intensity by I_0. The obtained absorbance is dependent on the molar concentration $[J]$ of the absorbing species J, the optical path length l. The molar absorption coefficient ε takes into account the quantum mechanical probability of the transition between the initial and final vibrational state (see equation 2.1) and leads to the transition dipole moment:

$$\left[\mu_q\right]_{fi} = \langle \psi_f^* | \widehat{\mu_q} | \psi_i \rangle. \tag{2.22}$$

The wave functions of the initial (ψ_i) and final (ψ_f) vibrational state are represented as well as the electric dipole moment operator $\hat{\mu}_q$

$$\hat{\mu}_q = \sum_\alpha e_\alpha \cdot q_\alpha \tag{2.23}$$

using e_α as the charge of an atom α and q_α as distance to the center of gravity of the molecule. The information, if a normal mode is IR active can be received by expanding the operator of the electric dipole moment $\hat{\mu}_q$ in a Taylor series with respect to the normal coordinates Q_k. In case of a harmonic oscillator only the linear terms need to be contemplated

$$\hat{\mu}_q = \mu_q^0 + \sum_{k=1}^{3N-6} \hat{\mu}_q^k \cdot Q_k \tag{2.24}$$

with

$$\hat{\mu}_q^k = \left(\frac{\partial \mu_q}{\partial Q_k}\right)_0 \tag{2.25}$$

Hence, the transition probability transforms into equation

$$\left[\mu_q\right]_{fi} = \langle \psi_f^* | \widehat{\mu_q} | \psi_i \rangle = \mu_q^0 \langle \psi_f^* | \psi_i \rangle + \sum_{k=1}^{3N-6} \hat{\mu}_q^k \langle \psi_f^* | Q_k | \psi_i \rangle. \tag{2.26}$$

The first term of equation (2.26) equals zero based on the orthogonality of the wavefunctions ψ_f and ψ_i. As an IR-active transition is related to a non-zero transition probability the second term has to take a value different from zero provided that two prerequisites are fulfilled:

First, the electric dipole moment of the molecule needs to change during the vibrational displacement of the atoms ($\hat{\mu}_q^k \neq 0$). Second, the quantum number between the states i and f differ by one within the harmonic approximation ($\langle \psi_f^* | Q_k | \psi_i \rangle \neq 0$). These considerations apply to all three Cartesian coordinates ($q = x, y, z$), so that the absorbance A of unpolarized light of randomly oriented molecules arises from the sum of the transition probabilities along all three components:

$$A \propto \left([\mu_x]_{if}^2 + [\mu_y]_{if}^2 + [\mu_z]_{if}^2\right). \tag{2.27}$$

However, using linear polarized light on an oriented sample allows to address the individual components of the transition dipole moment $[\mu_q]_{if}$ and, by this, to receive more detailed information about the studied system.

2.1.2 Infrared Spectroscopy

2.1.2.1 Fourier Transform Infrared Spectroscopy

Nowadays modern IR spectrometers operate based on the principle of the Fourier Transform (FT) IR Spectroscopy. This method is advantageous over the previously applied dispersive technique using a monochromator as light filter, due to the reduced measuring time and an improved signal-to-noise ratio, since the complete light intensity of a light source is detected.

The Michelson Interferometer is a central unit of a FTIR spectrometer (Figure 2.1) and consists of a beam splitter and a fixed as well as a movable plane mirror, both oriented perpendicularly to each other. The irradiated polychromatic IR light is transmitted and reflected by the beam splitter onto the two mirrors. Afterwards, both beams are recombined again in one beam and are directed at the sample. Assuming an optical path difference of $\delta = 0$, there is an equal distance between both mirrors and the beam splitter, hence the phase difference between both beams is zero leading to equal outgoing and incoming radiation. A change in the position of the movable mirror leads to an interference of the beams. Each wavelength λ encounters alternating constructive $(\delta = 2n \cdot \frac{1}{2}\lambda)$ and destructive interference $(\delta = (2n + 1) \cdot \frac{1}{2}\lambda)$ and results in a δ-dependent cosinusoidal modulation reflecting the respective wavelength λ.

The signal which is accumulated on the detector is a superposition of the cosine functions of all frequencies of the polychromatic IR radiation and is referred to as an interferogram (Figure 2.1).
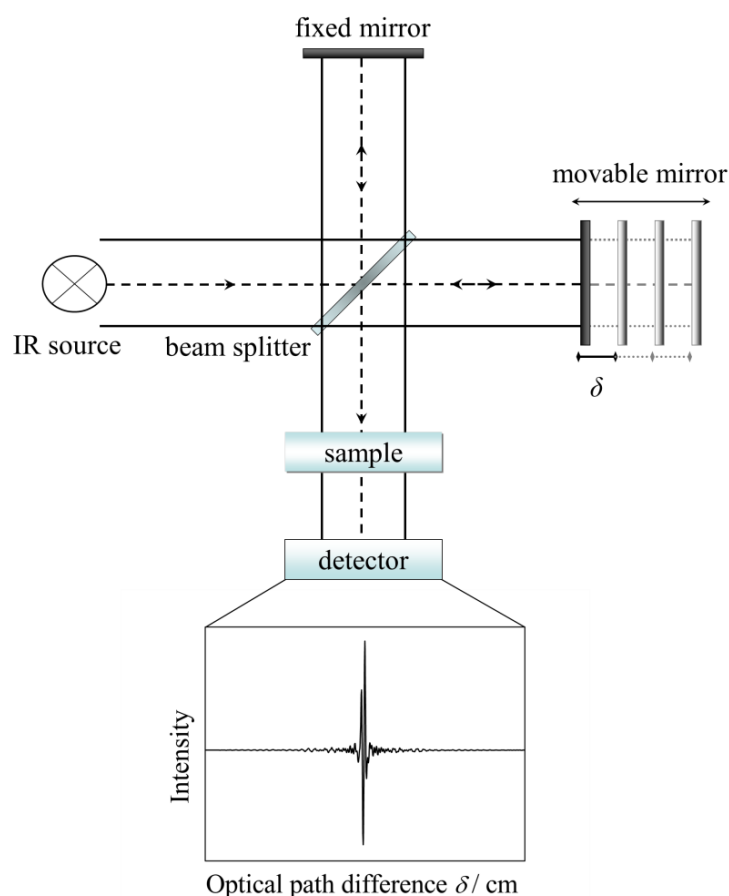
Figure 2.1 Scheme of a Michelson Interferometer. The irradiated IR light splits after passing a beamsplitter into two beams that are reflected at a fixed and movable mirror and merged before passing the sample and detector. The created interferogram depicts the optical path difference δ of the movable mirror. Reprinted with kind permission from Jacek Kozuch (2013). *Structure-Function Relationships of Membrane Proteins - Spectroelectrochemical Investigation of Artificial Membranes*, Technische Universität Berlin, Fakultät II.[134]

Eventually, by use of the Fourier transform, this optical path length dependent interferogram (time domain) is then transformed into an IR spectrum (frequency domain)

$$I(\tilde{v}) = \int\limits_{-\infty}^{+\infty} I(\delta) \cos(2\pi\tilde{v}) \mathrm{d}\delta.$$

(2.28)

This integral takes an infinite motion of the movable mirror into account. The effective optical path difference is restricted to a few centimeters, therefore the interferogram has to be multiplied with an appropriate apodization function (i.e. a triangular function) to bring the edges of the interferogram smoothly to zero. This treatment, on the one hand, reduces artifacts in the spectrum, on the other hand there is also an impact on the shape of spectral bands that needs to be considered during the data analysis.

2.1.2.2 Attenuated Total Reflectance Infrared Spectroscopy

In this paragraph the attenuated total reflection (ATR) setup is described, since it is the foundation for the investigations conducted by surface-enhanced infrared absorption (SEIRA). The central unit of the technique is the internal reflection element (IRE) or ATR prism depicted schematically in Figure 2.2. At the interface to an optically less dense medium at an angle of incidence higher than the critical angle θ_c total reflection occurs. The refractive index of biological systems lies typically in the region of $n_1 \sim 1.44$.[22] Therefore, silicon ($n_{Si} = 2.34$), germanium ($n_{Ge} = 4.0$), or zinc selenide ($n_{ZnSe} = 2.4$) are used as materials for the IRE.[16]

Additionally to the total reflection an evanescent wave is propagated through the interface into the less dense medium without carrying any energy. In this process, the amplitude of the electric field decays exponentially in perpendicular direction to the surface (i.e. in z-direction):

$$E = E_0 exp\left(-\frac{z}{d_p}\right)$$

(2.29)
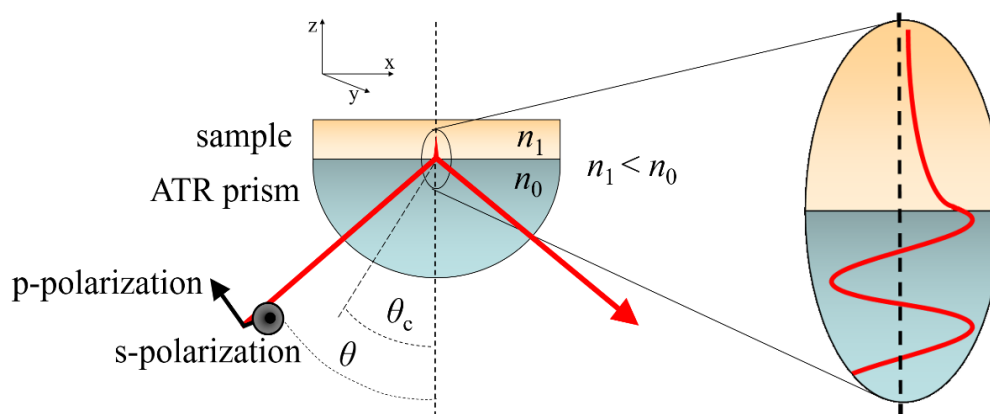
Figure 2.2. Schematic description of attenuated total reflection-infrared (ATR-IR) spectroscopy. The IR beam approaches the ATR prism in an angle θ that depends on the used material. It is composed of a perpendicular and parallel component (s-polarized and p-polarized) in respect to the plane of incidence of the electromagnetic field. Total reflection at the interface to an optically less dense medium ($n_1 < n_0$) requires a higher incident angle than the critical angle θ_c. Reprinted with kind permission from Jacek Kozuch (2013). *Structure-Function Relationships of Membrane Proteins - Spectroelectrochemical Investigation of Artificial Membranes*, Technische Universität Berlin, Fakultät II.[134]

The penetration depth d_p describes the distance at which the amplitude decayed to ca. 37 % ($\sim e^{-1}$) of its initial value. It depends on the angle of incidence θ, the wavelength of the radiation λ and the ratio of the refractive indices n_1/n_0 (of the IRE and the optically less dense medium, respectively):

$$d_p = \frac{\lambda}{2\pi\sqrt{sin^2\theta - \left(\frac{n_1}{n_0}\right)^2}}.$$

(2.30)

The wavelength of the incident radiation and the penetration depth are approximately in the same order of magnitude. In this work, a Si prism is used with an incident angle of 60° and a spectral region of 1000 to 4000 cm^{-1} (10 - 2.5 µm). That leads to a penetration depth of the evanescent wave between 2.6 and 0.7 µm, respectively. An absorbing medium deposited onto the surface of the IRE can couple with the electric field of the evanescent wave and absorb energy of the radiation leading to an attenuation of the total reflected beam. The perpendicular (s-polarized) and parallel (p-polarized) components of the incident radiation with respect to the plane of incidence (Figure 2.2) cause a polarization of the evanescent wave in the *x*- *y*- and *z*-directions. The decisive advantage of the ATR technique is the accessibility to the sample that is adsorbed on top of the IRE. That allows binding studies of substrates, cofactors and ligands and effects of different experimental conditions (e.g. pH, ionic strength and electrical potential) as the supernatant buffer solution can be exchanged very easily.[22] Furthermore, samples such as membrane proteins can be oriented preferably on the IRE to obtain information about the orientation of structural elements by the use of polarized light.[23]

2.1.2.3 Surface-enhanced Infrared Absorption Spectroscopy

The surface-enhanced infrared absorption (SEIRA) effect that exhibits mechanistic similarities to surface-enhanced Raman scattering (SERS) was first observed in ATR-IR experiments of organic compounds adsorbed to Ag and Au films.[24] This method paves the way for studies of adsorbed species in the vicinity of up to 8 nm to a nanostructured metal surface yielding enhancement of about two orders of magnitude.[25] Beyond that, the Au film is also an eligible working electrode for electrochemical investigations. This combination offers diverse opportunities to obtain

information about the functionality of biomolecules by means of SEIRA spectroscopy.[26] So far, a variety of proteins were adsorbed on nanostructured Au surfaces and studied spectro-electrochemically applying different approaches. A widely used procedure is the immobilization on SAM coatings on the Au film used to investigate [NiFe] hydrogenases,[27,28] bacterial complex I,[29] sensory rhodopsin II[30] and cellobiose dehydrogenase,[31] respectively. Yamakata et al. achieved to bind the KcsA potassium channel[32] directly on the Au film via terminal cysteine residues introduced by site-directed mutagenesis. Furthermore, elaborate artificial membrane systems were[33,34] developed and applied to the voltage-dependent membrane-bound anion channel hVDAC1[35] and cytochrome bo$_3$,[8] respectively.

2.1.2.4 Surface-Enhancement mechanism

A nanostructured surface containing metal islands is an essential prerequisite for the enhancement effect of SEIRA equivalent to the SERS mechanism.[16] In Figure 2.3 this surface is shown as an apposition of ellipsoidal metal particles. The total surface-enhancement in SEIRA, however, is a combination of independent effects:[36,37]

2.1.2.5 Electromagnetic (EM) mechanism - plasmon resonance

This mechanism is based on the excitation of collective electron resonances within the metal islands, known as localized plasmon modes. The electric field of the incident IR radiation polarizes the metal and evokes a dipole p which generates a local EM field surrounding the particles. A specific characteristic is the perpendicular polarization to the surface at every point of the metal particle (surface selection rule).

The magnitude depends on the sixth power of the distance to the metal surface d

$$|E_{local}|^2 = \frac{4p^2}{d^6}. \tag{2.31}$$
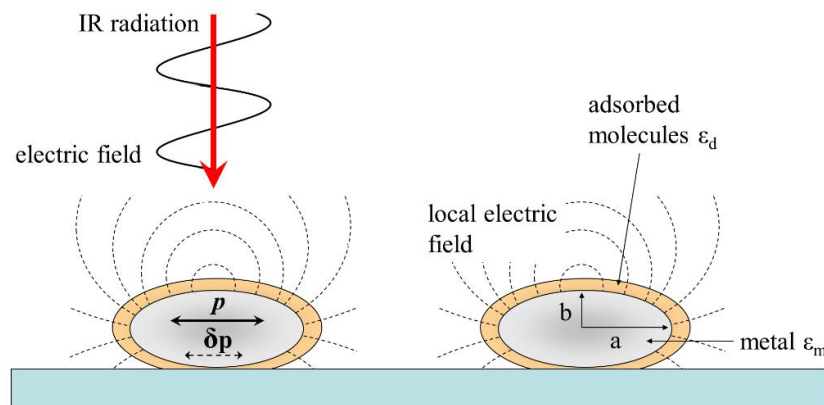
Figure 2.3 Electromagnetic enhancement mechanism (EM) of surface-enhanced infrared absorption (SEIRA) based on ellipsoidal metal particles. Due to the polarization of the metal islands by the electric field component of the incident IR radiation the dipole p induces an enhanced local electric field around the particles. This leads to the excitation of the vibrations of molecules adsorbed on the surface. Additionally, these molecular vibrations induce a dipole δp interfering with the optical metal properties. Reprinted with kind permission from Jacek Kozuch (2013). *Structure-Function Relationships of Membrane Proteins - Spectroelectrochemical Investigation of Artificial Membranes*, Technische Universität Berlin, Fakultät II.[134]

This explains the short-range enhancement of this mechanism (up to ca. 8 nm from the surface). In this way, the enhancement factor F at a distance d to the surface of a nanoparticle with a radius of a_0 can be determined by

$$F(d) = F(0) \cdot \left(\frac{a_0}{a_0 + d} \right)^6 . \qquad (2.32)$$

Molecules adsorbed on the surface can interact with this enhanced EM field and generate transitions between vibrational states. The extent of the enhancement depends on the dimensions as well as shape of the particles. Calculations using the Bruggemann effective medium theory have shown that ellipsoidal particles (high $\frac{a}{b} > 1$; Figure 2.3) lead to a high enhancement.[38]

2.1.2.6 Electromagnetic (EM) mechanism – effect on the optical properties of the metal

Additionally, the oscillating dipoles of adsorbed molecules can induce dipoles in the metal particles δ p. This implicates the change of the dielectric function of the metal and modulates the transmittance as well as reflectance of the metal film at the frequencies of the vibrations. Due to the larger absorptivity and volume fraction of metals compared to the surface molecules, this will determine an effective enhancement of the IR absorption.

2.1.2.7 Chemical mechanism - donor-acceptor interaction and charge transfer

In comparison to physical adsorption (physisorption), chemisorbed molecules display larger enhancements. This effect relies on a donor-acceptor interaction between the adsorbate and the metal which alters the vibrational polarizability of the molecules. In addition, a charge transfer exhibited by charge oscillations between the molecular orbitals and the metal might increase the absorption coefficient.

2.1.2.8 Uniformal orientation

The described processes chemisorption and physisorption often entail an alignment of the molecular dipoles with a preferential orientation in respect to the metal surface. Due to the surface selection rule, vibrations perpendicularly oriented to the surface causes a three times higher IR absorption compared to a parallel or randomly oriented situation.

The SEIRA method utilized in the ATR mode exhibits a strong dependence on the angle of incidence and the polarization of the IR radiation.[39] As shown in Figure 2.2, s-polarized IR radiation gives rise to strongly enhanced IR signals that increase further using higher angles of incidence. However, the interaction between the adsorbed species and s-polarized IR radiation, does not yield any effective signal, as described by Osawa.[40]

2.2 Electrochemical Impedance Spectroscopy

The development of new technologies in the last decades, e.g. solid-state batteries and fuel cells, increased the interest in application of the electrochemical impedance spectroscopy (EIS) as analytical method. It allows the characterization of the electrical properties at the interface connecting solid-solid and solid-liquid materials as well interfaces with electronically conducting systems.[41]

In the beginning, the application of this method concentrated on material sciences. Nowadays it is widely used for label-free studies making fluorescent dyes or radioactive labels redundant. Interesting research fields are for example cancer research,[42,43] neuroscience[44] or chemical catalytic reactions.[45]

The investigation of artificial biomimetic membrane systems by EIS is a further important topic[46,47] that importance increased with the aim of a biosensor development and the study of biomolecules, like proteins[48–50] and peptides[51] specifically interacting with lipid membranes.

2.2.1 Electrode Interfaces

A metal surface that is in contact to an aqueous medium containing an electrolyte exhibits a redistribution of charges resulting in a charged interface.[16] There is an increase or decrease of the electron density of the metal resulting in an excess concentration and even adsorption of oppositely charged ions to the electrode surface. This process even takes place at open circuit potential without any application of external potentials. The charge distribution in the bulk solution (Figure 2.4), can be understood on the basis of the electrical double layer model which combines the approaches of the Helmholtz and the Gouy-Chapman concept. The layer that is in direct contact to the electrode is composed of a compact film of specifically adsorbed ions combined with a highly ordered water matrix. This structure is characterized by a thickness of less than 1 nm and known as inner Helmholtz or Stern layer. Its formation requires a gain in free energy that compensates the partial loss of the hydration shell and usually countervails the charge of the electrode resulting in a sharp potential drop. Adjacent to the inner Helmholtz layer is the outer Helmholtz or diffuse double layer. Here, the ions can diffuse freely still adopting to a concentration gradient determined by the interfacial electric field. The potential distribution in the proximity of a metal can be described on the basis of a simple electrostatic model in which the charge densities σ_i at each interface have to be considered.[52] The charge density of the metal σ_M is given by Gauss' law using the potential difference between the metal φ_M and the inner Helmholtz layer φ_C:

$$\sigma_M = \frac{\varepsilon_0 \varepsilon_C}{d_C} (\varphi_M - \varphi_C).$$

(2.33)

In equation (2.33) ε_0 represents the permittivity, ε_C and d_C the dielectric constant and thickness of the inner Helmholtz layer, respectively. The decay of the charge density inside the outer Helmholtz layer σ_S is dependent on the potential difference between the inner Helmholtz layer and the bulk solution at an infinite distance to the electrode φ_S:

$$\sigma_S = \varepsilon_0 \varepsilon_S \kappa \frac{2kT}{e} sinh\left(\frac{e}{2kT}(\varphi_C - \varphi_S)\right)$$

(2.34)
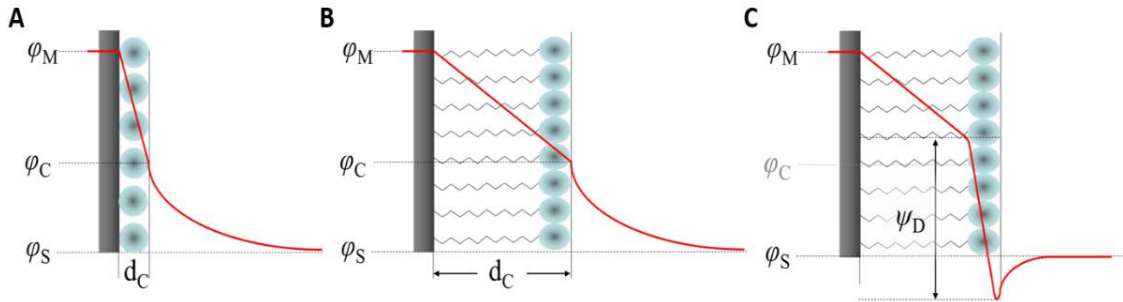
Figure 2.4 Depiction of the potential distribution in the electrical double layer. A: Metal surface with adsorbed ions, B: simplified model of a surface containing a self-assembled monolayer (SAM) with polar headgroups and C: elaborate model of a SAM adsorbed surface. Reprinted with kind permission from Jacek Kozuch (2013). *Structure-Function Relationships of Membrane Proteins - Spectroelectrochemical Investigation of Artificial Membranes*, Technische Universität Berlin, Fakultät II.[134]

In this equation, which is derived from the Gouy-Chapman theory, ε_S is the dielectric constant of the solution, T the temperature, and k and e the Boltzmann constant and the elementary charge, respectively. The thickness of the outer Helmholtz layer is given by the Debye length κ that defines the exponential decay of the potential to ca. 37 % ($\sim e^{-1}$) of its initial value and depends on the ionic strength of the solution I:

$$\kappa = \sqrt{\frac{\varepsilon_0 \varepsilon_S kT}{I}}. \tag{2.35}$$

The charge density of the inner Helmholtz layer σ_C can be calculated under consideration of the charge neutrality of the complete system:

$$\sigma_M + \sigma_C + \sigma_S = 0. \tag{2.36}$$

The application of an external potential difference to the metal electrode changes the potential of the metal φ_M. A particularly interesting state, the potential of zero charge (E_{PZC}), is achieved when φ_M equals φ_S and the absolute charge density on the metal surface and the effective electric field perturbing the solution becomes zero.

Coating the electrode with an amphipathic self-assembled monolayer (SAM), as described in Figure 2.4B, introduces a hydrophobic layer with a decreased dielectric constant ($\varepsilon_r \sim 2 - 3$) and with neutral, positively or negatively charged headgroups. Along this layer, the potential drops linearly according to this simple model. More elaborate models contain an additional component which is the dipole potential ψ_D generated by the polar headgroups (Figure 2.4C).[53] The profile of the potential is described more precisely and resembles a model of the potential distribution across a phospholipid membrane.

2.2.2 Theory of electrochemical impedance spectroscopy

This electrochemical method is used to investigate the dielectric properties of a medium in a frequency-dependent manner. An externally applied and alternating electric field interacts with the electric dipole moments of the analyte or of a dielectric medium, e.g. a self-assembled monolayer (SAM) or phospholipid membrane. In general, during an EIS experiment an alternating voltage of small amplitude is applied to an electrode and the phase shift (real part) and amplitude (imaginary part) of the resulting current are recorded. An EIS spectrum can be obtained by measuring the frequency range between 1 mHz and 1 MHz.

2.2.2.1 Electrical impedance

The frequency-dependent resistance is called electrical impedance $Z(\omega)$[54] that is defined according to Ohm's law as the ratio of the alternating voltage and the resulting current:

$$Z(\omega) = \frac{U(\omega)}{I(\omega)} \tag{2.37}$$

The application of a monochromatic signal $U(t) = U_0 \sin(\omega t)$ with a single frequency of $\nu = 2\pi\omega$ leads to a current $I(t) = I_0 \sin(\omega t + \Theta(\omega))$ with a phase shift Θ.[41,54] Therefore, the impedance can be described as:

$$Z(\omega) = \frac{U(t) = U_0 \sin(\omega t)}{I(t) = I_0 \sin(\omega t + \Theta(\omega))}. \tag{2.38}$$

Provided that there is an entirely resistive behavior the phase shift Θ is zero, and the responses of capacitive and inductive elements are $I(t) = [dU(t)/dt]C$ and $U(t) = [dI(t)/dt]L$, respectively, where C is the capacitance and L the inductance. The analysis of a system using these differential equations can be very complex. However, the use of the Fourier transform simplifies this treatment by conversion into the frequency domain (which is also the variable in a EIS measurement). This results in a voltage and current of $U(\omega) = U_0\pi$ and $I(\omega) = I_0\pi e^{i\omega}$, respectively, and in the solution of the differential equations for a resistive (2.39), capacitive (2.40) and inductive (2.41) behavior ($i = \sqrt{-1}$):

$$Z_R(\omega) = R \quad with \quad \Theta = 0 \tag{2.39}$$

$$Z_C(\omega) = (i\omega C)^{-1} \quad with \quad \Theta = -\frac{\pi}{2} \tag{2.40}$$

$$Z_L(\omega) = i\omega L \quad with \quad \Theta = +\frac{\pi}{2} \tag{2.41}$$

2.2.2.2 Complex Impedance

The impedance is a complex quantity and, therefore, can be described as:

$$Z(\omega) = R(\omega) + iX(\omega) = \text{Re}\big(Z(\omega)\big) + i\text{Im}\big(Z(\omega)\big) \tag{2.42}$$

where the real part R and the imaginary part X refer to the resistance and reactance, respectively. The reactance is the quantity offering information about the capacitive and inductive properties of a system (see equations 2.40 and 2.41).

The two coordinate values of the impedance vector illustrated in a Cartesian coordinate system can be represented as:

$$\text{Re}(Z) = R = |Z|cos\Theta \quad and \quad \text{Im}(Z) = X = |Z|sin\Theta \tag{2.43}$$

considering the phase angle Θ and the magnitude of the impedance $|Z|$

$$\Theta = \arctan\frac{X}{R} \quad and \quad |Z| = \sqrt{R^2 + X^2}. \tag{2.44}$$

The application of the Euler rule allows the conversion of the impedance Z in polar coordinates:

$$Z(\omega) = |Z|(\omega)e^{-i\Theta(\omega)} \tag{2.45}$$

2.2.2.3 The Admittance

Comparable to the rearrangement of the resistance yielding the conductance, the admittance Y is the inverse of the impedance:

$$Y = Z^{-1} = G + iB. \tag{2.46}$$

The real part represents the conductance G and the imaginary part B the susceptance and can be obtained using the partial fraction decomposition:

$$Y = Z^{-1} = \frac{1}{R + iX} = \frac{R}{R^2 + X^2} + i\frac{-X}{R^2 + X^2} \tag{2.47}$$

The impedance Z and the admittance Y can be presented by differentiation of resistive and capacitive components in series $Z = R_S(\omega) - iX_S(\omega)$ or in parallel $Y = G_P(\omega) - iB_P(\omega)$. This calculation leads to the following quantities for the reactance and susceptance:

$$X_S(\omega) = (\omega C_S(\omega))^{-1} \quad and \quad B_P(\omega) = \omega C_P(\omega) \tag{2.48}$$

2.2.2.4 Graphical representation of impedance data

The mathematical expressions of the impedance that are presented in the previous chapter can be visualized in the following graphical representations based on the equivalent circuit depicted in Figure 2.5.[54] This circuit is a suitable model of the electrical properties of a functionalized electrode harboring a tBLM that is in contact to an electrolyte. In this concept, the quantity $R_{Electrolyte}$ is the resistance of the electrolyte. Furthermore, the capacitance and resistance of the bilayer ($C_{Bilayer}/R_{Bilayer}$) and spacer region (C_{Spacer}/R_{Spacer}) of the corresponding tBLM are depicted (Figure 2.5). The most common ways of presenting impedance data are the Nyquist plot, Bode plot and Cole-Cole plot, which is used for the interpretation of the data in this work (see Figure 2.6).

The Nyquist plot relies on the complex impedance $Z = R + iX$. In this case, the imaginary part of the impedance $Im(Z(\omega)) = X(\omega)$ is plotted against the real part $Re(Z(\omega)) = R(\omega)$ as a function of the angular frequency $\omega = (2\pi)^{-1}\nu$.
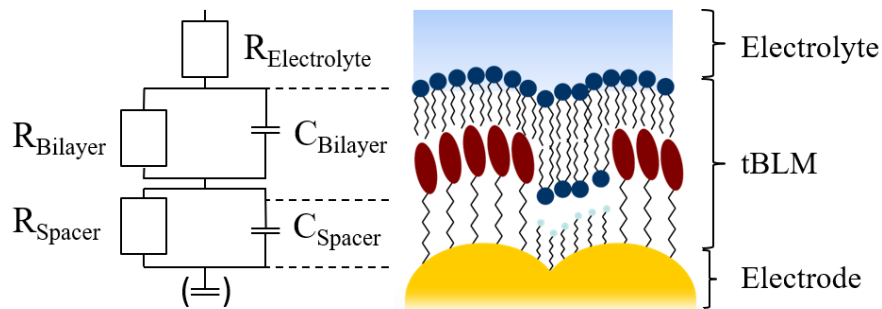
Figure 2.5 Tethered bilayer lipid membrane (tBLM) assembled on an electrode represented as an electrical circuit. The resistances $R_{Electrolyte}$, $R_{Bilayer}$ and R_{Spacer} depict the resistances of the electrolyte in contact with the hydrophilic phospholid headgroups, of the hydrophobic acyl chains combined with the cholestanol headgroup as well as the hydrophilic spacer, respectively. The quantities $C_{Bilayer}$ and C_{Spacer} are the corresponding capacitances. Adapted with kind permission from Jacek Kozuch (2013). *Structure-Function Relationships of Membrane Proteins - Spectroelectrochemical Investigation of Artificial Membranes*, Technische Universität Berlin, Fakultät II.[134]
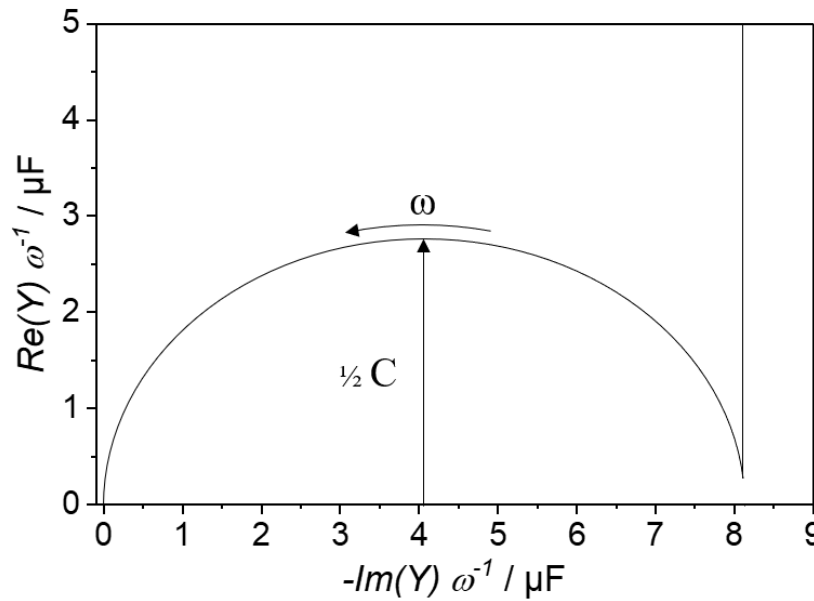
Figure 2.6 Schematic representation of the Cole-Cole plot. Reprinted with kind permission from Jacek Kozuch (2013). *Structure-Function Relationships of Membrane Proteins - Spectroelectrochemical Investigation of Artificial Membranes*, Technische Universität Berlin, Fakultät II.[134]

The Bode plot visualizes the magnitude of the impedance $|Z|$ and the phase difference Θ as a function of the frequency ν. A Bode plot of the described circuit can be divided in three spectral regions. Region I and III represent very high and low frequencies. The impedance is frequency-independent and displays a pure resistive behavior ($\Theta = 0$). At high frequencies (region I) the low resistance $R_{Electrolyte}$ (~100 Ω) is visible, whereas at low frequencies (region III) the summation of all resistances appears (similar to the Nyquist plot). Region II shows the transition between the described regions I and III. Due to the capacitances $C_{Bilayer}$ and C_{Spacer} there is a frequency-dependence of the impedance. Referred to equation 2.40 the phase difference approximates the value of $\Theta = \frac{-\pi}{2}$, and the total capacitance can be determined by $C = (\omega|Z|)^{-1}$.

Cole-Cole plot The admittance can be depicted in the Cole-Cole plot. For this representation a division of the imaginary and real part by the angular frequency ω is necessary (Figure 2.6). This representation allows the direct description of the capacitance (comprised of $C_{Bilayer}$ and C_{Spacer}) either by the use of the point of intersection with the $-Im(Y)\omega^{-1}$ axis or the radius of the half circle (equivalent to ½ C). The latter is used in this work to obtain information about the stability of the used tBLM systems.

2.2.2.5   Evaluation of impedance data in tBLM systems

A membrane system is characterized by two physical quantities, namely the capacitance and resistance. Additionally, the resistance of the electrolyte needs to be taken into account for the description. Due to its low magnitude (~100 Ω) it is monitored at high frequencies. However, by means of EIS, the capacitance of the electrode, the properties of the Helmholtz layer and the ionic reservoirs beneath the bilayer can be investigated. These parts of the system are usually not observable in the same frequency range as the resistance and capacitance of the membrane. Thus, they are not considered in the analysis of the modeled system. The presence of defects or pores, however, can increase the influence of the sub-membrane region of tBLMs.[55] Information about these electrical properties can be obtained by manual analysis of the impedance spectrum on the basis of the different representations or by modeling of the studied system.[56] The latter can be performed with the aid of the continuum theory[41] or using semi-empirical methods. In both cases,

the system is approximated by an equivalent circuit that provides the mathematical equations for a fit to the data. Semi-empirical methods have the advantage of using already established and optimized models for certain properties of the system. In this work the following concepts were used to investigate the tBLM system.

Ohmic Resistance of a Membrane A lipid bilayer is a barrier for ions and a variety of other molecules owing to its hydrophobic core. This property allows to treat a membrane as an isolator with the Ohmic resistance R.

Capacitance of a Membrane Moreover, the description of a lipid bilayer as a capacitor leads to the capacitance C:

$$C = \varepsilon_r \varepsilon_0 \frac{A}{d}. \tag{2.49}$$

In this equation the area and the thickness of the membrane are described by the quantities A and d, respectively. Whereas A depends on the dimensions of the experimental assembly, the thickness of a bilayer is influenced by the phospholipid composition and in a range of 4 - 6 nm.[57] The dielectric constant of the hydrophobic core is $\varepsilon_r = 2.1$ - 2.8. The hydrophilic headgroup region exhibits a value of ca. $\varepsilon_r = 20$ assuming a thickness of 0.6 - 1 nm.[58] However, subject to the level of solvation this value can increase up to the dielectric constant of water ($\varepsilon_r = 80$). Neglecting this contribution, the specific capacitance of a membrane with a hydrophobic part of 4 nm amounts to the value shown in equation 2.50, which is consistent with experimentally obtained values:

$$C = \frac{\varepsilon_r \varepsilon_0}{d} \approx 0.5 - 0.6 \, \mu F \, cm^{-2}. \tag{2.50}$$

2.3 Theoretical calculations

2.3.1 Molecular Dynamics Simulations

2.3.1.1 Molecular mechanics force field

Due to a high complexity many biomolecules are inaccessible to experimental studies. In order to overcome this issue, molecular dynamics (MD) simulations can complement experimental studies.[59] Hence, the analysis of MD trajectories is an efficient, atomistic approach to obtain information about the molecular mechanism of the interaction between AMPs and membrane mimics.[60]

MD simulations are based on classical mechanics, concisely on the Newton's second equation of motion using a classical molecular mechanics (MM) force field (FF). A force field is an assembly of equations and related constants, which reproduce the structural properties of a system describing its energy as a function of its atomic coordinates. Commonly, it is interpreted by means of a combinatorial description of two terms: the internal/bonded (intramolecular) and external/ non-bonded (intermolecular) forces within the system.

The bonded energy is constituted by the contribution of the bond stretching, angle bending, dihedral and improper torsions as well as the Urey-Bradley term and the correction map CMAP. Hooke's law is used to describe the bond stretching for the interaction between pairs of bonded atoms as the difference of the square of the displacement from the reference bond length. The energy is represented by a harmonic potential and the shape of the harmonic potential well is described by the force constant. The angle bending is obtained using a harmonic potential that is specified by the force constant and the difference between the angle to its equilibrium value. The bond torsions (dihedrals), evaluate the role of each bonded quartet of atoms in the system. The periodic potential exemplifying the bond torsions is defined throughout the force constant, the torsion, the phase shift together with the multiplicity. Improper torsions are usually known as out-of-plane bending and consequently defined by harmonic potentials in analogy to the bond stretching and angle bending functions. The Urey-Bradley term is used in specific cases to optimize the fit to vibrational spectra and out-of-plane motions. This component accounts for the cross-term for angle bending using 1.3 non-bonded interactions. Herein the force constant and the separation between the 1.3 atoms in the harmonic potential are reflected. The CMAP term is a numerical correction to overcome the inaccuracies of the conformational energetics in the backbone of the peptides. These defects were initially reflected by a high proportion of π-helical conformations for helical peptides.

The non-bonded interactions encompass pairs of atoms, which are separated by three or more bonds in the same molecule or between separated molecules. These regions are comprised of the electrostatics and Van der Waals interactions described by the 12-6 Lennard-Jones (L-J) potential. Coulomb's law is used to compute the electrostatic interactions between two atoms. The electrostatic potential depends on the partial charges, the distance between both atoms and the dielectric constant *in vacuo*. The electrostatic interaction between two charged particles decays slowly with the interatomic distance.

A variety of biomolecular protein FFs have been developed in the past years. In this work, a Chemistry HARvard Molecular Mechanics - CHARMM FF[61] was used because it is improved to fit accurately to the experimental studies. To run all simulations, a parallel MD code designed for

high-performance simulations of large biomolecular systems, named Nanoscale Molecular Dynamics (NAMD), was applied.[62]

2.3.1.2 Classical MD simulations

Through the integration of Newton's second equation of motion using a classical MM FF, the MD simulations are computed. Concisely, if the force acting on each atom of the system is known, the acceleration of a specific system can be calculated. Afterwards, the equations of motion are integrated resulting in a trajectory describing the progress of positions, velocities and accelerations of each particle in the studied system as a function of time.

If the potential energy of the system is known, such as in case of CHARMM,[61] the force on each atom of mass at its position can be computed. Subsequently, the new positions of the particles can be calculated as a function of time.

Herein, the trajectory of the particle is directly defined by its initial coordinates, initial velocities and initial acceleration. In the Protein Data Bank (PDB),[63] the crystallographic structure is available and employed for defining the initial coordinates. Additionally, the acceleration can be directly computed as the derivation of the potential energy function. While the initial distribution of velocities has to be estimated, usually the Maxwell-Boltzmann distribution is employed at a defined temperature T.

2.3.1.3 MD simulations protocol

The standard protocol used for the performance of the MD simulations can be divided in the following stages: preparation of the system, dynamics and analysis of the trajectories.

Using the starting configuration taken from the PDB[63] possible lacking information, e.g. protonation state of the residues or missing atoms were added. Afterwards, the system has to be solvated and ionized according to the experimental conditions of interest and an energy minimization of the system is required in order to avoid possible steric instabilities. For that purpose, an extension of the steepest descend algorithm was applied, named the conjugate gradient method.[64,65] Once that energy minimization is achieved, the equilibration phase allows the system to reach a thermal equilibrium. In the second stage, the production run is executed with the aim of determining the dynamic properties of the system. The output of a classical MD simulation is a trajectory describing the time dependent evolution of all atoms of the system in a defined period of time. Different macroscopic properties such as energy, temperature, pressure or volume can be evaluated according to statistical mechanics. Additionally, the post-processing of the collected data allows the evaluation of interaction energies, distances and angles and many more properties of interest which can be calculated by the use of plug-ins. In this thesis, properties such as monitoring of the secondary structure and the calculation of the dipole moment (μ) have been applied for an analysis of the trajectories of the AMPs. Besides these properties also root mean square deviation (RMSD), root mean square fluctuation (RMSF), the interaction energy (IE) and time-dependent contact map (TdCM) as well as radial distribution function (RDF) can be used for detailed investigations.

2.3.1.4 Properties computed for the analysis of the trajectories

To monitor the secondary structure, the program STRIDE[66] was used. It is based on a knowledge-algorithm taking into account the combination of the hydrogen bond energy and statistically derived backbone torsional angle information.

The calculation of the dipole moment leads to information regarding the separation between the positive and negative charges in the system is determined. It serves as reference for the calculation of the distance of the protein to the center of mass (COM). It takes into account the mass per atom, the total mass of the protein as well as the coordinates per particle. Once this is defined, together with the partial charges defined from the force field, and the distance per atom, to the reference point is known, it is feasible to compute the dipole moment.

2.3.2 DFT calculations

In the density functional theory (DFT), the total energy E of an electronic system is determined by its electron density r. The total energy is written in terms of the energy of n non-interacting electrons and a term E_{ex} that takes into account the complicated correlated motion of the electrons.

The calculations were performed on the BP86 level of theory and the 6-31g* basis set for all atoms and the implemented polarizable continuum model simulating water as the solvent. During the investigation of alamethicin, DFT is used to calculate a primary structural model of the α-helix/3_{10}-helix and alternative α-helix/α-helix structures, respectively as well as vibrational frequencies of alamethicin (see chapter 6.3.3) The calculation of 4-aminothiophenol was obtained using the 6-31g* basis set for C, H, N, and O atoms, for the heavier S the TZVP basis set, and for Au LanL2DZ (using a pseudo core potential) were applied (see chapter 8.2.3). All geometry optimizations were performed using the keywords "opt=tight" and "int=ultrafine".

3 BIOLOGICAL MEMBRANES

3.1 Phospholipids

The cellular plasma membrane constitutes the outer barrier of eukaryotic and prokaryotic cells as well as cellular compartments, e.g. mitochondria. It contains two leaflets of lipids and has a thickness of 4 nm.[67] Glycerophospholipids are the most abundant class of lipids present in plasma membranes of eukaryotic and prokaryotic cells. These amphipathic molecules are comprised of two hydrophobic acyl chains (*sn*-1 and *sn*-2 residue) that are connected to glycerol forming the diacylglycerol backbone (DAG).[68,69] A phosphate group bound to DAG is the basis of the hydrophilic head group in the simplest structure leading to phosphatidic acid (PA). Its esterification to a choline (phosphatidylcholine, PC), glycerol (phosphatidylglycerol, PG), ethanolamine (phosphatidylethanolamine, PE), serine (phosphatidylserine, PS) or inositol (phosphatidylinositol) results in zwitterionic or charged head groups at physiological pH. The saturated or *cis*-unsaturated acyl chains exhibit different lengths.

The combination of these properties leads to a rich variety of phospholipids[70] forming different assemblies in aqueous phases.[71] Besides lipid-specific parameters, i.e. location and number of double-bonds, head group charge and size, acyl chain length and branching, extrinsic conditions like temperature and concentration determine the fluidity.[72–74] The transition temperature T_m represents the transition from the gel phase (quasi-crystalline; L_β) below T_m to the fluid phase (liquid-crystalline phase; L_α) above T_m that is conceded by unsaturated acyl chains.[75]

This results in the formation of mesophase structures, while the formation of monolayers and bilayers are distinguished from non-bilayer phases, like hexagonal and cubic phases.[68] These latter assemblies are relevant in transient biomembrane states, e.g. fusion, fission and pore formation.[75]

Figure 3.1 shows the phospholipid structures of 1-palmitoyl-2-oleyl-sn-glycero-3-phosphatidylcholine (POPC), 1-palmitoyl-2-oleoyl-*sn*-glycero-3-phospho-(1'-*rac*-glycerol) (POPG) and 1-palmitoyl-2-oleoyl-*sn*-glycero-3-phosphate (POPA) that were used in this work. These lipids contain a saturated 16:0 acyl chain in the sn-1 position and an unsaturated 18:1 chain in the sn-2 position. The cylindrically shaped and zwitterionic POPC is a bilayer-forming lipid due to its spontaneous curvature close to zero.[76] The transition temperature T_m of -2 °C leads to the liquid state at room temperature. For that purpose POPC was used in all presented studies as main lipid component. The negatively charged POPG is characterized by T_m of -2 °C as well. Due to the conical shape with a small head group the anionic POPA is a non-bilayer forming lipid resulting in a negative curvature of the membrane. Furthermore, the lipid is characterized by a transition temperature of 28 °C.[77–79]
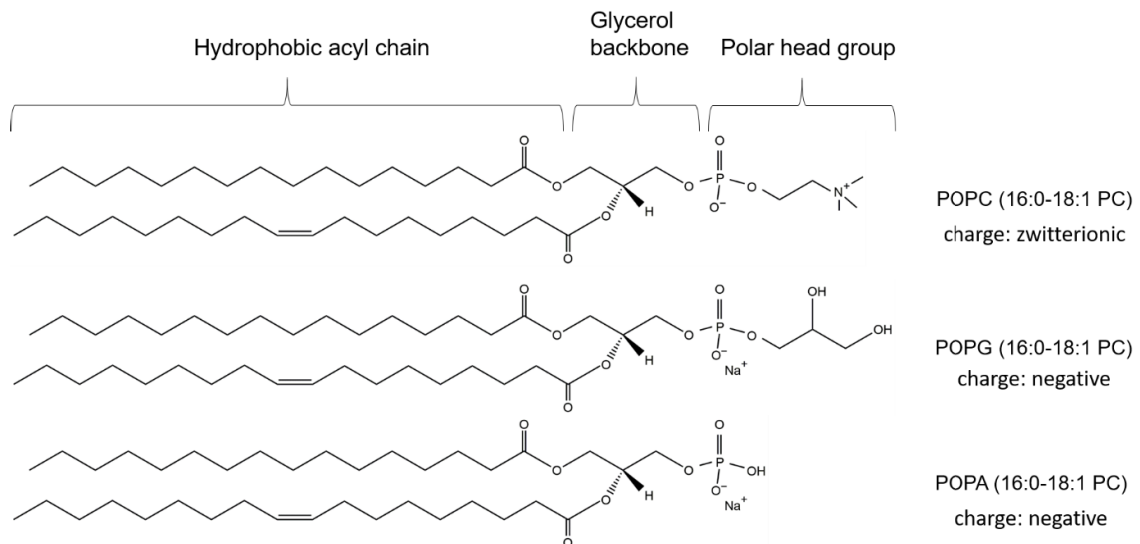
Figure 3.1 Chemical structure of the phospholipids 1-palmitoyl-2-oleyl-sn-glycero-3-phosphatidylcholine (POPC), 1-palmitoyl-2-oleoyl-*sn*-glycero-3-phospho-(1'-*rac*-glycerol) (POPG) and 1-palmitoyl-2-oleoyl-*sn*-glycero-3-phosphate (POPA). The hydrophobic acyl chains, glycerol backbone and polar head group are specified. The charge at neutral pH and chain length as well as number of double bonds are indicated.

3.2 Fluid Mosaic model of biomembranes

In 1972, Singer and Nicolson introduced the "fluid mosaic model" of bilayer membranes on the basis of thermodynamic data.[80] In their concept, a fluid bilayer matrix comprised of phospholipids harbors integral as well as peripheral proteins and glycoproteins. The model considers rapid and dynamic lateral movements of membrane components and changes of their topographic distribution, which was confirmed by subsequent structural, spectroscopic and physical investigations of protein rotation and motion.[80–84]

During the last 40 years this concept was further improved.[85–87] In particular, Simons and Ikonen added knowledge about the role of the protein arrangement within bilayer membranes by the discovery of lipid rafts.[5] These nanoscale (10-100 nm) assemblies[88] are highly dynamic, asymmetric and contain phosphatidylcholine in the outer and sphingolipids in the inner leaflet, whereas sterols are equally distributed on both sides. Different studies proved the existence of lipid rafts in mammalian cells,[89] plants[90] as well as in gram-positive[91] and gram-negative[92] bacteria. The resultant membrane segregation facilitates signal transduction,[93] apoptosis,[94] protein sorting,[95] cell recognition[96] and other functions.

In 2014, the refined "Fluid-Mosaic Membrane Model" (F-MMM)[6] was presented, which includes the recent advances. This concept emphasizes the mosaic structure of membranes with different domains and aspects of lateral protein mobility. In the following section the structural similarities and differences of eukaryotic and bacterial membranes are illustrated.

3.3 Eukaryotic membranes

The outer leaflet of eukaryotic membranes is mainly composed of PC and sphingomyelin representing 80% of the lipid components. The aminophospholipid PE exists in the both layers, however, occurrence in the inner leaflet is higher and PE is the main lipid besides anionic PS.[97,98] AMPs show a low affinity to eukaryotic membranes due to the high amount of zwitterionic lipids, the absence of a strong transmembrane potential and especially the existence of cholesterol in both leaflets.[4,99,100]

3.4 Bacterial membranes

Bacterial plasma membranes as well as the surrounding cell wall exhibit a different composition for gram-positive and gram-negative bacteria (Figure 3.2). In the following section these structural differences are described.
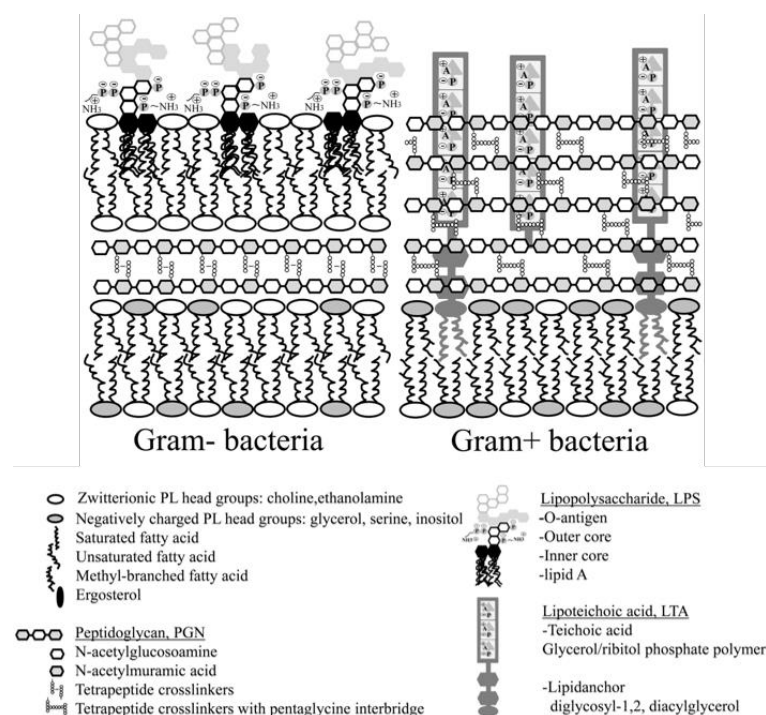
3.4.1 Gram-negative bacteria

The cell envelope of gram-negative bacteria is composed of the inner (cytoplasmic) membrane (IM) and the outer membrane (OM) (Figure 3.2 left). The periplasm in between these two barriers is comprised of a peptidoglycan (PGN) layer of a thickness of 7-8 nm.[101]

The IM of the bacterial strains *E.coli* and *P. aeruginosa* are composed of the zwitterionic phospholipid PE (ca. 60-75%), negatively charged PG (ca. 20-25%) and in the latter case also the anionic cardiolipin (CL, ca. 11%).[102–105] The OM contains negatively charged lipopolysaccharide (LPS) leading to a strong negative surface charge.[106] Due to transmembrane β-barrel proteins named porins or outer membrane proteins it is permeable to hydrophilic molecules of a size up to 600 Da.[107]

3.4.2 Gram-positive bacteria

Gram-positive bacteria are surrounded by a plasma membrane that is covered by many PGN layers of 40-80 nm in thickness (Figure 3.2 right).[108] The cytoplasmic membrane of *S. aureus* comprises PG (ca. 57%), Lysyl-phosphatidylglycerol (LPG, ca. 38%), and CL (ca. 5%).[109,110] In contrast the membrane composition of *B. subtilis* includes PG (ca. 70%), PE (ca. 12%) and CL (ca. 4%) in its plasma membrane.[111–113]

A further characteristic component of the gram-positive cell wall is lipoteichoic acid (LTA). It consists of a glycerol/ribitol phosphate polymer named teichoic acid, which is connected to the plasma membrane by a lipid anchor (diglycosyl-1,2, diacylglycerol).[114]

Figure 3.2 Representation of gram-negative (left) and gram-positive (right) cell envelopes. Reproduced with permission from Malanovic, N. and Lohner, K. Gram-positive bacterial cell envelopes: The impact on the activity of antimicrobial peptides *Biochimica et Biophysica Acta* 1858, 936–946 (2016).[108]
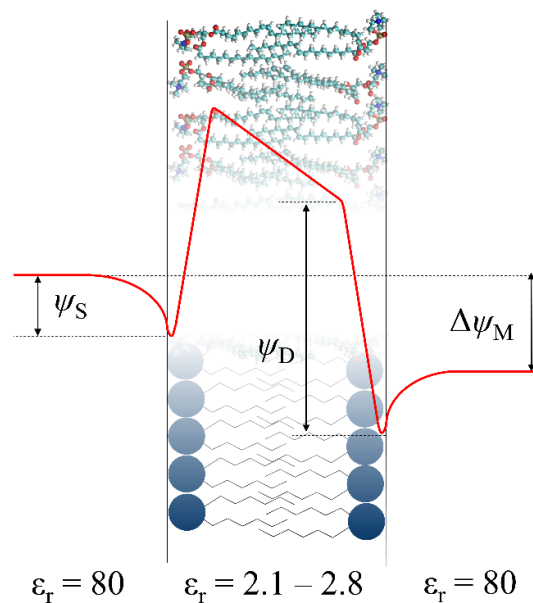
3.5 Transmembrane potential

The passage of the membrane barrier requires a variety of carriers embedded in the bilayer membrane, e.g. ion-channels. These molecules conduct the transmembrane ion transport leading to an imbalanced ion concentration and thus, to an electrical potential difference $\Delta\psi_M$ between the N-side and P-side of the membrane. The magnitude of the transmembrane potential is in the range of 10-100 mV.[115]

Due to the structural arrangement of bilayer membranes combining zwitterionic or charged head groups, with a hydrophobic membrane core and oriented water dipoles the potential distribution is not linear, instead it shows a characteristic profile (Figure 3.3).

Most of the cellular membranes are characterized by a negative surface potential ψ_S due to an amount of 10-20% of lipids with negatively charged head groups.[115,116] In eukaryotic cells phosphatidylserine contributes to the overall charge, bacterial cell envelopes contain phosphatidylglycerol and cardiolipin (*vide supra*).[117–119] The surface potential can be described by the Gouy-Chapman-Stern model.[119–121]

The alignment of lipid residues and water dipoles cause a sharp increase in the dipole potential ψ_D within the lipid head group region. In the hydrophobic membrane core, the potential decreases linearly by the transmembrane potential difference $\Delta\psi_M$.

Experimental estimations and MD simulations for saturated phosphatidylcholines led to an estimation of ψ_D in a range of of 200 - 500 mV[122,123] and 300 - 1,000 mV, respectively.[124,125] The associated electric fields have a magnitude of 10^8 and 10^9 V m^{-1}.

Figure 3.3 Electrical potential distribution over a phospholipid bilayer membrane. $\Delta\psi_M$ represents the transmembrane potential, ψ_S the surface potential and ψ_D the dipole potential. The relative permittivity ε_r is indicated for water and the lipid bilayer. (Reprinted with kind permission from Jacek Kozuch (2013). *Structure-Function Relationships of Membrane Proteins - Spectroelectrochemical Investigation of Artificial Membranes*), Technische Universität Berlin, Fakultät II.[134]

3.6 Biomimetic membrane systems

Structural and functional investigations of membrane proteins and dynamic peptide-membrane interactions in a systematic way require stability and the flexibility of fluid bilayer membranes at the same time.

Biomimetic membrane systems adsorbed on metal interfaces are two-dimensional planar constructs, which are widely used to monitor peptide and protein incorporation into bilayer membranes by spectro-electrochemical approaches.[30,48,51,126–130] For that purpose, nanostructured Au electrodes are functionalized by organic self-assembled monolayer (SAM) molecules, that are connected to the metal by a thiol-group. Due to the specific SAM head-groups hydrophobic, hydrophilic and/or charged surfaces are provided.[131–133] On this basis lipid bilayers and monolayers can be assembled by spreading of unilamellar liposomes on top of the SAM.[134]
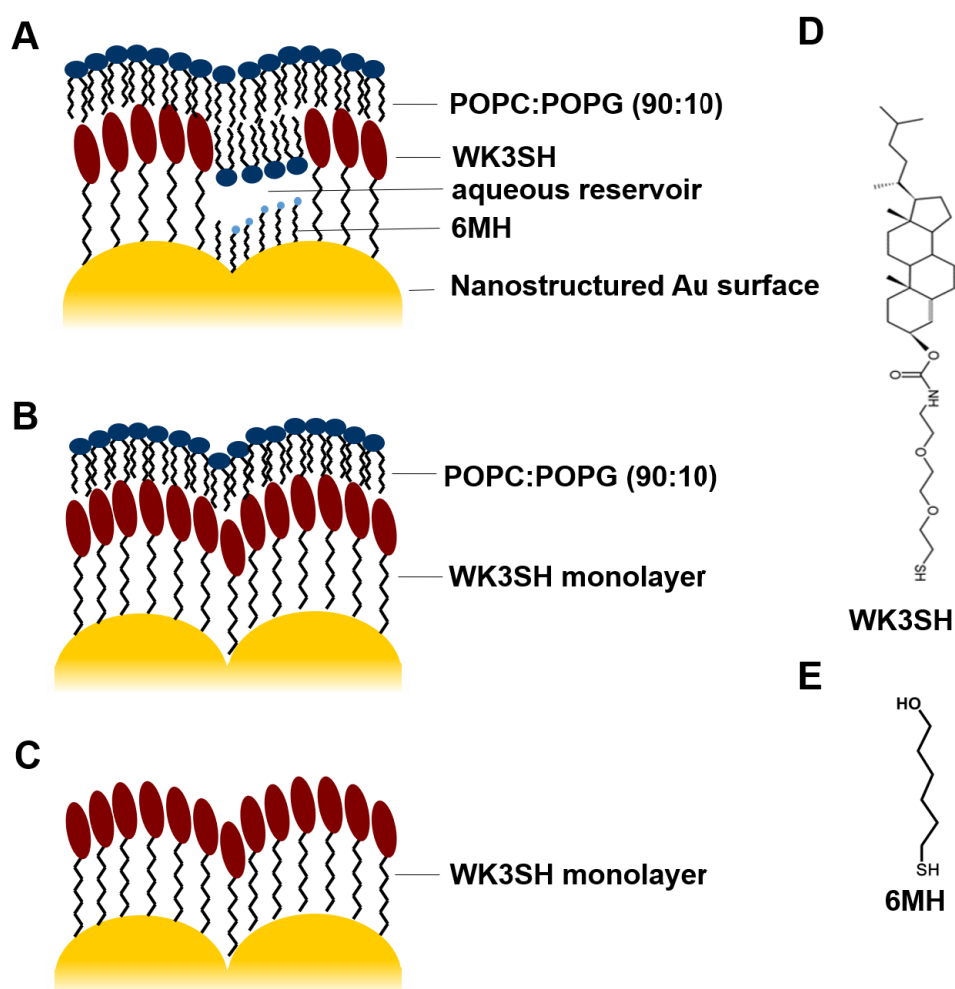
Figure 3.4 A: Tethered bilayer lipid membrane (tBLM). B: Tethered hybrid lipid membrane (tHLM). C: WK3SH monolayer providing a hydrophobic surface as reference. Nanostructured Au surfaces are covered by a mixed self-assembled monolayer of hydrophobic WK3SH (D) and hydrophilic 6-Mercaptohexanol (E, 6MH) or a WK3SH monolayer, respectively. Spreading of POPC:POPG (90:10) liposomes leads to alternating lipid bilayer/monolayer islands (A) or a lipid monolayer (B). Adapted with permission from Wiebalck, S., Kozuch, J., Forbrig, E., Tzschucke C. C., Jeuken L. J. C., Hildebrandt P. Monitoring the Transmembrane Proton Gradient Generated by Cytochrome bo3 in Tethered Bilayer Lipid Membranes Using SEIRA Spectroscopy. *J. Phys. Chem. B* 129**,** 2249–2256 (2016). Copyright (2016) American Chemical Society.[325]

In this work, different biomimetic constructs were used to investigate biomolecules by SEIRA spectroscopy in combination with electrochemistry. The established tethered bilayer membrane system (tBLM)[8,35,134] was optimized for the study of cationic AMPs by introduction of negatively charged phospholipids (Figure 3.4A). The assembly required a mixed SAM comprised of the hydrophobic cholestanyl-linker [(β-cholestanoxy)ethoxy)ethoxy)ethanethiol] (WK3SH, Figure **3.4**D)[8] and the hydrophilic 6-mercaptohexanol (6MH, Figure 3.4E). This surface was covered by alternating islands of bilayers and monolayers of POPC:POPG phospholipids in a molar ratio of 90:10, resulting in an anionic surface. In between the 6MH-spacer and the hydrophilic headgroups of the lower membrane leaflet, an aqueous reservoir avoids the contact of the bilayer with the metal electrode. Furthermore, this allows for the investigation of proteins and peptides that incorporate in a transmembrane arrangement.

In comparison, a tethered hybrid lipid membrane (tHLM) based on a pure WK3SH monolayer was constructed on a nanostructured Au surface (Figure 3.4B). The POPC:POPG (90:10) lipid monolayer was connected by the hydrophobic acyl chains to the hydrophobic cholestanyl-headgroup. This system restricted a transmembrane incorporation of biomolecules. It represented a suitable reference system to study differences in the insertion process of peptides in lipid bilayers and monolayers. The construction of a pure WK3SH monolayer enabled the study of peptide attachment on hydrophobic surfaces compared to hydrophilic lipid surfaces.

The investigation of the bacterial Complex I (CpI) was conducted using a supported-lipid membrane (SLM) that allowed the monitoring of the transmembrane proton translocation by means of SEIRA (Figure 6.22). A 4-aminothiophenol (4-ATP) SAM was adsorbed to the nanostructured Au surface. 4-ATP was used to observe a protonation or deprotonation of the surface, since it can exist in two different forms (depicted in Table A7 in chapter 8.2.3). The adsorption of POPC, POPA and the quinone DMN[9] in a ratio of a 80:10:10 lipid mixture led to lipid membranes, that allowed the protein incorporation and functional assays.

4 ANTIMICROBIAL PEPTIDES AND MEMBRANE PROTEINS

Antimicrobial peptides (AMPs) and membrane proteins are two classes of biomolecules that are involved in the processes at cellular plasma membranes with contradictory effects. On the one hand, AMPs belong to the host defense mechanisms protecting it by collective binding and disruption of pathogenic membranes or its translocation to target intracellular sites. Currently, the construction of novel AMPs on the basis of natural templates represents a promising approach for developing future antibiotics.

On the other hand, the interplay of specialized membrane proteins stabilizes the cellular homeostasis due to versatile functions. The signal transduction at the membrane, proton and electron transfer, potential dependent ion translocation and enzymatic reactions are facilitated by these proteins.

The study of such biomolecules needs the use of non-invasive methods in a "native-like" environment that can be provided by artificial membrane systems. Especially, the application of SEIRA spectroscopy proved to be a suitable method to relate structural and functional information of peptides as well as membrane proteins embedded in biomimetic membrane systems even under consideration of potential-dependent processes.[8,30,49,135] This chapter provides information about the general structure of proteins peptides. Furthermore, the AMPs cathelicidin LL-37 and alamethicin as well as the membrane protein bacterial Complex I are introduced.

4.1 Structure of peptides and proteins

Peptides and proteins are composed of 20 different proteinogenic and a variety of non-proteinogenic (e.g. in case of alamethicin) L-α-amino acids, which are connected via a peptide (amide) bond. The primary structure of a protein is characterized by its amino acid sequence that determines intramolecular interactions, i.e. hydrogen bonding processes. This leads to folding of the primary structure into defined secondary structures, e.g. α-helix, β-helix, β-sheet, turns, and random coils (Figure 4.1).

The hydrogen bonds between the C=O and N-H group of the third succeeding neighbor leads to right-handed spiral-like α-helices. In this structure, each helix turn is comprised of 3.6 amino acids. The amide C=O bonds are aligned in parallel and directed towards the helical C-terminus (Figure 4.1). For that reason, the amino acid residues are oriented externally resulting in hydrophobic, hydrophilic or amphipathic α-helices depending on the polarity of the residues. Membrane proteins are composed of helices with hydrophobic moieties, which permit protein incorporation and structural stabilization within the hydrophobic membrane part of the bilayer.

The parallel or antiparallel arrangement of linear peptide chains known as β-strands results in the formation of β-sheet structures (Figure 4.1). The amino acid residues are located at both sides of the β-strand, since all amide C=O bonds are aligned antiparallel to each other within each strand. This structure is characterized by hydrogen bonds between opposing peptide bonds. In parallel sheets the orientation of these hydrogen bonds are oriented at distorted angles to the sheet direction. However, antiparallel sheets possess hydrogen bonds that are normal to the sheet direction and parallel to each other.
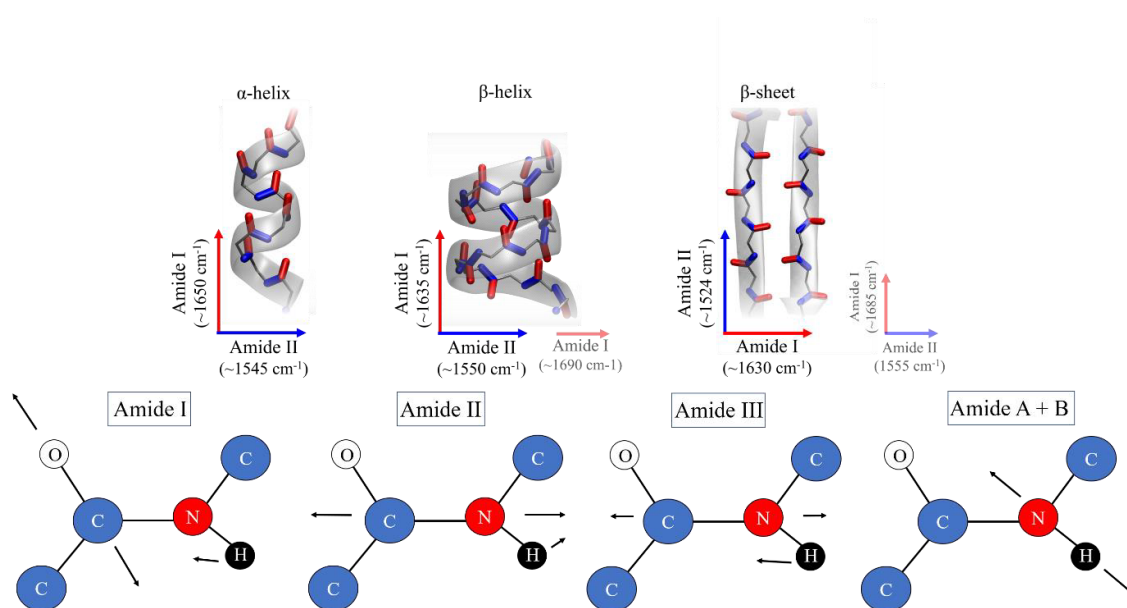
Figure 4.1 Scheme of the amide vibrations of the peptide and protein backbone. Top: Orietation and spectral wavenumber of amide I and amide II vibration in a α-helix (left), β-helix (middle) and β-sheet). The C=O bonding of the amide I (red) and the C-N bonding of the amide II mode (blue) are shown. Bottom: Scheme of the amide modes of the peptide and protein backbone. Reprinted with kind permission from Jacek Kozuch (2013). *Structure-Function Relationships of Membrane Proteins - Spectroelectrochemical Investigation of Artificial Membranes*, Technische Universität Berlin, Fakultät II.[134]

Turns are segments that are comprised of a maximum number of five amino acids. They show a U-like conformation changing the direction of propagation by 180°.The formation of α-, β-, or γ-turns is dependent on the position of the hydrogen bonds. Random coils do not exhibit regular structural elements.

β-helices originate from an association of β-strands to a β-sheet that propagates in a helical pattern. One can distinguish between parallel and antiparallel β-helices which differ substantially and can occur, both, in a left and right-handed manner.[136,137]

The combination of different secondary structures characterizes the tertiary structure of proteins. The main factors, which stabilize this arrangement are electrostatic and hydrophobic interactions as well as covalent and hydrogen bonds. The further assembly of tertiary structural elements leads to the quaternary structure.

Table 4.1 Assignment of amide vibrations associated with the peptide and protein backbone. The group vibrations are depicted in Figure 4.1. Reprinted with kind permission from Jacek Kozuch (2013). *Structure-Function Relationships of Membrane Proteins - Spectroelectrochemical Investigation of Artificial Membranes*, Technische Universität Berlin, Fakultät II.[134]

Designation	Wavenumber [cm^{-1}]	Group vibrations
Amide A	3310-3270	N-H stretching
Amide B	3010-3030	N-H stretching
Amide I	1700-1600	C=O stretching, minor contribution of N-H bending
Amide II	1580-1480	combined C-N stretching/N-H bending
Amide III	1300-1230	combined C-N stretching/N-H bending (different proportions and signs)

A loss of these structural conformations due to external factors, e.g. high temperatures or non-physiological pH values, leads to irreversible denaturation and malfunction of proteins, which is related to several diseases.[138,139]

4.1.1 Infrared spectroscopic properties

By means of IR spectroscopy peptides and proteins can be investigated by specific spectral contributions of the polyamide backbone (i.e. secondary and tertiary structure) and of amino acid side chain residues.[140] The examination of side chain modes is still a challenge due to a small number of contributing vibrations.[141] However, the protein backbone amide modes (Figure 4.1 and Table 4.1) cover the complete molecule and indicate comparably strong vibrational intensities. Information about the secondary and tertiary structure of proteins can be achieved by analysis of amide I and amide II modes. These modes are dominated by the C=O stretching (with minor contributions of the N-H bending), and a combination of N-H bending and C-N stretching, respectively. The amide I position is highly dependent on the hydrogen bonds and thus the frequency of this mode can be related to structural elements, e.g. α-helices, β-helices, β -sheets, turns, and random coils.

Moreover, transition dipole moment coupling within structural elements can result in a separation of amide bands into symmetric and asymmetric components (in-phase and out-of-phase vibration) with different frequencies and polarizations.[140,142] This allows theoretical and experimental studies on the spectral composition of the amide I band envelope providing information about the protein backbone.[140,143,144] The amide II band was also investigated by theoretical calculations that resulted in information about the position and polarization as well.[145] In the following the amide I and amide II positions are described for common secondary structures depicted in Figure 4.1.

α-helix The amide I IR absorption of α-helical structures is located at frequencies between 1657 cm^{-1} and 1648 cm^{-1}. The transition dipole moment is oriented in parallel to the helix axis. The amide II band position is at ca. 1545 cm^{-1} with a perpendicular polarization.

β -sheet The amide I band exhibits two components because of dipole moment coupling.[140] The main absorption at ca. 1630 cm^{-1} has a transition dipole moment that is oriented perpendicular to the propagation direction of the chain. The second absorption located at ca. 1685 cm^{-1} has a direction of the transition dipole moment along the chain. The amide II band is also characterized by a main component at ca. 1524 cm^{-1} and a weaker component at ca. 1555 cm^{-1} with parallel and perpendicular polarizations.[145]

β -helix This structural element reveals a main amide I component at ca. 1635 cm^{-1} and a minor component at 1690 cm^{-1}.[136] The orientation of the transition dipole moment is perpendicular and parallel to the helix axis for these components, due to the helical structure.

Turn The amide I band absorption of turns ranges from 1690 to 1630 cm^{-1}, due to their hydrogen bonds, but it is mostly observed at 1686 and 1662 cm^{-1}.

SEIRA spectroscopy is sensitive to IR absorptions of molecules in close vicinity (~ 8 nm) to the nanostructured Au film, while contributions from the bulk solution can be neglected. Furthermore, on the basis of the surface-selection rule, particularly strong signals are recorded for IR modes with transition dipole moment changes perpendicular to the surface.[36] This fact can be used for an estimation of the orientation of ordered transmembrane helices of membrane proteins or enzymes. Whereas the modes in the amide II region result from dipole moment changes along the membrane plane and perpendicular to the helix axis, the amide I modes are preferentially polarized along the helix axis.[146,147] Thus, the ratio of amide I to amide II band intensity provides

a quantity describing the orientation of peptides and proteins at SEIRA-active surfaces. In the case that this ratio is higher than the isotropic/non-polarized ratio a preferential orientation of helices perpendicular to the surface is expected, whereas in the opposite case of smaller ratios helices are aligned preferentially along the surface.[8,25,29,30,148]

4.2 Antimicrobial peptides

The development of modern antibiotics in the first half of the last century was a mile stone in the history of medicine and allowed the treatment of many infectious diseases transmitted by bacteria. However, very soon after introducing these drugs into clinics, first antimicrobial resistances started to develop. Bacterial resistance is a naturally occurring adaption of pathogens to antibiotics that are mostly produced by other microorganisms. An important example are the widely used ß-lactam antibiotics, which undergo an enzymatic cleavage of the ß-lactam ring by ß-lactamases resulting in a dysfunction.[149] Genetic studies revealed that the responsible resistance genes already exist for 100 million years without development of resistances.[150] This finding clearly shows that emergence of multi-drug resistant pathogens[151] in the last decades is attributable to different manmade factors, e.g. increasing prescription of antibiotics in therapies, their use in agriculture, migration and environmental pollution.

According to the World Health Organization this is one of today's major global health threats.[151,152] Within the next decades an "antibiotic crisis" can be the consequence, in case there is a lack of substitutes.[153] A subsequent increase of the probability of morbidity and mortality results also in vastly rising economic costs each year. Novel antibacterial substances need to fulfill the requirements of a high toxicity against microbes, by being non-toxic to host cells at the same time.

The research field investigating antimicrobial peptides (AMPs), a highly promising class of amphipathic, short peptides (10-100 amino acids),[154] aims to develop alternatives to conventional antibiotics using a completely different approach. AMPs belong to the natural defense system of many organisms, ranging from microorganisms over plants to the innate immune system of humans.[155]

AMPs are mostly cationic, composed of L-amino acids and adopt linear, α-helical (e.g. cathelicidin, alamethicin and magainin[156]) or β-sheet (e.g. defensins)[157] secondary structures, which can be stabilized by different numbers of disulphide bonds formed by cysteine residues.[158,159]

These molecules exhibit a broad-spectrum activity being bactericidal and bacteriostatic against gram-negative and gram-positive bacteria.[114] Moreover, activity against fungi, parasites, viruses and even tumor cells is reported.[160] In higher eukaryotic organisms, AMPs are also known as "host defense peptides," a term that highlights the pleiotropic functions and additional immunomodulatory activities".[161] An interesting subgroup are also cell penetrating peptides.[162] They are able to pass the plasma membrane without disturbing its structural integrity to target intracellular sites, offering their use as transporters for therapeutic substances, e.g. drugs, nucleic acids or chemotherapeutics.[163–165]

However, AMPs also exhibited to some extent hemolytic activity.[166–168] Therefore, it is crucial to increase the understanding of the overall mechanisms of action. On this basis, natural templates can be used for the synthesis of target specific mutated peptides, which are non-hemolytic and result in future antibiotic drugs.

4.2.1 Modes of peptide-membrane interaction

The main mode of action of AMPs is based on their specific but diverse interactions with the cellular membrane of the infectious invader. Figure 4.2. illustrates different modes of action of α-helical peptides.[162] In many cases these molecules show a disordered secondary structure in solution and the formation of the α-helical structure after membrane binding. According to Sani et al. this leads to a higher rigidity of the peptide amide backbone. Hydrogen bonds between the N−H group and C=O group allow for a disruption of the surface tension and structural stabilization even in a fluid membrane environment.[162]

In contrast to eukaryotic membranes, that exhibit a neutral net charge at the outer leaflet of the cell membrane, bacterial plasma membranes are anionic due to the phospholipid composition. This leads to an electrostatic attraction of cationic AMPs and a high attachment affinity. After secondary structure formation hydrophobic forces trigger the further steps due to a high amount of hydrophobic residues in the peptide. The exact mechanism of insertion and disruption depends on the peptide's structural properties, that determine its charge, amphipathicity, hydrophobicity as well as three-dimensional characteristics, i.e. polar angle and stereo geometry.[4]
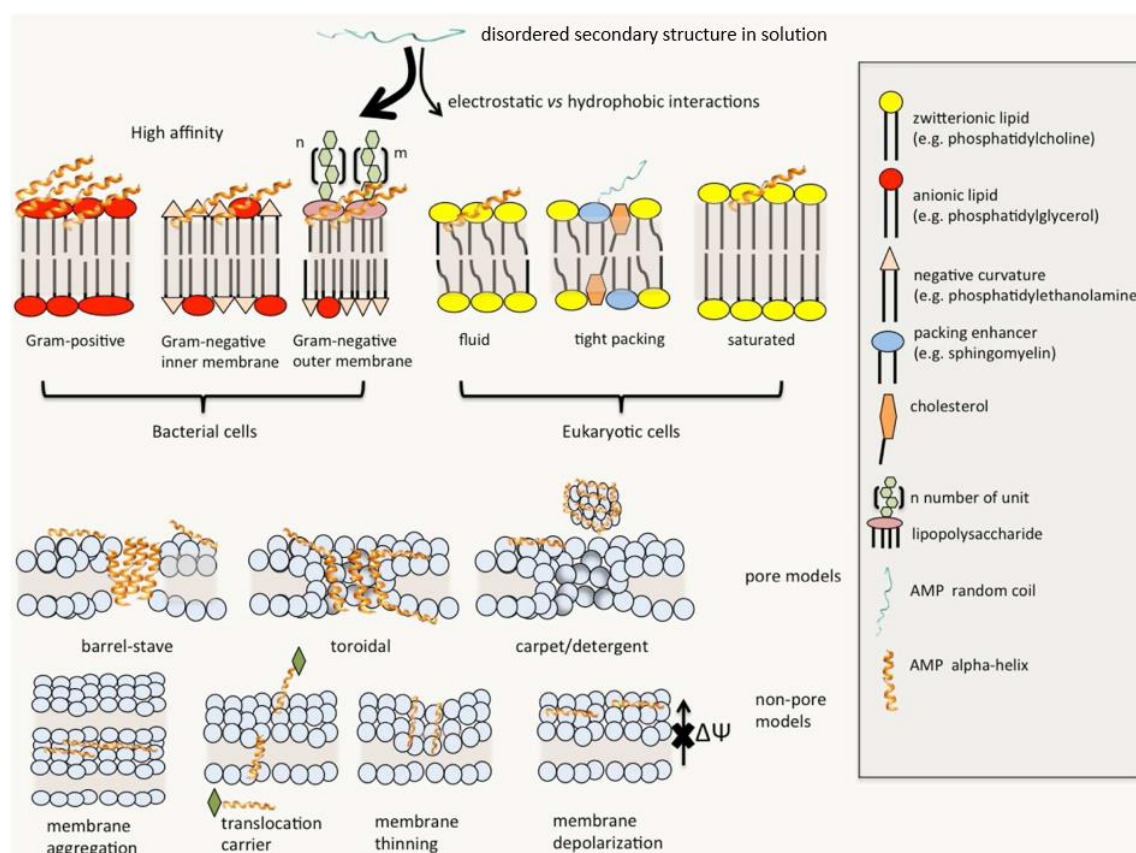
Figure 4.2 Scheme of mode of interaction between α-helical AMPs and bilayer membranes of bacterial and eukaryotic cells. After peptide binding induced by electrostatic forces the peptides adopt an amphipathic secondary structure and further interact due to hydrophobic forces. Different pore models and non-pore models are represented. Adapted with permission from Sani, M.-A. & Separovic, F. How Membrane-Active Peptides Get into Lipid Membranes. *Acc. Chem. Res.* 49, 1130–8 (2016). Copyright (2016) American Chemical Society [162]

Several models have been proposed and involve the formation of barrel-stave or wormhole-like (toroidal) pores spanning the membrane as well as lysis according to the carpet model.[161,169] However, the detailed underlying mechanisms proved to be very complex and non-identical even within certain structural classes of AMPs.[4]

The Shai-Huang-Matsuzaki model combines several pore models shown in Figure 4.2.[170–173] It proposes a carpet-like attachment, lipid displacement and to some extent an integration into the target cell membrane.[174] Moreover, non-pore forming models that consider membrane aggregation[175] and thinning,[176,177] cell permeation and internal target binding[162,165,178,179] as well as depolarization of the transmembrane potential[180] are stated in literature. However, for many peptides the exact mechanism of action remains elusive. Thus, predicting activity of AMPs for the design of novel drugs is still a major challenge.

4.2.2 Human Cathelicidin LL-37 and the fragments LL-32 and LL-20

The human antimicrobial peptide (AMP) LL-37 belongs to the family of cathelicidins. The precursor is called human 18-kDa cationic antibacterial protein (hCAP18). It contains a N-terminal signal cathelin (cathepsin L inhibitor) domain[181] that is highly conserved.[182] The C-terminal cleavage of the protein by proteinase 3, a serine proteinase, results in the formation of the mature peptide composed of 37 amino acid moieties.[183]

LL-37 is produced by neutrophils at epithelial surfaces, e.g. skin and mucosa, in concentrations of ca. 2-5 µg/mL.[184,185] Different investigations revealed a significant inflammation dependent up-regulation leading to concentrations between 15 µg/mL and 1.5 mg/mL to protect the host from invading pathogens.[185–187] Besides the antimicrobial activity and ability to inhibit biofilm formation[188–190] it displays diverse immunomodulatory functions.[191,192] Furthermore, LL-37 plays a role in wound healing,[193] chemotaxis of neutrophils as well as mast cells[194,195] and regulates apoptosis.[196-198] Interestingly, it becomes evident that binding of LL-37 to membrane proteins of eukaryotic cells, e.g. G-protein coupled receptors or receptor tyrosine kinases triggers signaling cascades.[199]

A very important mechanism of action is the interaction of LL-37 with bacterial cell wall compartments and the plasma membrane. The study by Sochacki et al. showed that the AMP saturates and passes the outer membrane of gram-negative *E. coli* and accumulates in the periplasmic space where it interacts with LPS and the inner membrane.[200]

LL-37 is a cationic (+6) and amphipathic AMP containing charged, hydrophobic and hydrophilic amino acids. Studies in SDS micelles revealed that the residues 2-31 form an α-helical secondary structure with a bend between the residues G14 and E16 and a disordered C-terminus (residues 32-37; Figure 4.3).[11]

Besides D-amino acid substitutions,[201] the synthesis, isolation and investigation of peptide fragments of LL-37 is a promising approach for the development of therapeutic analogs that are active against different bacterial strains.[10,11,194,202–205] The fragment FK 13, investigated by Li et al., is comprised of residues equivalent to the amino acid chain F17- R29 of LL-37 and is referred as "core peptide", due to its high antibacterial activity (see Figure 4.3).[10,11] In a previous study Dannehl et al. synthesized LL-37 and the fragments LL-32 as well as LL-20, which did not contain the complete peptide core region. Each peptide contained an amidated C-terminus and an unstructured N-terminus. The physical-chemical characteristics were analyzed by Infrared reflection absorption spectroscopy, X-ray scattering and Circular dichroism spectroscopy in aqueous solution leading to an unstructured conformation.

In this work an approach combining infrared spectroscopy and MD simulations is addressed to investigate LL-37, LL-32 and LL-20. First, the secondary structure of the peptides in solution, that sets the foundation for studies using artificial membranes, is determined by FT-IR spectroscopy. To study the peptide-membrane interaction the tBLM was constructed as described in section 3.6 and SEIRA spectroscopy was applied.

The distance-dependent signal attenuation (up to 8 nm) is an important characteristic of this technique that allows the distinction of the vibrational modes of the tBLM as well as peptides from the bulk solution. Moreover, it offers necessary information about the position of the peptides during their membrane interaction. Another specificity of SEIRA is the enhancement of transition dipole moments of the amide I and amide II modes depending on the peptide's orientation within the membrane.[206]

These aspects were analyzed by incubation of LL-37, LL-32 and LL-20 into a negatively charged lipid membrane consisting of POPC:POPG (90:10). The obtained SEIRA spectra allowed for the calculation of the amide I/amide II ratio leading to information about the orientation of all peptides. Moreover, the peptide position with regard to the bilayer surface can be estimated.

Molecular Dynamics (MD) simulations were conducted taking the experimental conditions into account and provide information about the structure of LL-37, LL-32 and LL-20 as well as their interaction with a simulated POPC:POPG (90:10) membrane. Eventually the obtained
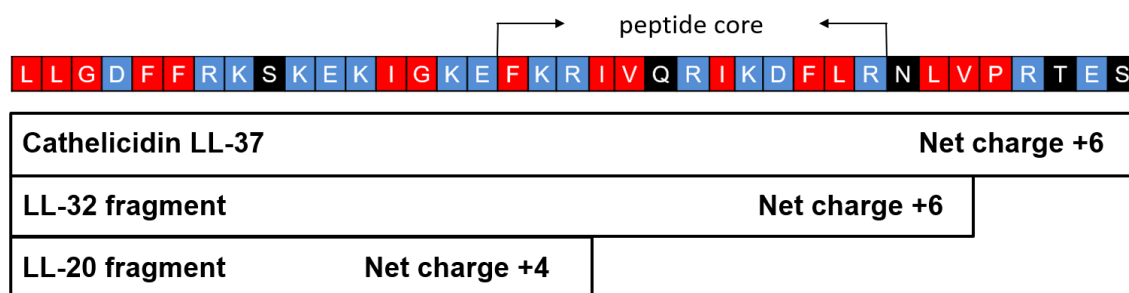
Figure 4.3 Scheme of the amino acid chain of cathelicidin LL-37 and the fragments LL-32 and LL-20. The peptide core between the residues F17 and R29 is highlighted. There are non-polar (red), polar charged (blue) and polar non-charged (black) residues depicted. The previously described peptide core is comprised of the residues F17 – R29. Adapted with kind permission from Alejandra de Miguel (2017). *Elucidating the Mechanism of Action of Antimicrobial Peptides by means of Computational Approaches*, Technische Universität Berlin, Fakultät II.[287]

experimental and theoretical data are rationalized in the context of the peptide's primary structure and the role of the "core peptide" will be analyzed.

4.2.3 Alamethicin

The information presented in this section are reproduced from Forbrig et al.[206] Alamethicin (ALM) is a 20-amino acid long AMP and was isolated for the first time from *Trichoderma viride*.[207] It belongs to the class of peptaibols, a group of fungal secondary metabolites.[13] It has been studied thoroughly due to its antibacterial and antifungal activity, and provided valuable insight into the antibiotic membranolysis by AMPs.[13] At the same time, due to its property of transmembrane potential-induced ion channel formation, it is predestined as a model system to improve the mechanistic understanding of voltage-dependent ion channels in general.[208] The amino acid sequence of ALM is characterized by a large number of hydrophobic residues, in particular the non-proteinogenic amino acid 2-aminoisobutyric acid (Aib), an acetylated N-terminus, the C-terminal phenylalaninol (Pheol), and a proline at position 14 (Figure 4.4). As shown by X-ray crystallography,[209] NMR[210] and optical spectroscopy,[211] ALM adopts a helical structure with a Pro-14-induced bend resulting in an α-helical N-terminal part and a 3_{10}-helical or α-helical C-terminal fragment. This causes alignment of the few polar amino acids Glu-18, Gly-11 and Gln-7 on one side of the helix and thus renders ALM amphipathic with a hydrophobic and hydrophilic patch, and a strong dipole moment corresponding to a net negative charge at the C-terminus (see illustration in Figure 6.16 in chapter 6.3.3).[212] Due to its amphipathic nature, ALM can interact either with the membrane surface in a horizontal manner or get inserted into the membrane vertically to form voltage-dependent ion channels according to the barrel-stave model.[13] In this model, a cylindrical array of 4-12 parallel ALM helices is established, in which the hydrophobic sides face the hydrophobic membrane core, while the hydrophilic parts create a water-filled conductive pore with a diameter of ca. 1.8 to 2.6 nm.[213] The process of insertion into the membrane is either induced by high ALM concentrations in solution and on the membrane surface[214] or governed by interaction of the strong dipole moment with the interfacial electric field.[208,215] In both cases, not only the structure, but also the peptide-membrane interactions and the resulting orientation and positioning within the membrane play a central role for the activity. This is not only true for ALM but for AMPs in general. Therefore, many attempts were made to gain insight into the orientation of ALM[210,216–219] and other AMPs in phospholipid bilayer systems.[220–223] However, monitoring these processes in situ and under control of the electrochemical potential is accompanied by many technical difficulties. In this respect, IR spectroscopy is a particularly appropriate method since it can be combined with electrochemical approaches and does not rely upon peptide labeling due to the intrinsic anisotropy of peptide backbone vibrational modes, i.e. the amide I and amide II normal modes.[146]

These normal modes are composed mainly of the amide group's C=O stretching [ν(CO)] and a combination of the N-H bending [δ(NH)] and C-N stretching [ν(CN)] coordinates, respectively. The transition dipole moments (TDM) of the amide I and II modes were shown to be oriented ca. 29° - 40° and 77° - 79° with respect to the main helix axis for model helices.[224–226] Accordingly, IR spectra of helical peptides or proteins are frequently interpreted by assuming the TDM vectors of the amide I and amide II as being approximately parallel and perpendicular to the helix axis.[30,34]

Ac – Aib – Pro – Aib – Ala – Aib – Ala – Gln – Aib – Val – Aib – Gly – Leu – Aib – Pro – Val – Aib – Aib – Glu – Gln - Pheol

Figure 4.4 Primary structure of alamethicin containing the non-proteinogenic amino acids 2-aminoisobutyric acid (Aib) and phenylalaninol (Pheol).

However, the above estimates have to be considered with caution. First, they refer to a linear conformation of the helix and, second, they lack the information about the direction to which the TDM vectors are inclined. A linear conformation of the helix is, however, only a crude approximation in many cases such that the contributions of TDM vectors with different inclination angles to the IR spectrum are not considered. Thus, if more exact and quantitative spectral analyses are required, the orientation of the TDM vectors of the amide I and amide II have to be determined specifically for individual peptides or proteins. Computational methods provide an elegant way of obtaining this information, which otherwise are very difficult to access experimentally, given that the structure of the peptide or protein can be simulated appropriately. Density functional theory (DFT) calculations have been shown to describe the IR spectra of peptides with increasing accuracy,[227–229] although computational costs currently restrict this approach to peptides or small protein fragments. These limitations can be overcome by using other theoretical methods.[230,231]

In this work, the spontaneous and potential-induced incorporation of ALM into a tethered hybrid lipid membrane (tHLM) and tethered bilayer lipid membrane (tBLM) was monitored in-situ in order to determine the structure and orientation of the peptide during these processes (Figure 1). The tethering offers a higher stability compared to other commonly used supported membrane systems when assembled on nanostructured surfaces for spectroelectrochemical studies.[33,34] For that purpose, potential-controlled surface-enhanced infrared absorption (SEIRA) spectroscopy was employed, using an Au-coated attenuated total reflection (ATR) element.[232] The coated ATR element serves as the support for a new class of tBLMs lacking IR signals in the amide region,[8] and also acts as the working electrode to control the electrochemical potential. At the same time, it amplifies the IR signals of molecules in the direct vicinity to the Au surface (up to ca. 8 nm) and thus selectively probes the tBLM as well as attached or incorporated peptides without interference of spectral contributions from the bulk solution.

The key feature of SEIRA for this work is the polarization of the enhanced IR radiation along the surface normal. In this way, vibrations with TDMs oriented in parallel to the surface normal (surface-selection rule)[232] were observed and thus the (re-)orientation of molecules in the membrane system can be determined. In order to obtain the vectors of TDMs for ALM, the IR spectrum was calculated using DFT and a new and more exact mathematical model for re-orientation of peptides detected by SEIRA spectroscopy was applied. By combining the results from experiment and theory, information about the dynamics of orientational changes of ALM during the spontaneous incorporation and upon interaction with a transmembrane potential was obtained. In this way, information about the directionality of ALM incorporation into the tBLM were obtained. In conclusion, the quantitative determination of the orientation of a peptide using SEIRA is demonstrated. This paves the way for studying further AMPs and testing novel derivatives for potential antimicrobial activity.

4.3 Bacterial respiratory electron transport chain

Cellular organisms harvest and transform energy obtained from the environment and store it in form of adenosine triphosphate (ATP) to stabilize homeostasis. For that purpose carbohydrates are used as energy source that are metabolized in the glycolysis and are forwarded to the Krebs cycle.[233] In this step succinate and NADH are formed that originates from the reduction of nicotinamide adenine dinucleotide (NAD^+). The redox molecules enter the respiratory chain and induce an electron-transport between carriers of different redox-potentials. This process establishes a transmembrane proton-motive force by membrane bound respiratory complexes that translocate protons. In adaptation to the environmental conditions, specific respiratory components, i.e. dehydrogenases, quinones, cytochromes, reductases, and terminal oxidases are combined to facilitate an optimal respiration and energy conservation. In prokaryotic organisms either dioxygen serves as terminal electron acceptor (aerobic respiration), or inorganic molecules, e.g. sulfate, carbon dioxide, nitrate or nitrite (anaerobic respiration). The electrochemical gradient is used by the F1Fo ATPase to couple the transmembrane H^+ translocation to the synthesis of ATP from adenosine diphosphate (ADP) and inorganic phosphate (P_i). To stabilize the membrane potential exchange proteins transport anions and protons against OH- and H^+-gradients, respectively. A further prerequisite is that these processes occur at membranes that exhibit a low permeability for protons and ions.[235-237]

4.3.1 Bacterial Complex I

The respiratory complex I (CpI, NADH:quinone oxidoreductase) of aerobic organisms plays an important role in the energy transduction processes, being the main entry point to the respiratory chain of mitochondria and many bacteria.[237–239] It catalyzes the two electron oxidation of NADH and the reduction of quinone, coupled to charge translocation from the negatively charged side (N-side, prokaryotic cytoplasm or mitochondrial matrix) to the positively charged side (P-side, prokaryotic periplasm or mitochondrial intermembrane space) of the respective membrane (Figure 4.5).[240] The charge translocation results in the formation of a transmembrane potential difference, fostering endergonic processes such as ATP synthesis, active transport or motility and is thus essential for life.[241] The mitochondrial and bacterial CpI share 14 subunits, which compose the "minimal functional unit". The mitochondrial complex also harbors several accessory subunits, summing up to 45 subunits.[242,243]

CpI contains two structural/functional domains: the hydrophilic peripheral arm, responsible for the catalytic activity and the membrane part in which ion translocation takes place.[241,244–247] In bacteria, the latter has a curved shape with a total length of 180 Å and is constituted by seven hydrophobic subunits. The peripheral arm has a Y shape, a length of 130 Å and is composed of seven hydrophilic subunits.[248] It also contains from 8 to 10 iron-sulphur clusters responsible for the electron transfer over nearly 100 Å from a flavin mononucleotide (FMN), which receives the electrons directly from NADH, to the quinone binding sites.[248–251] Currently, one of the key questions about CpI function is how this coupling of electron transfer and proton translocation occurs, since the two processes take place in different parts of the enzyme, separated by large distances. This is suggested to be related to conformational changes involving shifts of helices at the quinone binding site at the interface of the peripheral and membrane domains and a movement of the peripheral arm.[248,252–256] The aim of this work is to monitor the process involved in this coupling mechanism by SEIRA spectroscopy. The reconstitution of purified membrane
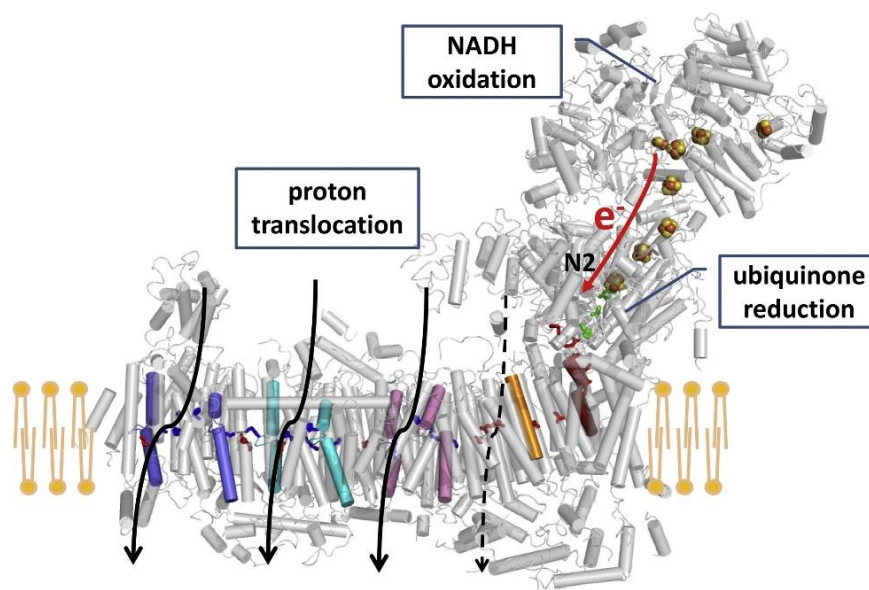
Figure 4.5 Redox-linked proton translocation by complex I including an electron transfer from the NADH oxidation site to the ubiquinone reduction site via a chain of iron–sulfur clusters; residues of the ubiquinone reduction site are shown in green. The membrane-bound arm contains three antiporter type subunits with discontinuous helices (marine; cyan; pink) regulating the proton translocation (black arrows). Further helices in the proximal part of the membrane arm are highlighted in orange and red. A forth proton pathway is depicted by a dashed arrow. In the center of the membrane arm a series of protonable residues (basic, blue; acidic, red) terminates below the ubiquinone reduction site with a loop comprising a cluster of highly conserved acidic residues. Conformational changes linked to the redox chemistry of ubiquinone are proposed to induce an electric pulse that ultimately triggers proton translocation events in the membrane arm. Reprinted from *Biochimica et Biophysica Acta*, 1857, Wirth, C., Brandt, U., Hunte, C., Zickermann, V., Structure and function of mitochondrial complex I, 902-914, Copyright (2018), with permission from Elsevier.[326]

enzymes on surfaces modified with biomimetic membranes allows to study both, the catalytic process and associated structural rearrangements by a combination of methodologies.[33] In a previous study the entire respiratory CpI was functionally reconstituted from *Rhodothermus marinus* in a biomimetic SLM on a 4-ATP SAM.[50] The enzyme's activity with respect to both of its functions (NADH:quinone oxidoreduction and proton translocation) was maintained. Here, this investigation is extended using the technique of SEIRA spectroscopy in combination with electrochemistry to provide additional structural insights into the previously applied electrochemical approach.

Previously, the more elaborate tethered bilayer lipid membrane system was used to investigate the peptide incorporation of the voltage-dependent peptide alamethicin (see chapter 6.3) into membranes and the generation of a transmembrane potential by cytochrome bo_3 by Wiebalck et al.[8] However, this study is based on a more simple setup for several reasons: (a) the possibility to obtain a much higher protein coverage, (b) less spatial restrictions of the aqueous reservoir that allows more efficient orientational control of CpI with its protruding arm and (c) the ability of 4-ATP to act as a spectroscopic pH sensor with much less spectral overlay than quinone/quinol difference bands in another approach.[8] SEIRA spectroscopy is particular advantageous since structural and orientational changes in the protein and its surrounding can be readily monitored. The methodology has also been successfully applied in studies of several membrane proteins[8,34,49,135] including CpI.[29] However, in the study of Kriegel et al., CpI was immobilized with the hydrophilic domain facing the flat gold electrode,[29] in an opposite orientation compared to the electrochemical reference study used as basis for this work,[50] by an engineered His-tag at a peripheral subunit or a NADH-SAM.

5 EXPERIMENTAL SECTION

5.1 Surface-enhanced Infrared Absorption (SEIRA) Spectroscopy

SEIRA spectra were recorded using a Bruker IFS 66 v/s or Tensor 27 FTIR-spectrometer equipped with a MCT (Mercury Cadmium Telluride) photo-conductive detector cooled with liquid N_2. The Michelson interferometer, the globar, as well as the detector of the spectrometer were used under vacuum. The sample chamber was purged with nitrogen gas to achieve a water-vapor free atmosphere. A homemade Kretschmann-ATR setup was adjusted to an angle of incidence of 60° leading to an effective measuring area of 7 mm × 3 mm. For each spectrum, 400 scans were accumulated in the spectral range of 4000 to 1000 cm^{-1} and at a spectral resolution of 4 cm^{-1}. SEIRA spectra were analyzed using an OPUS 7.0 software (Bruker) and Origin 2017 (OriginLab).

5.1.1 Preparation of the spectroelectrochemical cell

An Au-covered ATR Si prism was inserted into a homemade spectroelectrochemical SEIRA cell as illustrated in Figure 5.1. Electrochemical treatments were performed using a three-electrode configuration: the Au film (real area of ca. 1.65 cm^2; geometric area of 0.79 cm^2 corrected by the roughness factor of 2.1 - vide infra; newly determined for each Au film using the Au-oxide reduction charge density method), a Pt-wire, and an Ag/AgCl (3 M KCl) electrode serving as working, counter, and reference electrodes, respectively (all potentials are referred to the Ag/AgCl electrode).
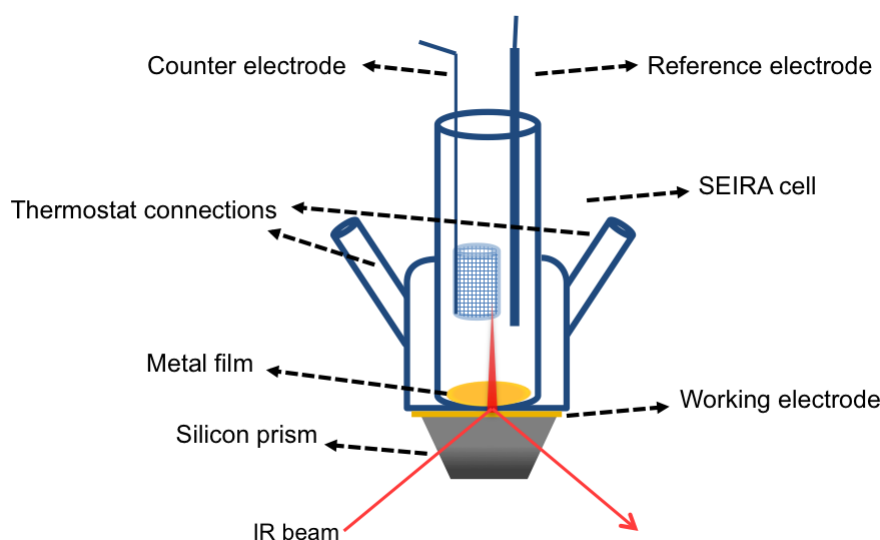
Figure 5.1 Representation of the spectroelectrochemical SEIRA cell. three-electrode system. The nanostructured Au metal-film serves as signal amplifier and working electrode in a three-electrode system with counter and reference electrode. The incident IR beam irradiates the silicon prism in an angle of 60° with respect to the surface normal. Reprinted with kind permission from Barbara Gonzalez (2018). *Spectroelectrochemical study of biomolecules in artificial membrane systems*, Technische Universität Berlin, Fakultät II.[329]

5.1.2 Electroless Au deposition

The silicon prism was prepared by electroless deposition of a nanostructured Au film as described by Miyake et al.[257] In a first step, the surface of the ATR Si prism was polished by means of alumina powder (Microgrit WCA-9, grain size: ca. 6 μm) and rinsed with water to achieve a hydrophobic surface. The prism was immersed into a 400 g/L NH$_4$F solution for 2 min to remove the oxide layer on the Si surface. The Au film was deposited at a temperature of 65 °C by adding the Au plating solution onto the Si surface. After 1 min, the Au deposition was aborted by dilution with water. The plating solution is composed of an aqueous 1:1:1 (volume ratio) admixture of a 2 % (w/w) HF solution, a 0.03 M NaAuCl$_4$·2H$_2$O solution, and reduction solution comprised of 0.3 M Na$_2$SO$_3$, 0.1 M Na$_2$S$_2$O$_3$·5H$_2$O, and 0.1 M NH$_4$Cl. The deposition is due to the reduction of Au^{III} and the oxidation of the Si surface:

$$Si^0(s) + 6F^-(aq) \rightarrow SiF_6^{2-}(aq) + 4e^- \tag{4.1}$$

$$AuCl_4^-(aq) + 3e^-(aq) \rightarrow Au^0(s) + 4Cl^-(aq) \tag{4.2}$$
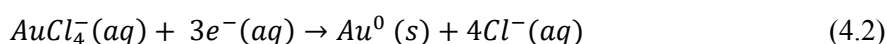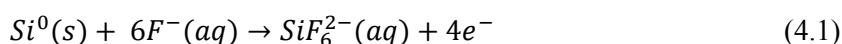
5.1.3 Electrochemical cleaning of the Au surface

The deposited Au film was cleaned electrochemically by performing cyclic voltammetry. Six oxidation/reduction cycles between the potentials of 0.1 and 1.4 V in a 0.1 M H$_2$SO$_4$ solution were conducted. To avoid the generation of reactive oxygen species, O$_2$ was removed from the solution by purging constantly with an Ar stream. The voltammogram was characterized by an Au oxidation at potentials above 1.1 V and a single reduction peak centered at ca. 0.92 mV. The reduction peak was used to estimate the real area of the Au electrode by the Au-oxide reduction charge density method. The necessary charge to reduce the surface Au-oxide was determined from the peak and compared with the specific charge density of 400 μC cm^{-2}.[258]

The electrochemical cleaning (in 0.1 M HClO$_4$) leads to a surface area of 1.65 cm^2. Due to a geometric area of 0.79 cm^2 there is an estimated roughness factor of 2.1. In the course of the study three different biomimetic membrane systems were constructed (see. chapter 5.2). For that purpose, distinct self-assembled monolayer (SAM) were adsorbed on the nanostructured Au surface.

5.1.4 Adsorption of the SAM on the Au surface

To obtain a tBLM system a mixed SAM comprised of [(β-cholestanoxy)ethoxy)ethoxy)ethanethiol] (WK3SH) (synthesized according to ref.[8]) and 6-mercaptohexanol (6MH, Sigma Aldrich) was formed on the Au surface by incubation for 14 h in 1-propanol (Merck) at 4 °C. As shown previously, taking a WK3SH/6MH mixture with a molar ratio of 60:40, a mixed and phase-separated SAM is formed with ca. 80 % being occupied by WK3SH.[8] The tHLM system, however, is based on a pure monolayer of WK3SH diluted in 1-propanol and formed following the same incubation protocol. To stop the incubation the surface was rinsed with 20mM Tris/100mM NaCl pH 7.4 buffer three times.

For the SLM assembly, a 0.13 mg/mL 4-aminothiophenol (4-ATP) solution in ethanol was incubated for 14 h at 4 °C.[259] After the incubation the SAM was removed by washing with 100 mM phosphate-buffered saline (PBS) pH 5.8 for three times. Buffer solutions were prepared using Milli-Q-water with a resistance of > 18 MΩ cm.

5.2 Assembly of biomimetic membrane systems

5.2.1 Liposome preparation and tBLM / tHLM formation

In this procedure 9μl of 1-palmitoyl-2-oleoyl-sn-glycero-3-phosphocholine (POPC) in chloroform (25 mg/mL, Avanti Polar Lipds) and 1μl of 1-palmitoyl-2-oleoyl-sn-glycero-3-phospho-(1'-rac-glycerol) (sodium salt) (POPG) in chloroform (25 mg/mL, Avanti Polar Lipids) were diluted in a mixture of 50μL methanol and 50μL chloroform. The solution was dried under a nitrogen stream and traces of solvent were removed under vacuum overnight. After addition of 0.5 mL of buffer the solution underwent 3 cycles of 10 min incubation and 1 min of vortexing. The obtained phospholipid solution possessed a concentration of 0.5 mM and was extruded with an extruder (Avanti Polar Lipids) equipped with polycarbonate filters (100 nm pore diameter) leading to unilamellar liposomes.

The freshly prepared unilamellar POPC:POPG (90:10) liposomes were added onto the mixed WK3SH/6MH SAM or pure WK3SH in 20mM Tris/100mM NaCl pH 7.4 buffer for 2-3 h to form the tBLM or tHLM, respectively. The formation was monitored by SEIRA spectroscopy and all experiments were carried out at 25 °C.

5.2.2 Liposome / proteoliposome preparation and SLM formation

This preparation protocol was adapted from Gutiérrez-Sanz et al.[50] For the liposome preparation a volume of 200 μL of POPC in chloroform (10 mg/mL, Avanti Polar lipids) was mixed with 180 μL of 1-palmitoyl-2-oleoyl-sn-glycero-3-phosphate (sodium salt) (POPA, 1 mg/mL, Avanti Polar Lipids) solvent and with 35 μL of 1.5 mg/mL 2,3-dimethyl-1,4-naphthoquinone (DMN)[9] in a 50/50 chloroform/methanol (Sigma Aldrich) mix. This step was repeated three times followed by evaporation of the solution under a N_2 stream and under vacuum overnight to remove traces of solvent. The addition of 100mM PBS, pH 5.8 was added to form a 2 mg/mL suspension of phospholipids that was extruded with an extruder (Avanti Polar lipids) equipped with a porous membrane (100 nm pore diameter) leading to unilamellar liposomes.

Two types of proteoliposomes were used: POPC:POPA (90:10) liposomes with and without DMN (50 μg/mL). In both cases, CpI was inserted in the same way: 10 μL a of 6.2 mg/mL CpI was added to 500 μL of the liposome suspension and stirred by vortexing, adding 15 mg of CALBIOSORB adsorbent biobeads (Calbiochem) every 45 min of stirring. The biobeads were added to remove the detergent from the complex I sample, thus facilitating its reconstitution in the liposomes. The biobeads were washed with 100mM PBS, pH 5.5 before use.

The freshly prepared unilamellar liposomes were added onto the 4-ATP SAM in 100mM PBS pH 7 buffer for 2-3 h to form the SLM respectively. The addition of the proteoliposomes in the same way led to the construction of the SLM with incorporated CpI (1-step-procedure in chapter 6.4.2).

5.3 Electrochemistry

Electrochemical measurements were conducted using a μAutolabIII/FRA2 instrument (Metrohm Autolab) and controlled with the FRA and GPES software packages (Metrohm Autolab). In a three-electrode configuration comprised of a homemade Pt-counter electrode and an Ag/AgCl (3 M KCl) reference electrode (World Precision Instruments, Inc.), the Au film served as the working electrode (Figure 5.1; real area of 1.65 cm^2, determined from the Au-oxide reduction charge; roughness factor and geometrical area were 2.1 and 0.79 cm^2, respectively).

Electrochemical impedance spectroscopy (EIS) was recorded in the frequency range from 0.05 Hz to 100 kHz at a potential of 250 mV (vs Ag/AgCl) and amplitude of 25 mV (rms). EIS measurements yielded capacitances of ca. 1.2 - 1.3, 0.8 - 0.9, and 0.7 - 0.8 $\mu F \cdot cm^{-1}$ for the mixed WK3SH/6MH SAM, the pure WK3SH-SAM, and the tHLM/tBLM system, respectively (see Figure 6.2)[8] The 4-ATP SAM and SLM exhibited both a capacitance of 8.1 $\mu F \cdot cm^{-1}$ (Figure 6.3).

5.4 Voltage-dependent incorporation of alamethicin into tBLM/tHLM systems

Addition of ALM (Sigma Aldrich) in a concentration of 1 μg/mL led to coverage of the membrane surface of the tHLM and incorporation into the lipid bilayer islands of the tBLM. Potentials were applied between +500 and −400 mV. SEIRA spectra were acquired after 6 min of equilibration at the respective potential. At this time point no further potential-induced spectral changes were detected. All amide I/amide II intensity ratios were determined based on integrated intensities of the amide bands unless stated otherwise. In this way, all components of the spectra contributing to the intensity were taken into account and errors based on differences in relative spectral positions are avoided. Experiments were performed in H_2O (instead of D_2O) to prevent complications in relating amide I/amide II ratios to tilt angles due to changes in position, composition and transition dipole orientation of the amide II (vs. amide II'). Due to the selection rules of SEIRA, bulk H_2O display only a minor contribution in the spectra (see Figure A2).

5.5 Cathelicidin LL-37 and the fragments LL-32 and LL-20

5.5.1 Peptide synthesis

The peptides were kindly provided by Prof. Dr. Thomas Gutsmann, Research Center Borstel, Germany. In the following the synthesis protocol reported by Dannehl et al. will be presented.[12]

The peptides were synthesized with C-terminal amidation by the solid-phase peptide synthesis technique on an automatic peptide synthesizer (model 433 A; Applied Biosystems) on Rink amide resin according to the fastmoc synthesis protocol of the manufacturer, including the removal of the N-terminal Fmoc-group. The peptide was cleaved from the resin and deprotected with 90% trifluoroacetic acid (TFA), 5% anisole, 2% thioanisole, 3% dithiothreitol for 3 h at room temperature. After cleavage the suspension was filtered and the soluble peptides were precipitated with ice-cold diethylether followed by centrifugation and extensive washing with ether. Peptides were purified by RP-HPLC using a Jupiter 4μ Proteo column (Phenomenex). Elution was done by using a gradient of 0–70% acetonitrile in 0.1% (TFA) to purities above 95%. The purity was determined by analytical reversed-phase HPLC (UV 214 nm) and matrix-assisted laser-desorption-time-of-flight mass spectrometry (MALDI-TOF MS, Bruker). The masses were 4492 Da (LL-37), 3922 Da (LL-32) and 2465 Da (LL-20), respectively. The peptides were dissolved in buffer with 20 mM Tris 100 mM NaCl at pH 7 to a concentration of c = 1 mg/mL. The aqueous solutions were prepared using ultrapure water (specific resistance of 18.2 MΩcm) produced by a Millipore reverse osmosis unit.

5.5.2 Fourier transform infrared spectroscopy

Up to 3 μL of a peptide sample of LL-37, LL-32 and LL-20 at a concentration of 5 mM were deposited on a CaF_2 window with a 2 μm deepening. The sample was homogenously distributed over the whole surface within the deepening. The hydrated sample film was then sealed with a

plain CaF$_2$ window. To avoid further sample dehydration, additional isolation of the sample was provided by a thin layer of silicone grease between both windows. The CaF$_2$ sandwich was placed in a suitable window holder. IR samples were measured at room temperature. Infrared spectra were recorded in a Bruker IFS66v/s spectrometer equipped with a liquid-nitrogen-cooled MCT detector (J15D series, EG&G Judson).

5.5.3 SEIRA spectroscopic investigation

The peptides LL-37, LL-32 and LL-20 were incubated on the tBLM in 20 mM Tris 100 mM NaCl pH 7 leading to a concentration of 1-10 µg/mL. Furthermore, the peptides were incubated on the pure WK3SH-SAM in 20 mM Tris 100 mM NaCl pH 7 in a final concentration of 1-60 µg/mL. The incubation was observed by SEIRA difference spectroscopy, where the tBLM or WK3SH spectrum served as reference spectrum, respectively.

5.6 Bacterial complex I

Bacterial respiratory NADH:menaquinone oxidoreductase (complex I, CpI) isolated from *Rhodothermus marinus* was kindly provided by Manuela M. Pereira from Instituto de Tecnologia Química e Biológica António Xavier, Universidade Nova de Lisboa, Lisbon, Portugal. Bacterial strains and growth conditions as well as membrane preparation and solubilization are described based on the protocol established by Pereira et al.[260]

5.6.1 Bacterial strains and growth conditions

 A spontaneous nonpigmented mutant of *R. marinus*, strain PRQ-62B, was used. This strain, isolated from the beach Praia da Ribeira Quente at the island of Sao Miguel, Azores, was shown to be almost identical to the type strain DSM 4253.[261] The cells were grown on Degryse medium 162,[262] supplemented with 0.25% yeast extract, 0.25% tryptone, 1% NaCl, and 100 mM glutamate at 65 °C and pH 7.5. Reactors of 30 L or 300 L were used, at the IBET/ITQB Fermentation Plant, usually with an aeration of 380 L/min and 42 rpm stirring. Different aeration conditions were also tested. Cell density, dissolved oxygen, and pH were continuously monitored. The cells were harvested at the midexponential phase, at the beginning of the stationary phase, or at the late stationary phase, by microfiltration on a Sartocon II system and subsequently centrifuged at 10000g and frozen at -70 °C until use.

5.6.2 Membrane preparation and solubilization

Frozen cells were thawed and suspended in 20 mM Tris-HCl, pH 8, and then disrupted by passing through a Manton-Gaulin pressure cell at 12 000 psi. Unbroken cells were separated by centrifugation at 10000g for 15 min and the suspension obtained was then centrifuged at 200000g for 1 h at 4 °C. The membranes were successively washed with 1 mM EDTA in 20 mM Tris-HCl, pH 8, then 1.5 M NaCl in 20 mM Tris- HCl, pH 8, and finally 20 mM Tris-HCl, pH 8. The supernatants as well as the membrane pellets after each step were studied by visible and EPR spectroscopies. The membranes were resuspended in the last buffer with a concentration of approximately 20 mg/mL. The membrane fraction thus obtained was solubilized with dodecyl β-D-maltoside in the proportion of 2g of detergent/g of protein. This suspension was centrifuged at 200000g for 1 h at 4 °C.

5.6.3 Protein purification

This step was performed based on an optimized protocol by Fernandes et al.[263] that was described by Gutiérrez-Sanz et al.[50]

The sample was submitted to two successive high performance Q-Sepharose columns, using 20 mM Tris-HCl (pH 8.0), 1 mM phenylmethanesulfonyl fluoride (PMSF, Roth), and 0.1% n-dodecyl-b-D-maltoside (DDM, Glycon Biochemicals GmbH) as buffer, and was eluted in a linear gradient, 0-1 M NaCl. The fraction containing CpI was then applied to a gel filtration S200 column, eluted with 20 mM Tris-HCl (pH 8.0), 1 mM PMSF, 0.1% DDM, and 150 mM NaCl, and finally applied on a Mono-Q column (GE Healthcare) using 20 mM Tris-HCl (pH 8.0), 1 mM PMSF, and 0.1% DDM as buffer. CpI was again eluted in a linear gradient, 0-1 M NaCl.

5.6.4 SEIRA spectroscopic analysis of CpI activity

In the 2-step procedure, the constructed SLM (see chapter 5.2.2) was washed with 100 mM PBS pH 5.8. After a buffer exchange to 100 mM PBS pH 7, 8µL of a 26mg/mL solution of CpI was incubated in 5 mL with 15 mg CALBIOSORB adsorbent biobeads (Calbiochem) in a metal net. Before, the biobeads were sonicated for three times in ethanol for 5 min and rinsed for three times with 100 mM PBS pH 7. CpI was incubated for 2 h and the process was monitored with SEIRA.

The solution of 60 µM NADH was added to the system. The incubation was observed by SEIRA difference spectroscopy, where the spectrum of the SLM including CpI served as reference spectrum, respectively. In parallel chronoamperometry at a stable voltage of 200 mV was conducted to measure the current.

A pH titration of 100 mM PBS in the range of pH 3 to pH 9 was conducted. The solution was acidified by 85 (wt%) phosphoric acid (Sigma Aldrich) and the pH was measured using a pH electrode inside the SEIRA cell. SEIRA difference spectra were calculated using the spectrum of pH 7 as reference spectrum.

5.7 Density Functional Theory (DFT) calculations

5.7.1 DFT-IR spectra of alamethicin

Geometry optimization and normal mode analysis were performed using Gaussian 09 (Revision D.01)[264] on the BP86 level of theory,[265,266] the 6-31g* basis set for all atoms and the implemented polarizable continuum model simulating water as the solvent. As a primary structural model an "α-helix/3_{10}-helix" structure was calculated. As initial geometry chain B of the crystal structure of ALM (PBD ID 1amt)[209] was used with dihedral angles of the backbone adjusted to the ones obtained from recent molecular dynamics simulations performed by Nagao et al.[210] Alternatively, to account for the "α-helix/α-helix" conformation of ALM chain C of the crystal structure was optimized, which is reported in the Appendix with the entire evaluation performed in this work yielding analogous results. Further structures were optimized as well (e.g. chain B of crystal structure without changing the dihedral angles, structure with prototypical α-helix dihedral angles, or with α-helical and 3_{10}-helical angles for the N-terminal and C-terminal part, respectively), but were not in agreement with the structures reported in literature. In analogy to the work of Keiderling and co-workers,[267,268] the backbone dihedral angles were constrained to the adjusted starting values to reduce the degrees of freedom and thus facilitate the calculation of the 288 atom-sized molecule. Transition dipole moments (TDMs) were extracted from the frequency calculation and treated manually using GNU octave[269] to derive the polarized

theoretical spectra as well as to simulate amide I/amide II ratios for different orientations. Assignment of the normal modes to vibrations was performed by evaluation of potential energy distribution of the normal modes using a homemade script.[270,271]

5.7.2 DFT-IR Spectra of 4-ATP

To understand the two different pH regimes observed in the SEIRA difference spectra, various 4-ATP structures were calculated using DFT. Thereby, the thiol hydrogen was substituted by an Au atom to account for structural changes upon binding to the Au surface. Geometry optimization and vibrational analysis were performed on the BP86 level of theory[265,266] using Gaussian 09.[272] For C, H, N, and O atoms the 6-31g* basis set was chosen, for the heavier S the TZVP basis set, and for Au LanL2DZ (using a pseudo core potential) were employed.[273,274] Geometry optimization using periodic boundary conditions (PBC) was performed by specifying two translation vectors that span the plane parallel to the supporting surface. As expected, imaginary frequencies (between 0 and -100 cm^{-1}) resulted from the normal mode analysis based on this procedure, which were identified as torsional movements of whole 4-ATP molecules. However, this is comprehensible and unavoidable because normal mode analysis cannot be performed together with PBC. Furthermore, the low value (> -100 cm^{-1}) of these frequencies shows that the frequency region of interest (1400 – 1800 cm^{-1}) can be reliably evaluated. Assignment of the calculated normal modes was obtained by evaluating the respective potential energy distributions.[270,271]

5.8 Molecular Dynamics (MD) simulations

5.8.1 All-atom MD simulations of LL-37 and its fragments LL-32 and LL-20 in solution

The starting geometry for LL-37 was extracted from the Protein Data Bank (PDB-entry: 2K6O).[11] Consequently, employing this structure as template, the initial configurations for the fragments were developed.

The three peptides were modeled with a neutral N-terminus and an amidated C-terminus yielding an overall charge of +6, +6, and +4 for LL-37, LL-32 and LL-20, respectively. In order to reproduce the used experimental conditions, the protonation states of all ionizable groups were set according to the physiological pH 7.

Afterwards, a two-step protocol was performed in order to solvate and ionize the systems using the SOLVATE and IONIZED plugins of the VMD software:[275] i) the peptides were individually solvated in cuboid boxes of TIP3P water molecules[276] (of around 80 x 50 x 50 Å3 per system) and ii) in order to reproduce the experimental conditions, a sufficient amount of ions was added to the solvated system mimicking an ionic strength of 100 mM NaCl buffer. Subsequently, the systems underwent 20000 steps of energy minimization followed by a thermal equilibration at 300 K. Heavy-atoms were initially constrained, followed by unconstrained MD simulations. The thermally equilibrated peptides in aqueous solution were simulated for 100 ns at 300 K in a NPT ensemble under constant atmospheric pressure and temperature using the Langevin Piston method.[277,278] With the purpose of obtaining the equilibrium structure of the three peptides, the production run was done under periodic boundary conditions with extended electrostatics using Particle Mesh Ewald Summation[279] and a cutoff distance of 12 Å for the Van der Waals interactions. SHAKE algorithm[280] was used to constrain all bond lengths between heavy and hydrogen atoms assuring a time step of 2 fs.

5.8.2   All-Atom MD simulation of LL-37 and its fragments LL-32 and LL-20 interacting with lipid membranes

In order to explore the peptide attachment to the membrane surface at atomistic resolution, the individually equilibrated peptide monomers were studied in a complex simulation system including a lipid bilayer.

In agreement with the experimental setup, a biological membrane was modeled by a mixture of 1-Palmitoyl-2-oleoyl-sn-glycero-3-phosphocholine (POPC) and 1-palmitoyl-2oleoyl-sn-glycero-3-phosphoglycerol (POPG) molecules in a 90:10 proportion. The POPC:POPG bilayer with a surface area of 80 x 80 Å^2 was constructed with CHARMM-GUI.[281]

To investigate the individual peptide-membrane interactions, three systems were generated. The three peptides were initially placed 10 Å above the lipid bilayer. The membrane-peptide systems were solvated in 80 x 80 x 400 Å^3 TIP3P box and ionized following the same guideline as explained before (*vide supra*).

In the course of the study the production run was extended until 300 ns in the NPT ensemble under constant atmospheric pressure and temperature using the Langevin Piston method and 300 K, together with a constant cell size along the surface area.[277,278] The strength of the peptide-membrane interaction was evaluated by computing the number of contacts. A contact between two atoms is defined by an interatomic distance below 3 Å.

6 RESULTS AND DISCUSSION

The following section describes the results obtained in a combined experimental approach using SEIRA and EIS. For that purpose, the previously described tBLM[8,34] and SLM systems[50] were constructed on nanostructured Au surfaces. Additional DFT calculations and MD simulations complement the experimental results. First, the interactions of the human cathelicidin LL-37 and its derivatives LL-32 and LL-20 with a tBLM system were characterized spectroelectrochemically. In addition, MD simulations with the same parameters were processed. In a second project, the voltage-dependent and pore-forming AMP alamethicin was incorporated into the tBLM under application of electrochemical potentials to achieve information about the incorporation kinetics and angle of the peptide with respect to the bilayer normal.

Furthermore, the bacterial Complex I (CpI) was embedded into the SLM system in two different approaches to study the NADH dependent transmembrane proton translocation. For that purpose, a (de-)protonable SAM was chosen for the assembly that was employed as pH sensor affording information about the orientation of the protein on the electrode.

6.1 Assembly of biomimetic membrane systems

6.1.1 Tethered bilayer lipid membrane (tBLM) and tethered hybrid lipid membrane (tHLM) system

For the tBLM construction a mixed SAM consisting of the two surface-active molecules, i.e. [(β-cholestanoxy)ethoxy)ethoxy)ethanethiol] (WK3SH)[8] and 6-mercaptohexanol (6MH), was adsorbed on a nanostructured Au electrode. The tHLM assembly, however, required a pure monolayer of WK3SH.[8] Afterwards, POPC:POPG (90:10) liposomes were spread on top of the SAM layer leading to a lipid layer of alternating lipid bilayer and lipid monolayer areas (tBLM) or exclusively a lipid monolayer (tHLM). Figure 6.1 shows the SEIRA difference spectrum of the
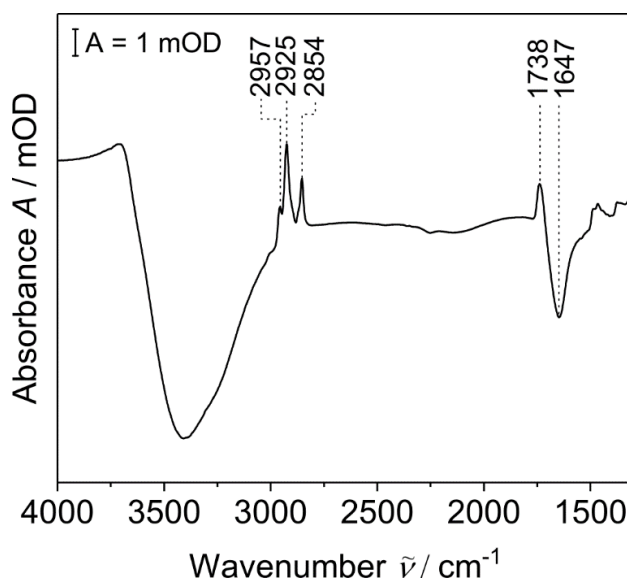
Figure 6.1 SEIRA difference spectrum of POPC:POPG (90:10) liposome spreading on top of a WK3SH/6MH self-assembled monolayer (SAM) surface in H_2O. The respective SAM spectrum was used as reference (n = 2 independent experiments).
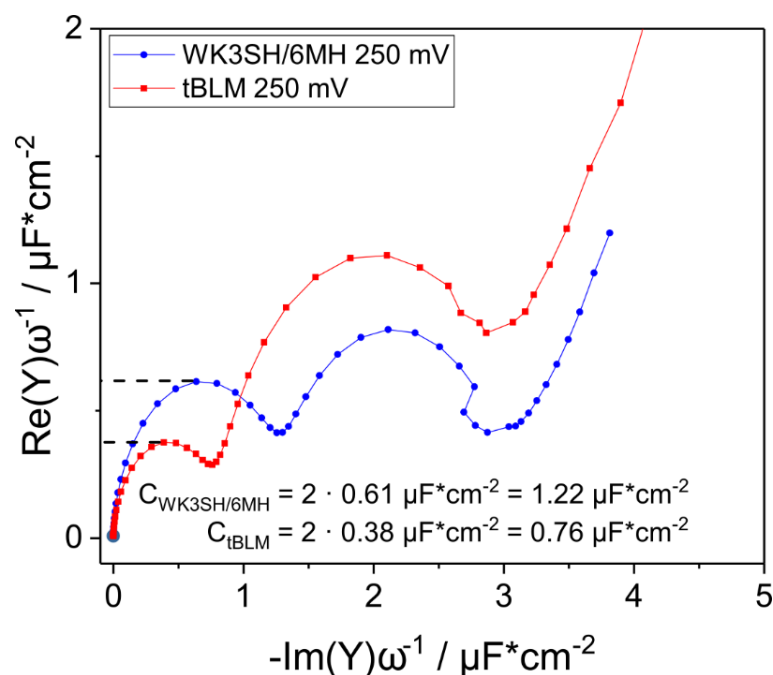
Figure 6.2 Frequency-weighted Cole-Cole plot of impedance spectra of WK3SH/6MH SAM (blue circles) and tethered bilayer lipid membrane (tBLM, red squares) in the range of 0.05 Hz to 100 kHz at a constant potential of 250 mV. The value $C_{1/2}$ (dashed line) and the capacitances of the mixed SAM ($C_{WK3SH/6MH}$) and tBLM (C_{tBLM}) are indicated. (n = 2 independent experiments).

POPC:POPG (90:10) membrane taking the spectrum of the mixed SAM as reference. Vibrational modes with positive intensity are characteristic of lipids, which are deposited onto the SAM, e.g. the v(C=O) stretching vibration at 1738 cm^{-1} and the symmetric (s) and antisymmetric (as) vibrational CH_n bands ($v_s(CH_2)$, $v_{as}(CH_2)$, and $v_{as}(CH_3)$) at 2854 cm^{-1}, 2925 cm^{-1} and 2957 cm^{-1},[224] and thus indicate the successful tBLM formation. In addition, the negative bands at ca. 3400 cm^{-1} and 1647 cm^{-1} can be assigned to water molecules that are removed from the SAM interface at the same time. This process was also monitored using electrochemical impedance spectroscopy (EIS) which proves a successful assembly of the tBLM system as shown in a frequency-weighted Cole-Cole-plot (Figure 6.2) and previously described for the tHLM system.[8] The capacitance was estimated by reading out the radius of the first semicircle and calculation of its diameter. The capacitance of the mixed WK3SH/6MH SAM ($C_{WK3SH/6MH}$) was determined to be 1.22 $\mu F*cm^{-2}$ (Figure 6.2 blue circles). Upon addition of the POPC:POPG (90:10) liposomes the capacitance of the assembled tBLM ($C_{WK3SH/6MH}$) decreased to 0.76 $\mu F*cm^{-2}$ (Figure 6.2 red squares). This value is in concordance with data by Wiebalck et al., showing a similar of value $C_{tBLM} = 0.76$ $\mu F*cm^{-2}$ for a tBLM using POPC phospholipids and thereby confirms a successful tBLM formation.[8,126] The capacitance values for the pure WK3SH monolayer and tHLM system were estimated to be 0.9 $\mu F*cm^{-2}$ and 0.7-0.8 $\mu F*cm^{-2}$, respectively.[8]

6.1.2 Supported lipid membrane (SLM) system

The SLM system required the functionalization of the nanostructured Au surface by a 4-aminothiophenol (4-ATP) SAM, which was formed by overnight incubation. Additionally, liposomes consisting of POPC:POPA:DMN (80:10:10) were adsorbed on the 4-ATP modified surface. The SEIRA difference spectrum is depicted in Figure 6.21B for better comparison.

The capacitance of 4-ATP obtained by EIS is shown in Figure 6.3 (C_{ATP}, blue circles). A value of 8.1 $\mu F*cm^{-2}$ is determined that is equal to the capacitance of the SLM (C_{SLM}, red squares). In
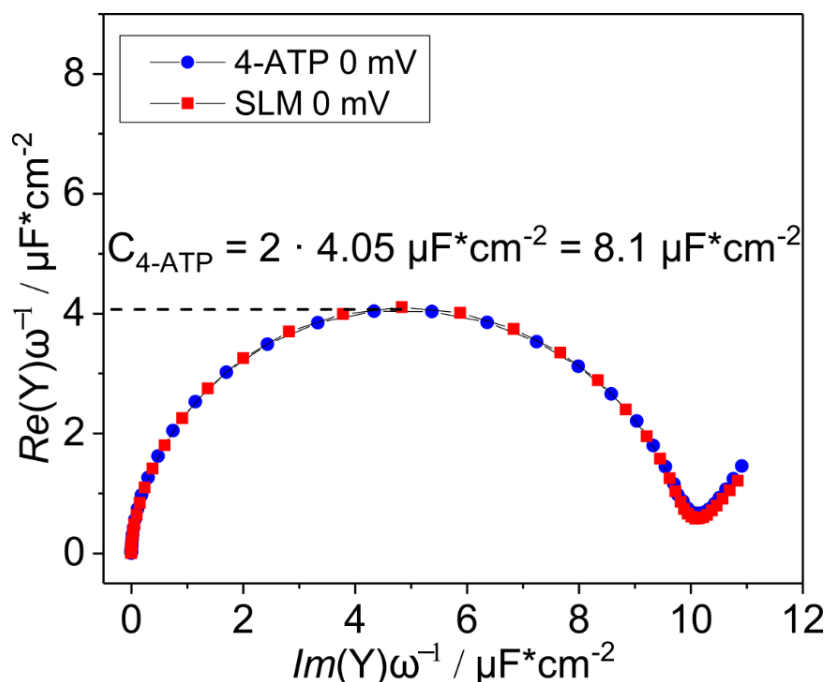
Figure 6.3 Frequency-weighted Cole-Cole plot of impedance spectra of 4-aminothiophenol SAM (4-ATP) and the supported lipid membrane (SLM) system in the range of 0.05 Hz to 100 kHz at a constant potential of 0 mV (n = 2 independent experiments). Adapted with permission from Gutiérrez-Sanz, O.; Forbrig, E.; Batista AP.; Pereira MM.; Salewski, J.; Mroginski MA.; Götz, R.; De Lacey, AL.; Kozuch, J.; Zebger, I. Catalytic Activity and Proton Translocation of Reconstituted Respiratory Complex I monitored by Surface-enhanced Infrared Absorption Spectroscopy. *Langmuir* 2018 *34* (20), pp 5703-5711. Copyright (2018) American Chemical Society.[328]

comparison to the tBLM system (see Figure 6.2 in chapter 6.1.1) this value is more than six times higher than $C_{WK3SH/6MH}$ and even more than ten-fold of C_{tBLM}. This leads to a much lower resistance of the system and to a less stable SLM system. Therefore, the qualitative analysis yields to the assumption that intact vesicles and lipid fragments are adsorbed on the SAM surface.

6.2 Cathelicidin LL-37 and its derivatives LL-32 and LL-20

In this interdisciplinary project IR spectroscopic experiments were combined with MD simulations to provide insights into the relation between structure and function as well as the resulting mode of interaction of LL-37, LL-32, and LL-20 with different environments.

First, transmission FT-IR experiments of the three peptides in buffer were performed to evaluate the secondary structure in solution. Second, the incorporation of the peptides into the tBLM constituting a hydrophilic, negatively charged POPC:POPG (90:10) lipid surface was monitored. SEIRA spectroscopy allowed to track spectral changes associated with mechanistic details of the peptide-membrane interaction. As reference, the peptides were incubated on a layer of pure cholestanyl-headed WK3SH-SAM to obtain information about the interaction with a hydrophobic surface. Furthermore, a comparison of both experimental approaches led to information about the peptides' position related to the bilayer membrane.

In addition, Dr. Alejandra de Miguel working in the group of Prof. Dr. Maria-Andrea Mroginski, Technische Universität Berlin, Germany, simulated the secondary structure of the peptides in solution. In a next step, the peptide-membrane interaction was investigated by simulating a POPC:POPG (90:10) membrane together with each peptide for 300 ns.

6.2.1 Determination of the solution structure by Fourier Transform IR Spectroscopy

The investigation of LL-37, LL-32, and LL-20 by FT-IR transmission in buffer solution leads to very similar spectra (Figure 6.4). The band assignment of the amide I and amide II region requires a modeling of the spectra with four and two Lorentzian functions, respectively. LL-37 and LL-32 exhibit centered amide I and amide II vibrations visible at 1652 cm^{-1} and 1550 cm^{-1} (Figure 6.4A and Figure 6.4B) that indicate an α-helical secondary structure.[140] Furthermore, contributions of amino acid side chains can be assigned to bands at 1681 cm^{-1}, 1666 cm^{-1}, 1637-1634 cm^{-1} as well as 1531 cm^{-1}.[140] Even though an exact assignment in general turns out to be complicated due to the overlap of spectral contributions, it can be estimated that these components originate especially from Arg (R) and Lys (K) residues (see Figure 4.3). On the one hand the guanidinium group of Arg (R) entails very intense asymmetric and symmetric vibrations at 1695-1652 cm^{-1} and 1614-1663 cm^{-1}, respectively; on the other hand Lys (K) gives rise to an asymmetric and symmetric ammonium vibration at ca. 1630 cm^{-1} and 1530 cm^{-1}. Moreover, the backbone amide vibrations of Asn (N) and Gln (Q) arise at ca. 1680 cm^{-1} and in the range around 1610 cm^{-1}, alike the asymmetric COO$^-$ mode of Glu (E) and Asp (D) that can be observed.[140] Both spectra show similar amide I/amide II ratios with values of 2.1 ± 0.2 for LL-37 and 2.0 ± 0.1 for LL-32. The investigation of LL-20 leads to an IR spectrum exhibiting a much worse signal-to-noise ratio. The reason is a decreased solubility as many charged amino acid residues are missing in comparison to the other variants (Figure 6.4C). The main amide I and II vibrations are ascribed at 1649 cm^{-1} and 1556 cm^{-1}. The side chain vibrational modes at ca. 1681, 1666, 1634, and 1531 cm^{-1} can be assigned in this case to Arg (R), Lys (K), Glu (E) and Asp (D).[140] Since the amide I and II are less clearly pronounced due to the shorter peptide sequence, the amide I/amide II ratio of 1.8 ± 0.1 is somewhat lower.
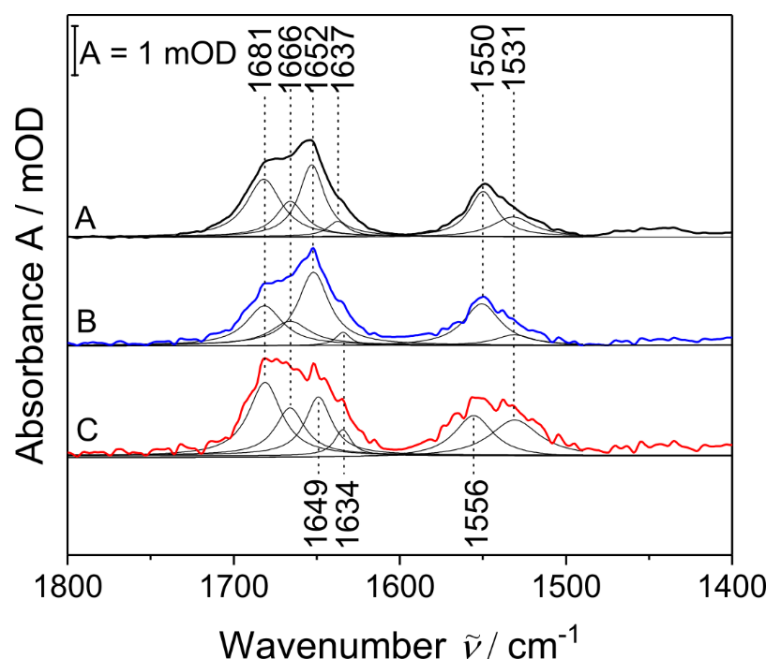
Figure 6.4 FT-IR transmission spectra in 20mM Tris/100mM NaCl buffer at pH 7.4 at 25°C. A: LL-37, B: LL-32, and C: LL-20. By means of four and two Lorentzian functions absorptions in the amide I and amide II region were determined (n = 2 independent experiments). Adapted with kind permission from Alejandra de Miguel (2017). *Elucidating the Mechanism of Action of Antimicrobial Peptides by means of Computational Approaches*, Technische Universität Berlin, Fakultät II.[287]

6.2.2 Surface-enhanced IR spectrocopical investigations using tethered bilayer lipid membranes

The peptide-bilayer membrane interaction of cationic LL-37 and its derivatives LL-32 and LL-20 was investigated by means of a tethered bilayer membrane (tBLM) system,[34] which consisted of negatively charged POPC:POPG (90:10) lipids.

The peptide incubation on the tBLM and, in separate experiments, on the hydrophobic WK3SH-surface was monitored using SEIRA resulting in the spectra plotted in Figure 6.5. There are clear differences in the adsorption process of the peptides onto the negatively charged membranes observable. Again, LL-37 and LL-32 are characterized by similar spectra with sharp and pronounced amide I and II bands at ca. 1655 cm^{-1} and 1550 cm^{-1} (red traces in Figure 6.5A and Figure 6.5B). The additional spectral contributions observed in the transmission IR experiment can be detected as well at 1681 cm^{-1}, but with much less relative intensity. This is due to the surface selection rule in SEIRA that allows detecting solely normal modes with a transition dipole moment perpendicular to the surface. Also, due to this effect, the amide I/amide II ratio is changed in the SEIRA spectra and determined to be 0.6 ± 0.1 for LL-37 and LL-32, which is in line with a uniform horizontal orientation of both α-helical peptides when bound to the membrane. However, while LL-37 shows amide mode intensities of ca. 2 mOD and 4 mOD (for amide I and amide II) (Figure 6.5A red trace and Figure 6.6A), the intensities of LL-32 are smaller by a factor of ca. 10 (0.3 and 0.6 mOD for amide I and amide II) (Figure 6.5B red trace and Figure 6.6C). This suggests an enhanced binding of LL-37 or its deeper incorporation into the membrane core (based on the distance dependence of SEIRA with d^{-6}).

Furthermore, as shown in Figure 6.6B, the amide I/amide II ratio of LL-37 changes during the process of membrane binding from ca. 0.4 to 0.6. The value for LL-32, however, stays constant
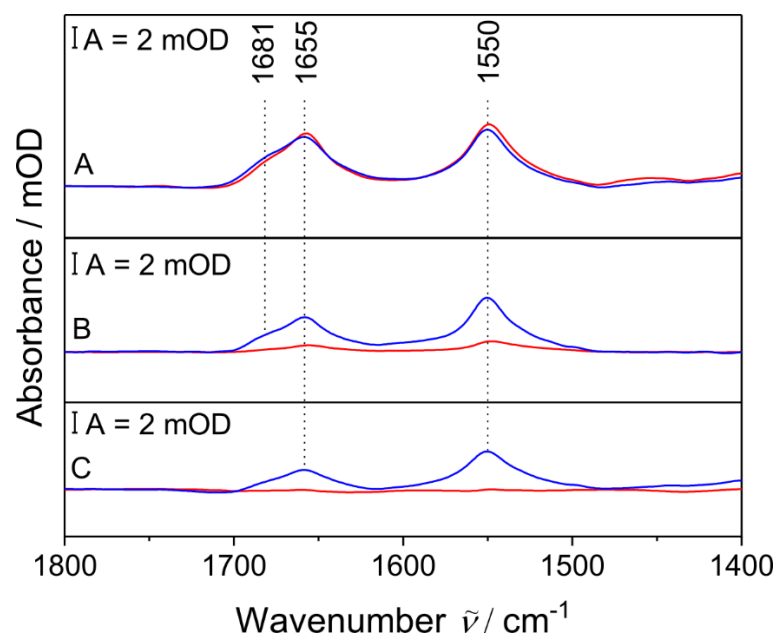
Figure 6.5 A: Incubation of 1 μg/mL LL-37 on tBLM consisting of POPC:POPG in a ratio of 90:10 (red) and incubation of 1μg/mL LL-37 in on pure hydrophobic WK3SH-SAM (blue). B: Incubation of 1 μg/mL LL-32 on tBLM consisting of POPC:POPG in a ratio of 90:10 (red) and incubation of 60 μg/mL LL-32 on pure hydrophobic WK3SH-SAM (blue). C: Incubation of 10 μg/mL LL-20 on tBLM consisting of POPC:POPG in a ratio of 90:10 (red) and incubation of 10 μg/mL LL-20 on pure hydrophobic WK3SH-SAM (blue). All experiments were done in in 20 mM Tris/100 mM NaCl buffer at pH 7.4 at 25 °C (n = 2 independent experiments). Reprinted with kind permission from Alejandra de Miguel (2017). *Elucidating the Mechanism of Action of Antimicrobial Peptides by means of*
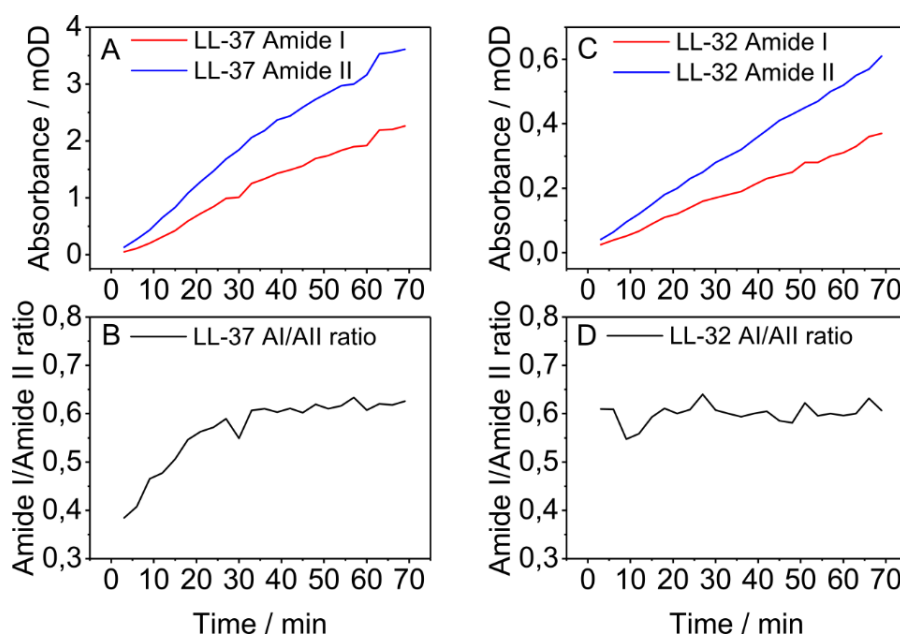
Figure 6.6 Development of amide I (red) and amide II (blue) band intensities (at maximum) over an incubation time of 70 min for LL-37 (A) and LL-32 (C) on lipid bilayer membrane consisting of POPC:POPG (90:10) in 20mM Tris/100mM NaCl buffer at pH 7.4 at 25 °C. The related amide I/amide II (AI/AII) ratios are depicted in B and D. Incubation of 1μg/mL LL-37 and LL-32 (n = 2 independent experiments). Reprinted with kind permission from Alejandra de Miguel (2017). *Elucidating the Mechanism of Action of Antimicrobial Peptides by means of Computational Approaches.* Technische Universität Berlin, Fakultät II [287]

at a value of ca. 0.6 (Figure 6.6D). This may reflect that LL-32 experiences a rather simple one-step process of direct binding to the membrane surface. Binding of LL-37, however, involves a process including more steps, which may explain the 10-times higher intensity. Binding of both peptides to the hydrophobic WK3SH-SAM leads in both cases to very similar spectra with intensities of ca. 2 and 4 mOD (blue traces in Figure 6.5A and Figure 6.5B) despite the use of a 60 times higher concentration for LL-32. The amide bands exhibit a ratio of ca. 0.6. In both cases there is a strong influence of hydrophobic interactions during the adsorption process of the peptides on the SAM surface.

In contrast, incubation of LL-20 shows barely any intensity of amide I and amide II modes even though a ten-fold concentration compared to the other derivatives was applied. Thus, a very weak attraction towards the lipid surface due to the absence of many charged residues can be concluded. Binding studies using the WK3SH-SAM surface, however, reveals a spectrum with comparable intensities as described for LL-37 and LL-32 (as well as a similar amide I/amide II ratio of 0.5) demonstrating a strong tendency for hydrophobic interactions (blue trace in Figure 6.5C).

6.2.3 Molecular Dynamics Simulations

6.2.3.1 Solution structure of LL-37, LL-32 and LL-20

The three-dimensional structures of LL-37 in complex with SDS micelles,[10] DPC micelles[282] and to D8PG (bacterial membrane model)[11] have been determined by NMR spectroscopy in earlier studies. Here, LL-37 adopts an α-helical arrangement of variable length, depending on the nature of the interacting membrane model (residues 2-31 in SDS and D8PG or residues 4-33 in DPC). The interaction of LL-37 with DPC micelles results in breakage of the α-helical secondary structure at residue K12. More detailed studies focusing on the structure and dynamics of isolated LL-37 and its variants in solution, however, have not been conducted so far.

In order to determine the equilibrium structure of the three peptides, 100 ns long all atom MD simulations were carried out in aqueous solution. A steady Root-Mean-Square-Deviations (RMSD) value of the backbone heavy atoms was calculated for LL-37 and LL-32 (ca. 3 Å) as well as for LL-20 (ca. 1.5 Å). This reflects a thermal stability of the secondary structure. For LL-37 and LL-32, the α–helical region covers residues 1 to 31, which is in line with NMR observations, while the remaining residues form an unstructured VPRTES-terminus (Figure 6.7A and Figure 6.7B). In case of LL-20, the α-helical motif includes the entire peptide chain (Figure 6.7C). Deviations from the steady behavior of the RMSD plots are mainly due to a prompt bending of the α-helical backbone. LL-37 and LL-32 exhibit a breakage of the α-helix between the residues K8-K12 (α-helical structures shown in Figure 6.8: B, C, D, E and G), which is in line with previously obtained experimental data.[282] Another bending site is located within the peptide core region at the positions R19-R23 (Figure 6.8: A, B, F, H). Both positively charged bending regions contain hydrophilic amino acids, i.e. S9 and Q22, respectively (Figure 4.3). However, LL-20 contains only one hinge region within the α-helix structure between the residues K8-K12 (Figure 6.8: I, J, K, and L).

Even though LL-37 and LL-32 possess an equivalent charge (+6) the calculations revealed varying average dipole moments of 256 Debye (LL-37) and 135 Debye (LL-32) and thus distinct orientations of the polar side chains. Due to a lower number of positively charged
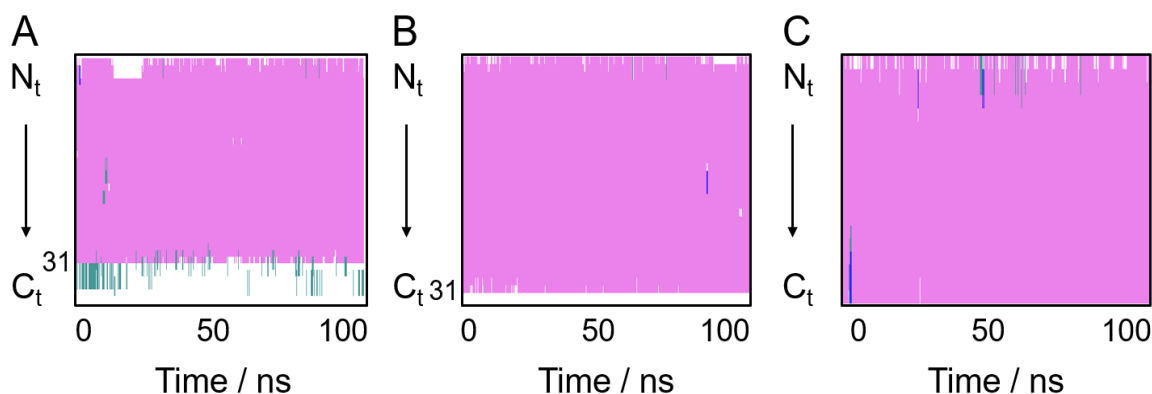
Figure 6.7 Monitoring of the secondary structure of LL-37 (A), LL-32 (B) and LL-20 (C). The structural elements are depicted by different colors: α-helix - pink, 3$_{10}$-helix - blue, isolated bridges - green, extended configuration - yellow, turns - teal, π-helix - red, coil - white. Reprinted with kind permission from Alejandra de Miguel (2017). *Elucidating the Mechanism of Action of Antimicrobial Peptides by means of Computational Approaches*, Technische Universität Berlin, Fakultät II.[287]
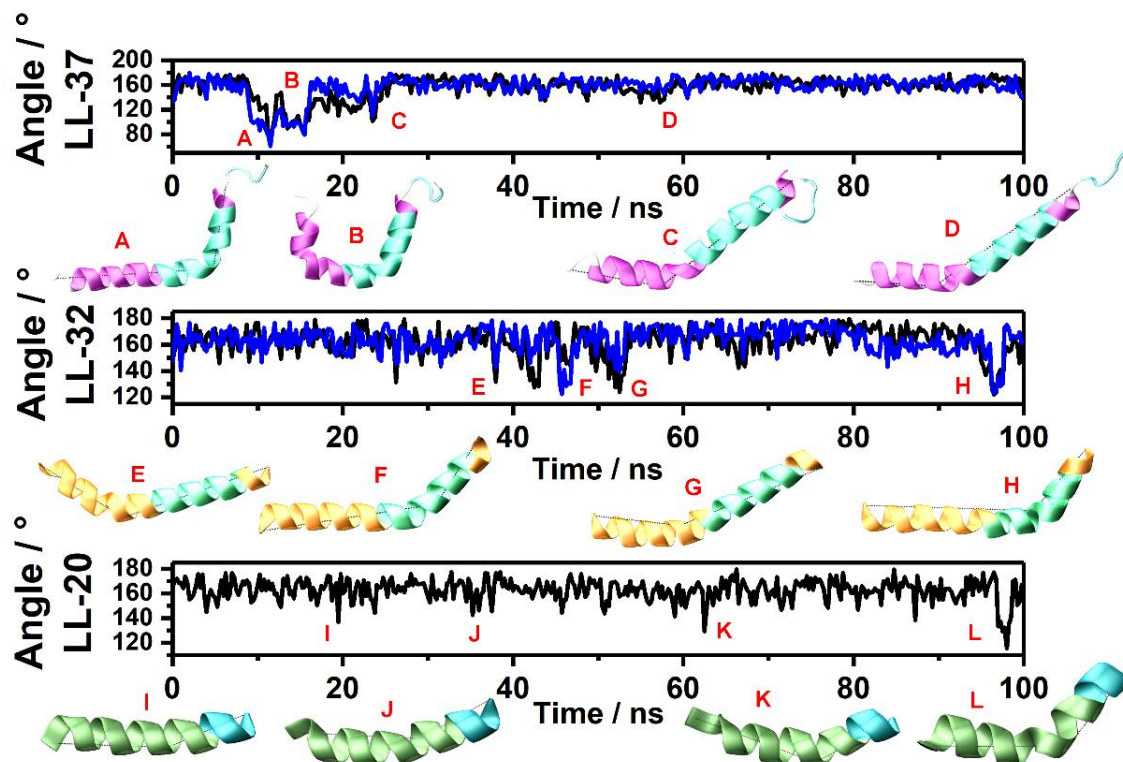
Figure 6.8 Visualization of the peptide bending site of LL-37 (top), LL-32 (middle) and LL-20 (bottom). LL-37 and LL-32 bend at the residues L1-K12-V32 (black traces) and (blue traces). LL-20 bends at the positions L1-K12-I20 (black trace). Reprinted with kind permission from Alejandra de Miguel (2017). *Elucidating the Mechanism of Action of Antimicrobial Peptides by means of Computational Approaches*, Technische Universität Berlin, Fakultät II.[287]

residues, LL-20 exhibited a dipole moment of only 50 Debye. Previous investigations showed, that the formation of inter- and intra-molecular salt bridges were an important factor for the secondary structure stabilization in physiological buffers, where ions serve as quenchers.[283,284] Based on this information, the dynamics of the salt bridge formation was analyzed in the course of all-atom simulations (100 ns).

Additionally to LL-37 and the described fragments, a LL-20 mutant, which includes a substitution of valine at position 9 by a serine and is named S9V-LL-20, was investigated. This led to a specific validation of the dynamics of the first twenty amino acids allowing a direct comparison with the results received by Wang et al.[285] in experiments with LL-23V9. Figure 6.9 displays the probability of the salt bridge formation between the amino acid side chain residues. A direct comparison of LL-37 and LL-32 reveals for both peptides that the residues D4-R7, D4-K8, E11-K8, E11-K15 and E16-R19 are significantly involved in salt bridge formation (Figure 6.9A). An additional salt bridge between the moieties D26-R29 existed in LL-32. Two further salt bridges between R34-E36 and E36-K8 contributed to the secondary structure formation of LL-37. The peptide core region (residues F17-R29), however, lacks a salt bridge formation in both peptides. The fragment LL-20 and the mutant S9V-LL-20 indicate a similar salt bridge formation compared to LL-37 and LL-32 resulting in salt bridges between the side chain residues D4-R7, D4-K8, E11-R7, E11-K8, E11-K15, E16-K12 and E16-R19 (Figure 6.9B).

Interestingly, all peptide studies showed the formation of salt bridges involving mainly the residues 1 to 19 with strong contributions of the moieties D26, R29, R34 and E36 for LL-37 and LL-32, respectively. Furthermore, by comparison of LL-20 and its mutant a very similar behavior was observable. In conclusion, MD simulations in an aqueous environment indicate
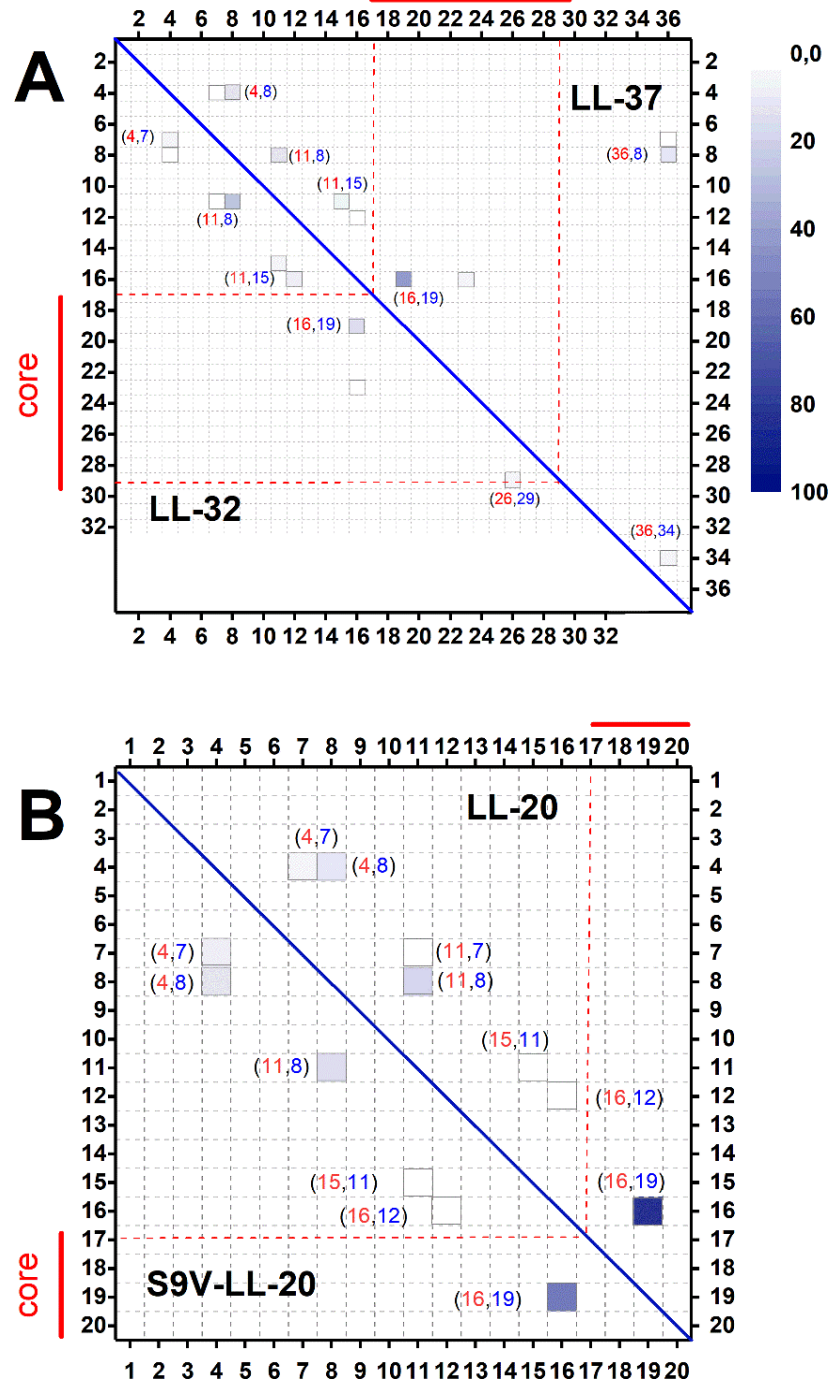
Figure 6.9 Probability of side chain salt bridge formation of LL-37 and LL-32 (A) as well as LL-20 and S9V-LL20 (B). The amino acid chain 1-19 and the VPRTES-terminus exhibit the highest number of salt bridges. Reprinted with kind permission from Alejandra de Miguel (2017). *Elucidating the Mechanism of Action of Antimicrobial Peptides by means of Computational Approaches*, Technische Universität Berlin, Fakultät II.[287]

a lack of salt bridges in the peptide core region, which hypothesizes the presence of unique properties in this region.

6.2.3.2 Determination of trajectories for monomers of LL-37, LL-32 and LL-20 in a lipid membrane environment

So far, the mechanism and dynamics of peptide attachment of LL-37 and its derivatives to membrane surfaces has not been investigated at atomic resolution. Therefore, 300 ns long all-atoms MD simulations of the three peptides in the presence of mixed POPC:POPG (90:10) lipid bilayers were performed. The peptides were initially placed 10 Å above the lipid surface to assure an unbiased attachment.

The different length of LL-37, LL-32 and LL-20 led to differences in the dynamic behavior and adsorption process. Figure 6.10 depicts the number of average contacts of the three peptides with the membrane surface. The analysis showed that LL-37 interacted during the whole simulation time with the membrane and there was a significant increase of the contact number after ca. 200 ns (Figure 6.10 purple trace). Meanwhile, LL-32 exhibited a rather modest, but stable number of membrane contacts during the entire simulation (Figure 6.10 orange trace), with five-fold less contacts in comparison to LL-37 (Table 6.1). The shortest fragment LL-20 revealed a few contacts in the beginning, however after 50 ns desorption from the surface took place (Figure 6.10 green trace).

There are several reasons explaining this observation. First, only the residues 17-20 of the essential peptide core are conserved in this fragment (see Figure 4.3). Second, the salt bridge formation of the charged moieties (Figure 6.9B) that stabilizes the secondary structure blocks the interaction of these residues with the membrane. Moreover, the decreased binding affinity correlates with the shorter peptide length due to entropic reasons.[286]

The adsorption mechanism was analyzed in more detail by measuring the distance between the center of mass (COM) of the peptides (COM$_{peptide}$) and membrane (COM$_{membrane}$) visualized in Figure 6.11. Based upon these calculations, distinct modes of attachment of LL-37 and LL-32 in
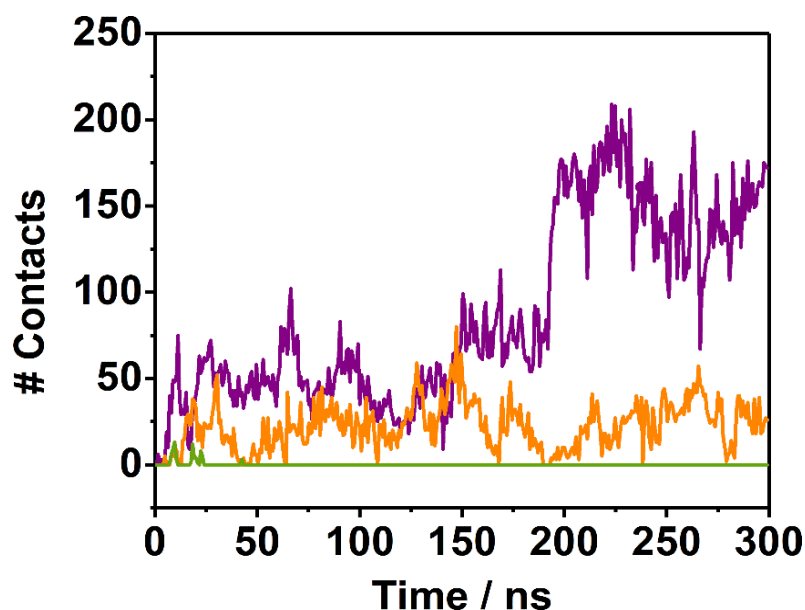
Figure 6.10 Monomer-membrane interaction of LL-37 (purple trace), LL-32 (orange trace) and LL-20 (green trace) analyzed by the number of contacts during 300 ns of all-atom MD simulations. LL-37 and LL-32 a reveal distinct interaction behavior with the membrane surface, whereas LL-20 does not adsorb to the surface. Reprinted with kind permission from Alejandra de Miguel (2017). *Elucidating the Mechanism of Action of Antimicrobial Peptides by means of Computational Approaches*, Technische Universität Berlin, Fakultät II.[287]

Table 6.1 Number of hydrophobic and electrostatic interactions during the attachment process of peptide monomers and POPC:POPG (90:10) membranes represented for LL-32 and LL-37. Reprinted with kind permission from Alejandra de Miguel (2017). *Elucidating the Mechanism of Action of Antimicrobial Peptides by means of Computational Approaches*, Technische Universität Berlin, Fakultät II.[287]

	Hydrophobic interactions	Electrostatic interactions
LL-32	5	32
LL-37	120	90

a lipid environment were observed. While LL-37 immersed into the membrane (Figure 6.11 left purple trace), LL-32 adsorbed stable on the surface (Figure 6.11 left - orange trace). Compared to the average distance of $COM_{membrane}$ to the membrane surface (20 Å), the distance COM_{LL-37} to $COM_{membrane}$ is about 5 Å shorter.

Moreover, there are differences in the forces driving the adsorption process (Table 6.1). The attachment of LL-32 to the surface is predominantly mediated by electrostatic interactions. On the other hand, a combination of electrostatic and hydrophobic forces accounts for stronger interactions between LL-37 and the membrane. This information is in line with experimental data previously presented by Henzler-Wildman et al.[288]

A detailed analysis of the insertion of LL-37 suggested a stepwise process. The core residues (F17-R29) played an essential role for the approach of the peptide anchoring to the anionic membrane by residue R23. By means of the moiety R34 a transient attachment of the VPRTES-terminus (residue 32-37) was induced, which destabilized the initial arrangement. This promoted the immersion of LL-37 into the surface of the membrane by its hydrophobic N-terminus. In its final state after 300 ns of simulation, the peptide is completely immersed in the interface between the hydrophobic core and hydrophilic headgroups. Thus, the hydrophilic side of the peptide but also its loose VPRTES-terminus pointed towards the solution.

In contrast, MD simulations of LL-32 showed the adsorption of the peptide on the membrane surface instead of its immersion. Similar to LL-37, the core residues of LL-32 (F17-R29) steer the interactions with the surface using the residue R23 as an anchor. However, after stabilization on the top of the lipid bilayer ca. 30 Å away from COM$_{membrane}$, the peptide
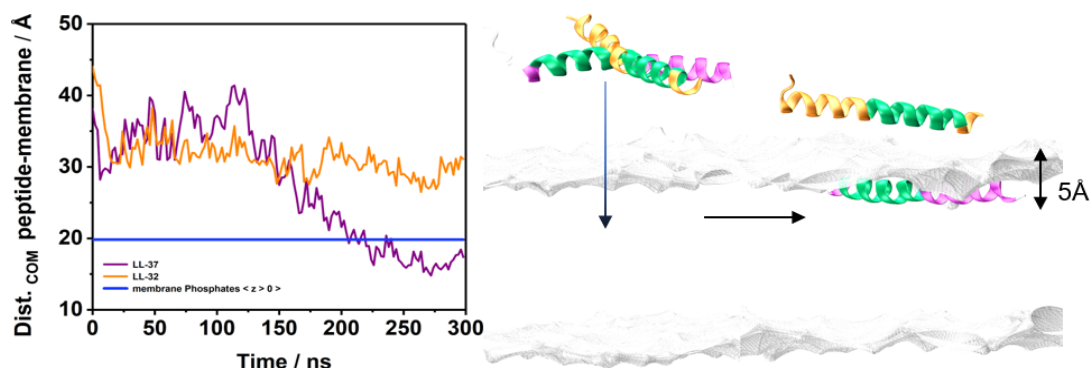
Figure 6.11 Left: Representation of the distance between the center of mass (COM) of peptides and membrane during 300 ns of all-atom MD simulations. LL-37 inserts (purple trace) in the interface between hydrophilic POPC:POPG headgroups and hydrophobic membrane core, while LL-32 remains over the surface (orange trace). The blue trace depicts the average z-coordinates of the phosphate headgroups of the membrane (upper leaflet) as reference point for immersion. Side chains of both peptides are not displayed for clear visualization. Right: Visualization of the attachment process of LL-37 (pink/green) and LL-32 (yellow/green). After incorporation the distance between LL-37 and the surface is about 5Å. Reprinted with kind permission from Alejandra de Miguel (2017). *Elucidating the Mechanism of Action of Antimicrobial Peptides by means of Computational Approaches*), Technische Universität Berlin, Fakultät II.[287]

exhibits about 37 contacts with the POPC:POPG surface (Table 6.1) without any immersion into the membrane.

6.2.4 Conclusion

The antibiotic activity of LL-37 is closely related to its interaction with the cellular membrane of infectious pathogens. However, due to diverse modes of action, not only their inherent structure, but also the dynamics leading to specific orientations and locations within the membrane are essential. Although several efforts have been made during the last years to gain a detailed understanding of the mechanism of action of LL-37, a lot of aspects still remain elusive.

According to the experimental results obtained in transmission measurements all three peptides adopt an α-helical structure in solution, since the amide bands of LL-37 and LL-32 appear at the same position. Indeed, MD simulations of LL-37 in solution also predict an α-helical structure of the peptide but also an unstructured VPRTES -terminus (residues 32-37).[284] The amide I position of LL-20 is downshifted by ca. 2 cm^{-1}, which is not in line with a general upshift of the amide I band of shorter α-helical fragments.[141] This may be explained on the basis of a straighter, more rigid α-helix associated to stronger H-bonds within the amide backbone. On the other hand, MD simulations also confirmed, that salt bridge formation leads to a pronounced curvature of the α-helices of LL-37 and LL-32.

The peptide adsorption on a POPC:POPG (90:10) membrane demonstrated major differences in their activities. First, SEIRA spectra of LL-20 showed barely any peptide signals and thus, no binding to the membrane surface. In agreement with the experimental observation, the MD simulation proved only very weak interaction of LL-20 with the anionic surface. This can be rationalized based on the fact that many charged residues have been removed (in total 3 Arg, 1 Lys, 1 Asp, 1 Glu) by truncating LL-37. Although still seven positively charged and three negatively charged amino acids are present in LL-20, these are engaged in salt bridge formation.

Thus, the secondary structure is stabilized and most of the charge is compensated. Interestingly, stable salt bridges are only formed between charged side chains located within the 20 first residues. Most charged side chains of the remaining residues (20-37) are not involved in salt bridges. Furthermore, LL-20 lacks the moiety R23 which has been identified as an anchor during the adsorption process of LL-37 and LL-32.

This suggests that the peptide core (residues 17-29) is determined by the dynamics of salt bridge formation. The lack of salt bridges in the cathelicidin core leads to flexible cationic side chains, which are available for the interaction with an anionic surface and are responsible for a five-fold increase of the total dipole moment of the peptide.

In agreement with this conclusion, LL-37 and LL-32 display binding to the membrane while maintaining their helical structure. However, LL-37 binds to a much higher extent, i.e. with ca. 10 times higher intensity of the amide bands. This can be explained either by a 10-fold higher concentration of adsorbed peptides or based on the distance dependent surface enhancement effect in SEIRA. Hence, it is hypothesized that LL-37 was located closer to the Au surface and thus, immersed more deeply into the membrane. These results are consistent with the MD simulations of LL-37 and LL-32 in a lipid environment, which showed the preservation of the secondary structure of both peptides upon adsorption to the POPC:POPG surface.

During the incubation of LL-32 the amide I/amide II ratio stayed constant at a value of ca. 0.6. These distinct amide I/amide II ratios suggested a one-step adsorption process for LL-32, where the peptide adopted a horizontal orientation with a side-on binding to the membrane. However, LL-37 showed an evolution of the amide I/amide II ratio from ca. 0.4 to 0.6 and the insertion process involved several steps. In a first step, there is an insertion into the membrane in a tilted orientation. Afterwards, the peptide adopts an orientation parallel to the surface within the membrane characterized by the increase of the amide ratio.

MD simulations supported these data. In case of LL-32, a one-step process is predicted where the peptide directly adsorbs on the anionic surface primarily via electrostatic interactions. LL-37 incorporated in a two-step process, initiated by the electrostatic attachment of the peptide on the surface. The following immersion was induced by hydrophobic forces. In studies using model peptides based on magainin, Dathe et al. also showed the importance of electrostatic interactions in the initial phase of peptide-membrane attachment. At the same time it was demonstrated that membrane binding and immersion needed a fine balance of electrostatic attraction to the lipid headgroups and hydrophobic interaction with the membrane core.[289,290]

During this insertion process, especially the residue R34 of the VPRTES-terminus is responsible for the destabilization of the initial electrostatic arrangement and promotion of the parallel membrane insertion via the hydrophobic N-terminus. Due to the parallel orientation of LL-37 and its derivatives the barrel-stave model of integration can be ruled out, which is in agreement with previous investigations using ^{15}N solid-state NMR site-specifically labeled LL-37.[291]

These findings increase the knowledge regarding the mechanism used by LL-37 and its interplay with bacterial cell membranes. In the literature conflicting data are discussed suggesting the carpet model or toroidal pore model.[288,291–293] The difference in the results depends on different conditions such as the membrane composition. Hence, both pathways could represent different stages of peptide attachment, as stated by Wang.[293] The presented experimental data and computational trajectories support the carpet model mechanism, which could be a part of a complex process combining different mechanistic hypotheses.

6.3 Voltage-dependent incorporation of alamethicin into a tethered lipid bilayer membrane system

This section describes and discusses the results of the investigation of the potential-dependent peptaibol alamethicin (ALM) in two different artificial membrane systems, namely tethered hybrid lipid membrane (tHLM) and tethered bilayer membrane (tBLM). Furthermore, the angles of ALM in its horizontally adsorbed and vertically incorporated state were calculated by density functional theory (DFT), carried out by Dr. Jacek Kozuch, Department of Chemistry, Stanford University, Stanford, USA. The presented results are reproduced from Forbrig et al.[206]

6.3.1 SEIRA spectroscopic analysis of ALM adsorption and incorporation

Figure 6.13 shows SEIRA spectra of the incubation of ALM separately incubated on a tHLM (A) and a tBLM (B; see Figure 6.12 for graphical description) at open circuit potential (E_{OCP} ~ +70 mV). These two systems have been chosen, since the tHLM system does not provide any space for incorporation of ALM into the hydrophobic membrane core due to the rigid cholestanyl-headed WK3SH-SAM. However, the peptide can incorporate into lipid bilayer fragments of the tBLM system. The surface-enhancement of the IR absorption scales with d^{-6}.[40] This enables only a detection of molecules adsorbed or removed from the surface as positive or negative peaks in the difference spectra.[34] In both systems, the positive bands in the spectral range between 1800 cm^{-1} and 1500 cm^{-1} clearly show amide bands proving the adsorption of the peptide.[34] After incubation with tHLMs (Figure 6.13A), these bands are centered at 1660 and 1550 cm^{-1} with shoulders at 1678 cm^{-1}, 1639 cm^{-1}, 1619 cm^{-1}, and 1532 cm^{-1}. Based on DFT calculations, which will be discussed in detail later, the bands at 1660 cm^{-1} and 1639 cm^{-1} are assigned to both the N-terminal and the C-terminal helices of ALM, since considerable intensities were predicted at both positions. The shoulders at 1678 cm^{-1} and 1619 cm^{-1} can be assigned to the C=O and the asymmetric COO$^-$ stretching modes [ν(C=O) and ν_{as}(COO$^-$)] of Gln and Glu, respectively.[141] In addition, there is a contribution by the C-terminal helix to the component at 1678 cm^{-1} due to absent or weak intramolecular hydrogen bond (H-bond) interactions. The signals at 1550 cm^{-1} and 1532 cm^{-1} are due to the amide II bands of the N-terminal and C-terminal helix fragments, respectively, and the band at 1742 cm^{-1} can be assigned to the ν(C=O) stretching mode of lipids.[34,224] Additionally, the absorption at 3319 cm^{-1} represents the amide A band of ALM.[141]
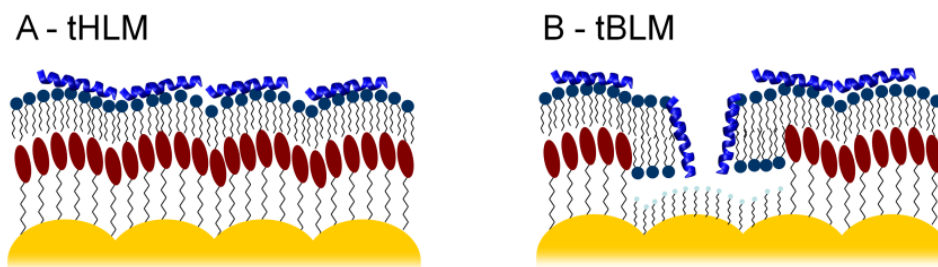
Figure 6.12 Schematic cross-section of tethered hybrid lipid bilayer membrane (tHLM, A) and tethered bilayer lipid membrane (tBLM, B). Whereas the tHLM contains a SAM layer of the cholestanyl-linker WK3SH covered by a lipid monolayer, the tBLM system additionally comprises 6-mercaptohexanol spacer molecules allowing the formation of lipid bilayer islands over an aqueous compartment and full incorporation of transmembrane peptides. . Reprinted with permission from Forbrig, E.; Staffa, JK.; Salewski, J.; Mroginski MA.; Hildebrandt, P.; Kozuch, J. Monitoring the Orientational Changes of Alamethicin during Incorporation into Bilayer Lipid Membranes *Langmuir* 2018 *34* (6), pp 2373-2385. Copyright (2018) American Chemical Society.[206]
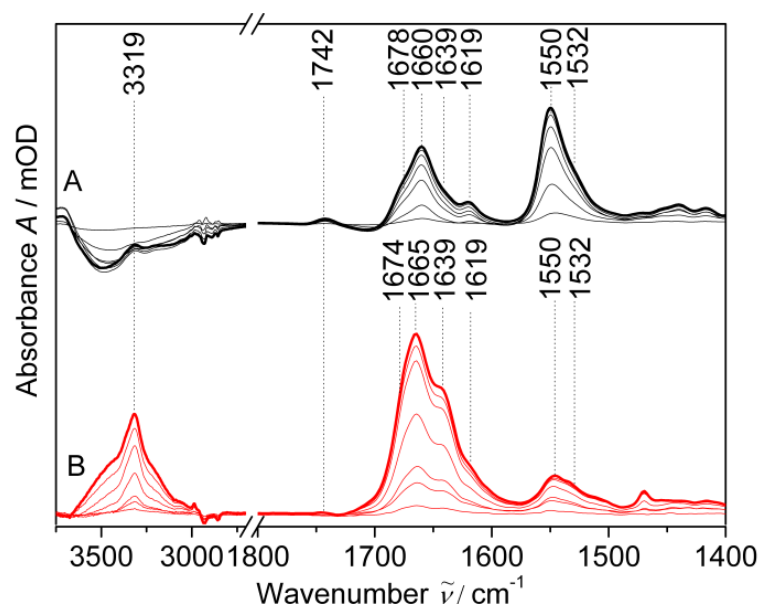
Figure 6.13 SEIRA difference spectra representing the incubation of ALM with tHLMs (A - black) and tBLMs (B - red), using the tHLM and tBLM spectra as the reference, respectively. The intermediate spectra refer to 1.5, 25, 30, 60, 120, 180, and 240 min after addition of ALM to the bulk buffer solution (n = 2 independent experiments). Reprinted with permission from Forbrig, E.; Staffa, JK.; Salewski, J.; Mroginski MA.; Hildebrandt, P.; Kozuch, J. Monitoring the Orientational Changes of Alamethicin during Incorporation into Bilayer Lipid Membranes *Langmuir* 2018 *34* (6), pp 2373-2385. Copyright (2018) American Chemical Society.[206]

The incubation of ALM with tBLMs (Figure 6.13B) leads also to positive amide A, amide I, and amide II bands, which proves the adsorption of ALM. The amide I band is centered at 1665 cm^{-1}, which is still in line with the previous assignment, and the high-frequency shoulder is shifted to 1674 cm^{-1}. These shifts can be rationalized based on different orientations, which enhance different amide vibrations to a different extent (vide infra), and minor structural changes of the peptide. This is in line with published MD simulations that did not show significant conformational changes upon insertion of ALM.[294]

Interestingly, there is a significant difference in the amide I/amide II SEIRA intensity ratio (R_{SEIRA}; integrated absorption) of ca. 1.15 for tHLMs and 4.5 for tBLMs under saturated adsorption conditions. In contrast, in isotropic transmission IR experiments ALM showed an amide I/amide II ratio (R_{iso}) of 2.55 (see Figure 6.17; according to peak intensity the ratios are 0.7, 4.6, and 2.0, respectively).[211] To rationalize these findings it has to be considered that the SEIRA intensity of a mode scales with the square of the cosine of the tilt angle of its TDM with respect to the surface normal.[232] The TDMs of amide I and amide II of an α-helix are reported to be oriented approximately along (α = 29° - 40°) or perpendicular (β = 77° - 79°) to the helix axis, respectively.[146,224] Therefore, the calculated R_{SEIRA} values can be ascribed to different orientations of ALM: (1) a horizontal adsorption of ALM on top of the tHLM and (2) a vertical transmembrane orientation of ALM in tBLMs, as observed by Yang et al. in experiments and Mottamal et al. in simulations.[214,294] By this means, either the amide I or the amide II mode of ALM is preferentially enhanced, as visible in the SEIRA spectra. This explanation is further supported by the overlapping broad adsorption band at ca. 3400 cm^{-1} that can be assigned to the stretching mode of water.

During the adsorption of ALM on tHLMs, this band leads to a negative signal in the SEIRA difference spectrum due to the removal of water from the lipid/solution interface upon interfacial

ALM binding. In the study using tBLMs, a positive signal appeared, which leads to the assumption of a water channel formation across the membrane by transmembrane ALM helices.

Figure 6.14 shows time traces of the amide I and amide II intensities along with the corresponding R_{SEIRA} values after correction for the spectral contribution of water (bending mode at ca. 1650 cm^{-1}; Figure A2 and Figure A1). The adsorption on tHLMs (Figure 6.14, black traces) leads to an increase of both intensities in a roughly mono-exponential manner associated with a slight increase of R_{SEIRA} from ca. 0.95 to 1.15. This behavior indicates the direct adsorption of ALM onto the membrane surface associated with only a slight reorientation of the peptides. On tBLMs (Figure 6.14, red traces), the data indicate a more complicated kinetic that levels off after ca. 80 min. In particular, R_{SEIRA} changes considerably from ca. 2 to 4.5 demonstrating an adsorption process with a subsequent major reorientation of ALM. The kinetic traces of the SEIRA intensities were simulated on the basis of a three-step process (3-step-model depicted in the box in Figure **6.14**) that will be described in the next chapter.
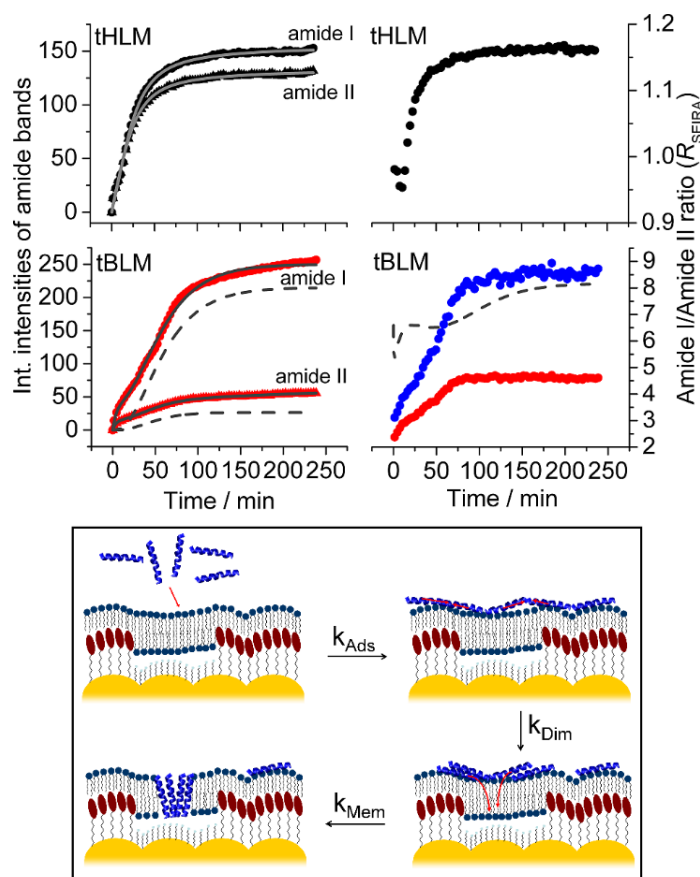
Figure 6.14 Time-dependent evolution of the integrated intensities of the amide I and II bands of ALM (left) and the amide I/amide II intensity ratio (right) when incubated on tHLMs (black) and tBLMs (red). The adsorption onto tHLMs and the incorporation into tBLMs was described using a set of differential equations representing a three-step process of adsorption (Langmuir kinetic), dimerization (second-order reaction) and incorporation (Langmuir kinetic, gray lines) depicted in the box below. In the case of tHLMs only the first two processes were considered. The gray dashed lines refer to the amide I and II intensities, and its ratio of membrane-incorporated components of ALM resulting from the fitting. The blue trace (bottom right) represents the intensity ratio corrected for non-incorporating, horizontally adsorbed ALM molecules in the tBLM system (n = 2 independent experiments). Reprinted with permission from Forbrig, E.; Staffa, JK.; Salewski, J.; Mroginski MA.; Hildebrandt, P.; Kozuch, J. Monitoring the Orientational Changes of Alamethicin during Incorporation into Bilayer Lipid Membranes *Langmuir* 2018 *34* (6), pp 2373-2385. Copyright (2018) American Chemical Society.[206]

6.3.2 3-step kinetic model of incorporation

The incorporation process into tBLMs follows a three-step-process:

Step 1: a direct adsorption of ALM onto the membrane surface:

$$P_{Sol} \xrightarrow{k_{Ads}} P_{Ads}$$
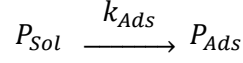
(P_{Sol} : peptide in solution)

(P_{Ads} : peptide adsorbed to membrane surface)

(k_{Ads} : rate constant for adsorption)

Step 2: peptide-peptide interaction on the surface yielding dimers[170]

$$P_{Ads} \xrightarrow{k_{Dim}} P_{Dim}$$
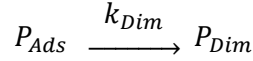
(P_{Dim} – peptide dimers)

(k_{Dim} – rate constant for the dimerization)

Step 3: reorientation to incorporate into the membrane core leading to a transmembrane arrangement

$$P_{Dim} \xrightarrow{k_{Mem}} P_{Mem}$$
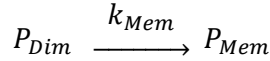
(P_{Mem} – incorporated peptide)

(k_{Mem} – rate constant for incorporation)

Step 1 can be described by the Langmuir adsorption model, due to spatial restrictions on the surface

$$\frac{dP_{Sol}}{dt} = -k_{Ads} \cdot P_{Sol} \cdot \left(P_{Ads,max} - P_{Ads}\right) \tag{6.1}$$

(P_{Sol} : concentration of peptide in bulk solution)

($P_{Ads,max}$: maximum amount of peptide adsorbed on membrane surface)

(P_{Ads} : amount of peptide adsorbed on the membrane surface)

(k_{Ads} : rate constant for adsorption)

In total this leads to a second-order reaction: a first-order reaction with respect to the peptide in solution (P_{Sol}) and a first-order reaction with respect to the free binding sites on the surface ($P_{Ads,max} - P_{Ads} - P_{Dim}$). $P_{Ads,max}$ is a variable value, since in the beginning 100% of the surface area can be occupied, but after incorporation of ALM the maximum surface area is reduced. Based on the SAM composition of 20% 6MH ($x_{6MH} = 0.2$) and the maximum concentration of incorporated peptide ($P_{Mem,max}$), $P_{Ads,max}$ is multiplied by:

$$f = 1 - x_{6MH} \frac{P_{Mem}}{P_{Mem,max}} \tag{6.2}$$

(P_{Mem}: amount of peptides in membrane core)

($P_{Mem,max}$: maximum amount of peptide incorporated into membrane core)

Combining equation $\frac{dP_{Sol}}{dt} = -k_{Ads} \cdot P_{Sol} \cdot \left(P_{Ads,max} - P_{Ads}\right)$

(6.1 and 6.2 leads to the rate of adsorption

$$\frac{dP_{Sol}}{dt} = -k_{Ads} \cdot P_{Sol} \cdot \left(P_{Ads,max}\left(1 - x_{6MH}\frac{P_{Mem}}{P_{Mem,max}}\right) - P_{Ads}\right) \tag{6.3}$$

Step 2 is a second-order reaction, since a dimerization of peptides is proposed as a time-dependent step. Consequently, the change in concentration of adsorbed peptide depends on $-\frac{dP_{Sol}}{dt}$ and the dimerization process:

$$\frac{dP_{Ads}}{dt} = -\frac{dP_{Sol}}{dt} - k_{Dim} \cdot P_{Ads}{}^2 \tag{6.4}$$

(k_{Dim} : rate constant for dimerization)

$$\frac{dP_{Ads}}{dt} = +k_{Ads} \cdot P_{Sol} \cdot \left(P_{Ads,max}\left(1 - x_{6MH}\frac{P_{Mem}}{P_{Mem,max}}\right) - P_{Ads}\right) - k_{Dim} \cdot P_{Ads}{}^2 \tag{6.5}$$

Step 3 The final incorporation into the membrane core, again goes along with limited space. Therefore a Langmuir-like kinetic can be employed. Thus, the concentration of the dimerized adsorbed peptides increases due to dimerization and decreases due to incorporation:

$$\frac{dP_{Dim}}{dt} = +k_{Dim} \cdot P_{Ads}{}^2 - k_{Mem} \cdot P_{Dim} \cdot \left(P_{Mem,max} - P_{Mem}\right) \tag{6.6}$$

(P_{Dim} : amount of peptide dimerized from adsorbed species)
$P_{Mem,max}$: maximum amount of peptide incorporated into membrane core)
k_{Mem} : rate constant for incorporation)

The rate of incorporation is given by:

$$\frac{dP_{Mem}}{dt} = k_{Mem} \cdot P_{Dim} \cdot \left(P_{Mem,max} - P_{Mem}\right) \tag{6.7}$$

For the conversion into SEIRA intensities, the concentrations are multiplied by species-specific factors. These factors combine the extinction coefficients of the amide I or amide II normal mode, the orientation of the species, and the effective surface-enhancement.

$$I_{SEIRA} = F_{Ads} \cdot P_{Ads} + F_{Dim} \cdot P_{Dim} + F_{Mem} \cdot P_{Mem} \tag{6.8}$$

F_{Ads} : surface-enhancement factor for adsorbed species

F_{Dim} : surface-enhancement factor for dimerized species

F_{Mem} : surface-enhancement factor for membrane-embedded species

As starting parameters, $P_{Ads,max}$ and $P_{Mem,max}$ were estimated from the crystal structure and literature values,[14,209] as $7.08 \cdot 10^{-2}$ nmol and $1.86 \cdot 10^{-2}$ nmol, respectively, taking into account an electrode surface area of 1.5 cm^2 and $x_{6MH} = 0.2$. These values relate to specific areas of 360 Å^2 and 280 Å^2 per adsorbed or incorporated molecule, respectively. Furthermore, at $t = 0$, the concentration of P_{Sol} was set to 10^{-6} M (with a volume of V = 1 mL), while P_{Ads}, P_{Dim} and P_{Mem} were set to 0 mol/cm^2 – similar to the conditions used in the experiment. In order to fit the kinetic

equations to the experimental results on tHLMs, k_{Mem} was fixed to $k_{Mem} = 0$, since no incorporation was possible.

Table A2 as well as Figure A5 – Figure A7 represent the results of the simulation. The graphs and the associated χ^2 values show a very good fit in all cases. The most intuitive values in the model are displayed by $P_{Ads,max}$ and $P_{Mem,max}$, since there is a relation to the size and distribution of ALM in the described membrane system. Interestingly, regardless of tHLMs or tBLMs and amide I or amide II mode, $P_{Ads,max}$ did not change considerably from the theoretical value of a fully densely packed layer of ALM molecules. For a surface of 1.5 cm^2, the estimation of this value led to $7.08 \cdot 10^{-2}$ nmol from a specific area of 360 Å^2 per vertically adsorbed ALM. First, this supports the validity of our kinetic model and points to a high density of peptide adsorbed to the membrane surface. The variable $P_{Mem,max}$ also provides a similar value of $4.37 \cdot 10^{-5}$ nmol (on $0.2 \cdot 1.5$ cm^2) for all fits, which is, however, diminished by a factor of ca. 400 from a theoretical densely packed arrangement of transmembrane ALM helices. Again, the fact that this value does not exceed the theoretical maximum value supports and validates the described model of ALM incorporation. Furthermore, it indicates the formation of channels in the membrane according to the barrel-stave model and neglects an "unlimited" and more random incorporation of peptide into the membrane interior.

In this kinetic model consisting of three states (adsorbed, dimerized and incorporated ALM), the initial assumption is that principally each state has a constant orientation (with the associated R_{SEIRA} value), when the kinetic parameters are equal for amide I and amide II. This situation is displayed in Table A2 using the fitting results with the headers "Amide I" and "Amide II*" – in this case the values of the variables k_{Ads}, k_{Dim}, k_{Mem}, $P_{Ads,max}$, and $P_{Mem,max}$ from the fit of the amide I intensity were adopted for the amide II. However, allowing these parameters to vary in the fit, provides an indirect description of the reorientation of each species, since amide I and amide II may change with different kinetic constants (pair of data with headers "Amide I" and "Amide II"). As this is only an indirect description of the reorientation, a detailed discussion of the differences of the kinetic parameters is not provided, instead the amide I/amide II ratios that result from this fit are described (Figure A7). In particular, the investigation is focused on the modelled amide I/amide II ratios of each component of ALM at the end of the incubation.

On tHLMs (Figure A7, left), the kinetic model provides a very good assessment of the time trace of the R_{SEIRA} value; only during the first 10 min a considerable deviation is observed. From the experiment, R_{SEIRA} changes from ca. 0.95 to 1.15, which was tentatively ascribed to the adsorbed and dimer species, respectively. Our kinetic model provides very similar R_{SEIRA} values for these two components of 0.85 and 1.16, which in this case even maintain relatively unchanged during the course of immobilization. It is understandable that the value for the adsorbed species differs more notably, but still within a reasonable range (0.95 vs. 0.85), as this species appears only temporarily.

In case of tBLMs, the overall evolution of measured R_{SEIRA} values is also modeled very well, but displays a slightly different shape in particular in the beginning of the incubation. This is due to the complicated trace of the amide I intensity on tBLMs, which was fitted with good but somewhat larger errors in all fits (Table A2 and Figure A6). This again can be rationalized on the basis that a simplified model was used consisting of three species without a direct description of reorientation processes. Thus, in Figure A7 (right), the R_{SEIRA} values show a rather complex time course, which equilibrate at 0.8, 1.3, and 8.2 for the adsorbed, dimer and incorporated species. The first two values match very well with those obtained using tHLMs (0.85 and 1.16), supporting the validity of this approach and as well as kinetic model. In this way, the third value of 8.2 offers

a prediction of the amide I/amide II ratio of the incorporated transmembrane helices that is otherwise directly inaccessible.

The blue data set in Figure A7 (right) demonstrates the time course of R_{SEIRA} after the SEIRA spectra were corrected for horizontally adsorbed ALM species on tHLM-like fragments of the tBLM using the SEIRA spectra measured of tHLMs. Intriguingly, this correction results in a final R_{SEIRA} value of ca. 8.5 that is in line with the expected value of 8.2, as obtained from the kinetic model.

As shown in Figure 6.14, this model provides a very good description of the experimental data for both tHLMs (taking only step 1 and step 2 into account) and tBLMs. This description indirectly supports a mode of action of ALM, in which it forms distinct ion channels of 4–12 molecules as described by the barrel-stave model in literature.[13,14] As explained in detail, the 3-step-model yields a maximum coverage of ca. 50 pmol cm^{-2} of horizontally adsorbed ALM molecules on the membrane surface and of ca. 150 fmol cm^{-2} of transmembrane incorporated ALM helices. These values correspond to a densely packed monolayer of ALM on the membrane, and transmembrane ALM ion channels occupying ca. 0.25 % of the possible area of the membrane, respectively. The latter value may be slightly underestimated, since in previous work similar amide intensities of proteins were estimated to yield a coverage of ca. 1–10 %.[8,49] The gray dashed lines in Figure 6.14 display the SEIRA intensities and the ratio of the transmembrane-incorporated ALM fraction resulting from the kinetic model. Accordingly, ALM starts incorporating into the membrane core only after a time offset of ca. 20 min due to the required peptide-peptide interactions and reaches a predicted final amide I/amide II ratio of ca. 8.2. This value differs from the observed value of 4.5, since the tBLM is composed of a considerable amount of WK3SH-supported fragments, analogous to the tHLM, so that the SEIRA spectrum of the ALM/tBLM system reflects also a significant portion of ALM adsorbed on the membrane
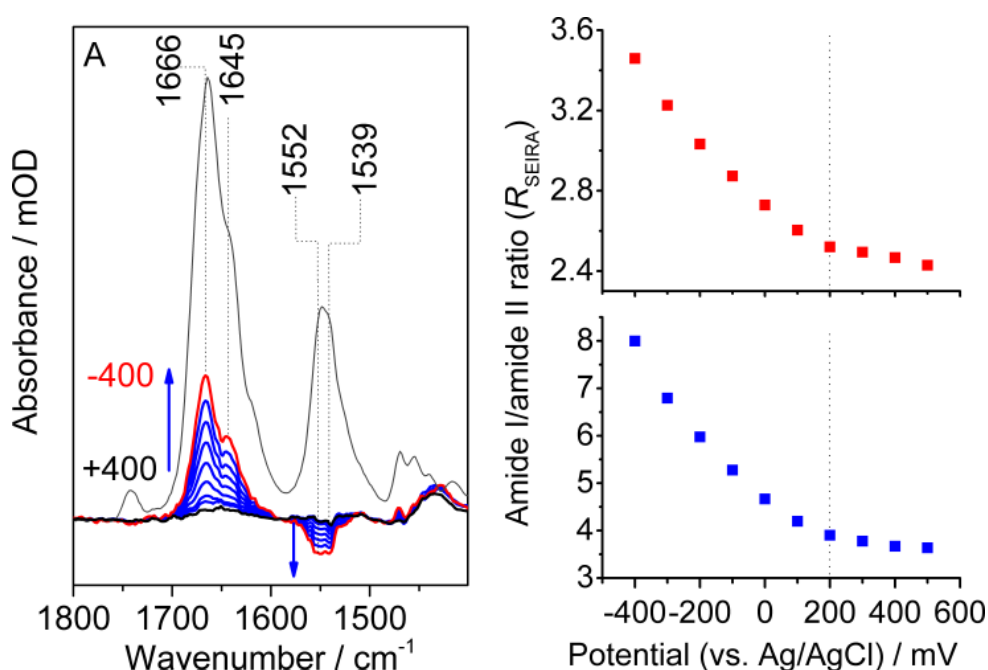
Figure 6.15 Left: Potential-dependent SEIRA difference spectra of ALM initially incubated at +500 mV onto tBLMs, taking the potential of +500 mV as a reference. Black and red difference spectra refer to potentials at +400 and -400 mV, respectively, while blue spectra refer to the intermediate potential (in steps of 100 mV). The gray spectrum shows the absolute ALM SEIRA spectrum at +500 mV taking the tBLM spectrum as a reference. Right: Amide I/amide II ratios of the difference spectra without correction (top, red) and after correction for horizontally bound ALM (bottom, blue) (n = 2 independent experiments). Reprinted with permission from Forbrig, E.; Staffa, JK.; Salewski, J.; Mroginski MA.; Hildebrandt, P.; Kozuch, J. Monitoring the Orientational Changes of Alamethicin during Incorporation into Bilayer Lipid Membranes *Langmuir* 2018 *34* (6), pp 2373-2385. Copyright (2018) American

surface, which cannot incorporate into the membrane. To correct for this contribution, the SEIRA data from the experiments with tHLMs were used (no incorporation; Figure 6.12 and Figure A2). Then the corrected R_{SEIRA} values, as shown by the blue trace in Figure 6.14 (right), increase from 3 to 8.5, which is in line with the final R_{SEIRA} value of 8.2 predicted by the kinetic model.

Thus, it can be concluded that the corrected trace of R_{SEIRA} describes the ALM fraction that incorporates into the tBLM and forms ion channels very well.

The most intriguing property of ALM is its potential-dependent formation of ion channels due to the interaction of the dipole moment of ALM with the interfacial electric fields.[208,215] In a separate experiment, the adsorption was aborted at an early stage with $R_{SEIRA} \approx 2.4$ (Figure 6.15). Then the potential was decreased gradually from +500 mV to -400 mV (vs. Ag/AgCl 3M KCl) to induce incorporation into the membrane via the transmembrane potential. Prior to measuring each spectrum, the respective potentials were applied for 6 min, after which no further spectral changes were detected. SEIRA difference spectra show clear indications of a reorientation of ALM, i.e. positive amide I and negative amide II difference signals. This results in a change of R_{SEIRA} from 2.4 to 3.5, which reflects the adoption of a more vertical orientation within the membrane. In consideration of the WK3SH-supported fraction, the same correction of the data as described above was employed to the spectra yielding an even more pronounced increase of R_{SEIRA} from ca. 3.5 to 8. Interestingly, R_{SEIRA} does not increase linearly with more negative potentials. Instead there are two regimes, i.e. a plateau regime above ca. +200 mV and a steep increase towards negative potentials. At the same time, no sharp difference bands or peak shifts are detectable in the difference spectra. This behavior indicates a stiff structure of ALM that is not significantly altered upon the incorporation and channel formation.

6.3.3 DFT calculations and vibrational analysis of ALM

DFT calculations and normal mode analysis of ALM have been performed using the approach previously reported by Keiderling and coworkers.[227,228,295] Due to the size of peptides such as ALM (e.g. 288 atoms) and the resultant difficulty to perform DFT calculations, the torsion angles of the backbone were fixed to reduce the degrees of freedom in the calculations. To account for the two possible ALM structures, the primary structural model (the α-helix/3_{10}-helix conformer) was calculated using the dihedral angles obtained from a recent NMR/MD study by Nagao et al.[210] to the crystal structure of ALM (chain B; PBD ID 1amt)[209] as starting geometry. In an alternative calculation chain C of the crystal structure was directly used for the α-helix/α-helix conformation and the analogous evaluation led to similar results (see Appendix). Prototypical α-helix and 3_{10}-helix dihedral angles, as used by Keiderling et al., were avoided, since the kink-inducing Pro-14 leads to a non-prototypical H-bond pattern, particularly in the C-terminal fragment of the ALM helix.

It was shown experimentally and theoretically that ALM adopts similar conformations in different environments, i.e. in water, organic solvents or in vesicles.[209,211,294,296] Such an intrinsically stable structure is consistent with the present SEIRA results, which provide no indication for perturbations of the helical structures upon spontaneous and potential-induced incorporation (Figure 6.13 and Figure 6.15), thereby further justifying the conformational constraints. Thus, the DFT-optimized structures are assumed to be maintained during the entire process of membrane
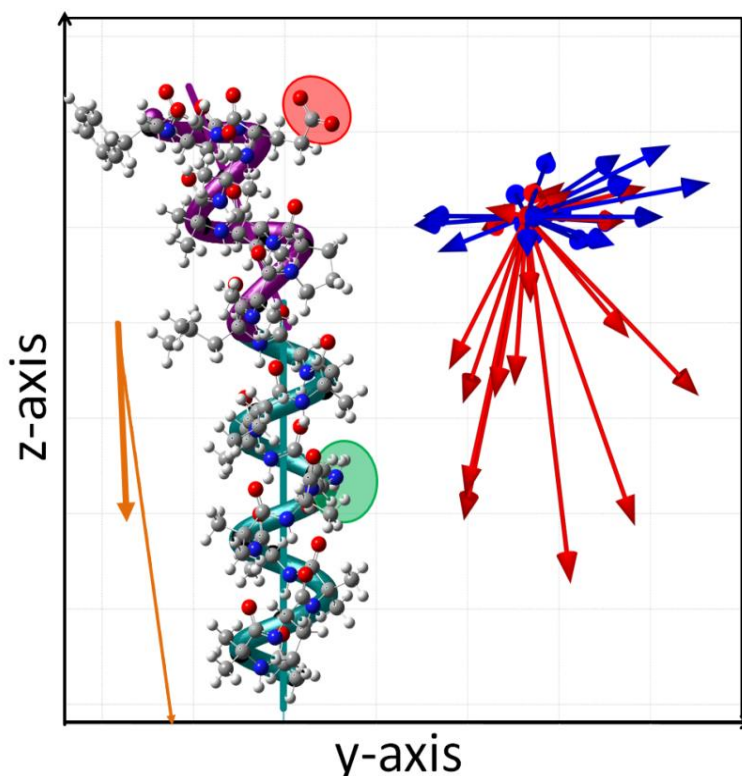
Figure 6.16 ALM structures obtained from DFT calculations for a α-helix/3$_{10}$-helix conformation of ALM (see section 8.1.4 for the alternative α-helix/α-helix conformation). The structure is shown from the "side" (hydrophobic and hydrophilic side of ALM on the left and right, respectively). The cyan and magenta ribbons and lines underlying the structures indicate the orientation of the N-terminal and C-terminal helix axes, respectively. The light red and light green circles highlight the position of Glu-18 and Gln-7; the orange arrows depict the vector of the dipole moments of the entire structure (thin arrows, 212 D) or of the backbone (bold arrows, 100 D) in the yz-plane. The red and blue arrows refer to the vectors of the TDMs of the amide I and amide II modes of ALM, respectively. Reprinted with permission from Forbrig, E.; Staffa, JK.; Salewski, J.; Mroginski MA.; Hildebrandt, P.; Kozuch, J. Monitoring the Orientational Changes of Alamethicin during Incorporation into Bilayer Lipid Membranes *Langmuir* 2018 *34* (6), pp 2373-2385. Copyright (2018) American Chemical Society.[206]

binding and incorporation. The calculation was performed in an isotropic environment of water as a solvent using the polarizable continuum model implemented in Gaussian09.[272] It should be noted that specific interactions with the membrane surface, the membrane core or other ALM molecules are not taken into account in this way. However, the structural rigidity of ALM discussed above seems to justify this simplified approach that may not be applicable for other peptides with a strong conformational plasticity. To account for more specific interactions either (i) a complex anisotropic dielectric environment or (ii) explicit lipid or ALM molecules must be added to the system.

Both extensions of the approach would complicate the DFT calculation severely, since (i) membranes and their interface to water show a very complex anisotropic distribution of the dielectric constant (ranging from 2–350)[297,298] and (ii) including more molecules in the calculation would again increase the computational costs substantially. The optimized structure of the "α-helix/3$_{10}$-helix" ALM conformer is displayed in Figure 6.16 showing the peptide from the "side" so that the axes of both helices lie in the yz-plane (analogous "α-helix/α-helix" structure is shown in Figure A11).

In this way, the hydrophobic patch is oriented to the left side, while the hydrophilic side with the residues of Glu-18 and Gln-7 faces to the right side. The two helical parts are kinked by ca. 23° (see Table A3) due to Pro-14 that impedes amide H-bonds, which is in line with MD simulations and crystal structures (ca. 20°).[209,210] The N-terminal part adopts a regular α-helical structure (ca.

3.4 residues per turn, radius of ca. 2.3 Å, translation per residue of 1.5–1.6 Å), while the C-terminus is structured as a narrower α-helix that is distorted towards a 3_{10}-helix conformation (3.3 residues per turn, radius of 2.0 Å, translation per residue of 1.3 Å; Table A3). As expected for a helix, the dipole moment (Figure 6.16, thin orange arrow) is oriented approximately along the helix axes with an inclination of ca. 11° from the N-terminal α-helix axis towards the C-terminal helix. Schwarz et al. reported an experimentally obtained dipole moment of ca. 75 D,[299] which disagrees with the value of 212.3 D obtained from the optimized structure. However, it must be taken into account that the experimental value results from ALM dissolved in octanol/dioxane, where the charge of Glu-18 may be shrouded due to H-bonds, and the solvent compensates the helix dipole. In fact, the dipole of the backbone yields a magnitude of 100 D at a tilt of 2°. Thus, the 212 D can be rationalized mainly as a superposition of the helix dipole (ca. 100 D) and the contribution of Glu-18 (charge difference of 1 e⁻ over 3 nm corresponding to ca. 144 D).

This is further supported by the alternative α-helix/α-helix structure (see Table A4 and Figure A11 to Figure A13) where a similar backbone dipole is observed, but the total dipole is 57 D and positioned almost perpendicular to both helices due to a different positioning of Glu-18 and intramolecular H-bonding with Gln-19. This observation clearly demonstrates that constrained movement or extended flexibility of the side chain can be crucial for the function of peptide antibiotics.

The groups of arrows in Figure 6.16 represent the TDM vectors of the amide I (red) and amide II (blue) normal modes. In general, the components of the amide II are oriented within a plane
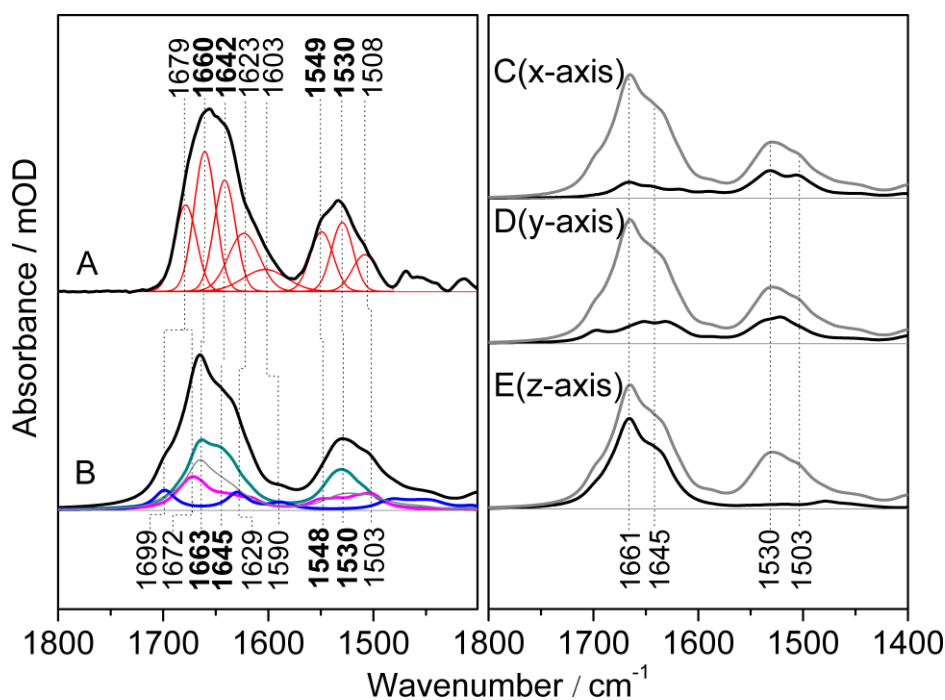
Figure 6.17 Left: Comparison of transmission IR spectrum of ALM in aqueous solution (A) and the simulated DFT-IR spectrum of α-helix/3_{10}-helix structure of ALM (B, half width set to 12 cm⁻¹). Red bands in A indicate the Gaussian fit to the experimental spectrum, while the spectra in cyan, magenta, blue and gray refer to the combined spectral components originating from the N-terminal α-helix, C-terminal 3_{10}-like helix, amino acid side-chains, and unassigned components, respectively. These components were derived from evaluating the potential energy distribution of the normal modes. Right: Simulated polarized DFT-IR spectra of ALM referring to the axes shown in Figure 6.16. Gray traces represent the isotropic spectra (n = 2 independent experiments). Reprinted with permission from Forbrig, E.; Staffa, JK.; Salewski, J.; Mroginski MA.; Hildebrandt, P.; Kozuch, J. Monitoring the Orientational Changes of Alamethicin during Incorporation into Bilayer Lipid Membranes *Langmuir* 2018 *34* (6), pp 2373-2385. Copyright (2018) American Chemical Society.[206]

approximately perpendicular to the helix axes, while the amide I components display a considerably larger scattering, albeit with a preferential orientation along the helix axes. In both cases, the multiple normal modes arise from different couplings of TDMs. The averaged TDM vectors of the amide I and II manifolds are inclined by ca. 7° and 101° from the α-helix axis, respectively (see Appendix), and are oriented almost orthogonally (90° ± 8.5°) to each other. These values differ from the values reported previously,[146,224] which can be rationalized on basis of the kinked helix structure of ALM. The alternative α-helix/α-helix structure affords similar results with deviating tilt angles by 2°–5°, which are within the experimental accuracy of the present approach. Thus, this alternative structure along with the associated theoretical IR spectra provides an equivalent picture for the following evaluation of the SEIRA spectra as summarized in Figure A11 to Figure A13.

The resulting calculated IR spectrum (DFT-IR spectrum; Figure 6.17B)[227] of the α-helix/3_{10}-helix structure is in very good agreement with the transmission IR spectrum of ALM measured in aqueous solution (Figure 6.17A).[211,300] The calculations afford several partially overlapping amide I components for each of the two secondary structure elements as shown by the intrinsic calculated spectra for the N-terminal α-helix (cyan) and C-terminal helix segment (magenta). As a consequence, the DFT-IR spectrum displays a maximum at 1663 cm^{-1} in the overall amide I profile, which largely albeit not exclusively originates from the most intense components of the short N-terminal α-helix. The shoulder at 1645 cm^{-1} can be ascribed as well to the N-terminal α-helix and is shifted due to the lack of H-bonds of the peripheral amides of the helix. The positions of these maxima agree very well with those of the experimental IR spectrum at 1660 and 1642 cm^{-1}. The good agreement also holds for other experimental IR bands at 1679, 1623, and 1603 cm^{-1} that can be assigned to side chain modes of Gln-7, Glu-18, and Gln-19 (blue spectrum; 1699, 1629, 1590 cm^{-1}). The notable deviation of up to 20 cm^{-1} of the IR bands of the Gln residues is due to H-bonds in aqueous solution, which are not considered in the DFT calculation.

The maximum intensity of the C-terminal 3_{10}-like helix is predicted at 1672 cm^{-1} in the DFT-spectrum and thus may contribute to the component at 1679 cm^{-1} in the experimental spectrum. The pronounced upshift of this mode compared to the corresponding mode of the prototypical helix (vide supra) can be ascribed to the shortness of this helix fragment and its distorted H-bond pattern. Also, in the amide II band region experimental and calculated spectra agree very well. The maximum, located at 1530 cm^{-1} in both spectra, is again ascribed to the N-terminal α-helix. The shoulders at 1549 and 1508 cm^{-1} in the experimental IR spectrum correspond to the two components of the C-terminal helix in the DFT spectra at 1548 and 1503 cm^{-1}. IR intensity below 1500 cm^{-1} originates from CH$_n$ bending modes of the amino acid residues. In total, the DFT-IR spectrum yields an amide I/amide II ratio of 2.58, which agrees very well with the value of 2.55 determined from the transmission IR spectrum in solution and is also in line with literature values of ca. 2.4–2.7 determined from organic solvents and vesicle dispersions.[211] The comparison of the experimental IR spectrum and the DFT-IR spectrum of the α-helix/α-helix structure is shown in Figure A12. While the overall shapes of the amide bands are in general less well reproduced, a similar assignment can be made, which is in line with the IR spectroscopic similarity of α-helices and 3_{10}-helices.[268]

Figure A5 (right) displays the polarized DFT-IR spectra along the axes defined in Figure 6.16, i.e. the α-helix axis being parallel to the z-axis and the y-axis traversing ALM from the hydrophobic to the hydrophilic side. As a result of the orientations of the TDMs, the z-polarized

spectrum shows a prominent amide I mode, but almost negligible intensity of amide II, resulting in an intensity ratio of ca. 27.5. For the x- and y-polarization, ratios of ca. 0.68 and 1.28 are obtained. Interestingly, the amide I and II band shapes change depending on the polarization, which is in line with the SEIRA spectra (Figure 6.13). For ALM in tBLMs and tHLMs the experimental maximum intensity is found at 1665 and 1660 cm^{-1}, respectively, suggesting that the amide I components of the α-helix are more prominent in the vertical orientation while losing their impact when oriented horizontally – similar to the z-polarized and the x-polarized DFT-IR-spectrum.

6.3.4 Theoretical analysis of the reorientation of ALM monitored by SEIRA spectroscopy

Due the SEIRA selection rules,[36] it is possible to determine the orientation of a peptide with respect to the surface based on the intensities of the amide I and amide II modes. It has to be noted that the following treatment only holds when the molecule does not rotate around its own axis (no twist), but a pure inclination in one plane may take place (here, defined as the yz-plane; see inset in Figure 7). Such a rotation around its own axis would involve a change of the projections of the TDM vectors onto the plane of interest. Since ALM has a defined hydrophobic and hydrophilic side, no rotation around its own axis is expected, as the hydrophobic side will stay in contact with the membrane core and does not turn towards the bulk solution or the interior of the ion channel.

In the simplest case of two normal modes, the SEIRA intensities are determined by their extinction coefficients ε_1 and ε_2, and the orientation of their TDM vectors given by the angles α and β with respect to the main molecule axis. In this way, the intensity ratio R is related to the tilt angle θ by:

$$R = \frac{I_1}{I_2} = \frac{\varepsilon_1}{\varepsilon_2} \cdot \frac{cos^2(\theta + \alpha)}{cos^2(\theta + \beta)} \tag{6.9}$$

As shown in Figure A8 (black curve), the intensity ratio varies according to this equation between $+\infty$ and 0, when θ takes the values $-\alpha$ or $-\beta$, respectively. For the amide I/amide II ratio based on the DFT calculation (red curve), however, only a finite maximum and a minimum > 0 is reached, since both bands display intensities for all orientations in space (Figure 6.16, right). In a more elaborate model, the intensities of all amide I and amide II normal modes are summed up. The total orientation-dependent amide I intensity can be obtained by:

$$I_{aI} = \sum_i f_{aI,i} \cdot \varepsilon_{aI,i} \cdot \cos^2(\theta + \alpha_i) \tag{6.10}$$

where i denotes the ith normal mode of the amide I component "aI". Here, the factor $f_{aI,i}$ is the fraction of the extinction coefficient observed in the plane of orientation, i.e. the yz-plane. This expression can be simplified by separating the sum into two fractions consisting of an orientation-dependent and an orientation-independent (offset) term:

$$I_{aI} \approx f_{aI} \cdot \varepsilon_{aI} \cdot [(1 - a) \cdot \cos^2(\theta + \alpha) + a] \tag{6.11}$$

where a denotes the fraction of the orientation-independent offset contributing to the intensity and f_{aI} and ε_{aI} denote the averaged extinction coefficient fraction and the total extinction coefficient of the amide I, respectively. The quantity α is the inclination angle of the orientation-dependent total amide I with respect to the peptide axis. In this way, the intensity ratio yields:

$$R = \frac{I_{aI}}{I_{aII}} = f \cdot R_{iso} \cdot \frac{[(1-a) \cdot \cos^2(\theta + \alpha) + a]}{[(1-b) \cdot \cos^2(\theta + \beta) + b]} \tag{6.12}$$

with $f = f_{aI}/f_{aII}$ being the ratio between extinction coefficient fractions, $R_{iso} = \varepsilon_{aI}/\varepsilon_{aII}$ the intensity ratio determined from an isotropic IR experiment in solution, while b and β refer to the respective quantities of the amide II intensity.
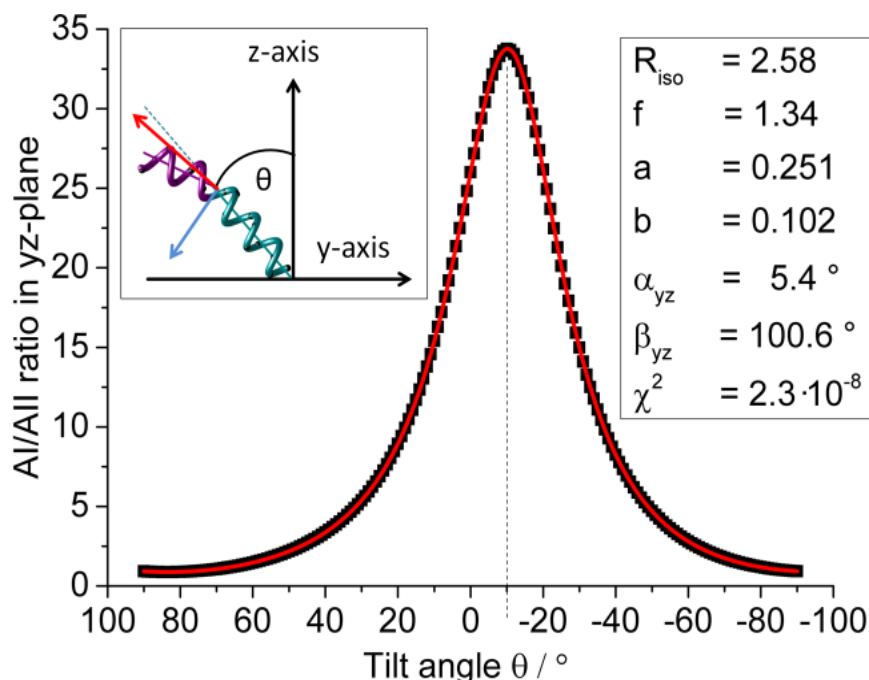
Figure 6.18 Simulated amide I/amide II ratios of ALM α-helix/3_{10}-helix structure during reorientation, i.e. as a function of the tilt angle θ as displayed in the top left inset. ALM reorients such that the hydrophobic side faces downwards (but not sideways) to match the hydrophobic interaction with a horizontally oriented membrane surface; red and blue arrows indicate the orientation of amide I and amide II TDMs. The abscissa (tilt angle) is flipped, so that the angles match the image in the inset. The red line and the inset on the right display the results of fitting equation 6.12 to the data. Reprinted with permission from Forbrig, E.; Staffa, JK.; Salewski, J.; Mroginski MA.; Hildebrandt, P.; Kozuch, J. Monitoring the Orientational Changes of Alamethicin during Incorporation into Bilayer Lipid Membranes *Langmuir* 2018 *34* (6), pp 2373-2385. Copyright (2018) American Chemical Society.[206]

Based on its structural features, ALM binds to a membrane surface with its hydrophobic side facing the membrane core and the hydrophilic part facing the bulk solution. When reorienting into the membrane to form ion channels, the hydrophobic side stays attached to the membrane core, while the hydrophilic part faces the channel center. Consequently, no internal rotation of ALM is needed for the incorporation and equation 6.12 can be applied. This is also true for a transmembrane potential-induced incorporation, as the dipole moment of ALM is oriented along the helical structure (vide supra).[206]

Simulating this process based on the DFT-IR spectra of the α-helix/3_{10}-helix structure yields orientation-dependent amide I/amide II ratios shown in Figure 6.18. These values were calculated neglecting the contribution of the amino acid residues which, in the experiment, do not adopt a single orientation with respect to the helices as obtained by DFT, but reorient based on rotation around single bonds. Using $R_{iso} = 2.58$ determined from the DFT-IR spectrum of ALM, a highly accurate fit to the data obtained from reorienting the DFT-optimized structure can be calculated. The amide I and amide II modes are oriented by 5.4° and 100.6° towards the hydrophilic side (in the plane of reorientation or yz-plane) and thus mostly along and perpendicular to the N-terminal α-helix, respectively. For the alternative α-helix/α-helix structure angles of 7.7° and 94.9° are obtained, again within the experimental accuracy (Figure A13). Moreover, the fractions of isotropic intensities are 0.25 and 0.1, which reflect the stronger scattering TDM vectors of the amide I components compared to the amide II (Figure 6.18). These values vary from 0.260 to

0.109, and 0.129 to 0.099 along with α and β (−7° < α < 6° and 79° < β < 101°; see Table A5) when the reorientation is performed in a plane different from the yz-plane, and thus underpin the importance of knowing the orientation of the TDMs with respect to the exact helix structure. For the chosen orientation, f is determined to be 1.34 and varies between 1.3 and 1.35 for other planes.

6.3.5 Determination of tilt angles of ALM in membranes

In view of the very good agreement of calculated and measured IR spectra, the isotropic offset values and the extinction fraction obtained from the DFT-IR spectra for the analysis of the SEIRA spectra can be adopted, since these values are not experimentally accessible. In addition, the spectroscopically determined amide I/amide II ratio of 2.55 was used and the tilt angles of both ALM structures were determined based on equation $R = \frac{I_{aI}}{I_{aII}} = f \cdot R_{iso} \cdot \frac{[(1-a)\cdot\cos^2(\theta+\alpha)+a]}{[(1-b)\cdot\cos^2(\theta+\beta)+b]}$ (6.12 for the adsorption on tHLMs, tBLMs and the potential-induced incorporation (Figure A13). Figure 6.19 shows the averaged tilt angles along with the deviation between the two structures as error bars demonstrating that both structures yield similar results within the experimental accuracy. During binding to tHLMs, ALM initially adopts an orientation of ca. 78° for the first 10 min and then slightly reorients to 69°.

According to the kinetic model used above, this can be ascribed to individual ALM molecules bound to the membrane surface that reorient upon interaction with or in proximity to other ALM molecules (Figure A5 and Figure A7). The deviation from a "perfect" horizontal orientation of 90° is reasonable based on the negatively charged Glu-18 residue at the hydrophilic side of the peptide and the kink of the C-terminal helix and is in line with MD simulations.[294] Although this part of the peptide faces the bulk solution, it is likely to experience a substantial repulsion from the negatively charged membrane surface (10% POPG), inducing a slight tilt up to 78° in the initial phase of binding (Figure 6.20). Upon increasing peptide density and potential interaction among the adsorbed ALM molecules, this repulsion increases as reflected by the final tilt angle of 69°.[214] This process may be associated with an increased, thermodynamically unfavorable exposure of the hydrophobic side of the peptide (including the phenyl group of Pheol-20) to the hydrophilic membrane surface. Therefore, the driving force for the incorporation into lipid bilayers may involve the optimization of hydrophobic interactions.

Upon binding to tBLMs, the tilt angle of ALM changes from initially 43° to 21° after correction for the horizontally bound ALM fraction on cholestanol-supported membrane fragments (or 50° to 34° averaged over the entire tBLM surface, see Figure 6.19). It needs to be
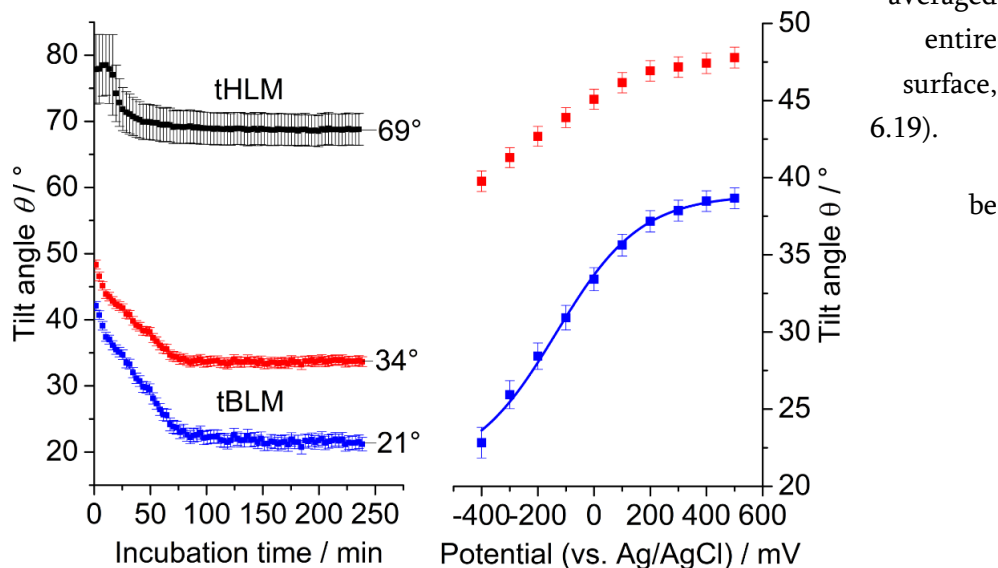
Figure 6.19 Left: Tilt angles of ALM calculated using equation 6.12 for the incubation on tHLMs (black) and tBLMs (red – before correction; blue – after correction for horizontally adsorbed species). Right: Potential-dependent tilt angles of ALM after initial incubation on tBLMs. Red and blue data points refer to uncorrected and corrected angles; the blue line represents the fit using equation 8.1 (E_Δ = -3 mV ± 17 mV; $dkT/\Delta\mu$ = 152 mV ± 10 mV; χ^2 = 7.8·10^{-5}; see Figure A9 for further details; n = 2 independent experiments). Reprinted with permission from Forbrig, E.; Staffa, JK.; Salewski, J.; Mroginski MA.; Hildebrandt, P.; Kozuch, J. Monitoring the Orientational Changes of Alamethicin during Incorporation into Bilayer Lipid Membranes *Langmuir* 2018 *34* (6), pp 2373-2385. Copyright (2018) American Chemical Society.[206]

considered that these angles, even after the correction, reflect the mean orientation of an ensemble of ALM molecules in different (meta)stable states and not the true re-orientation process of single ALM molecules (Figure A6 and Figure A7).[294,301] According to the described kinetic model (Figure 6.14 and a study by Guidelli,[301] these states involve horizontally adsorbed ALM molecules (e.g. monomers and/or oligomers), and vertically incorporated ALM helices (Figure A5 - Figure A7). Although the exact orientation of these states can change during the incorporation process, the main contribution to changes of the measured tilt angle is represented by a shift of the molar fractions between these states (Figure A9).

On tBLMs, the present time resolution did not allow detecting ALM molecules bound to the membrane surface in an early state. However, using the experiment on tHLMs, a tilt angle of ca. 78° as the starting orientation prior to incorporation into the bilayer can be estimated and the change of angles between 43° and 21° can be rationalized in terms of differing ratios between the initial horizontal and the final incorporated species. After ca. 1 h of incubation a plateau is reached with θ = 21° for membrane incorporated ALM molecules (Figure 6.19). This is in line with previous results obtained by ATR-IR, MD simulations, NMR and EPR spectroscopy[210,216,217,219,294,302] and thus represents the orientation of transmembrane helices that allow the formation of ion channels. Figure values (10°–35°) can be attributed to different lipid compositions, phase of the lipid molecules and ALM concentrations, as well as the underlying structural model.

Figure 6.19 (right) shows the calculated angles when the incorporation is induced by applying a potential at the supporting electrode. Overall, the plot shows two approximately linear regimes. At potentials above ca. 200 mV, the orientation is almost unchanged with ca. 38° (corrected value), while below this potential the tilt angle decreases to 22° at −400 mV and thus reaches a similar value as for spontaneous incorporation. More negative potentials were not accessible (and thus a putative plateau at negative potentials was not detected) due to the onset reductive desorption of the SAM and formation of reactive oxygen species which decrease the stability of the tBLM.

Among the functional IR studies on ALM in membranes,[214,216,218,219,303] in particular the concurrent spectroelectrochemical study on solid-supported BLMs[127] and tBLMs[304] by the Lipkowski group is mostly related to our present data.

tHLM horizontally adsorbed

$\theta = 69° \pm 5°$
$\theta_{C\text{-term.}} = 93° \pm 6°$
$\theta_{dipole} = 74° \pm 7°$

tBLM vertically incorporated

$\theta = 21° \pm 1°$
$\theta_{C\text{-term.}} = 45° \pm 2°$
$\theta_{dipole} = 26° \pm 3°$
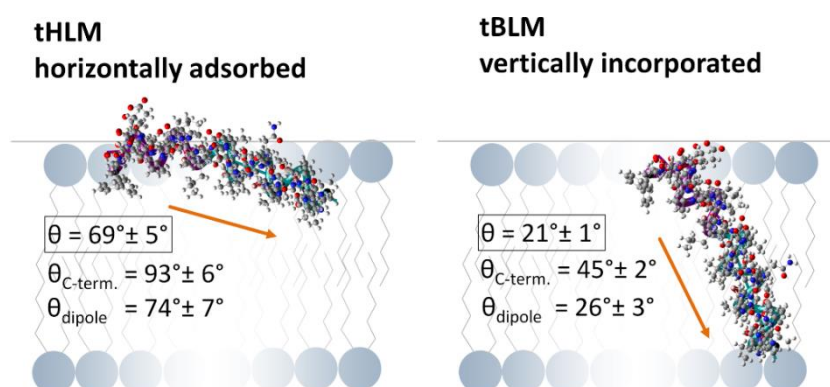
Figure 6.20 Schematic representation of the orientation of ALM when adsorbed on tHLMs (top) or incorporated into tBLMs (bottom); the electrode is situated below the lipid membranes. Insertion into the tBLM happens spontaneously or controlled by the potential when the electric field vector points from the solution to the metal corresponding to $E < E_0$. The structures are depicted according to Figure 6.16 and the dipole moment of the backbone is represented by orange vectors.). Reprinted with permission from Forbrig, E.; Staffa, JK.; Salewski, J.; Mroginski MA.; Hildebrandt, P.; Kozuch, J. Monitoring the Orientational Changes of Alamethicin during Incorporation into Bilayer Lipid Membranes *Langmuir* 2018 *34* (6), pp 2373-2385. Copyright (2018) American Chemical Society.[206]

Despite several differences in the experimental design and evaluation that can affect absolute orientations, a very similar behavior of ALM is observed. First, a similar gradual potential-induced reorientation of ALM to yield ca. 15° is observed over a broad potential difference of up to ca. -500 mV.[127] In the follow-up paper of the authors, a tBLM was formed on a DPTL thiolipid SAM (analogous to the present tHLM) from vesicles of different ALM/lipid ratios.[304] Interestingly, up to a content of 10 mol% ALM, the peptide maintains in a rather horizontal state with a gradual reorientation by ca. 10°, which resembles the trace of ALM on tHLMs in Figure 8 (black squares). Accordingly, since in our experiments the surface concentration of ALM increases steadily over the period of the reorientation (Figure 3 top, left), it is likely that both our and Lipkowski's work demonstrates a similar reorientational process.

This in line with an estimated surface coverage of 60 % at a content of 10 mol% ALM (based on the area of 360 Å^2 for horizontally adsorbed ALM and 68 Å^2 for a POPC lipid)[49,209] that can still accommodate ALM on the membrane surface. Only a further increase of the ALM content (15 mol%, equivalent to ca. 94% surface coverage) leads to a more drastic reorientation towards a vertical state. However, either due to a not high enough

concentration of ALM in the supernatant solution or a more rigid cholestanyl-SAM of the tHLM system, this is not observed.

6.3.6 Spontaneous insertion of ALM into membranes

It was shown previously that the horizontal state of ALM is more stable than the vertical state by ca. $\Delta G_0 \approx 5$ kJ/mol[294,301] (when the degeneracy factor is taken into account by Guidelli et al.) in absence of an electric field associated with a transmembrane potential. Here, experiments without application of an external potential were carried out at open circuit, corresponding to E_{OCP} ~ +70 mV. Taking into account the potential drop over the 6MH SAM, the actual transmembrane potential difference is likely to be small (see next section) and thus, these experiments primarily refer to the spontaneous incorporation of ALM. The separate potential-dependent experiments shown in Figure 6.19 (right) confirm this observation, since an application of ca. +70 mV did not lead to an efficient introduction into the membrane (vide infra).

In general, the main potential-independent contribution to the free energy for ALM binding to and integration into the bilayer originates from minimizing the exposure of the hydrophobic peptide surface area to a polar environment providing a high entropy gain (hydrophobic effect). Additional contributions to the free energy of adsorption on the surface may result from electrostatic (Glu-18) and dipole-dipole interactions with the POPC head groups. Support for such dipole-dipole interactions may be derived from the orientation of the dipole moment of the choline head group, which was found to be inclined by ca. 70° with respect to the membrane normal for DMPC.[305] As shown in Figure 6.20, in the horizontal conformation, the dipole moment of ALM's backbone adopts a similar inclination angle (ca. 74°), but with opposite direction, thus, enabling optimal anti-parallel dipole-dipole interaction. Incorporation may be achieved in particular by increasing the density of surface-bound species, which would lead to an increased negative charge density on the membrane interface and thus a stronger contribution of repulsive interactions in-between ALM molecules and with negatively charged lipids (10% POPG in this work). To compensate for this, ALM molecules would alter their orientation on the membrane (as observed in our experiments from 78° to 69°), which according to previous MD simulations[294] would energetically approach the transition state orientation leading to incorporation (see Figure A9). Here, unfavorable intermolecular contacts of the hydrophobic residues can be, to some extent, reduced via dimer formation as suggested by the kinetic analysis.

6.3.7 Potential dependence of ALM binding to membranes

To rationalize the results depicted in Figure 6.20 (right), the potential-dependent contributions to the energy balance of ALM integration into the membrane need to be taken into account. The main driving force for the potential-controlled insertion results from the interfacial electric field $\vec{F}$ that is perpendicular to the membrane surface. This electric field interacts with the peptide´s dipole moment $\vec{\mu}$ (according to convention a parallel arrangement leads to stabilization) resulting in an alteration of the difference in free energy between the vertical and horizontal states according to

$$\Delta G = -\Delta\mu \cdot F + \Delta G_0 \tag{6.13}$$

Here $\Delta\mu$, F and ΔG_0 are the difference of the dipole projections onto the electric field vector $\vec{F}$, the magnitude of the electric field, and the difference of free energy in absence of an electric field. The tBLM system allows controlling the electric field using the applied potential

according to $F = (E - E_0) \cdot d^{-1}$, where E and E_0 represent the applied electrochemical potential and the potential associated with $F = 0$ (vs. the reference electrode), so that ΔG can be expressed as

$$\Delta G = -\frac{\Delta \mu}{d}(E - E_0) + \Delta G_0 \tag{6.14}$$

In the simplest picture, d stands for the thickness of the hydrophobic core of the bilayer (ca. 3 nm), while in a more elaborate model it would be equal to a complex factor modeling the dielectric layers of the membrane as derived by Staffa et al.[306] From equation 6.13 and 6.14 it is visible that application of an electric field of at least $F_\Delta = \Delta G_0 \cdot \Delta \mu^{-1}$, which is equivalent to an electrode potential of $E_\Delta = E_0 + \Delta G_0 \cdot d \cdot \Delta \mu^{-1}$, can efficiently stabilize the vertical state incorporated in the membrane (see graphic representation of this model in Figure A9). According to this model and analogous to Guidelli et al.,[301] the change in orientation can be modeled using a Boltzmann distribution of these two states (see Figure A9 and Figure A10). It can be assumed that at negative potentials an angle of 21° will be adopted by ALM molecules, as determined from the potential-independent experiments as the final incorporated state.

The blue curve in Figure 6.19 (right) depicts the fit and demonstrates a very good match of this simple model with the experiment and thus complements the accordance of this model with electrochemical data[301] and theoretical findings[294] (Figure A9). Under the assumption d = 3 nm, as suggested by Guidelli et al.,[301] a dipole moment difference of −24 D for the transition between horizontal and vertical states can be calculated (the negative sign is due to the orientation of the dipole moment towards the electrode). This is a reasonable value considering the commonly accepted absolute dipole moment of ALM of ca. 75 D[299] or the computationally determined value of 100 D for the ALM backbone. The inflection point is determined to be $E_\Delta = -3$ mV. This quantity is associated with a substantial error since it strongly depends on the plateau value at negative potentials, which could not be detected due to restrictions of the system (vide supra). Based on $\Delta G_0 \approx 5$ kJ/mol,[294,301] one obtains $E_\Delta - E_0 = \Delta G_0 \cdot d \cdot \Delta \mu^{-1} \approx -270$ mV, implying that E_Δ is distinctly more negative than E_0. The potential E_0 refers to the transmembrane potential of zero (vs. 3 M KCl Ag/AgCl), which is related albeit not identical to the effective potential of zero charge $E_{pzc,eff}$ of the Au/tBLM system. The difference between both quantities arises from the asymmetry of the tBLM and the restricted aqueous reservoir between bilayer and 6MH head groups that may distort the typical potential distribution across a membrane.[307] Therefore, for 6MH-supported membrane fragments, E_0 is expected to lie in a range between the $E_{pzc,eff}$ of Au/6MH and $E_{pzc,eff}$ of Au/tBLM, as previously suggested by Jeuken.[308] To estimate both $E_{pzc,eff}$ values, EIS was employed to determine the potential of minimum capacitance.[309]

The EIS results agree well with literature obtained by different techniques (see section 0). Despite the low capacitance of the tBLM system, the presence of a minimum of capacitance in the SEIRA-tBLM system can be understood based on the flexibility of the constituents when affected by an electric field[49,308] and the roughness of the electrode. Accordingly, E_0 is expected to lie in a potential range from 140 to 300 mV, which is somewhat higher than the potential of zero charge for pure polycrystalline Au (+10 mV) due to the contribution of the

dielectric coating.[310,311] The value E_Δ = -3 mV derived from the fit in Figure 6.19 falls into this range taking $E_\Delta - E_0 \approx$ -270 mV into account. This potential shift implies that electric fields of $|\vec{F}| > 10^8$ Vm^{-1} are required to incorporate ALM into the membrane core. These fields are in the same range as those determined at membrane model interfaces such as at the head group region of metal-supported SAMs using the vibrational Stark effect.[306,310] However, it should be noted that this model does not consider potential-induced changes of specific interactions due to conformational or orientational changes of lipid head groups or side chains, which may exert very high local electric fields.[312] Accordingly, for $E < E_0$, the direction of the membrane-spanning electric field vector points from the solution to the metal surface such that ALM must intrude into the bilayer via its N-terminus (Figure 6.20) as reported previously,[208] if compensated for the interaction energy at the membrane interface. Conversely, in case of $E > E_0$, the direction of the electric field vector is reversed and insertion of ALM should occur via its C-terminus. Here, however, Glu-18 needs to pass through the hydrophobic part of the membrane, a process that should involve a very high activation barrier and thus would be kinetically hindered. Our data support the hindered intrusion via the C-terminus, since for $E > E_0$ (i.e. +400 mV) incubation of ALM onto tBLMs did not yield any considerable amide intensity in the SEIRA spectrum (Figure A4), pointing at a strongly hindered adsorption and incorporation.

Taking into account that the angles derived from the SEIRA data reflect the change in the equilibrium between the stable horizontal and vertical species (ca. 74°, 66° and 20°, respectively; vide supra), it is furthermore surprising that for $E > E_0$ the apparent angle did not change towards 74° or 66° for the horizontal orientation but remained at ca. 38°. This suggests that incorporation into the membrane is not an entirely reversible process under the present conditions and in the potential range used in this work, possibly due to channel formation that perturb the capacitive behavior of the membrane.

6.3.8 Directional control of ALM oligomer insertion into bilayers

In general, the direction of ALM insertion into bilayers may be different if it occurs spontaneously (potential-independent) or under potential control. Previous investigations on the interaction of ALM with phospholipid vesicles provided evidence for insertion via the N-terminus (Figure 6.20).[13,208] However, since the kinetics of spontaneous incorporation demonstrated the importance of peptide-peptide interactions, incorporation as anti-parallel dimers or oligomers is conceivable. In fact, MD simulations have shown that both parallel ALM channels as well as anti-parallel bundles are possible stable transmembrane states of ALM.[313,314] Although the mechanism of their formation remains still elusive, such anti-parallel assemblies were previously suggested for the non-conducting channel state. In contrast, channel opening was attributed to the potential-induced transition to parallel bundles, in which widening of the pore results from repulsive dipole-dipole interactions and a stabilization is accomplished by the net dipole of water molecules within the channel.[296]

In the presence of potential differences across the bilayer, an additional determinant for the directionality of peptide integration is the direction of the electric field, which for the present Au-tBLM system depends on E_0 (vide supra). Accordingly, these data indirectly suggest that both the spontaneous and potential-induced incorporation occurs preferentially over the N-terminal

helix, whereas C-terminal incorporation generally is strongly impeded by the charged Glu-18 group. This conclusion is supported by the fact that in case of $E > E_0$ no considerable incorporation of ALM into tBLMs was observed, even though the resulting electric field provided a driving force for integration via the C-terminus based on a favorable alignment of the ALM's dipole moment. Generally, the existence of ALM in different forms prior to incorporation can be expected, i.e. as monomers, parallel and anti-parallel oligomers (where the negative charge of the COO- group can be screened by e.g. H-bonds). However, based on our data, the applied electric field at $E > E_0$ did not facilitate binding and reorientation with transmembrane alignment of any of these ALM forms. Therefore, conversely, it can be assumed that for anti-parallel oligomers the same should hold true at $E < E_0$ (Glu-18 impedes the incorporation) and the oligomer is hindered from incorporation by the reversed electric field. Consequently, it can be rationalized that ALM primarily incorporates into membranes via its N-terminus both spontaneously and potential-dependent. Such a mechanism does not strictly exclude the existence of anti-parallel transmembrane bundles. As reported previously, the initial directionality of ion conductance of ALM channels is lost in the course of experiments,[315] which may imply flipping of ALM molecules after parallel ion channels are established. POPC molecules that are structurally unrelated to ALM but also amphipathic, have been shown to have a high barrier for flipping motions between bilayer leaflets ($t_{1/2} > 1000$ h) unless water-filled defects emerge in membranes that facilitate such motion.[316] ALM channels show a high flexibility in their composition (4–12 ALM helices) and ability to transform between these forms. Therefore, it is conceivable that a transformation or transient collapse of channels induces defects in the bilayer that lower the barrier for flipping events of ALM when already incorporated in the membrane.

6.3.9 Conclusions

For the investigations of the interaction between ALM and artificial membranes a combined SEIRA-tBLM methodology, augmented with the presented theoretical approach using DFT calculations and an extended mathematical model, provides insight on a qualitative and quantitative level. The interplay between ALM and membranes demonstrated a rigid helical structure that is maintained during spontaneous and transmembrane potential-induced incorporation. ALM adopts inclination angles of ca. 69° - 78° and 21° in its horizontally adsorbed and transmembrane incorporated states, respectively. Further evaluation of the complex incorporation kinetics confirms the importance of initial peptide-peptide interactions. Specifically, the data indicate that anti-parallel oligomers of ALM are excluded from incorporation into membranes, regardless of the presence or direction of the transmembrane potential. Consequently, primarily monomers or parallel ALM bundles are incorporated via their N-terminus when ALM reaches a critical concentration on the membrane surface or the membrane is polarized so that the dipole moment of ALM is stabilized. Thus, initially ion channels composed of parallel helices are established, which is in line with the commonly proposed barrel-stave model. The presented DFT-IR spectra are in good agreement with the experimental spectra and the very good fit of the described mathematical model validates the theoretical calculations. However, extending the current approach to the analysis of AMPs that show considerable structural plasticity and major changes in the secondary structure upon binding to membranes requires further refinements. In these cases, more elaborate theoretical approaches (e.g. in combination with MD simulations) must be employed for a more accurate description, in particular considering structural dynamics of specific peptide-peptide and peptide-lipid interactions.

6.4 Complex I activity incorporated in a supported lipid membrane system by (de-)protonation of 4-amino-thiophenol

The experimental data presented in this section were obtained in collaboration with Dr. Oscar Gutiérrez-Sanz, Instituto de Catalisis y Petroleoquimica, Madrid, Spain and DFT calculations were conducted by Dr. Jacek Kozuch, Department of Chemistry, Stanford University, Stanford, USA. The presented results are reproduced from Gutiérrez-Sanz et al.[328]

Bacterial Complex I (CpI) shuttles protons from the N-side to the P-side of prokaryotic cell membranes, as well as along the mitochondrial inner membrane to maintain a proton gradient that is essential for the synthesis of ATP.[241] This work focuses on the mechanistic coupling of the electron transport within the peripheral arm of CpI and the subsequent proton gating within in the membrane bound arm. Based on the incorporation of CpI into a supported lipid membrane (SLM) system, its activity was investigated by means of SEIRA spectroscopy combined with electrochemistry. A nanostructured Au electrode was functionalized by the self-assembled monolayer 4-aminothiophenol (4-ATP), which on the one hand exhibits a (de)protonable amino group as well as characteristic IR active vibrational modes. These properties allow its use as pH sensor. The NADH-induced opening of the TM domains of CpI can be indirectly analyzed by measuring pH changes at the SAM/membrane interface (see Figure 6.25, Figure A17 and Table A7).[317]

First, the 4-ATP SAM assembly was monitored in ethanol. SEIRA difference spectra revealed characteristic bands that were assigned to 4-ATP (Figure 6.21A) and its protonated form 4-ATP-H$^+$ (see Figure 6.25, Figure A19, Figure A20 and Table A7). The bands at 1488 cm^{-1} and 1595 cm^{-1} exhibit major contributions of aromatic ν(CC) and δ(CH) vibrational modes. Furthermore, the δ(NH$_2$) mode of 4-ATP and a combination of δ(NH$_3$) and δ(CH) modes of 4-ATP-H$^+$ are visible. An overlap of the δ(NH$_2$) and δ(NH$_3$) modes of the protonated and deprotonated form is depicted by the band at 1628 cm^{-1}.

The incorporation of CpI into a SLM system was realized by two different approaches leading to complementary results, namely the 1-step and 2-step approach. First, the construction and acquired results of the latter approach will be described in detail.

6.4.1 2-step approach of adsorption

The successful assembly of a biomimetic SLM system was the prerequisite for the subsequent membrane integration of CpI. Figure 6.21 shows the respective difference spectra of the construction process, where the corresponding SEIRA spectrum of the 4-ATP SAM in 100 mM phosphate buffered-saline (PBS) solution (pH 7) was chosen as reference.

To obtain a lipid membrane, preformed large unilamellar vesicles consisting of a mixture of ca. 80:10:10 POPC:POPA:DMN were spread on top of the surface of the 4-ATP SAM. The related SEIRA difference spectrum (Figure 6.21B) shows low intensity spectral contributions of the lipids, i.e. the ν(CO) stretching vibration at 1732 cm^{-1} and the corresponding symmetric (s) and antisymmetric (as) aliphatic adsorption bands found at 2854 cm^{-1} (ν_s(CH$_2$)), 2924 cm^{-1} (ν_{as}(CH$_2$)), and 2958 cm^{-1} (ν_{as}(CH$_3$)). The band positions indicate

a high fraction of gauche conformers as well as a high fluidity of the bilayer.[224] The rather low band intensities can be interpreted by the distance dependence of the SEIRA effect.[232] The spectrum reveals a combination of a significant amount of intact vesicles (size of about 100 nm) together with the existence of fragments of a bilayer membrane that formed on the SAM. Exclusively, the small lipid fraction in the vicinity of the 4-ATP SAM interacts directly with it and contributes to the SEIRA spectrum, affecting also the described vibrational modes of 4-ATP at 1595 cm^{-1} and 1488 cm^{-1}. Furthermore, there is a replacement of water molecules on the surface by lipids, which is ascribed by a negative band at ~3500 cm^{-1} (ν_s(OH) stretching mode of water).[49] The corresponding weaker δ(OH) bending mode at ca. 1650 cm^{-1} overlaps with the δ(NH) of 4-ATP at about 1630 cm^{-1}, resulting in a negative band around 1610 cm^{-1}. In the following step, CpI was added to the bilayer fragments. The spectrum in Figure 6.21C represents a considerable increase of the lipid bands between 2800-3000 cm^{-1}, as well as the appearance of the protein backbone related amide I band at 1657 cm^{-1} and amide II band at 1550 cm^{-1}.

These bands are the marker bands demonstrating CpI incorporation into the SLM system. In comparison to the CH$_2$/CH$_3$ stretchings there is a low relative intensity of ν(CO) at 1732 cm^{-1}. Perhaps the presence of CpI leads to an unfavourable orientation of this lipid vibrational mode for a SEIRA spectroscopic detection.[49] The subsequent exchange of buffer solution induces a substantial intensity increase of the amide I band up to ca. 2.5 mOD and amide II band to 2 mOD. However, the band positions remain stable and an intensity decrease of characteristic lipid bands occurs (Figure 6.21D).[318] This can be explained by the removal of residual detergent traces, leading to a reorganization of CpI within the SLM system with a higher content of adsorbed protein at the SAM surface. In comparison, Kriegel et al. observed amide I band intensities of ca. 3 mOD and concluded a high CpI protein density.[29] Furthermore, the utilization of the described tBLM system (vide supra) leads to a phospholipid band intensity of ca. 4 mOD at 2926 cm^{-1}.[8,49]

Based on these studies, the combination of the low intensity of lipid signals (ca. 0.6 mOD at 2924 cm^{-1}) and a high protein density indicates a coverage of ca. 80 % of the respective protein monolayer. This argumentation is in line with the impedance spectra showing a capacitance value of 8.1 μF*cm^{-2} (see Figure 6.3) that is about ten times higher than in case of the tBLM system (Figure 6.2 in chapter 6.1.1) and other biomimetic membrane systems that provide a more efficient insulation and less defects.[8,34,319] However, this approach allows adsorbing proteins at a much higher density and, more importantly, utilizing the pH sensing ability of 4-ATP.

The amide I band intensity in Figure 6.21D is larger than the corresponding amide II absorption, revealing a ratio of ca. 1.26. A single helix oriented perpendicularly to the Au surface can yield a value of up to 16.[34] It needs to be taken into consideration that these values were calculated using SEIRA spectroscopic data. This method differs from other polarized IR techniques due to the distinct distance (d) dependent surface enhancement scaling with a value of d^{-6} and may provide different values for the amide band ratio.
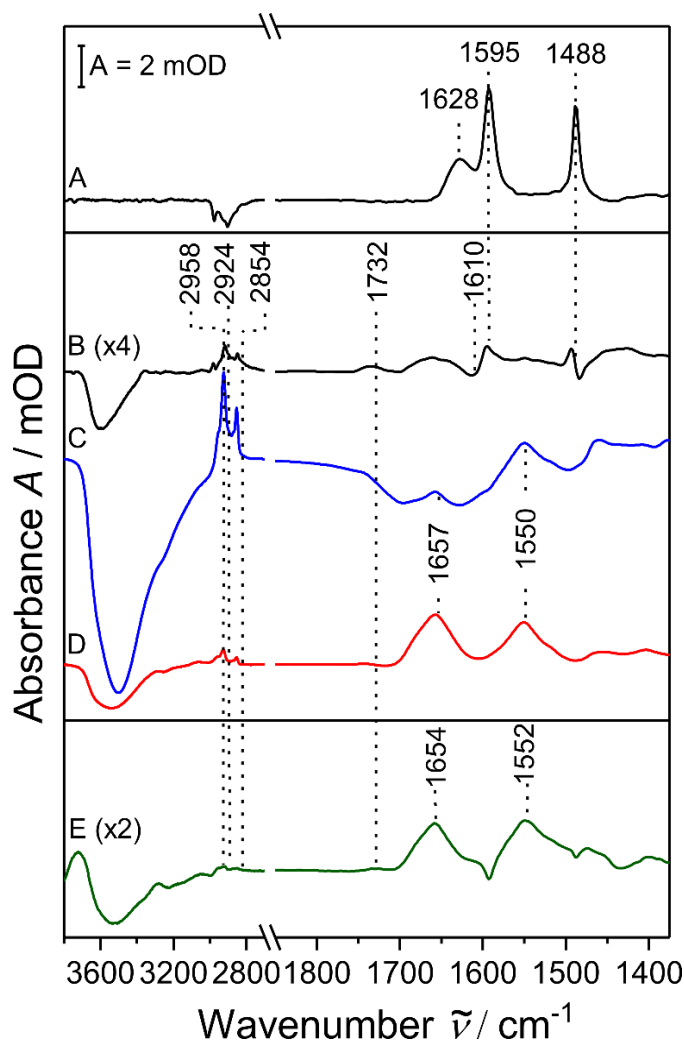
Figure 6.21 Difference spectra of: (A) 4-ATP SAM after overnight incubation using bare gold as reference (both in ethanol at 25 °C); (B) Supported lipid membrane (SLM) minus 4-ATP SAM (both in 0.1 M PBS at pH 5.8); (C) Incubation of CpI for 90 min minus SLM (both in 0.1 M PBS, at pH 7); (D) CpI after exchange with fresh 0.1 M PBS at pH 7. (E) Proteoliposomes harboring CpI after overnight SAM incubation at 4 °C using 4-ATP as reference. B to D were recorded at 25 °C. For a better comparison traces B and E were multiplied by a factor of 4 and 2, respectively (n = 2 independent experiments). Adapted with permission from Gutiérrez-Sanz, O.; Forbrig, E.; Batista AP.; Pereira MM.; Salewski, J.; Mroginski MA.; Götz, R.; De Lacey, AL.; Kozuch, J.; Zebger, I. Catalytic Activity and Proton Translocation of Reconstituted Respiratory Complex I monitored by Surface-enhanced Infrared Absorption Spectroscopy. *Langmuir* 2018 *34* (20), pp 5703-5711. Copyright (2018) American Chemical Society.[328]

In contrast, complex membrane proteins include further structural elements, e.g. turns between the helices. Therefore, an oriented immobilization on an Au surface leads to lower ratios in a range between ca. 1.2 (photosystem I,[147] cytochrome *bo*$_3$[8] or the membrane-bound hydrogenase)[27,148] and 2.2 (sensory rhodopsin[30]). This observation is further supported by results obtained during orientation inversion of a highly oriented cytochrome c oxidase sample immobilized via an N-terminal or C-terminal His-tag and reconstituted into a SLM system, where the detected ratio changes within this range. This leads to the estimation that a ratio between ca. 1.2 and 0.8 ($\approx$ 1/1.2) indicates a helical protein with low preferential or random orientation, while for a ratio < 0.8 the helices are oriented preferentially in parallel to the surface.

Consequently, it can be deduced that the here observed ratio of 1.26 reflects a preferentially perpendicular orientation of the transmembrane α-helices of CpI with respect to the surface. This reveals a functionally relevant orientation of the transmembrane α-helices of CpI in the SLM system with the peripheral arm facing the bulk solution as represented in Figure 6.22.
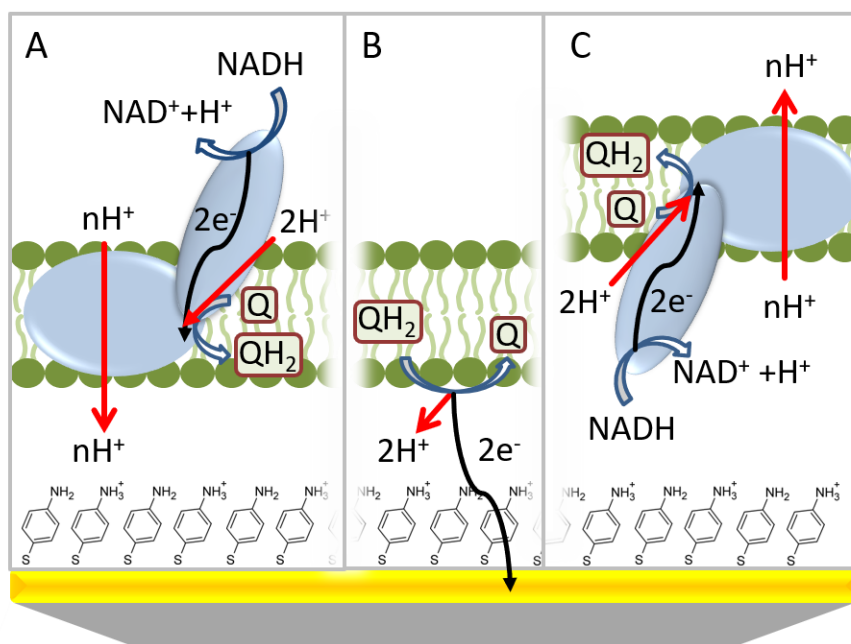
Figure 6.22 Biomimetic supported lipid membrane construct harboring bacterial Complex I (CpI) adsorbed on a nanostructured Au electrode that is functionalized by a 4-aminothiophenol SAM (4-ATP). The orientation of CpI determines the catalytic NADH oxidation-induced net proton flow resulting in (A) acidification or (C) alkalization of the space between bilayer membrane and SAM (by nH^+ or $-(n+1)H^+$ per NADH, respectively, with n considered to be 4, based on studies of the mitochondrial enzyme).[327] Reoxidation of the quinone (B) presumably leads to a simultaneous acidification by $1H^+$ per e^-. Adapted with permission from Gutiérrez-Sanz, O.; Forbrig, E.; Batista AP.; Pereira MM.; Salewski, J.; Mroginski MA.; Götz, R.; De Lacey, AL.; Kozuch, J.; Zebger, I. Catalytic Activity and Proton Translocation of Reconstituted Respiratory Complex I monitored by Surface-enhanced Infrared Absorption Spectroscopy. *Langmuir* 2018 *34* (20), pp 5703-5711. Copyright (2018) American Chemical Society.[328]

6.4.2 1-step approach of adsorption

In this procedure, the formation of the biomimetic SLM construct was achieved by overnight incubation of CpI containing PA:PC-proteoliposomes in presence of Bio-Beads. Figure 6.21E depicts the SEIRA spectrum obtained after the deposition of the proteoliposomes using the spectrum of the 4-ATP SAM as a reference. The decrease of the absorbance in the region of ca. 3500 cm^{-1} is in agreement with the removal of adsorbed water molecules (vide supra).[49] The positive bands at 1654 cm^{-1} and 1552 cm^{-1} represent the amide I and amide II bands of CpI. The shift of the position of the amide bands by 2-3 cm^{-1} in comparison to the 2-step approach might be explained by different orientations of the protein on the SAM surface, which results in SEIRA spectra of different CpI subunits. This reasoning is supported by the absence of characteristic lipid IR bands, e.g. $v(CH_2/CH_3)$ and $v(CO)$ stretchings at 2800-3000 cm^{-1} and ca. 1730 cm^{-1}. The negligible intensity of the lipid bands leads to the conclusion that the bilayer is located in a larger distance relative to the surface. This could be rationalized by a distribution of the two possible orientations of CpI, i.e. with the peripheral arm facing either the bulk solution (Figure 6.22A) or the SAM (Figure 6.22C), respectively. In this case the perpendicularly oriented transmembrane helices would contribute less to the spectral intensity due to the limited detection of SEIRA spectroscopy up to a distance of 8 nm. The spectrum rather illustrates secondary structure elements of the peripheral arm. This is supported by lower amide I and II band intensities of 1.1 and 1.2 mOD, respectively. Furthermore, the amide I/amide II ratio of 0.93 is in a range that represents randomly oriented helices.

6.4.3 Investigation of CpI function in biomimetic supported lipid membranes

A successful incorporation of CpI in a functional relevant conformation within the biomimetic SLM system using the 2-step approach needs to be demonstrated. For that purpose, the enzyme's electro-catalytic and proton translocation activity were analyzed.

6.4.3.1 Spectroelectrochemical measurement of NADH induced CpI activity

First, chronoamperometry that was recorded at 200 mV (vs. 3 M KCl Ag/AgCl) exhibited an increase of the oxidative catalytic current of ca. 0.4 µA after addition of NADH (60 µM). This observation proves that the protein exchanges electrons with the electrode via the DMN pool distributed within the lipid layer (see Figure 6.23 left).[50] The measured activity of CpI is complemented by SEIRA data, which offer further information regarding (re)orientation as well as protonation changes of the SAM. The large distance of the respective substrate binding sites to the metal surface impeded the detection of direct spectral fingerprints of NADH or DMN binding. Instead there is a positive difference band at 1591 cm^{-1} and a negative difference band at 1489 cm^{-1} which can be assigned to reversible protonation of 4-ATP (Figure 6.23 right, Figure **6.24**B and Figure 6.24C) induced by a proton translocation of CpI. Spectral side chain contributions of specific amino acids, e.g. aspartate or glutamate in this region[141] can be excluded due to the larger distance of the enzyme to the surface compared to the SAM or bilayer. In different control experiments the addition of NADH to pure 4-ATP, to the SLM without DMN and CpI and to the SLM with DMN but without CpI, respectively, did not lead to any spectral changes (Figure A16).
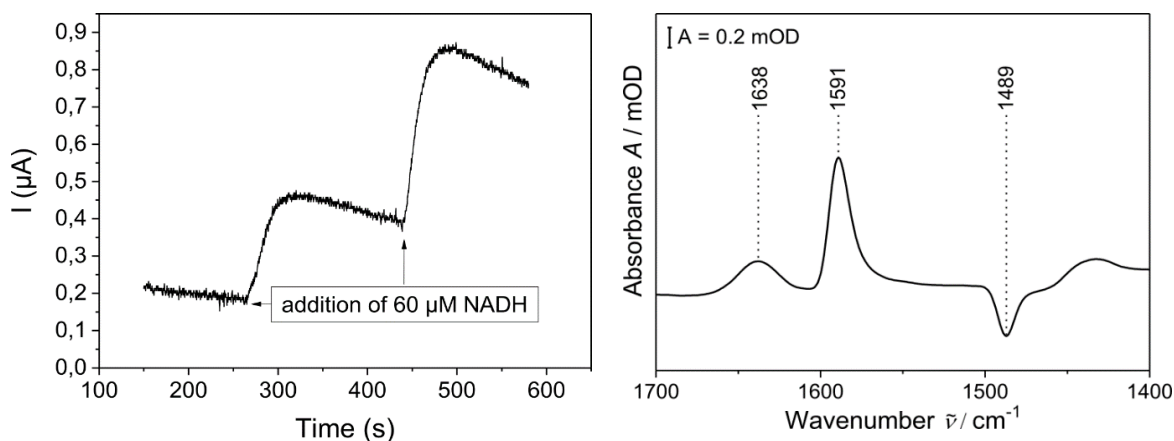
Figure 6.23 (A) Chronoamperometric trace recorded at 200 mV on the stepwise assembled supported lipid membrane / CpI construct. The subsequent addition of 2x 60 µM NADH solution in PBS 0.1 M pH 7 to the CpI / SLM system leads to a significant increase of the catalytic current. (B) SEIRA difference spectrum taken after first addition of a 60 µM NADH solution in PBS 0.1 M pH 7. The bare CpI / supported lipid membrane system incubated in the same buffer was used as reference (n = 2 independent experiments). Adapted with permission from Gutiérrez-Sanz, O.; Forbrig, E.; Batista AP.; Pereira MM.; Salewski, J.; Mroginski MA.; Götz, R.; De Lacey, AL.; Kozuch, J.; Zebger, I. Catalytic Activity and Proton Translocation of Reconstituted Respiratory Complex I monitored by Surface-enhanced Infrared Absorption Spectroscopy. *Langmuir* 2018 *34* (20), pp 5703-5711. Copyright (2018) American Chemical Society.[328]
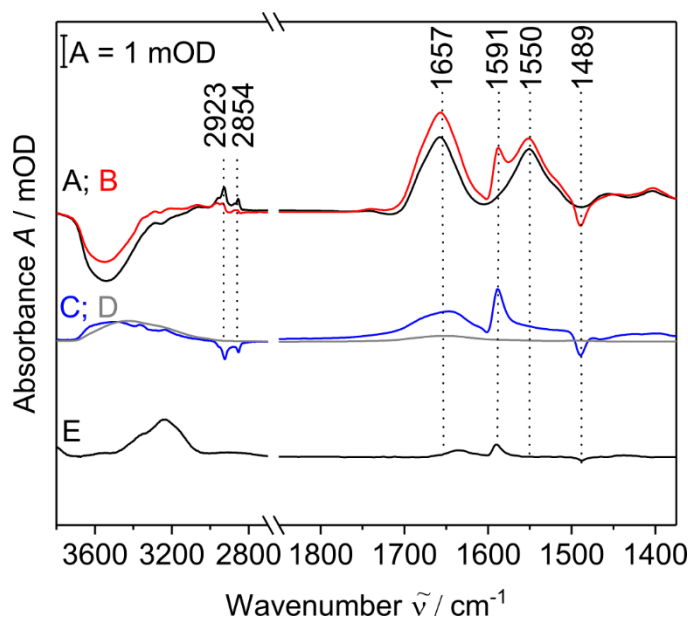
Figure 6.24 SEIRA difference spectra of stepwise procedure: Difference spectra of (A) 90 min incubated CpI in 0.1 M PBS minus bare SLM in 0.1 M PBS, at pH 7 (see also Figure 6.21D); (B) NADH addition to CpI after buffer exchange in 0.1 M PBS minus SLM in 0.1 M PBS, at pH 7; (C) NADH addition to CpI after buffer exchange in 0.1 M PBS minus CpI after buffer exchange in 0.1 M PBS, at pH 7; (D) water spectrum on bare Au surface scaled to match the $\nu(H_2O)$ band at ca. 3500 cm^{-1}; (E) 4-ATP SAM in PBS 0.1 M at pH 5 minus 4-ATP SAM in PBS 0.1 M at pH 7 (n = 2 independent experiments). Reprinted with permission from Gutiérrez-Sanz, O.; Forbrig, E.; Batista AP.; Pereira MM.; Salewski, J.; Mroginski MA.; Götz, R.; De Lacey, AL.; Kozuch, J.; Zebger, I. Catalytic Activity and Proton Translocation of Reconstituted Respiratory Complex I monitored by Surface-enhanced Infrared Absorption Spectroscopy. *Langmuir* 2018 *34* (20), pp 5703-5711. Copyright (2018) American Chemical Society.[328]

6.4.3.2 pH titration of the 4-ATP-SAM

Another important aspect of the investigation is the verification of 4-ATP as a pH-dependent proton sensor by means of a pH-titration of 4-ATP from pH 9 to pH 3 that was conducted in parallel to SEIRA measurements in the difference mode (see Figure 6.25). To allow a comparison with the NADH-induced spectral changes of the CpI-bilayer system, which were measured at a bulk pH of 7, also a reference spectrum at pH 7 was recorded. In general, the difference spectra collected during the pH titration exhibit changes of the 4-ATP SAM related IR bands at ca. 1590 cm^{-1} and 1485 cm^{-1}, and a broad difference band of the H$_2$O related $\delta(OH)$-bending vibration at ca. 1650 cm^{-1}.

Under alkaline pH conditions in the range from pH 9 to pH 7, a negative difference band at 1591 cm^{-1} and a positive band at 1487 cm^{-1} can be observed. However, acidic conditions between pH 7 and pH 5 lead to reversed spectral changes and a positive difference band at 1591 cm^{-1} accompanied by a negative difference band at 1487 cm^{-1}.

These bands indicate a protonation of the 4-ATP SAM at decreased pH values. As shown in Figure A17, the band intensities of the 1591 cm^{-1} absorption follow a broadened sigmoidal shape, revealing a pK$_a$ value of 6.4 ± 0.1. This is in line with a pK$_a$ value of 6.9 ± 0.5 that was determined by capacitance measurements.[320] A further decrease of the pH values below pH 5, implicates spectral changes showing a negative band at 1596 cm^{-1} and a positive band at 1484 cm^{-1}. Hence, two protonation states of 4-ATP can be deduced, i.e. in the ranges of $5 \leq pH < 9$ and pH < 5. On a molecular level these spectral changes are based on a competition involving two processes: a) a structural variation due to a loss of coupling between the ATP molecules of the SAM upon protonation ($\Delta_{structural}$; ca. 1610 cm^{-1}(+) / 1494 cm^{-1}(-); see Figure A22) and b) the actual
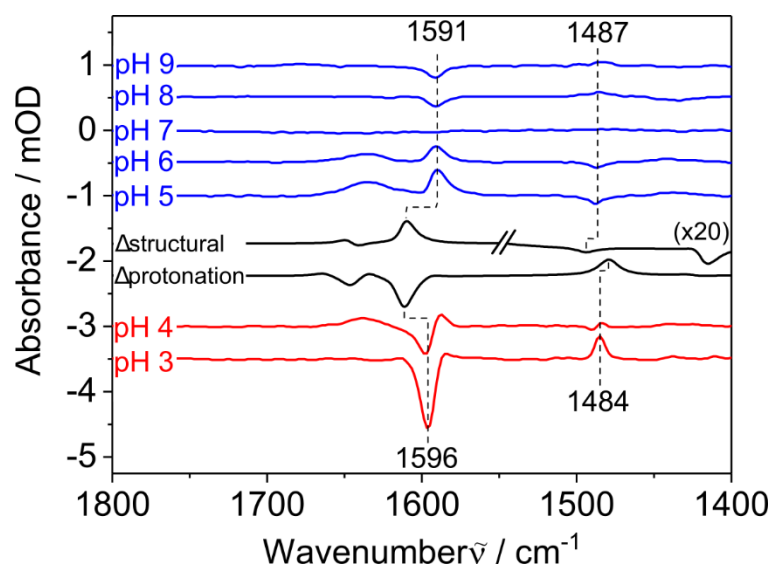
Figure 6.25 SEIRA spectroscopic pH-titration of the 4-ATP SAM in the range of pH 3 to pH 9 in 0.1 M PBS using the spectrum at pH 7 as reference. Phosphoric acid was used to acidify the bulk solution. The pH was measured with a pH electrode. The corresponding black colored spectra are IR spectra calculated by a DFT approach (low vs. high pH) demonstrating the related spectral effects of the loss of vibrational coupling, or protonation of single 4-ATP molecules. The spectral region < 1550 cm^{-1} of the difference spectrum $\Delta_{\text{structural}}$ was magnified by a factor of 20 for better visualization (n = 2 independent experiments). Adapted with permission from Gutiérrez-Sanz, O.; Forbrig, E.; Batista AP.; Pereira MM.; Salewski, J.; Mroginski MA.; Götz, R.; De Lacey, AL.; Kozuch, J.; Zebger, I. Catalytic Activity and Proton Translocation of Reconstituted Respiratory Complex I monitored by Surface-enhanced Infrared Absorption Spectroscopy. *Langmuir* 2018 *34* (20), pp 5703-5711. Copyright (2018) American Chemical Society.[328]

pH-dependent difference spectrum of single ATP molecules ($\Delta_{\text{protonation}}$; ca. 1611 cm^{-1}(-) / 1481 cm^{-1}(+); see Figure A21).

Both effects reveal similar spectral features, but with opposite signs of intensity changes likewise to the observed spectra in the pH-titration (Figure 6.25). Assuming a completely deprotonated 4-ATP SAM as initial scenario, at first the protonation leads to only a few protonated molecules (minor contribution of $\Delta_{\text{protonation}}$). A more pronounced effect is a severe perturbation of the structural homogeneity of the SAM (major contribution of $\Delta_{\text{structural}}$). The following increased number of protonated molecules, results in a dominant spectral contribution of $\Delta_{\text{protonation}}$ and a superposition of the spectral effect called $\Delta_{\text{structural}}$. This transition is apparent in the difference spectrum of pH 4 vs. pH 7, where both 4-ATP peaks exhibited first-derivative shaped difference bands. The 4-ATP difference bands related to the NADH-induced spectral changes shown in Figure 6.24C (positive band at 1591 cm^{-1} / negative band at 1489 cm^{-1}) are compared with those spectra obtained in the 4-ATP titration experiment depicted in Figure 6.25 at moderate pH values of 5-9 (positive band at 1591 cm^{-1}/ negative band at 1487 cm^{-1}) and at strong acidic conditions at pH < 5 (negative band at 1596 cm^{-1} / positive band at 1484 cm^{-1}). Taking this into account, the spectral variations after NADH addition (Figure 6.24E) are in agreement with the spectra that indicate a protonation equivalent to pH 5-6 (see Figure 6.25). The described observations are comprehensible, as a pH change by more than two units due to the CpI-induced proton translocation is not very probable. In conclusion, the SEIRA difference spectra of the CpI-bilayer system with positive and negative intensities of the difference bands at 1591 cm^{-1} and 1489 cm^{1} prove a NADH-induced protonation of the 4-ATP SAM.

It needs to be considered that the low insulation of the membrane system, allows the detection of this pH change only under turnover conditions. The proton translocation includes two different sources, namely the enzyme and quinone pool.[8] The exact stoichiometry of transmembrane proton translocation by bacterial CpI is still under discussion. At the moment, the number of translocated protons is known to be n = 4 per NADH molecule.[321] Therefore, one fraction that contributes to
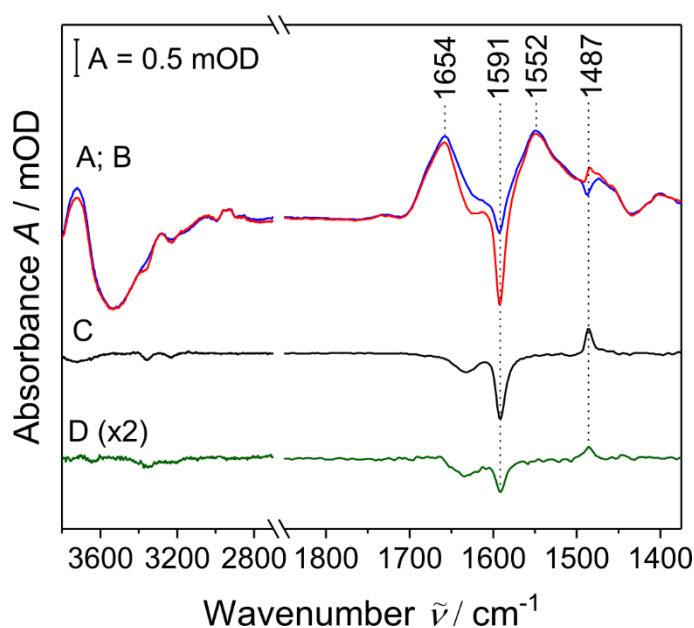
Figure 6.26 Difference spectra related to the reconstitution of a supported lipid membrane (SLM) system with CpI by the 1-step procedure. (A) Addition of proteoliposome solution to the ATP-SAM surface using it as reference; (B) Addition of NADH to reconstituted SLM with 4-ATP SAM as reference; (C) B minus A (D) 4-ATP at pH 8 minus 4-ATP at pH 7, multiplied by a factor of 2 for better visualization (n = 2 independent experiments). Adapted with permission from Gutiérrez-Sanz, O.; Forbrig, E.; Batista AP.; Pereira MM.; Salewski, J.; Mroginski MA.; Götz, R.; De Lacey, AL.; Kozuch, J.; Zebger, I. Catalytic Activity and Proton Translocation of Reconstituted Respiratory Complex I monitored by Surface-enhanced Infrared Absorption Spectroscopy. *Langmuir* 2018 *34* (20), pp 5703-5711. Copyright (2018) American Chemical Society.[328]

the pH change originates from the net proton translocation of CpI towards the SAM. This supports the hypothesis of a preferential orientation of CpI within the biomimetic membrane system with the peripheral arm directed to the bulk solution. In this case the transferred proton number per NADH at the SAM/bilayer interface is $+4H^+$ or $+nH^+$, Figure 6.22A. The addition of CpI to a preformed bilayer membrane/liposome system is in concordance with its incorporation into the biomimetic SLM system in such a preferential orientation due to spatial restrictions. If the contributions of a quinol reoxidation are excluded, a 50:50 mixture of both orientations of CpI within the bilayer membrane would lead to an alkalization ($-1\ H^+$ per NADH; Figure 6.22) at the CpI-bilayer membrane/4-ATP SAM interface.[8]

A further fraction of the proton translocation is added by DMN. After reduction by the protein (and uptake of two protons), a specific amount of DMN will pass the electrons to the electrode and stabilize its previously established redox equilibrium. This oxidation is accompanied by a maximum release of two protons per DMN molecule ($DMNH_2 \rightarrow DMN + 2\ e^- + 2\ H^+$; Figure **6.22**B) at the bilayer membrane/SAM interface augmenting the acidification.

The interdependence between these processes relies on the ratio of protein to DMN (ca. 1:1.34) and the proportion of both protein orientations, as well as the rate of $DMNH_2$ oxidation at the electrode. Besides this, the SEIRA spectra reveal a concurrent increase of the amide I and amide II band intensities with a mutual change of the amide I/amide II ratio from 1.26 to 1.34 (Figure **6.24**B).

Since the amide I band can overlap with the O-H vibrational modes of water, a reference spectrum of water is represented in Figure 6.24D for comparison to exclude these effects. The spectrum, which is scaled to the O-H-stretching region at 3500 cm^{-1} (Figure 6.24C) clearly indicates that the corresponding O-H-bending mode at 1650 cm^{-1} is not observable. Therefore, the broad positive band at ca. 1650 cm^{-1} in Figure 6.24B can be ascribed to a rising intensity in the amide I region.

Theoretical calculations of Di Luca et al. verified a relation between the described amide band increase and a reorientation of the α-helical and/or other secondary structural components of CpI, which presumably play a role in a proton-channel formation.[254] In addition to conformational changes within the integral transmembrane domains, charge-induced movements of the whole peripheral arm or its structural elements upon NADH and quinone binding is discussed.[253,256] A further investigation of possible conformational changes in the future will require a detailed analysis of a series of CpI mutants. The 1-step formation of the biomimetic membrane/CpI construct and the previous interpretation obtained by the 2-step procedure lead to complementary information. Upon addition of NADH a slight decrease of the amide I band intensity at 1654 cm^{-1} is detectable (Figure 6.26B) and the amide II band intensity at 1552 cm^{-1} remains unchanged. The slight observable change of the amide I/amide II ratio from 0.93 to 0.88 induced by NADH addition notifies an enzyme incorporation that is preferentially in a reverse orientation in comparison to the 2-step procedure. Furthermore, the changes occur more distant from the electrode and indicate that a larger fraction of CpI interacts with the SAM via the peripheral arm as illustrated in Figure 6.22C. In comparison, Kriegel et al. also presented a SEIRA study using an immobilization of CpI in a reversed orientation with its peripheral arm bound via a His-tag to a Ni-NTA SAM and NADH SAM, respectively. This investigation revealed an amide I/amide II ratio in the range of 1.[29]

Analogous to the evaluation of the 2-step procedure, the SEIRA difference spectra after NADH addition are compared with the spectral pH titration data of the 4-ATP SAM. There are distinct spectral changes after addition of NADH at 1591 cm^{-1} (negative) and at 1487 cm^{-1} (positive) visible, see Figure 6.26A to Figure 6.26C. This observation confirms the difference spectra of the basic pH regime taken during the pH titration (Figure 6.26D and Figure 6.25). Thus, a net proton translocation in direction of the bulk solution can be deduced that has an alkalizing effect on the SAM. Additionally, the alkalization hints at a diffusion of NADH through the bilayer membrane to the SAM surface, due to defects in the lipid membrane system implicated by a small resistance that is shown in the impedance spectra in Figure 6.3. These effects fit unambiguously into the previously described context of an intensity ratio change and the shifted amide I and amide II band positions. Taken all information together, a preferential "upside-down" orientation of CpI within the reconstituted SLM construct can be reasoned (Figure 6.22.C).

An important indicator supporting this explanation is the net proton translocation via the protein, which results in -5H$^+$ or -(n+1)H$^+$ per NADH at the SAM/bilayer membrane interface for an "upside-down" orientation. Therefore, it exceeds the effect of re-oxidation of DMN at the interface and more than 50% of the CpI molecules appear to be oriented with the peripheral arm towards the SAM surface. In a previous study by Gutiérrez-Sanz et al., which is the basis of the current work, a 1-step formation was developed on an Au(111) surface. This allowed the investigation of an electrochemically induced protonation of the 4-ATP SAM. The authors concluded a net orientation of active protein with the peripheral arm directed to the bulk solution, as depicted Figure 6.22A.[50] Therefore, the observed difference in orientation might be explained by the nanostructured surface of the SEIRA Au electrode. That is the reason for a less homogenously ordered biomimetic membrane system adsorbed on 4-ATP and residual intact vesicles.

6.4.4 Conclusions

The complementary results of this work demonstrate that CpI incorporated into the biomimetic SLM system is catalytically active and translocates protons. It also shows the capability of the used SEIRA (spectroelectrochemical) approach to monitor these two processes simultaneously. Depending on the type of construction procedure used for the biomimetic membrane system, i.e. the approach applying an incorporation of CpI into a bilayer membrane/liposome layer (2-step) or the assembly using CpI-containing proteoliposomes (1-step), the preferential orientation of the protein was obtained while maintaining its electro-catalytic activity. Based on 4-ATP as a spectroscopic pH sensor, the NADH-induced catalytic transmembrane proton transfer leads to an acidification of the 4-ATP SAM when CpI was incorporated in a 2-step process and thus oriented preferentially with the peripheral arm upwards. Adsorbing proteoliposomes directly onto the SAM provides a major CpI-fraction that is oriented upside-down resulting in an alkalinization of the SAM under turn-over conditions. Importantly, the two constructs report changes of the amide I/amide II band intensity ratio, which may reflect structural changes of CpI upon catalysis and proton translocation. Based on recent literature reports[248,252–255] both transmembrane α-helices and the interfacial region to the peripheral arm are proposed to experience pronounced structural changes. Thus, this work will pave the way for future structural and functional studies on the activity of CpI reconstituted in bilayer lipid membranes.

7 CONCLUSIONS

Biomimetic membrane systems In this work, different lipid membrane systems were constructed to relate the structural properties of AMPs and the bacterial Complex I (CpI) with their molecular mechanisms of interaction with lipid membranes by means of SEIRA spectroscopy.

AMPs were studied applying a tBLM system that was assembled by functionalization of a nanostructured Au surface with a WK3SH:6MH (80:20) SAM. A further spreading of POPC:POPG (90:10) liposomes led to a system comprised of alternating islands of lipid bilayer areas, including an aqueous reservoir underneath, and lipid monolayer compartments. This construct was suitable, since it provided the necessary flexibility and space to incorporate peptides in their transmembrane state. Also, the stability of the tBLM, analyzed by EIS measurements, corresponds to the requirements. The determined capacitance value of 0.76 $\mu F*cm^{-2}$ is in the range of previously described EIS studies using POPC membranes.

A pure layer of rigid hydrophobic cholestanyl-headed WK3SH-SAM adsorbed on the Au surface served as reference to study hydrophobic interactions of the amphipathic AMPs with the surface. The addition of POPC:POPG (90:10) liposomes onto the SAM surface resulted in a lipid monolayer assembly. This tHLM system served as another reference system due to the spatial restrictions.

To monitor the transmembrane proton translocation of CpI, the protein was embedded into a SLM system. The SAM 4-aminothiophenol (4-ATP), adsorbed on the nanostructured Au electrode, provided the ability of a protonation and deprotonation. A mixture of POPC:POPA:DMN (80:10:10) liposomes were adsorbed on the SAM surface to complete the SLM. Interestingly, EIS measurements revealed a ten-fold higher capacitance value of 8.1 $\mu F*cm^{-2}$, which provides the qualitative indication of intact vesicles and adsorbed lipid fragments on the SAM surface and is in line with a low bilayer resistance.

Peptide-membrane interaction of cathelicidin derivatives The human AMPs LL-37 and the mutated fragments LL-32 and LL-20, derived by C-terminal deletion of amino acid residues, were analyzed regarding different structural and functional properties. Complementary IR spectroscopic studies and MD simulations in solution obtained an α-helical secondary structure of the investigated peptides stabilized by salt bridge formation of charged residues. However in the peptide core (residues 17-29) there was no salt bridge formation detectable.

There is a significantly higher enhancement of normal modes with transition dipole moments perpendicularly oriented in respect to the SEIRA Au surface. Thus, a comparative SEIRA study adsorbing the peptides on the tBLM system and the hydrophobic WK3SH-headed SAM led to information about the orientation of the peptides. The obtained amide I/amide II ratio of 0.6 ±0.1 is in line with a uniform horizontal orientation of LL-37 and LL-32 with respect to the surface plane of both, the tBLM and WK3SH-SAM. However, over time LL-37 undergoes a change of the ratio from 0.4 to 0.6 indicating a multi-step process of interaction, whereas LL-32 adsorbs rather in a 1-step process due to a stable ratio. Interestingly, LL-20 adsorbs on the SAM surface in the same way, whereas it does not interact with the tBLM surface.

Taking into account the different thickness of the WK3SH-SAM and the tBLM the distance dependence of SEIRA offered information about the position of the peptides adsorbed onto or integrated into both systems by the intensity of the amide modes. Each peptide stayed on the WK3SH surface that is in a comparable distance to the Au surface like the hydrophobic core of

the membrane. For both systems, adsorption studies of LL-37 showed intensities for the amide I mode of 2 mOD and the amide II mode of 4 mOD. Hence, LL-37 adsorbs not only onto the WK3SH-SAM but also into the hydrophobic membrane core. The comparison of the amide mode intensities reveals for LL-32 comparable values during the interaction with WK3SH, but about ten-fold lower intensities in the peptide-tBLM interaction.

MD simulations (in a time range of 300 ns) proved the spectroscopic results by simulation of a POPC:POPG (90:10) bilayer membrane. LL-37 incorporates in a multi-step process that is mainly driven by insertion of the N-terminus into the membrane core induced by the VPRTES-terminus (residues 32-37). However, LL-32 adsorbs onto the membrane surface interacting with the phospholipid headgroups and LL-20 does not interact with the membrane. Detailed analysis of the peptide amino acid residues clarified that the peptide core comprised of residue 17-29 of LL-37 and LL-32 is essential for the interaction of the peptides with the studied lipid membrane. As LL-20 does not possess the residues 21-29, its α-helix is more rigid and a peptide-membrane interaction is inhibited.

Alamethicin The interaction of the AMP alamethicin (ALM) with biomimetic membranes was studied by incubation onto tBLMs, using tHLMs as a reference system. These processes were observed by SEIRA, monitoring the N-terminal α-helix and the C-terminal 3_{10}-helix of ALM by the amide I mode.

The investigation of the ALM-tHLM interactions led to a horizontal adsorption with respect to the surface plane. However, its transmembrane integration was spatially restricted. The interaction between ALM and the tBLM first started by a horizontal adsorption with an inclination angle of 69°-78° in respect to the surface normal. In dependence of the concentration and/or under control of the electrical potential a reorientation and transmembrane incorporation occurred resulting in an angle of 21°.

The developed kinetic model of peptide incorporation hypothesizes a 3-step process, highlighting the relevance of an initial peptide-peptide interplay. Anti-parallel peptide oligomers are not assumed to integrate in a voltage-dependent manner. But rather monomers and parallel oligomers are expected to incorporate with its α-helical N-terminus into the transmembrane part, if the dipole of ALM is stabilized due to membrane polarization. The obtained data is in line with the barrel-stave model that suggests an ion-channel formation by 4-12 ALM monomers.

DFT-calculated IR spectra complemented the experimental spectra. The α-helix/3_{10}-helix structure of ALM was calculated and the validity was proved by an extended mathematical model. As ALM is characterized by a rather rigid secondary structure the applied model was suitable. The calculation of more flexible peptides and proteins comprised of different secondary structure elements makes more complex theoretical methods, e.g. quantum mechanics/molecular mechanics or MD simulations, necessary.

Bacterial Complex I The catalytic activity and proton translocation of Complex I (CpI), embedded into the biomimetic SLM system, was shown by SEIRA combined with electrochemistry.

The study compassed two different procedures leading to preferential orientations of CpI on the SAM surface. In a 1-step procedure proteoliposomes including CpI were added to the 4-ATP SAM and functional CpI proteins were oriented preferentially with the peripheral arm directed to the surface. During the 2-step approach, CpI incorporation followed a previous assembly of the SLM by spreading of liposomes. In this construct CpI was preferentially oriented with its peripheral arm towards the bulk solution.

The (de)protonable pH sensor 4-ATP allowed the spectroscopic observation of an NADH induced proton translocation depicted in a pH change. Dependent on the orientation an alkalinization (1-step process) or acidification (2-step approach) was monitored. These data were validated by DFT calculations of 4-ATP.

Furthermore, spectral changes of the amide I/amide II band intensity ratio were noticeable. Such effects that can point to previously suggested structural changes of transmembrane α-helices in the interfacial region to the peripheral arm of CpI induced by catalysis and proton translocation.

This work showed that spectroelectrochemical studies of reconstituted membrane proteins like CpI allow to correlate structural and functional aspects provided that the stability of the SLM will be improved systematically.

Outlook This work revealed in a direct comparison of the SLM and tBLM system that the latter biomimetic construct is characterized by better insulating properties, mechanical stability and thus higher quality as a membrane model. Moreover, its suitability for the investigation of membrane-acitve AMPs was proven. Therefore, it can be emphasized that this system is advantageous for more elaborate investigations of biomolecules comprised of different secondary structure elements, e.g. proteins. Especially, the opportunity to combine the SEIRA approach with the application of electrical potentials is beneficial. The elucidation of processes dependent on the transmembrane potential, e.g. the gating mechanism of proton-channels or ion channels, based on the secondary structure is an important research field for the future.

However, to fully understand the potential-dependence of the underlying processes, it is necessary to determine the potential distribution from the electrode over the SAM, aqueous reservoir and bilayer membrane to the hydrophilic surface and the solution phase. In future investigations, the associated electric fields can be estimated on the basis of the vibrational Stark effect. The implementation of Stark-active chemical groups by labelling of the SAM or phospholipids can shed light on this issue. This allows to monitor the potential for each state of the system.

Furthermore, the phospholipid composition of the tBLM needs to be adapted to the composition of bacterial or eukaryotic cells, depending on the natural target of peptides or the native environment of proteins. For that purpose, isolated cell lipid extracts can be deployed to mimic the respective cell type. However, for the subsequent probing of membrane proteins a high purity is required, since a superposition of spectral features of residual proteins and the protein of interest has to be considered.

Another interesting research topic is the interaction of peptides and solubilized proteins with membrane proteins, i.e. G-protein coupled receptors that play an important role in the cellular signal-transduction. Based on the SEIRA difference mode, the addition of the binding partner to the tBLM and the subsequent interaction with the integrated membrane protein could be monitored in-situ.

The use of optimized biomimetic membrane models in collaboration with theoretical research methods has been demonstrated to be a powerful approach. Depending on the molecular properties and the specific targets of the system, DFT calculations, MD simulations or QM/MM simulations may represent the method of choice. By this means, the presented tBLM helps to increase the knowledge about fundamental processes at the cellular plasma membrane.

8 APPENDIX

8.1 Voltage-dependent incorporation of alamethicin into tethered bilayer lipid membranes

The information presented in this chapter are reproduced from Forbrig et al.[206]

8.1.1 Correction of SEIRA spectra
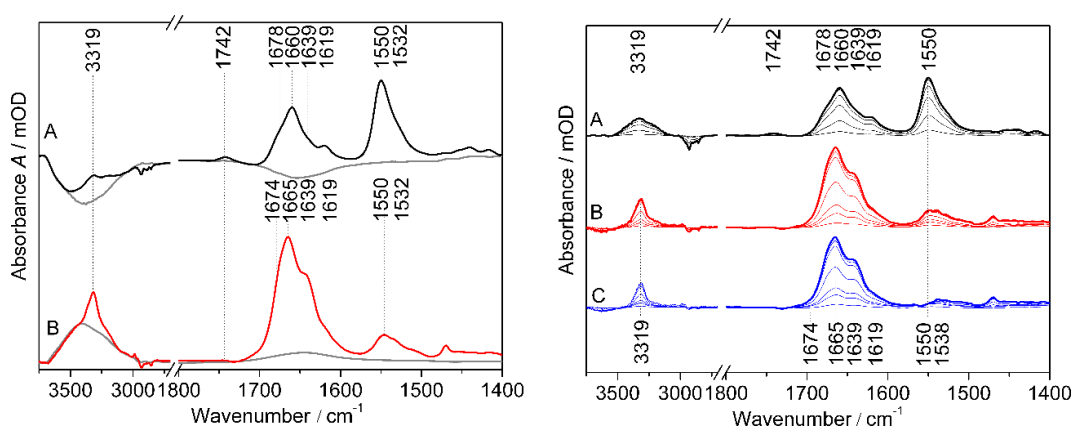
Figure A2 Left: Correction of water contribution (gray line) in the SEIRA spectra of tHLMs (A) and tBLMs (B). Right: SEIRA spectra of ALM incubated on tHLMs (A) and tBLMs (B) corrected for water contribution (see left panel and Figure 6.12), and on tBLMs with further correction for horizontally adsorbed ALM molecules (C; see Figure 6.12) using the spectrum of ALM on tHLMs (n = 2 independent experiments). Reprinted with permission from Forbrig, E.; Staffa, JK.; Salewski, J.; Mroginski MA.; Hildebrandt, P.; Kozuch, J. Monitoring the Orientational Changes of Alamethicin during Incorporation into Bilayer Lipid Membranes *Langmuir* 2018 *34* (6), pp 2373-2385. Copyright (2018) American Chemical Society.[206]
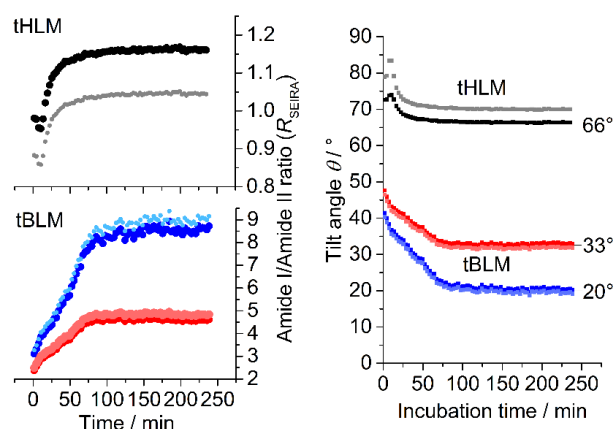
Figure A1 Presentation analogous to Figure 6.14 and Figure 6.19 displaying the impact of the correction depicted in Figure A2 on amide I/amide II ratios (left) and tilt angles (right). Black, red and blue traces represent the same traces as shown in chapter 6.3.5 with the same color code as in Figure A2 right. The faint colors (gray, light red, light blue) show the respective traces without correction for the contribution of water, leading to a negligible change for the tBLM system ($\Delta\theta \approx 1°$) and a small change for tHLMs ($\Delta\theta \approx 3° - 4°$). (n = 2 independent experiments) Reprinted with permission from Forbrig, E.; Staffa, JK.; Salewski, J.; Mroginski MA.; Hildebrandt, P.; Kozuch, J. Monitoring the Orientational Changes of Alamethicin during Incorporation into Bilayer Lipid Membranes *Langmuir* 2018 *34* (6), pp 2373-2385. Copyright (2018) American Chemical Society.[206]
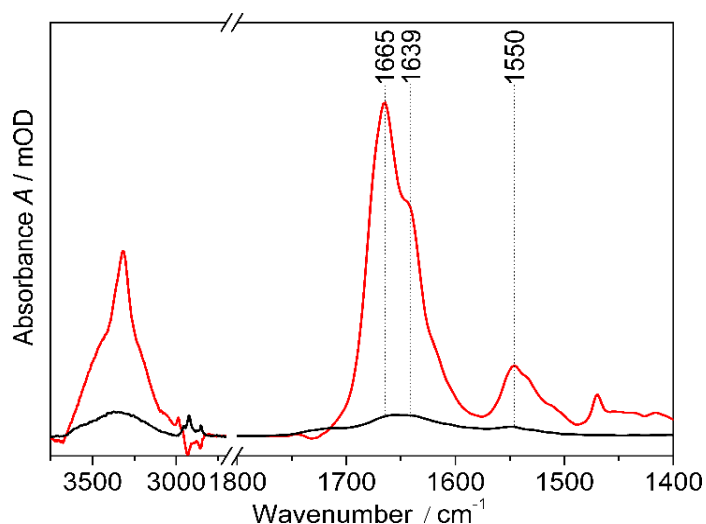
Figure A4 Comparison between SEIRA spectra of ALM after incubation on tBLMs under open circuit conditions (red) and under constant application of +400 mV (black). (n = 2 independent experiments) Reprinted with permission from Forbrig, E.; Staffa, JK.; Salewski, J.; Mroginski MA.; Hildebrandt, P.; Kozuch, J. Monitoring the Orientational Changes of Alamethicin during Incorporation into Bilayer Lipid Membranes *Langmuir* 2018 *34* (6), pp 2373-2385. Copyright (2018) American Chemical Society.[206]
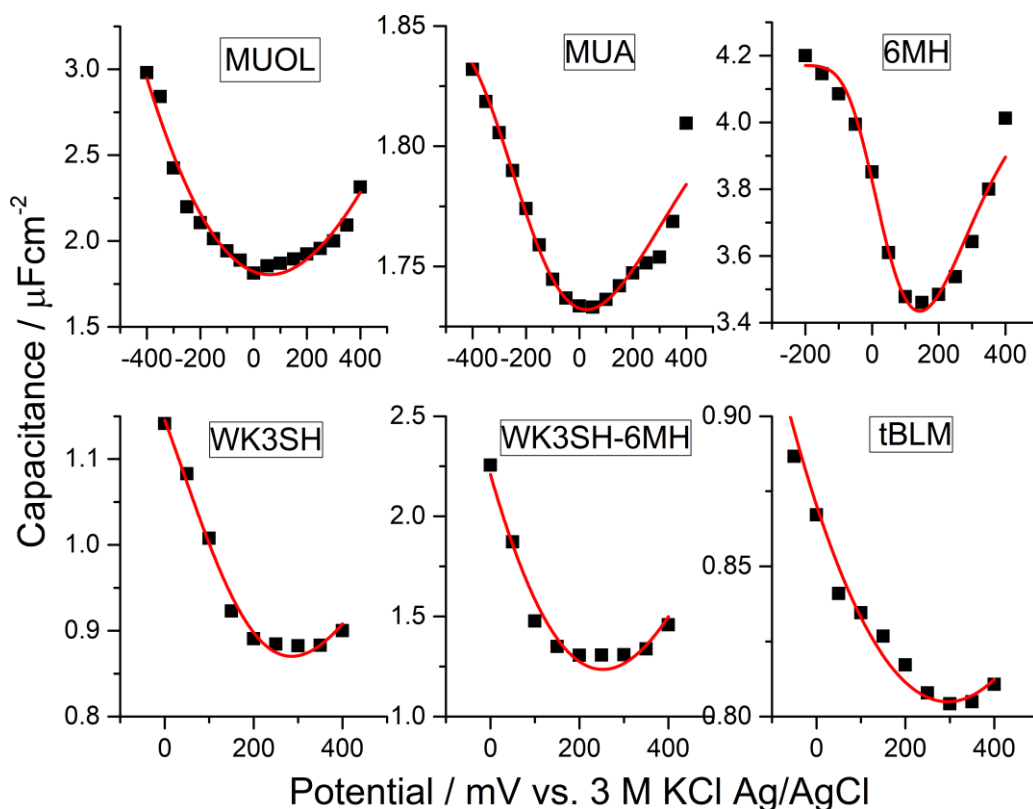
Figure A3 Potential-dependent capacitances of 11-mercaptoundecanoic acid (MUA), 11-mercaptoundecanol (MUOL), 6-mercaptohexanol (6MH), WK3SH, WK3SH/6MH, and the tBLM on SEIRA Au electrodes determined by electrical impedance spectroscopy. While the first two SAMs were measured in 50 mM NaClO$_4$, the latter four in were observed in buffer solution at pH 7. Red lines represent fits using a skewed distribution to determine the minimum of the capacitance (n = 3 independent experiments). Reprinted with permission from Forbrig, E.; Staffa, JK.; Salewski, J.; Mroginski MA.; Hildebrandt, P.; Kozuch, J. Monitoring the Orientational Changes of Alamethicin during Incorporation into Bilayer Lipid Membranes *Langmuir* 2018 *34* (6), pp 2373-2385. Copyright (2018) American Chemical Society.[206]

8.1.2 Estimation of the potential of zero charge

Table A1 Capacitance and potential of zero charge estimates of 11-mercaptoundecanoic acid (MUA), 11-mercaptoundecanol (MUOL), 6-mercaptohexanol (6MH), WK3SH, and the tBLM obtained by electrical impedance spectroscopy and comparison with previous data (vs. 3 M Ag/AgCl). In this work, the potential of zero charge was estimated from determining the minimum in capacitance (see Figure A3).[309] (n = 3 independent experiments) Reprinted with permission from Forbrig, E.; Staffa, JK.; Salewski, J.; Mroginski MA.; Hildebrandt, P.; Kozuch, J. Monitoring the Orientational Changes of Alamethicin during Incorporation into Bilayer Lipid Membranes *Langmuir* 2018 *34* (6), pp 2373-2385. Copyright (2018) American Chemical Society.[206]

| SAMs	SEIRA Au electrode – this work		Au(111) - Literature	
	Capacitance µF/cm²	Minimum of capacitance mV	Capacitance µF/cm²	E_{pzc} mV
MUA	1.7	25 ± 100	2[a]	-30[a]
MUOL	1.9	60 ± 100	1.2[a]	70[a]
6MH	3.4	145 ± 100	4.5[b]	-10 ± 130[b]
WK3SH	0.9	285 ± 100		
WK3SH/6MH	1.4	250 ± 100		
tBLM	0.8	295 ± 100		300 ± 30[c] (DPTL-based tBLM)

[a] data determined using immersion technique by Ramirez et al.[311] Values for MUA vary by up to 500 mV dependent on the pH.

[b] data determined using electro-wetting technique by Jeuken et al.[308,319] Other OH-terminated SAMs yielded values that scattered in a range of 600 mV, based on the applied technique, presumably due to different H-bonding situations in the respective reference state.

[c] data determined using immersion technique by Su et al.[127]

Considering the intrinsic inaccuracy involved with the determination of E_{pzc} values, the values presented in this work determined using electrical impedance spectroscopy lie in a range spanned by the values obtained by other techniques. The concordance of these values is particularly remarkable, since it was demonstrated in literature that values determined using different methods (capacitance measurements,[309] electrowetting,[322] immersion technique[311]) vary increasingly with an increasing extend of H-bonds with the SAM head groups. For instance, while for $C_{11}CH_3$ a value of ca. -0.4 ± 0.1 V was determined independently using all three techniques,[309,311,322] for C_xOH SAMs values differed by ca. 0.6 V (-0.03 V for $C_{11}OH$ using capacitance[309]; -0.01 ± 0.13 V for C6OH using electrowetting/contact angle measurements[308]; 0.54 V for $C_{12}OH$ using electrowetting[322]; 0.07 V for $C_{10}OH$ using the immersion technique on Au(111)).[311] For tBLM systems only the Lipkowski group[127] reported a value of ca. 300 mV. Although their system is based on the DPTL tether, their E_{pzc} and the value estimated in this work are in line with each other and suggest that the E_{pzc} of our tBLM system lies in the region of ca. 300 mV.

8.1.3 3-step kinetic model of incorporation

Table A2 Results of fitting the differential equation system to the data shown in Figure 6.14. All values refer to an electrode surface of 1.5 cm^2 and starting conditions of 1 nmol of ALM in 1 mL of solution. The columns "Amide II*" display the fitting results fixing k_{Ads}, k_{Dim}, k_{Mem}, $P_{Ads,max}$, and $P_{Mem,max}$ to the fitting results for the corresponding Amide I data set (grayed out – not shown graphically). The graphical presentations of the fits are shown in Figure A5 to Figure A7. The unit "int" represents the integrated intensity of the respective bands (n = 2 independent experiments). Reprinted with permission from Forbrig, E.; Staffa, JK.; Salewski, J.; Mroginski MA.; Hildebrandt, P.; Kozuch, J. Monitoring the Orientational Changes of Alamethicin during Incorporation into Bilayer Lipid Membranes *Langmuir* 2018 *34* (6), pp 2373-2385. Copyright (2018) American Chemical Society.[206]

	tHLM			tBLM		
	Amide I	**Amide II**	**Amide II***	**Amide I**	**Amide II**	**Amide II***
k_{Ads} (nmol^{-1}min^{-1})	$7.54 \cdot 10^{-5}$	$7.90 \cdot 10^{-5}$	$7.54 \cdot 10^{-5}$	$2.00 \cdot 10^{-4}$	$2.66 \cdot 10^{-4}$	$2.00 \cdot 10^{-4}$
k_{Dim} (nmol^{-1}min^{-1})	1.28	1.15	1.28	$2.67 \cdot 10^{-1}$	$3.42 \cdot 10^{-2}$	$2.67 \cdot 10^{-1}$
k_{Mem} (nmol^{-1}min^{-1})	-	-	-	$6.92 \cdot 10^{-1}$	4.97	$6.92 \cdot 10^{-1}$
$P_{Ads,max}$ (nmol)	$7.07 \cdot 10^{-2}$	$7.07 \cdot 10^{-2}$	$7.07 \cdot 10^{-2}$	$7.13 \cdot 10^{-2}$	$7.11 \cdot 10^{-2}$	$7.14 \cdot 10^{-2}$
$P_{Mem,max}$ (nmol)	$4.37 \cdot 10^{-5}$	$4.37 \cdot 10^{-5}$	$4.37 \cdot 10^{-5}$	$4.37 \cdot 10^{-5}$	$4.37 \cdot 10^{-5}$	$4.37 \cdot 10^{-5}$
F_{Ads} (int nmol^{-1})	$7.76 \cdot 10^{2}$	$8.44 \cdot 10^{2}$	$8.58 \cdot 10^{2}$	$6.10 \cdot 10^{2}$	$2.10 \cdot 10^{2}$	$2.07 \cdot 10^{2}$
F_{Dim} (int nmol^{-1})	$2.20 \cdot 10^{3}$	$1.89 \cdot 10^{3}$	$1.88 \cdot 10^{3}$	$6.10 \cdot 10^{2}$	$1.13 \cdot 10^{3}$	$3.91 \cdot 10^{2}$
F_{Mem} (int nmol^{-1})	-	-	-	$4.92 \cdot 10^{6}$	$6.02 \cdot 10^{5}$	$7.66 \cdot 10^{5}$
χ^2	$2.21 \cdot 10^{-2}$	$2.64 \cdot 10^{-2}$	$2.64 \cdot 10^{-2}$	$2.16 \cdot 10^{-1}$	$1.15 \cdot 10^{-3}$	$5.76 \cdot 10^{-3}$
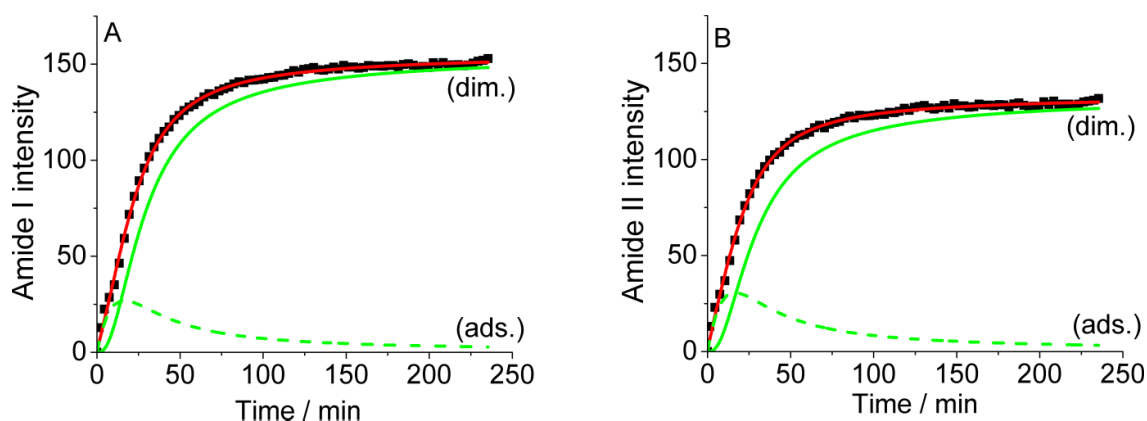
Figure A5 Results of fitting equation 6.8 (including step 1 and step 2 of the differential equation system) to the time traces of the amide I and amide II SEIRA intensities of ALM on tHLMs (black squares in A and B, respectively). The red lines represent the overall fit to the data, while the green full and dashed lines refer to the modeled intensities of the dimeric and adsorbed species. Reprinted with permission from Forbrig, E.; Staffa, JK.; Salewski, J.; Mroginski MA.; Hildebrandt, P.; Kozuch, J. Monitoring the Orientational Changes of Alamethicin during Incorporation into Bilayer Lipid Membranes *Langmuir* 2018 *34* (6), pp 2373-2385. Copyright (2018) American Chemical Society.[206]
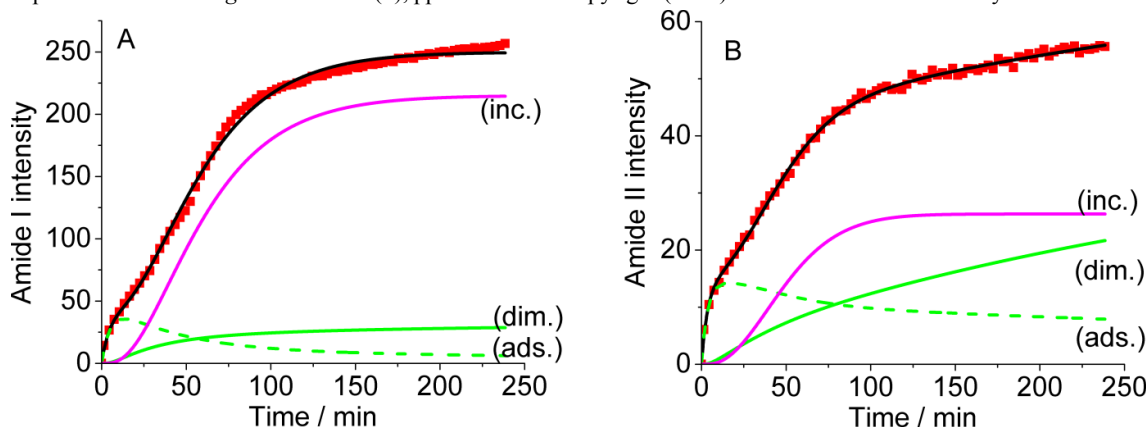
Figure A6 Results of fitting equation 6.8 to the time traces of the SEIRA intensities of amide I and amide II of ALM on tBLMs (red squares in A and B, respectively). The black lines represent the overall fit to the data, while the green full and dashed lines refer to the modeled intensities of the dimeric (dim.) and adsorbed (ads.) species. The magenta line depicts the intensities of incorporated (inc.) transmembrane ALM helices. Reprinted with permission from Forbrig, E.; Staffa, JK.; Salewski, J.; Mroginski MA.; Hildebrandt, P.; Kozuch, J. Monitoring the Orientational Changes of Alamethicin during Incorporation into Bilayer Lipid Membranes *Langmuir* 2018 *34* (6), pp 2373-2385. Copyright (2018) American Chemical Society.[206]
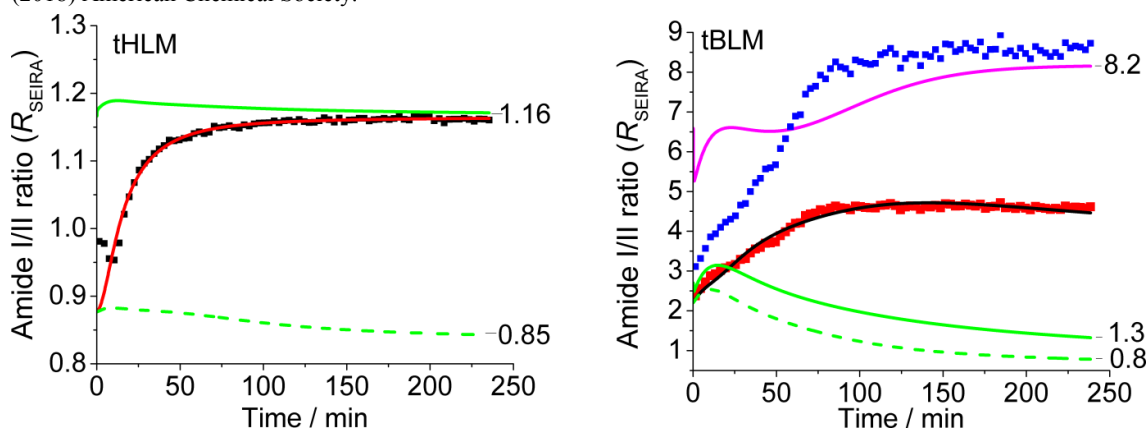
Figure A7 Amide I/Amide II ratios (R_{SEIRA}) of ALM from the SEIRA experiments and calculated from fitting the differential equation system. Left: tHLMs: black squares and the red line refer to the results of the experiment and the fitting, respectively. Right: tBLMs: red squares and black line display the results of the experiment and the fitting, respectively; the blue squares refer to the values after correction for the vertically adsorbed ALM fraction. Green full and dashed lines as well as the magenta line in both graphs depict the modeled intensity ratios of the dimeric, adsorbed, and incorporated species, respectively. Reprinted with permission from Forbrig, E.; Staffa, JK.; Salewski, J.; Mroginski MA.; Hildebrandt, P.; Kozuch, J. Monitoring the Orientational Changes of Alamethicin during Incorporation into Bilayer Lipid Membranes *Langmuir* 2018 *34* (6), pp 2373-2385. Copyright (2018) American Chemical Society.[206]

8.1.4 DFT optimization of ALM structures

Table A3 Data on the secondary structure of ALM α-helix/3₁₀-helix structure optimized by DFT, extracted from fitting two helix functions through the C-α atoms of the backbone of ALM. The angles are determined based on the helix axes obtained from the fit. Reprinted with permission from Forbrig, E.; Staffa, JK.; Salewski, J.; Mroginski MA.; Hildebrandt, P.; Kozuch, J. Monitoring the Orientational Changes of Alamethicin during Incorporation into Bilayer Lipid Membranes *Langmuir* 2018 *34* (6), pp 2373-2385. Copyright (2018) American Chemical Society.[206]

	N-terminal helix Aib-1 → Aib-13	C-terminal helix Aib-13 → Pheol-20
Residues per turn	3.38 ± 0.01	3.32 ± 0.02
Radius / A	2.28 ± 0.02	2.0 ± 0.1
Translation per residue / A	1.5 ± 0.1	1.3 ± 0.1
Angle vs N-terminal helix	-	23.4°
Angle of total dipole moment (212.3 D) vs helix fragments	10.8°	17.8°
Angle of back bone dipole moment (100.2 D) vs helix fragments	2.9°	21.5°

Table A4 Data on the secondary structure of ALM α-helix/α-helix structure optimized by DFT, extracted from fitting two helix functions through the C-α atoms of the backbone of ALM. The angles are determined based on the helix axes obtained from the fit. Reprinted with permission from Forbrig, E.; Staffa, JK.; Salewski, J.; Mroginski MA.; Hildebrandt, P.; Kozuch, J. Monitoring the Orientational Changes of Alamethicin during Incorporation into Bilayer Lipid Membranes *Langmuir* 2018 *34* (6), pp 2373-2385. Copyright (2018) American Chemical Society.[206]

	N-terminal helix Aib-1 → Aib-13	C-terminal helix Aib-13 → Pheol-20
Residues per turn	3.42 ± 0.02	3.4 ± 0.02
Radius / A	2.35 ± 0.09	2.32 ± 0.07
Translation per residue / A	1.60 ± 0.05	1.56 ± 0.03
Angle vs N-terminal helix	-	25.1°
Angle of total dipole moment (56.8 D) vs helix fragments	83.5°	86.3°
Angle of back bone dipole moment (96.8 D) vs helix fragments	7.3°	18.5°

8.1.5 Theoretical analysis of the reorientation of ALM monitored by SEIRA spectroscopy

8.1.5.1 Double-well potential model for ALM

According to the model described in Figure A9 and equations 6.13 and 6.14 in chapter 6.3.7 and analogous to Guidelli et al.,[301] the molar fraction x_v of vertical incorporated ALM molecules is given by the Boltzmann distribution according to

$$x_v = \frac{1}{1 + \frac{sin\theta_H}{sin\theta_V} exp\left(-\frac{E - E_\Delta}{dkT/_{\Delta\mu}}\right)}$$

(8.1)

where the factor $sin\theta_H/sin\theta_V$ reflects the ratio of the degeneracies of the horizontal and vertical orientations. Using the potential-dependent trace of the orientation in Figure 6.19, the applicability of this model can be tested assuming that at negative potentials an angle of 21° will be assumed by ALM molecules, as determined from the potential-independent experiments as the final incorporated state.
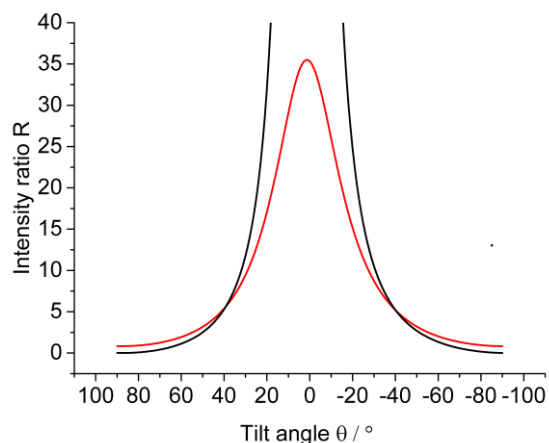
Figure A8 Intensity ratios comparing equation 6.9 (black) and equation 6.12 (red), using the same values for the respective constants. Reprinted with permission from Forbrig, E.; Staffa, JK.; Salewski, J.; Mroginski MA.; Hildebrandt, P.; Kozuch, J. Monitoring the Orientational Changes of Alamethicin during Incorporation into Bilayer Lipid Membranes *Langmuir* 2018 *34* (6), pp 2373-2385. Copyright (2018) American Chemical Society.[206]
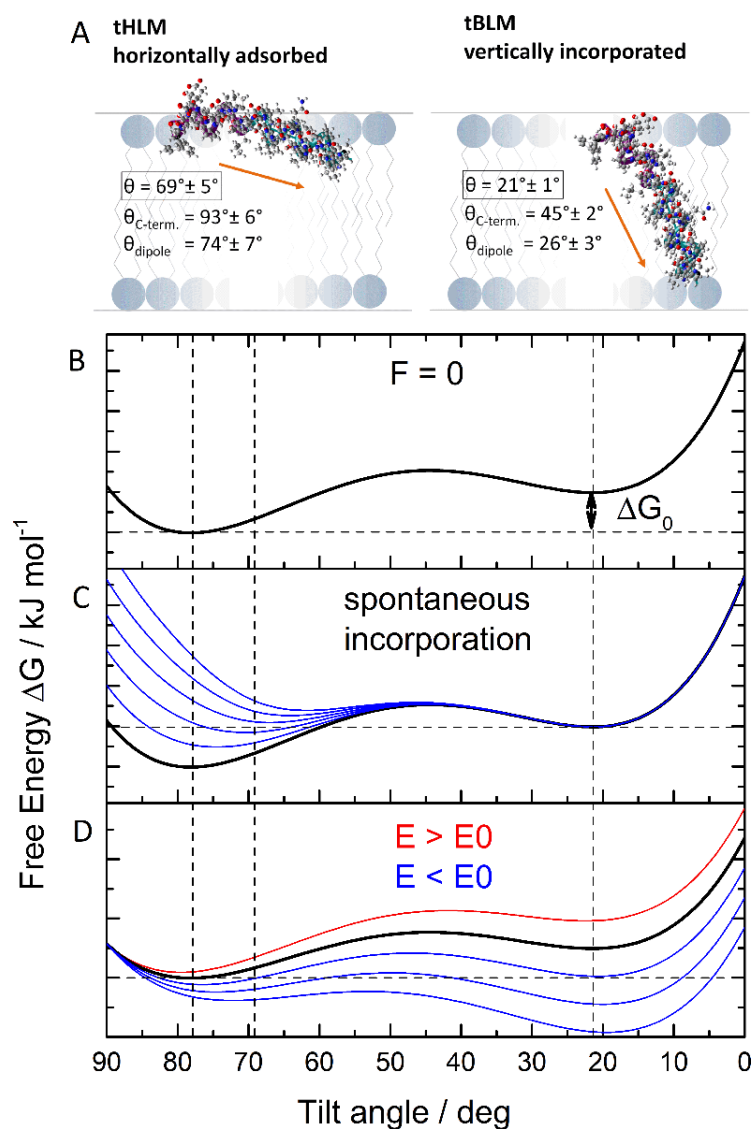
Figure A9 A: Double-well potential model for the incorporation of ALM in membranes dependent on the orientation of ALM. B: According to Mottamal et al.,[294] the horizontal state is more stable by $\Delta G_0 \approx 5$ kJ mol^{-1} than the vertically incorporated state with a transition state at intermediate tilt angles. C: During spontaneous incorporation the horizontal species becomes less stable due to increasing repulsive interactions. D: When applying electrochemical potentials to the electrode (analogously to equation 6.13), the two stable states become (de)stabilized due to interaction with the associated electric field. Reprinted with permission from Forbrig, E.; Staffa, JK.; Salewski, J.; Mroginski MA.; Hildebrandt, P.; Kozuch, J. Monitoring the Orientational Changes of Alamethicin during Incorporation into Bilayer Lipid Membranes *Langmuir* 2018 *34* (6), pp 2373-2385. Copyright (2018) American Chemical Society.[206]
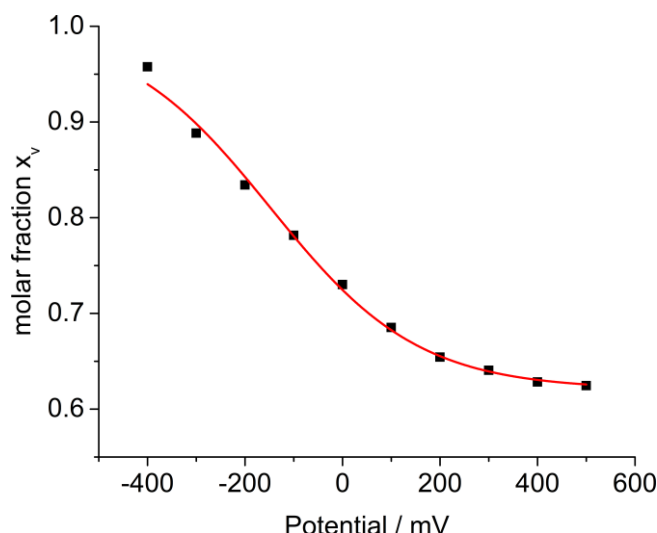
Figure A10 Plot of molar fraction of vertical ALM species x_v against the applied potential (vs. 3 M KCl Ag/AgCl). Molar fractions were estimated using a sum of weighted vectors $\vec{T} = (1 - x_v)\vec{H} + x_v\vec{V}$ where $\vec{T}$ is the vector of the averaged vector, and $\vec{H}$ and $\vec{V}$ are the unit vectors representing the orientation of horizontal and vertical species, respectively. The projection on the membrane normal yields the final relation between averaged, effective angle θ and x_v: $cos\theta = \frac{(1-x_v)}{|\vec{T}|}cos\theta_H + \frac{x_v}{|\vec{T}|}cos\theta_V$ with θ_V and θ_H being the tilt angles of vertical and horizontal species, respectively. The red line represents a fit using the Boltzmann equation $x_v = x_{v,pos} + \frac{x_{v,neg}-x_{v,pos}}{1+\frac{sin\theta_H}{sin\theta_V}exp\left(-\frac{E-E_\Delta}{dkT/\Delta\mu}\right)}$, which is equal to equation 8.1 augmented by an offset accounting for a fraction of vertically incorporated ALM prior to application of potentials. The result of the fit is: $x_{v,neg} = 1$ (constraint); $x_{v,pos} = 0.621 \pm 0.007$; $E_\Delta = -3$ mV $\pm$ 17 mV; $dkT/\Delta\mu = -152$ mV $\pm$ 10 mV; $\chi^2 = 7.8 \cdot 10^{-5}$. Reprinted with permission from Forbrig, E.; Staffa, JK.; Salewski, J.; Mroginski MA.; Hildebrandt, P.; Kozuch, J. Monitoring the Orientational Changes of Alamethicin during Incorporation into Bilayer Lipid Membranes *Langmuir* 2018 *34* (6), pp 2373-2385. Copyright (2018) American Chemical Society.[206]
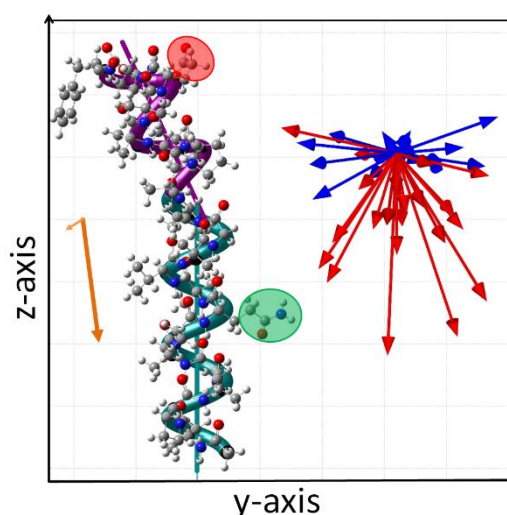
Figure A11 ALM α-helix/α-helix structure obtained from the DFT calculations, shown from the "side" (hydrophobic and hydrophilic side of ALM on the left and right, respectively), analogously to Figure 6.16. The cyan and magenta ribbons and lines underlying the structure indicate the orientation of the N-terminal α-helix and C-terminal α-like helix axes, respectively. The light red and light green circles highlight the position of Glu-18 and Gln-7, respectively; the thin orange arrow depicts the vector of the total dipole moment (56.8 D – arrow is directed from negative to positive and has a major component along the x-axis), while the bold orange arrow represents the dipole of the back bone (96.8 D). The red and blue arrows refer to the vectors of the TDMs of the amide I and amide II modes of ALM, respectively. Reprinted with permission from Forbrig, E.; Staffa, JK.; Salewski, J.; Mroginski MA.; Hildebrandt, P.; Kozuch, J. Monitoring the Orientational Changes of Alamethicin during Incorporation into Bilayer Lipid Membranes *Langmuir* 2018 *34* (6), pp 2373-2385. Copyright (2018) American Chemical Society.[206]
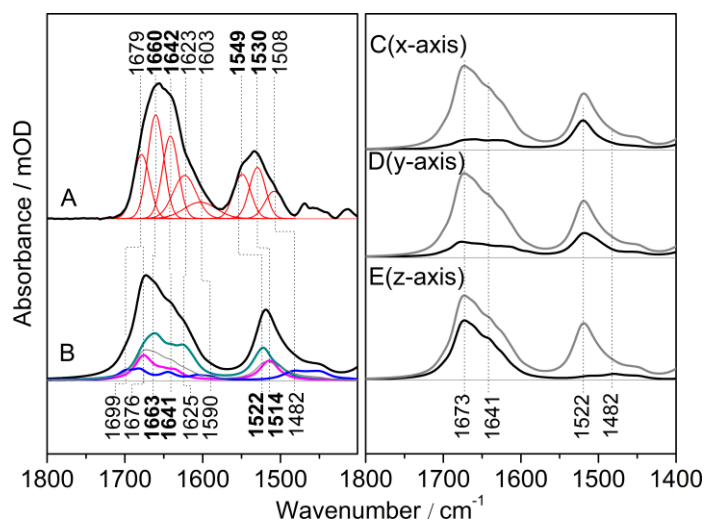
Figure A12 Presentation analogous to Figure 6.17: Left: Comparison of transmission IR spectrum of ALM in aqueous solution (A) and the simulated DFT-IR spectrum of ALM's α-helix/α-helix structure (B, half width set to 12 cm^{-1}). Red bands in A indicate the Gaussian fit to the experimental spectrum, while the spectra in cyan, magenta, blue and gray refer to the combined spectral components originating from the N-terminal α-helix, C-terminal α-helix, amino acid side residues, and unassigned components, respectively. These components were derived from evaluating the potential energy distribution of the normal modes. Right: Simulated polarized DFT-IR spectra of ALM referring to the axes shown in Figure 6.16. Gray traces represent the isotropic spectrum (n = 2 independent experiments). Reprinted with permission from Forbrig, E.; Staffa, JK.; Salewski, J.; Mroginski MA.; Hildebrandt, P.; Kozuch, J. Monitoring the Orientational Changes of Alamethicin during Incorporation into Bilayer Lipid Membranes *Langmuir* 2018 *34* (6), pp 2373-2385. Copyright (2018) American Chemical Society.[206]
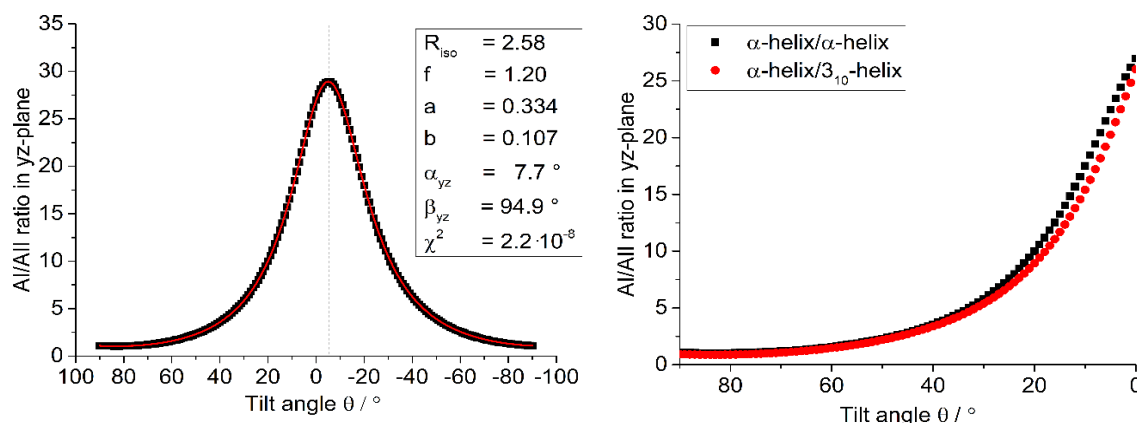
Figure A13 Left: Presentation analogous to Figure 6.18: Simulated amide I/amide II ratios of ALM's α-helix/α-helix structure during reorientation, i.e. as a function of the tilt angle θ as displayed in the inset in Figure **6.18**. ALM reorients such that the hydrophobic side faces downwards (but not sideways) to match the hydrophobic interaction with a horizontally oriented membrane surface. The red line and the inset on the right display the results of fitting equation 6.12 to the data. Right: Overlay of simulated amide I/amide II ratios for both structures in the relevant region between 0 and 90°. Reprinted with permission from Forbrig, E.; Staffa, JK.; Salewski, J.; Mroginski MA.; Hildebrandt, P.; Kozuch, J. Monitoring the Orientational Changes of Alamethicin during Incorporation into Bilayer Lipid Membranes *Langmuir* 2018 *34* (6), pp 2373-2385. Copyright (2018) American Chemical Society.[206]

8.1.6 Theoretical analysis of the reorientation of ALM monitored by SEIRA spectroscopy
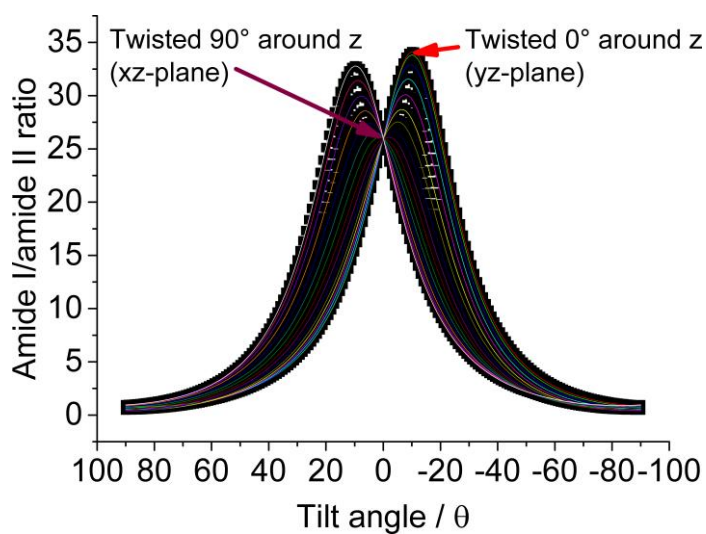
Figure A14 Amide I/amide II ratios (black squares) calculated different reorientations and twisting of ALM α-helix/3_{10}-helix structure, i.e. upon twisting ALM around its own axis before reorientation is performed. The colored lines represent the fit using equation 6.12. Table A3 summarizes the results of the fit. Reprinted with permission from Forbrig, E.; Staffa, JK.; Salewski, J.; Mroginski MA.; Hildebrandt, P.; Kozuch, J. Monitoring the Orientational Changes of Alamethicin during Incorporation into Bilayer Lipid Membranes *Langmuir* 2018 *34* (6), pp 2373-2385. Copyright (2018) American Chemical Society.[206]

Table A5 Results of fitting equation 6.12 to the curves depicted in Figure A8. The entries "yz-plane" and "xz-plane" indicate when the fit was performed to a reorientation within these planes. Reprinted with permission from Forbrig, E.; Staffa, JK.; Salewski, J.; Mroginski MA.; Hildebrandt, P.; Kozuch, J. Monitoring the Orientational Changes of Alamethicin during Incorporation into Bilayer Lipid Membranes *Langmuir* 2018 *34* (6), pp 2373-2385. Copyright (2018) American Chemical Society.[206]

Twisted around z-axis by (°)	f	a	b	α (°)	β (°)	α − β (°)
(yz-plane)						
0	1.34	0.251	0.102	5.4	100.6	-95.2
1	1.34	0.250	0.102	5.3	100.6	-95.3
2	1.34	0.249	0.101	5.2	100.7	-95.4
3	1.34	0.247	0.101	5.1	100.7	-95.6
4	1.34	0.246	0.101	5.0	100.7	-95.7
5	1.34	0.245	0.101	4.9	100.7	-95.8
6	1.34	0.243	0.100	4.8	100.8	-95.9
7	1.33	0.242	0.100	4.7	100.8	-96.0
8	1.33	0.240	0.100	4.6	100.8	-96.1
9	1.33	0.239	0.100	4.5	100.8	-96.3
10	1.33	0.237	0.100	4.4	100.8	-96.4
11	1.33	0.235	0.099	4.3	100.8	-96.5
12	1.33	0.234	0.099	4.2	100.8	-96.6
13	1.32	0.232	0.099	4.1	100.8	-96.7
14	1.32	0.230	0.099	4.0	100.8	-96.8
15	1.32	0.228	0.099	3.9	100.8	-96.9
16	1.32	0.227	0.099	3.8	100.8	-96.9
17	1.32	0.225	0.099	3.7	100.7	-97.0
18	1.32	0.223	0.099	3.6	100.7	-97.1
19	1.31	0.221	0.099	3.5	100.7	-97.2
20	1.31	0.219	0.099	3.4	100.7	-97.3
21	1.31	0.217	0.099	3.3	100.6	-97.4
22	1.31	0.215	0.099	3.2	100.6	-97.4
23	1.31	0.213	0.099	3.1	100.6	-97.5
24	1.30	0.211	0.099	2.9	100.5	-97.6
25	1.30	0.209	0.099	2.8	100.5	-97.6
26	1.30	0.207	0.099	2.7	100.4	-97.7
27	1.30	0.204	0.100	2.6	100.4	-97.8
28	1.30	0.201	0.100	2.5	100.3	-97.8
29	1.30	0.197	0.100	2.4	100.3	-97.9
30	1.30	0.194	0.100	2.3	100.2	-98.0
31	1.30	0.190	0.101	2.1	100.2	-98.0
32	1.30	0.187	0.101	2.0	100.1	-98.1
33	1.30	0.184	0.102	1.9	100.0	-98.1
34	1.30	0.181	0.102	1.8	100.0	-98.2
35	1.30	0.177	0.102	1.7	99.9	-98.2
36	1.30	0.174	0.103	1.6	99.8	-98.3
37	1.30	0.171	0.103	1.5	99.7	-98.3
38	1.30	0.168	0.104	1.3	99.7	-98.3
39	1.30	0.165	0.104	1.2	99.6	-98.4
40	1.30	0.162	0.105	1.1	99.5	-98.4
41	1.30	0.159	0.105	1.0	99.4	-98.4

Twisted around z-axis by (°)	f	a	b	α (°)	β (°)	α – β (°)
42	1.30	0.156	0.105	0.9	99.3	-98.4
43	1.30	0.153	0.106	0.8	99.2	-98.5
44	1.30	0.150	0.106	0.7	99.1	-98.5
45	1.30	0.148	0.107	0.5	99.0	-98.5
46	1.30	0.145	0.107	0.4	98.9	-98.5
47	1.30	0.143	0.108	0.3	98.8	-98.5
48	1.30	0.140	0.108	0.2	98.7	-98.5
49	1.30	0.138	0.109	0.1	98.6	-98.5
50	1.30	0.136	0.110	0.0	98.5	-98.5
51	1.30	0.133	0.110	-0.1	98.4	-98.5
52	1.30	0.131	0.111	-0.2	98.3	-98.5
53	1.30	0.129	0.111	-0.3	98.2	-98.5
54	1.30	0.127	0.112	-0.4	98.1	-98.5
55	1.30	0.125	0.112	-0.5	98.0	-98.5
56	1.30	0.124	0.113	-0.7	97.8	-98.5
57	1.30	0.122	0.113	-0.8	97.7	-98.5
58	1.30	0.120	0.114	-0.9	97.6	-98.5
59	1.30	0.119	0.114	-1.0	97.5	-98.4
60	1.30	0.118	0.115	-1.1	97.3	-98.4
61	1.30	0.116	0.115	-1.2	97.2	-98.4
62	1.30	0.115	0.116	-1.3	97.1	-98.4
63	1.30	0.114	0.116	-1.4	96.9	-98.3
64	1.30	0.113	0.117	-1.5	96.8	-98.3
65	1.30	0.112	0.117	-1.6	96.7	-98.3
66	1.30	0.112	0.118	-1.7	96.5	-98.2
67	1.30	0.111	0.118	-1.8	96.4	-98.2
68	1.30	0.110	0.119	-1.9	96.3	-98.1
69	1.30	0.110	0.119	-2.0	96.1	-98.1
70	1.30	0.110	0.120	-2.1	96.0	-98.1
71	1.30	0.109	0.120	-2.2	95.8	-98.0
72	1.30	0.109	0.121	-2.3	95.7	-98.0
73	1.30	0.109	0.121	-2.4	95.5	-97.9
74	1.30	0.109	0.122	-2.5	95.4	-97.8
75	1.30	0.110	0.122	-2.6	95.2	-97.8
76	1.30	0.110	0.123	-2.7	95.1	-97.7
77	1.30	0.110	0.123	-2.8	94.9	-97.7
78	1.30	0.111	0.123	-2.9	94.7	-97.6
79	1.30	0.112	0.124	-3.0	94.6	-97.5
80	1.30	0.112	0.124	-3.1	94.4	-97.5
81	1.30	0.113	0.125	-3.1	94.3	-97.4
82	1.30	0.114	0.125	-3.2	94.1	-97.3
83	1.30	0.115	0.125	-3.3	93.9	-97.3
84	1.30	0.116	0.126	-3.4	93.8	-97.2
85	1.30	0.117	0.126	-3.5	93.6	-97.1
86	1.30	0.119	0.126	-3.6	93.4	-97.0
87	1.30	0.120	0.126	-3.7	93.3	-97.0
88	1.30	0.122	0.127	-3.8	93.1	-96.9
89	1.30	0.123	0.127	-3.9	92.9	-96.8

Twisted around z-axis by (°)	f	a	b	α (°)	β (°)	α – β (°)
(xz-plane)						
90	1.30	0.125	0.127	-4.0	92.7	-96.7
91	1.30	0.127	0.127	-4.1	92.6	-96.6
92	1.30	0.129	0.128	-4.1	92.4	-96.5
93	1.30	0.131	0.128	-4.2	92.2	-96.4
94	1.30	0.133	0.128	-4.3	92.0	-96.3
95	1.30	0.135	0.128	-4.4	91.9	-96.3
96	1.30	0.137	0.128	-4.5	91.7	-96.2
97	1.30	0.139	0.128	-4.6	91.5	-96.1
98	1.30	0.142	0.128	-4.6	91.3	-96.0
99	1.30	0.144	0.128	-4.7	91.1	-95.9
100	1.30	0.147	0.128	-4.8	91.0	-95.8
101	1.30	0.149	0.129	-4.9	90.8	-95.7
102	1.30	0.152	0.129	-5.0	90.6	-95.6
103	1.30	0.155	0.129	-5.0	90.4	-95.4
104	1.30	0.157	0.129	-5.1	90.2	-95.3
105	1.30	0.160	0.128	-5.2	90.0	-95.2
106	1.30	0.163	0.128	-5.3	89.8	-95.1
107	1.30	0.166	0.128	-5.3	89.7	-95.0
108	1.30	0.169	0.128	-5.4	89.5	-94.9
109	1.30	0.172	0.128	-5.5	89.3	-94.8
110	1.30	0.175	0.128	-5.6	89.1	-94.7
111	1.30	0.178	0.128	-5.6	88.9	-94.5
112	1.30	0.181	0.128	-5.7	88.7	-94.4
113	1.30	0.185	0.127	-5.8	88.5	-94.3
114	1.30	0.188	0.127	-5.8	88.4	-94.2
115	1.30	0.191	0.127	-5.9	88.2	-94.1
116	1.30	0.194	0.127	-6.0	88.0	-93.9
117	1.30	0.197	0.127	-6.0	87.8	-93.8
118	1.30	0.201	0.126	-6.1	87.6	-93.7
119	1.30	0.203	0.126	-6.1	87.4	-93.6
120	1.30	0.206	0.126	-6.2	87.2	-93.4
121	1.30	0.208	0.126	-6.2	87.1	-93.3
122	1.31	0.210	0.126	-6.3	86.9	-93.2
123	1.31	0.212	0.126	-6.4	86.7	-93.0
124	1.31	0.214	0.125	-6.4	86.5	-92.9
125	1.31	0.216	0.125	-6.5	86.3	-92.8
126	1.31	0.218	0.125	-6.5	86.1	-92.6
127	1.32	0.220	0.125	-6.5	86.0	-92.5
128	1.32	0.221	0.125	-6.6	85.8	-92.4
129	1.32	0.223	0.124	-6.6	85.6	-92.2
130	1.32	0.225	0.124	-6.7	85.4	-92.1
131	1.32	0.227	0.124	-6.7	85.3	-92.0
132	1.32	0.229	0.124	-6.7	85.1	-91.8
133	1.33	0.231	0.123	-6.8	84.9	-91.7
134	1.33	0.232	0.123	-6.8	84.7	-91.5
135	1.33	0.234	0.123	-6.8	84.6	-91.4
136	1.33	0.236	0.122	-6.8	84.4	-91.2

Twisted around z-axis by (°)	f	a	b	α (°)	β (°)	α – β (°)
137	1.33	0.237	0.122	-6.9	84.2	-91.1
138	1.33	0.239	0.122	-6.9	84.1	-90.9
139	1.34	0.241	0.121	-6.9	83.9	-90.8
140	1.34	0.242	0.121	-6.9	83.7	-90.6
141	1.34	0.244	0.120	-6.9	83.6	-90.5
142	1.34	0.245	0.120	-6.9	83.4	-90.3
143	1.34	0.246	0.119	-7.0	83.2	-90.2
144	1.34	0.248	0.119	-7.0	83.1	-90.0
145	1.34	0.249	0.119	-7.0	82.9	-89.9
146	1.35	0.250	0.118	-7.0	82.8	-89.7
147	1.35	0.251	0.118	-7.0	82.6	-89.6
148	1.35	0.252	0.117	-7.0	82.5	-89.4
149	1.35	0.253	0.117	-6.9	82.3	-89.3
150	1.35	0.254	0.116	-6.9	82.2	-89.1
151	1.35	0.255	0.116	-6.9	82.1	-89.0
152	1.35	0.256	0.115	-6.9	81.9	-88.8
153	1.35	0.257	0.115	-6.9	81.8	-88.7
154	1.35	0.257	0.114	-6.9	81.7	-88.5
155	1.35	0.258	0.114	-6.8	81.5	-88.4
156	1.35	0.258	0.113	-6.8	81.4	-88.2
157	1.35	0.259	0.113	-6.8	81.3	-88.1
158	1.35	0.259	0.112	-6.7	81.2	-87.9
159	1.35	0.260	0.111	-6.7	81.1	-87.8
160	1.35	0.260	0.111	-6.7	80.9	-87.6
161	1.35	0.260	0.110	-6.6	80.8	-87.5
162	1.35	0.260	0.110	-6.6	80.7	-87.3
163	1.35	0.260	0.109	-6.5	80.6	-87.2
164	1.35	0.260	0.109	-6.5	80.5	-87.0
165	1.35	0.260	0.108	-6.4	80.4	-86.9
166	1.35	0.260	0.108	-6.4	80.3	-86.7
167	1.35	0.260	0.107	-6.3	80.2	-86.6
168	1.35	0.260	0.107	-6.3	80.2	-86.4
169	1.35	0.259	0.107	-6.2	80.1	-86.3
170	1.35	0.259	0.106	-6.1	80.0	-86.1
171	1.35	0.258	0.106	-6.1	79.9	-86.0
172	1.35	0.258	0.105	-6.0	79.9	-85.9
173	1.35	0.257	0.105	-5.9	79.8	-85.7
174	1.35	0.257	0.104	-5.9	79.7	-85.6
175	1.35	0.256	0.104	-5.8	79.7	-85.5
176	1.35	0.255	0.104	-5.7	79.6	-85.3
177	1.35	0.254	0.103	-5.6	79.6	-85.2
178	1.35	0.253	0.103	-5.6	79.5	-85.1
179	1.34	0.252	0.102	-5.5	79.5	-84.9
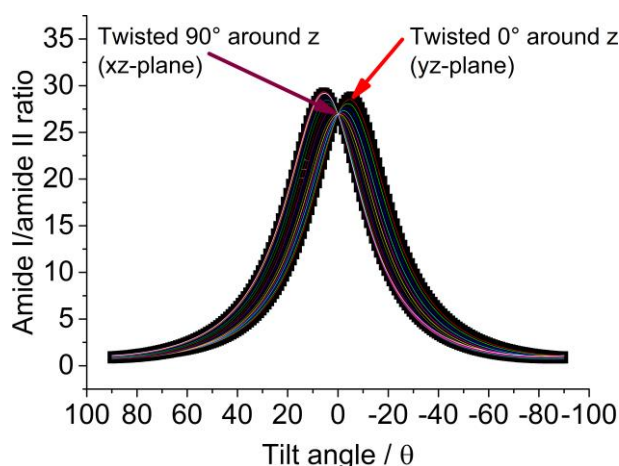
Figure A15 Amide I/amide II ratios (black squares) calculated different reorientations and twisting of ALM α-helix/α-helix structure, i.e. upon twisting ALM around its own axis before reorientation is performed. The colored lines represent the fit using equation 6.12. Table A4 summarizes the results of the fit. Reprinted with permission from Forbrig, E.; Staffa, JK.; Salewski, J.; Mroginski MA.; Hildebrandt, P.; Kozuch, J. Monitoring the Orientational Changes of Alamethicin during Incorporation into Bilayer Lipid Membranes *Langmuir* 2018 *34* (6), pp 2373-2385. Copyright (2018) American Chemical Society.[206]

Table A6 Results of fitting equation 6.12 to the curves depicted in Figure A8. The entries "yz-plane" and "xz-plane" indicate when the fit was performed to a reorientation within these planes.

Twisted around z-axis by (°)	*f*	*a*	*b*	*α (°)*	*β (°)*	*α − β (°)*
(yz-plane)						
0	1.20	0.334	0.107	7.7	94.9	-87.2
1	1.20	0.334	0.107	7.6	94.9	-87.3
2	1.20	0.334	0.107	7.5	94.9	-87.4
3	1.20	0.333	0.107	7.3	94.8	-87.5
4	1.20	0.333	0.107	7.2	94.8	-87.6
5	1.20	0.332	0.108	7.0	94.7	-87.7
6	1.20	0.331	0.108	6.9	94.7	-87.8
7	1.20	0.331	0.108	6.8	94.6	-87.9
8	1.20	0.330	0.108	6.6	94.6	-88.0
9	1.20	0.329	0.108	6.5	94.5	-88.1
10	1.19	0.328	0.108	6.3	94.5	-88.2
11	1.19	0.327	0.108	6.1	94.4	-88.3
12	1.19	0.326	0.108	6.0	94.4	-88.4
13	1.19	0.325	0.108	5.8	94.3	-88.5
14	1.19	0.324	0.108	5.7	94.2	-88.6
15	1.19	0.323	0.108	5.5	94.2	-88.7
16	1.19	0.322	0.108	5.3	94.1	-88.8
17	1.19	0.321	0.108	5.2	94.1	-88.9
18	1.18	0.320	0.108	5.0	94.0	-89.0
19	1.18	0.318	0.108	4.8	93.9	-89.1
20	1.18	0.317	0.108	4.7	93.9	-89.2
21	1.18	0.315	0.108	4.5	93.8	-89.3
22	1.18	0.314	0.108	4.3	93.7	-89.4
23	1.18	0.313	0.108	4.2	93.7	-89.5
24	1.17	0.311	0.108	4.0	93.6	-89.6
25	1.17	0.309	0.108	3.8	93.5	-89.7

Twisted around z-axis by (°)	f	a	b	α (°)	β (°)	α − β (°)
26	1.17	0.308	0.108	3.6	93.4	-89.8
27	1.17	0.306	0.108	3.5	93.4	-89.9
28	1.17	0.305	0.108	3.3	93.3	-90.0
29	1.16	0.303	0.108	3.1	93.2	-90.1
30	1.16	0.301	0.108	2.9	93.1	-90.2
31	1.16	0.300	0.108	2.8	93.1	-90.3
32	1.16	0.298	0.108	2.6	93.0	-90.4
33	1.16	0.296	0.108	2.4	92.9	-90.5
34	1.15	0.294	0.108	2.2	92.8	-90.6
35	1.15	0.293	0.108	2.1	92.7	-90.7
36	1.15	0.291	0.108	1.9	92.6	-90.8
37	1.15	0.289	0.108	1.7	92.6	-90.9
38	1.15	0.287	0.108	1.5	92.5	-90.9
39	1.15	0.285	0.108	1.4	92.4	-91.0
40	1.14	0.284	0.108	1.2	92.3	-91.1
41	1.14	0.282	0.108	1.0	92.2	-91.2
42	1.14	0.280	0.108	0.8	92.1	-91.3
43	1.14	0.278	0.108	0.7	92.1	-91.4
44	1.14	0.277	0.108	0.5	92.0	-91.5
45	1.13	0.275	0.108	0.3	91.9	-91.6
46	1.13	0.273	0.107	0.2	91.8	-91.6
47	1.13	0.271	0.107	0.0	91.7	-91.7
48	1.13	0.270	0.107	-0.2	91.6	-91.8
49	1.13	0.268	0.107	-0.3	91.5	-91.9
50	1.12	0.266	0.107	-0.5	91.5	-92.0
51	1.12	0.265	0.107	-0.7	91.4	-92.0
52	1.12	0.263	0.107	-0.8	91.3	-92.1
53	1.12	0.261	0.107	-1.0	91.2	-92.2
54	1.12	0.260	0.107	-1.2	91.1	-92.3
55	1.12	0.258	0.107	-1.3	91.0	-92.3
56	1.12	0.257	0.106	-1.5	90.9	-92.4
57	1.11	0.255	0.106	-1.6	90.8	-92.5
58	1.11	0.254	0.106	-1.8	90.8	-92.6
59	1.11	0.253	0.106	-2.0	90.7	-92.6
60	1.11	0.251	0.106	-2.1	90.6	-92.7
61	1.11	0.250	0.106	-2.3	90.5	-92.8
62	1.11	0.249	0.106	-2.4	90.4	-92.8
63	1.11	0.248	0.106	-2.6	90.3	-92.9
64	1.10	0.246	0.105	-2.7	90.2	-93.0
65	1.10	0.245	0.105	-2.9	90.2	-93.0
66	1.10	0.244	0.105	-3.0	90.1	-93.1
67	1.10	0.243	0.105	-3.2	90.0	-93.2
68	1.10	0.242	0.105	-3.3	89.9	-93.2
69	1.10	0.241	0.105	-3.5	89.8	-93.3
70	1.10	0.241	0.105	-3.6	89.7	-93.3
71	1.10	0.240	0.105	-3.8	89.6	-93.4
72	1.10	0.239	0.105	-3.9	89.6	-93.5
73	1.10	0.239	0.104	-4.1	89.5	-93.5

Twisted around z-axis by (°)	f	a	b	α (°)	β (°)	α – β (°)
74	1.10	0.238	0.104	-4.2	89.4	-93.6
75	1.10	0.237	0.104	-4.3	89.3	-93.6
76	1.09	0.237	0.104	-4.5	89.2	-93.7
77	1.09	0.237	0.104	-4.6	89.1	-93.7
78	1.09	0.236	0.104	-4.7	89.1	-93.8
79	1.09	0.236	0.104	-4.9	89.0	-93.8
80	1.09	0.236	0.104	-5.0	88.9	-93.9
81	1.09	0.236	0.104	-5.1	88.8	-93.9
82	1.09	0.235	0.103	-5.3	88.7	-94.0
83	1.09	0.235	0.103	-5.4	88.6	-94.0
84	1.09	0.235	0.103	-5.5	88.6	-94.1
85	1.09	0.236	0.103	-5.7	88.5	-94.1
86	1.09	0.236	0.103	-5.8	88.4	-94.2
87	1.09	0.236	0.103	-5.9	88.3	-94.2
88	1.09	0.236	0.103	-6.0	88.2	-94.3
89	1.09	0.237	0.103	-6.2	88.2	-94.3
(xz-plane) 90	1.09	0.237	0.103	-6.3	88.1	-94.4
91	1.09	0.237	0.103	-6.4	88.0	-94.4
92	1.10	0.238	0.103	-6.5	87.9	-94.5
93	1.10	0.238	0.103	-6.6	87.9	-94.5
94	1.10	0.239	0.102	-6.8	87.8	-94.5
95	1.10	0.240	0.102	-6.9	87.7	-94.6
96	1.10	0.241	0.102	-7.0	87.6	-94.6
97	1.10	0.241	0.102	-7.1	87.6	-94.6
98	1.10	0.242	0.102	-7.2	87.5	-94.7
99	1.10	0.243	0.102	-7.3	87.4	-94.7
100	1.10	0.244	0.102	-7.4	87.3	-94.8
101	1.10	0.245	0.102	-7.5	87.3	-94.8
102	1.10	0.246	0.102	-7.6	87.2	-94.8
103	1.10	0.247	0.102	-7.7	87.1	-94.9
104	1.11	0.248	0.102	-7.8	87.0	-94.9
105	1.11	0.249	0.102	-7.9	87.0	-94.9
106	1.11	0.251	0.102	-8.0	86.9	-94.9
107	1.11	0.252	0.102	-8.1	86.8	-95.0
108	1.11	0.253	0.102	-8.2	86.8	-95.0
109	1.11	0.254	0.102	-8.3	86.7	-95.0
110	1.11	0.256	0.102	-8.4	86.6	-95.1
111	1.12	0.257	0.102	-8.5	86.6	-95.1
112	1.12	0.259	0.102	-8.6	86.5	-95.1
113	1.12	0.260	0.102	-8.7	86.4	-95.1
114	1.12	0.262	0.102	-8.8	86.4	-95.1
115	1.12	0.263	0.102	-8.8	86.3	-95.2
116	1.12	0.265	0.102	-8.9	86.3	-95.2
117	1.12	0.266	0.102	-9.0	86.2	-95.2
118	1.13	0.268	0.102	-9.1	86.1	-95.2
119	1.13	0.269	0.102	-9.1	86.1	-95.2
120	1.13	0.271	0.102	-9.2	86.0	-95.2

Twisted around z-axis by (°)	f	a	b	α (°)	β (°)	α – β (°)
121	1.13	0.273	0.102	-9.3	86.0	-95.2
122	1.13	0.274	0.102	-9.4	85.9	-95.3
123	1.14	0.276	0.102	-9.4	85.8	-95.3
124	1.14	0.278	0.102	-9.5	85.8	-95.3
125	1.14	0.279	0.102	-9.5	85.7	-95.3
126	1.14	0.281	0.102	-9.6	85.7	-95.3
127	1.14	0.283	0.102	-9.6	85.6	-95.3
128	1.15	0.284	0.102	-9.7	85.6	-95.3
129	1.15	0.286	0.102	-9.7	85.5	-95.3
130	1.15	0.288	0.102	-9.8	85.5	-95.3
131	1.15	0.290	0.102	-9.8	85.4	-95.3
132	1.15	0.291	0.102	-9.9	85.4	-95.3
133	1.16	0.293	0.102	-9.9	85.4	-95.3
134	1.16	0.295	0.102	-9.9	85.3	-95.3
135	1.16	0.296	0.102	-10.0	85.3	-95.2
136	1.16	0.298	0.103	-10.0	85.2	-95.2
137	1.16	0.299	0.103	-10.0	85.2	-95.2
138	1.16	0.301	0.103	-10.1	85.2	-95.2
139	1.17	0.303	0.103	-10.1	85.1	-95.2
140	1.17	0.304	0.103	-10.1	85.1	-95.2
141	1.17	0.306	0.103	-10.1	85.0	-95.1
142	1.17	0.307	0.103	-10.1	85.0	-95.1
143	1.17	0.309	0.103	-10.1	85.0	-95.1
144	1.18	0.310	0.103	-10.1	85.0	-95.1
145	1.18	0.312	0.103	-10.1	84.9	-95.0
146	1.18	0.313	0.103	-10.1	84.9	-95.0
147	1.18	0.315	0.103	-10.1	84.9	-95.0
148	1.18	0.316	0.104	-10.1	84.9	-94.9
149	1.18	0.317	0.104	-10.1	84.8	-94.9
150	1.19	0.319	0.104	-10.1	84.8	-94.9
151	1.19	0.320	0.104	-10.0	84.8	-94.8
152	1.19	0.321	0.104	-10.0	84.8	-94.8
153	1.19	0.322	0.104	-10.0	84.8	-94.7
154	1.19	0.323	0.104	-9.9	84.7	-94.7
155	1.19	0.324	0.104	-9.9	84.7	-94.6
156	1.19	0.325	0.104	-9.9	84.7	-94.6
157	1.19	0.326	0.105	-9.8	84.7	-94.5
158	1.20	0.327	0.105	-9.8	84.7	-94.5
159	1.20	0.328	0.105	-9.7	84.7	-94.4
160	1.20	0.329	0.105	-9.6	84.7	-94.4
161	1.20	0.330	0.105	-9.6	84.7	-94.3
162	1.20	0.331	0.105	-9.5	84.7	-94.2
163	1.20	0.331	0.105	-9.5	84.7	-94.2
164	1.20	0.332	0.105	-9.4	84.7	-94.1
165	1.20	0.333	0.105	-9.3	84.7	-94.0
166	1.20	0.333	0.106	-9.2	84.7	-94.0
167	1.20	0.334	0.106	-9.1	84.7	-93.9
168	1.20	0.334	0.106	-9.0	84.8	-93.8

| Twisted around z-axis by (°)	f	a	b	α (°)	β (°)	α – β (°)
169	1.20	0.334	0.106	-9.0	84.8	-93.7
170	1.20	0.335	0.106	-8.9	84.8	-93.7
171	1.20	0.335	0.106	-8.8	84.8	-93.6
172	1.20	0.335	0.106	-8.7	84.8	-93.5
173	1.20	0.335	0.106	-8.6	84.9	-93.4
174	1.20	0.335	0.106	-8.4	84.9	-93.3
175	1.20	0.335	0.107	-8.3	84.9	-93.2
176	1.20	0.335	0.107	-8.2	84.9	-93.2
177	1.20	0.335	0.107	-8.1	85.0	-93.1
178	1.20	0.335	0.107	-8.0	85.0	-93.0
179	1.20	0.335	0.107	-7.9	85.0	-92.9

8.2 Complex I activity incorporated in a supported lipid membrane system by (de-)protonation of 4-aminothiophenol

8.2.1 Electrochemical control experiments

SEIRA spectroscopic control experiments were performed by adding NADH onto the SLM system in absence of both, CpI and DMN, the SLM including DMN but no CpI and the pure 4-ATP-SAM, whereby no spectral changes were observed (Figure A16). Therefore, NADH does neither interact with the SAM, nor with the SLM.

To investigate the electrical properties of the SLM impedance spectroscopy has been performed of the 4-ATP SAM before and after addition of vesicles (Figure 6.3). The frequency-weighted Cole-Cole plot does not exhibit changes between the two steps. In both cases a capacitance of 8.1 μF/cm^2 can be determined from the half-circles (see previous studies),[8,34,49,323] which relates to the capacitance of the 4-ATP SAM and is in line with the data reported in literature.[324] This can be explained based on intact vesicles adsorbed to the surface (as deduced from the SEIRA data described in the main text), which represents a negligibly small electrochemical resistance so that the SLM capacitance does not exert any influence. Furthermore, due to this small resistance, molecules such as NADH can diffuse towards the SAM surface.
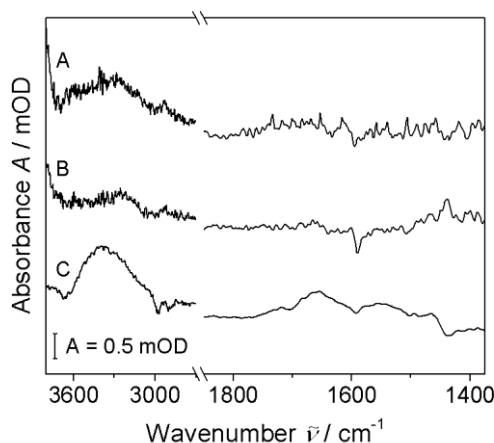
Figure A16 A: Difference spectrum after addition of 0.2 μg/mL NADH solution in PBS 0.1 M, pH 7 using the bare SLM system without DMN and CpI in PBS 0.1 M, pH 7 as reference. B: Difference spectrum after addition of 0.2 μg/mL NADH solution in PBS 0.1 M, pH 7 using the SLM system with DMN but without CpI in PBS 0.1 M, pH 7 as reference. C: Difference spectrum after the addition of 0.2 μg/mL NADH solution in PBS 0.1 M, pH 7 with 4-ATP SAM solution in PBS 0.1 M, pH 7 as reference. Reprinted with permission from Gutiérrez-Sanz, O.; Forbrig, E.; Batista AP.; Pereira MM.; Salewski, J.; Mroginski MA.; Götz, R.; De Lacey, AL.; Kozuch, J.; Zebger, I. Catalytic Activity and Proton Translocation of Reconstituted Respiratory Complex I monitored by Surface-enhanced Infrared Absorption Spectroscopy. *Langmuir* 2018 *34* (20), pp 5703-5711. Copyright (2018) American Chemical Society.[328]

8.2.2 pH-Titration of the 4-ATP-SAM

Since all functional spectroscopic experiments with CpI were conducted with a PBS solution at pH 7, a pH titration of the 4-ATP SAM was performed in the SEIRA difference mode choosing the corresponding spectrum recorded at pH 7 as the reference (Figure 6.25). In the range from pH 9 to pH 5, two prominent difference bands can be observed at 1591 cm^{-1} and 1487 cm^{-1} with increasing and decreasing intensity, respectively. These specific signatures can be assigned to the protonation of the 4-ATP SAM, as displayed in Figure 6.25. Thereby, the corresponding intensities of the 1591 cm^{-1} band follow a broadened sigmoidal shape with a respective pK$_a$ value of 6.4 ± 0.1 as displayed in Figure A17, found in a similar range as determined by capacitance measurements (6.9 ± 0.5).[320] At more acidic pH values of (pH < 5), the difference spectrum is further modified and now displays a negative band at 1596 cm^{-1} together with a positive band at 1484 cm^{-1}, which can be potentially related to the difference spectrum of the (almost) fully protonated 4-ATP-H$^+$ species vs. 4-ATP (see next section for the DFT based calculation of IR spectra). The corresponding spectroscopic band pattern in the pH range of 5 - 9, however, can be ascribed to the decrease in transition dipole moment coupling between the 4-ATP SAM molecules upon protonation.
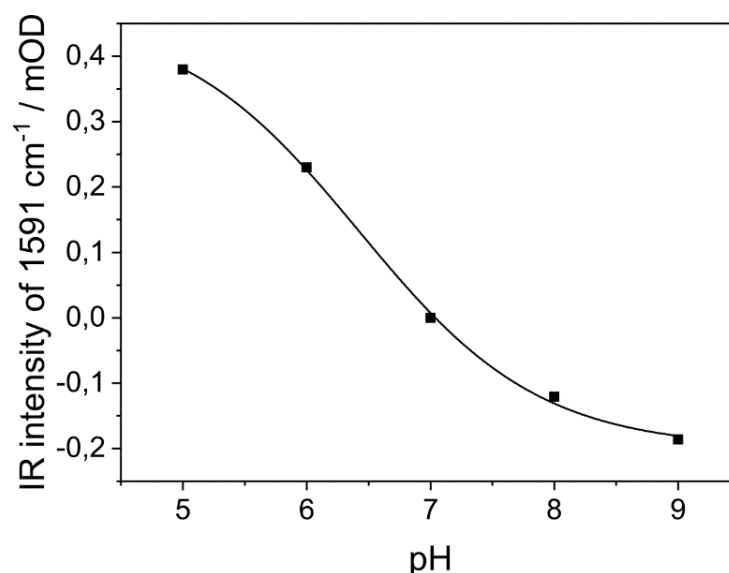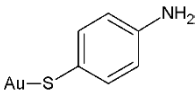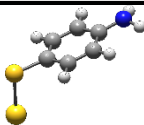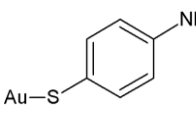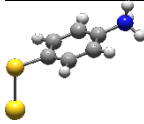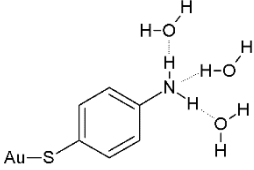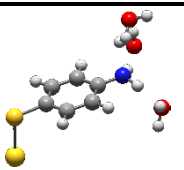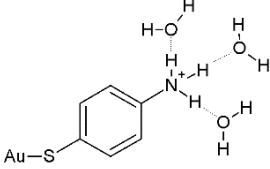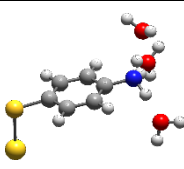
Figure A17 Shown is the pH-dependent SEIRA intensity of the 1591 cm^{-1} band in the related difference spectra choosing those at pH 7 as reference. A broadened sigmoidal function can be fitted to the data, thereby revealing a pK$_a$ value of 6.4 ± 0.1 for the 4-ATP SAM. Adapted with permission from Gutiérrez-Sanz, O.; Forbrig, E.; Batista AP.; Pereira MM.; Salewski, J.; Mroginski MA.; Götz, R.; De Lacey, AL.; Kozuch, J.; Zebger, I. Catalytic Activity and Proton Translocation of Reconstituted Respiratory Complex I monitored by Surface-enhanced Infrared Absorption Spectroscopy. *Langmuir* 2018 *34* (20), pp 5703-5711. Copyright (2018) American Chemical Society.[328]

8.2.3 DFT IR spectra of 4-ATP

Geometry optimization using periodic boundary conditions (PBC) was performed by specifying two translation vectors that span the plane parallel to the supporting surface. As expected, imaginary frequencies (between 0 and -100 cm^{-1}) resulted from the normal mode analysis based on this procedure, which were identified as torsional movements of whole 4-ATP molecules.

Table A7 Overview of calculated structures of 4-ATP and its protonated species 4-ATP-H$^+$ with and without H-bonds to explicit water molecules. Reprinted with permission from Gutiérrez-Sanz, O.; Forbrig, E.; Batista AP.; Pereira MM.; Salewski, J.; Mroginski MA.; Götz, R.; De Lacey, AL.; Kozuch, J.; Zebger, I. Catalytic Activity and Proton Translocation of Reconstituted Respiratory Complex I monitored by Surface-enhanced Infrared Absorption Spectroscopy. *Langmuir* 2018 *34* (20), pp 5703-5711. Copyright (2018) American Chemical Society.[328]

Abbreviation	Molecular structure	Optimized geometry
4-ATP		
4-ATP-H$^+$		
4-ATP·3H$_2$0		
4-ATP-H$^+$·3H$_2$0		

This, however, is comprehensible and unavoidable because normal mode analysis cannot be performed together with PBC. Furthermore, the low value (> -100 cm^{-1}) of these frequencies shows that the frequency region of our interest (1400–1800 cm^{-1}) can be reliably evaluated. Assignment of the calculated normal modes was obtained by evaluating the respective potential energy distributions.[270,271] 4-ATP and its protonated form 4-ATP-H$^+$ were optimized as isolated molecules and in the presence of three explicit water molecules to form H-bonds with the amino or ammonium group, respectively (Table A7).
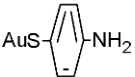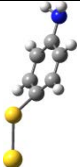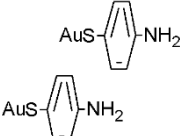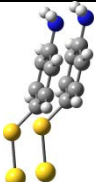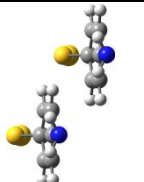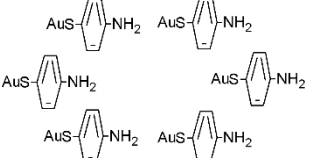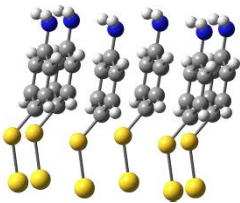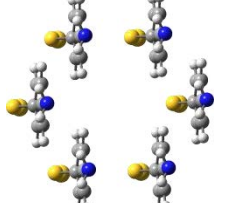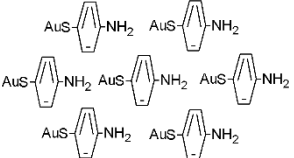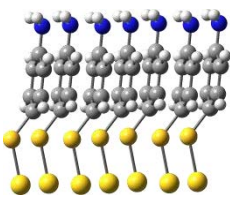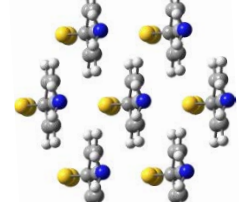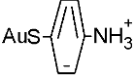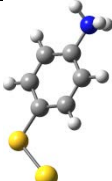
To account for transition dipole moment coupling (TDC) of normal modes within the formed SAM, a 4-ATP SAM fragment was calculated using PBC. However, using an Au(111) surface or other metals as supporting material was not feasible in the DFT-PBC calculation and led to problems for the total charge of the system. Therefore, a graphane sheet (planar sp^3 lattice of (CH)$_n$ in chair configuration) was used instead. This appeared to be a good alternative, since calculation times remained low. Moreover, positioning of 4-ATP molecules in a √3x√3 R30 SAM arrangement by replacing up-facing graphane hydrogens by 4-ATP resulted in a distance of 4.57 Å between the SAM molecules. In comparison, on Au(111) this distance is 4.98 Å. The DFT-PBC calculation was performed in the following way (various calculated structures are depicted in Table A8):

1. A C_6H_6 fragment was optimized using PBC (see Figure A18).
2. A hydrogen was replaced by the 4-ATP molecule (using its sulphur) and the coordinates of the remaining C_6H_5 fragment were fixed, so that only 4-ATP was optimized using PBC.
3. The C_6H_5 fragment was replaced by an Au atom and only the Au-S bond distance was optimized in a conventional calculation. In this way, the PBC-optimized structure of 4-ATP was maintained (the PBC-optimized 4-ATP structure will be referred in the following as 4-ATP').
4. 4-ATP' molecules were arranged based on the translation vectors of the PBC geometry optimization and a normal mode analysis was performed to visualize the effect of TDC on the resulting IR spectra.
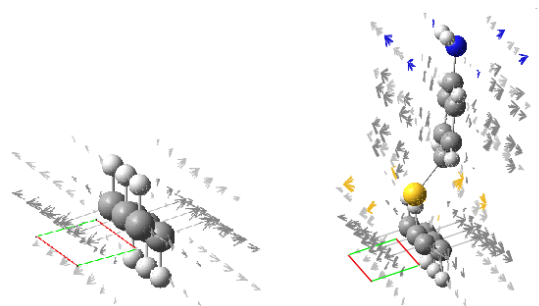
Figure A18 Optimized structure of a graphane sheet (left) and of 4-ATP bound to graphane (right). Reprinted with permission from Gutierrez-Sanz, O.; Forbrig, E.; Batista AP.; Pereira MM.; Salewski, J.; Mroginski MA.; Götz, R.; De Lacey, AL.; Kozuch, J.; Zebger, I. Catalytic Activity and Proton Translocation of Reconstituted Respiratory Complex I monitored by Surface-enhanced Infrared Absorption Spectroscopy. *Langmuir* 2018 *34* (20), pp 5703-5711. Copyright (2018) American Chemical Society.[328]

Table A8 Overview of various calculated structures of 4-ATP and its protonated species 4-ATP-H$^+$ using periodic boundary conditions (PBC). In structure (4-ATP'+H$^+$)$_1$, the central 4-ATP molecule of (4-ATP')$_7$ was protonated and a geometry optimization was performed under maintenance of the structure from the outer six 4-ATP molecules. The aromatic ring in the molecular structure is "distorted" due to a "from top view" to ease the representation of the arrangement of the molecules. Reprinted with permission from Gutiérrez-Sanz, O.; Forbrig, E.; Batista AP.; Pereira MM.; Salewski, J.; Mroginski MA.; Götz, R.; De Lacey, AL.; Kozuch, J.; Zebger, I. Catalytic Activity and Proton Translocation of Reconstituted Respiratory Complex I monitored by Surface-enhanced Infrared Absorption Spectroscopy. *Langmuir* 2018 *34* (20), pp 5703-5711. Copyright (2018) American Chemical Society.[328]

Abbreviation	Molecular structure	Optimized geometry (side view)	Optimized geometry (top view)
(4-ATP')$_1$			
(4-ATP')$_2$			
(4-ATP')$_6$			
(4-ATP')$_7$			
(4-ATP'+H$^+$)$_1$			

Since the DFT IR difference spectra are calculated as protonated vs. deprotonated species, they are compared to SEIRA difference spectra of the pH titration using the spectrum at pH 9 as reference, i.e. the condition where full deprotonation can be assumed (Figure A19).
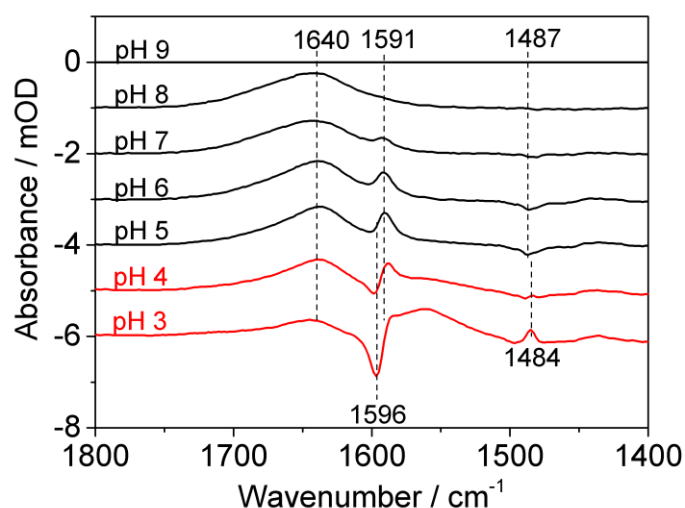
Figure A19 SEIRA spectroscopic pH-titration of the 4-ATP SAM in the range of pH 3 to pH 9 with the spectrum of pH 9 as reference spectrum. Reprinted with permission from Gutiérrez-Sanz, O.; Forbrig, E.; Batista AP.; Pereira MM.; Salewski, J.; Mroginski MA.; Götz, R.; De Lacey, AL.; Kozuch, J.; Zebger, I. Catalytic Activity and Proton Translocation of Reconstituted Respiratory Complex I monitored by Surface-enhanced Infrared Absorption Spectroscopy. *Langmuir* 2018 *34* (20), pp 5703-5711. Copyright (2018) American Chemical Society.[328]

8.2.4 Assignment of SEIRA bands of 4-ATP

Figure A20A shows the SEIRA spectrum of the ATP 4-SAM using the spectrum of ethanol on the bare gold electrode as reference. Three pronounced bands of the 4-ATP SAM are detected at 1630, 1593, and 1488 cm^{-1}. Based on the normal mode analysis these bands can be assigned to a mixture of the deprotonated and protonated species of 4-ATP, since ethanol, as a protic solvent, can also provide protons, see Figure A20B and Figure A20C. The band at 1630 cm^{-1} can be ascribed to $\delta(NH_2)$ and $\delta_{as}(NH_3)$ of both species. Its broad shape can be related to H-bonding
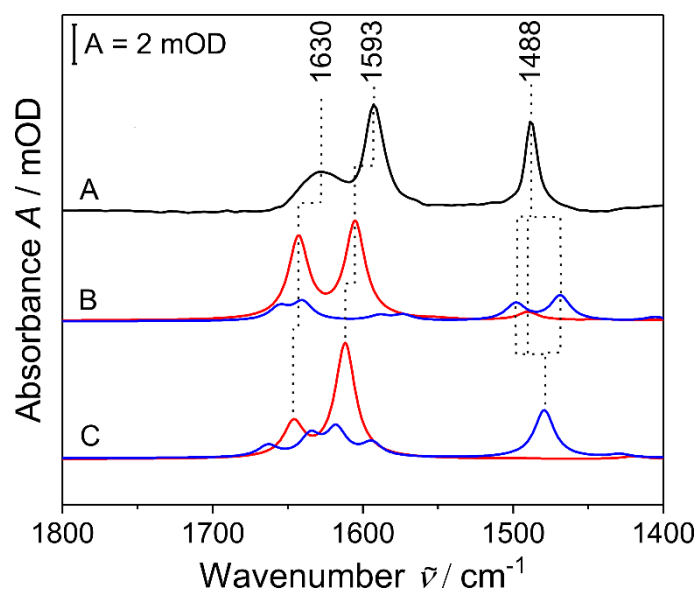
Figure A20 Comparison of SEIRA difference spectrum of 4-ATP SAM with DFT calculated IR spectra. (A): 4-ATP SAM in ethanol recorded using pure the Au surface ethanol as reference; (B): DFT-IR spectra of the corresponding 4-ATP (blue) and 4-ATP+H$^+$ (red, Table A7); C: DFT-IR spectra of (4-ATP')$_1$ and (4-ATP'+H$^+$)$_1$ using PBC optimization (blue and red, respectively; Table A8). Reprinted with permission from Gutiérrez-Sanz, O.; Forbrig, E.; Batista AP.; Pereira MM.; Salewski, J.; Mroginski MA.; Götz, R.; De Lacey, AL.; Kozuch, J.; Zebger, I. Catalytic Activity and Proton Translocation of Reconstituted Respiratory Complex I monitored by Surface-enhanced Infrared Absorption Spectroscopy. *Langmuir* 2018 *34* (20), pp 5703-5711. Copyright (2018) American Chemical Society.[328]

effects (Table A9). The most prominent band at 1593 cm^{-1} is assigned to a combined δ(NH$_2$)+ν(CC) vibrational mode of the deprotonated 4-ATP. The absorption at 1488 cm^{-1} results from a potential overlap of both species, where the major contribution is based on a combination of δ_s(NH$_3$) and/or δ(CH) of the protonated molecule. The deprotonated species displays hardly a δ(NH$_2$)+ν(CN) absorption in this region.

Table A9 Assignment of SEIRA bands in the 4-ATP SAM spectrum based on the DFT calculation of unconstraint 4-ATP and its protonated species as well as based on the calculation using periodic boundary conditions (n.d. = not detected). Percentage of the contributions of vibrations to each normal mode are obtained from analyzing the potential energy distribution. Reprinted with permission from Gutiérrez-Sanz, O.; Forbrig, E.; Batista AP.; Pereira MM.; Salewski, J.; Mroginski MA.; Götz, R.; De Lacey, AL.; Kozuch, J.; Zebger, I. Catalytic Activity and Proton Translocation of Reconstituted Respiratory Complex I monitored by Surface-enhanced Infrared Absorption Spectroscopy. *Langmuir* 2018 *34* (20), pp 5703-5711. Copyright (2018) American Chemical Society.[328]

ν_{SEIRA} 4-ATP SAM	ν_{DFT} 4-ATP	ν_{DFT} 4-ATP-H$^+$	Assignment	ν_{DFT} (4-ATP')$_1$	ν_{DFT} (4-ATP'-H$^+$)$_1$	Assignment
1630		1655.7	δ_{as}(NH$_3$) (90 %)		1663.2	δ_{as}(NH$_3$) (82 %) ν(CC) (7 %)
	1642.9		**δ(NH$_2$) (84 %)** **ν(CN) (7 %)**	**1646.1**		**δ(NH$_2$) (91 %)**
		1640.3	δ_{as}(NH$_3$) (99 %)		1634.9	δ_{as}(NH$_3$) (81 %)
					1617.8	ν(CC) (59 %) δ_{as}(NH$_3$) (14 %) δ(CH) (6 %)
1593	**1605.2**		**ν(CC) (57 %)** **δ(CH) (14 %)** **δ(NH$_2$) (10 %)** **δ(CC) (6 %)**	**1611.8**		**ν(CC) (61 %)** **δ(CH) (16 %)** **δ(CC) (8 %)** **δ(NH$_2$) (7 %)**
n.d.		1588.9	ν(CC) (69 %) δ_{as}(NH$_3$) (12 %)		1594.1	ν(CC) (62 %) δ(CH) (12 %) δ_{as}(NH$_3$) (10 %)
		1573.1	ν(CC) (61 %) δ(CH) (15 %) δ(CC) (6 %)			
1488		1498.2	δ_s(NH$_3$) (86 %)			
	1490.0		**δ(CH) (48 %)** **ν(CC) (30 %)** **ν(CN) (12 %)**	**1496.8**		**δ(CH) (51 %)** **ν(CC) (35 %)** **ν(CN) (5 %)**
		1468.2	δ(CH) (56 %) ν(CC) (29 %) δ_s(NH$_3$) (11 %)		1479.3	δ(CH) (55 %) δ_s(NH$_3$) (49 %) ν(CC) (15 %)

8.2.5 Acidic pH range (pH < 5)

Figure A21 shows the comparison of the experimentally derived "pH 3 vs. pH 9" SEIRA difference spectrum (spectrum A; taken from Figure A19) and three different DFT-calculated IR difference spectra of 4-ATP and its corresponding protonated species. These DFT-calculated IR difference spectra correspond to: (also see Table A7 and Table A8)

B) 4-ATP-H$^+$ vs. 4-ATP (unconstrained),

C) 4-ATP-H$^+ \cdot 3H_2O$ vs. 4-ATP$\cdot 3H_2O$ (unconstrained, explicitly added water molecules), and

D) (4-ATP'+H$^+$)$_1$ vs. (4-ATP')$_1$ (constrained, as calculated under PBC).

In addition, B', C' and D' display the corresponding absolute spectra for comparison and completeness.

All of these difference spectra show the same pattern of negative δ(NH)+ν(CC) bands of the 4-ATP molecule at ca. 1600 cm^{-1} and positive δ(NH$_3$)+δ(CH)+ν(CN) bands at ca. 1500 cm^{-1} assigned to the protonated 4-ATP+H$^+$. These bands correspond to the difference bands at 1596 and 1484 cm^{-1} in the experimentally derived "pH 3 vs. pH 9" SEIRA difference spectrum of the 4-ATP SAM. The δ(NH) vibration of 4-ATP centered at ca. 1640 cm^{-1} (DFT-IR spectra B and B') is not appreciable in the recorded SEIRA difference spectrum (spectrum A) due to H-bonds to water molecules and/or steric distortions of 4-ATP within the SAM. In the first case (DFT-IR spectrum C), this vibration is blue-shifted, split in coupled δ(NH)+δ(OH) vibrations, and decreased in its intensity, which can be detected as broadened band as in the SEIRA spectrum. In the latter case (DFT-IR spectrum D), the structural distortions decrease the intensity of δ(NH) vibration of 4-ATP. Also the split δ(NH$_3$)+δ(CH)+ν(CN) bands at ca. 1500 cm^{-1} in DFT-IR spectrum B are reduced to one band due to the H-bonds with water and distortions.
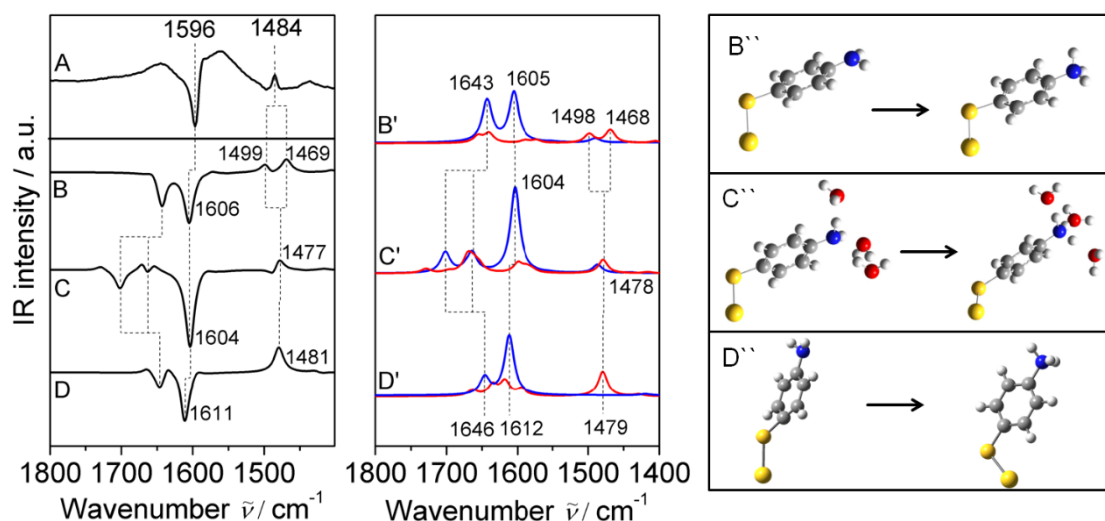
Figure A21 Left: Experimentally derived "pH 3 vs. pH 9" SEIRA difference spectrum of 4-ATP SAM (A) compared with DFT-IR difference spectra of 4-ATP and its protonated species obtained from different calculations (B – 4-ATP-H$^+$ vs. 4-ATP; C – 4-ATP-H$^+ \cdot 3H_2O$ vs. 4-ATP$\cdot 3H_2O$; D - (4-ATP'+H$^+$)$_1$ vs. (4-ATP')$_1$; see above). Middle('): absolute DFT-IR spectra related to the difference spectra in the left graph (4-ATP in blue; protonated species in red). Right(''): depiction of the corresponding DFT-calculated structures. Reprinted with permission from Gutiérrez-Sanz, O.; Forbrig, E.; Batista AP.; Pereira MM.; Salewski, J.; Mroginski MA.; Götz, R.; De Lacey, AL.; Kozuch, J.; Zebger, I. Catalytic Activity and Proton Translocation of Reconstituted Respiratory Complex I monitored by Surface-enhanced Infrared Absorption Spectroscopy. *Langmuir* 2018 *34* (20), pp 5703-5711. Copyright (2018) American Chemical Society.[328]

The recorded "pH 3 vs. pH 9" SEIRA difference spectrum of the pH-titration, see Figure A19, is thus in line with an (almost) fully protonated SAM. Therefore, below pH 5 pH-dependent SEIRA difference spectra are dominated by spectra of 4-ATP and its protonated species.

3.3 "Physiological" pH range (pH 9 - 5)

The SEIRA difference spectra in the physiological range of pH 9 to pH 5 show an inverted band pattern compared to very acidic conditions with slightly shifted bands: a positive difference band at 1591 cm^{-1} and a negative band at 1487 cm^{-1} (Figure A19; Figure A22A). Since the pK$_a$ value of ca. 6.5, obtained by analysis of this region is in line with experiments using other techniques,[320] the changes in the experimentally derived SEIRA difference spectra are in principle still related to the protonation of 4-ATP molecules, but dominated by concomitant effects. As shown by the following DFT-IR spectra, the prevailing effect is the annihilation of transition dipole moment coupling (TDC) in between the 4-ATP molecules upon protonation. Figure A22 demonstrates this effect by a comparison of the "pH 5 vs. pH 9" SEIRA difference with the following DFT-IR difference spectra:

B) 2·(4-ATP')$_1$ vs. (4-ATP')$_2$ (constrained, obtained from PBC-calculations) and

C) (4-ATP')$_6$ vs. (4-ATP')$_7$ (constrained, obtained from PBC-calculations).

Again B' and C' display the corresponding absolute spectra.

DFT-IR difference spectrum B displays the spectral changes when (4-ATP')$_2$ is calculated as a coupling "dimer" (blue spectrum B') or split into two non-coupling single molecules (4-ATP')$_1$ (red spectrum B'). Clearly, annihilating the TDC leads to a change in the relative intensities of the 4-ATP vibrations. In the present case the δ(NH$_2$) band at 1641.1 cm^{-1} is not affected, but the δ(NH$_2$)+ν(CC) absorption at 1611.8 cm^{-1} increases by ca. 30 % upon removal of the TDC leading to a positive difference band in spectrum B at ca. 1610 cm^{-1}. The intensity of the δ(NH$_2$)+ν(CN) band at 1496.8 cm^{-1}, although with very low absolute intensity (therefore shown multiplied by 20), is decreased by about 20 %, resulting in a weak negative difference band at 1494 cm^{-1} (difference spectrum B). This band pattern is in line with the experimentally observed behavior within the SEIRA spectra recorded in pH-dependence, see Figure 6.25 in chapter 6.4.3. Difference spectrum C emphasizes this effect even more and displays the impact of removing the central 4-ATP from an arrangement of seven stacking 4-ATP molecules. Normally the removal of one molecule would result in a decrease of all IR bands by a factor of ca. 14 %. However, in this case difference spectrum C shows a similar band pattern with a positive difference band at 1612 cm^{-1} (increase of 12 %) and a negative one at 1494 cm^{-1} (decrease of 30 %). Therefore, one can assume that, in the range between pH 9 and pH 5, SEIRA spectra are mainly perturbed by the loss of TDC upon protonation. This contribution in the "4-ATP-H$^+$ vs. 4-ATP" difference spectrum becomes more pronounced/stronger the more 4-ATP molecules are protonated, i.e. below pH 5. What has not been taken into account, yet, is the structural and orientational perturbation of 4-ATP molecules that encompass one protonated 4-ATP. Such a disturbance will emphasize the loss effect of TDC even more.
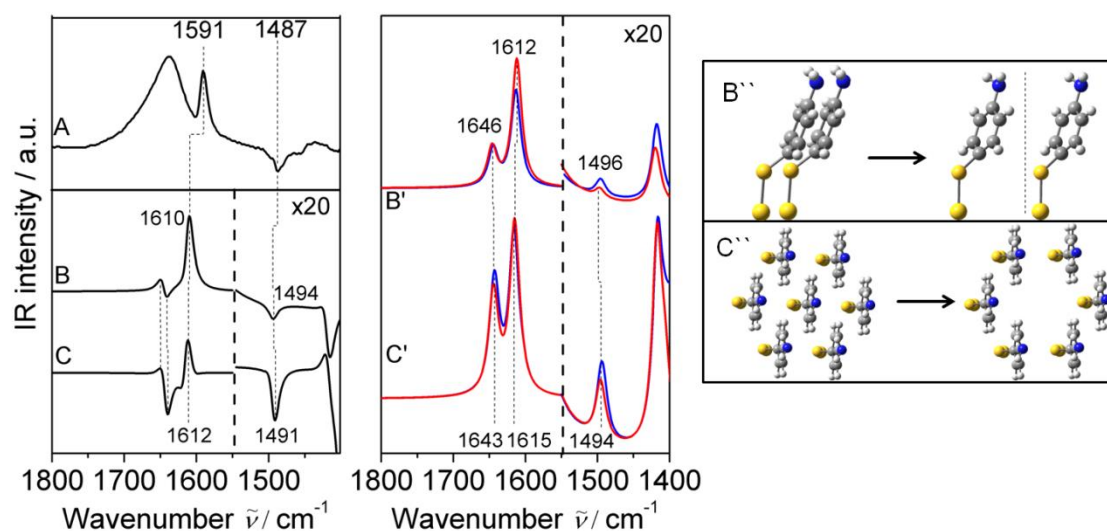
Figure A22 Left: Experimentally derived "pH 5 vs. pH 9" SEIRA difference spectrum of 4-ATP SAM (A) compared with DFT-calculated IR difference spectra of 4-ATP in different structural arrangements. Difference spectra B and C display the spectral changes related to a vibrational decoupling of two ATP' molecules and the corresponding spectral variations after removing the central 4-ATP' molecule from (4-ATP')$_7$, respectively. (B - 2·(4-ATP')$_1$ vs. (4-ATP')$_2$, C - (4-ATP')$_6$ vs. (4-ATP')$_7$; see above). Middle('): absolute DFT-IR spectra related to the difference spectra in the left graph (red vs. Blue, respectively). Right(''): depiction of the corresponding DFT-calculated structures. Reprinted with permission from Gutiérrez-Sanz, O.; Forbrig, E.; Batista AP.; Pereira MM.; Salewski, J.; Mroginski MA.; Götz, R.; De Lacey, AL.; Kozuch, J.; Zebger, I. Catalytic Activity and Proton Translocation of Reconstituted Respiratory Complex I monitored by Surface-enhanced Infrared Absorption Spectroscopy. *Langmuir* 2018 *34* (20), pp 5703-5711. Copyright (2018) American Chemical Society.[328]

REFERENCES

1.   Singh, S. B. & Barrett, J. F. Empirical antibacterial drug discovery—Foundation in natural products. *Biochem. Pharmacol.* **71,** 1006–1015 (2006).

2.   Singh, S. B., Young, K. & Silver, L. L. What is an 'ideal' antibiotic? Discovery challenges and path forward. *Biochem. Pharmacol.* **133,** 63–73 (2017).

3.   Hancock, R. E. W. & Sahl, H.-G. Antimicrobial and host-defense peptides as new anti-infective therapeutic strategies. *Nat. Biotechnol.* **24,** 1551–7 (2006).

4.   Yeaman, M. R. & Yount, N. Y. Mechanisms of Antimicrobial Peptide Action and Resistance. *Pharmacol. Rev.* **55,** 27–55 (2003).

5.   Simons, K. & Ikonen, E. Functional rafts in cell membranes. *Nature* **387,** 569–72 (1997).

6.   Nicolson, G. L. The Fluid-Mosaic Model of Membrane Structure: Still relevant to understanding the structure, function and dynamics of biological membranes after more than 40 years. *Biochim. Biophys. Acta - Biomembr.* **1838,** 1451–1466 (2014).

7.   Milenkovic, D., Blaza, J. N., Larsson, N. G. & Hirst, J. The Enigma of the Respiratory Chain Supercomplex. *Cell Metab.* **25,** 765–776 (2017).

8.   Wiebalck, S., Kozuch, J., Forbrig, E., Tzschucke C. C., Jeuken L. J. C., Hildebrandt P. Monitoring the Transmembrane Proton Gradient Generated by Cytochrome bo₃ in Tethered Bilayer Lipid Membranes Using SEIRA Spectroscopy. *J. Phys. Chem. B* **120,** 2249–2256 (2016).

9.   Kruber, O. On the 2, 3-dimethyl-naphthaline in pit coal tar. *Ber. Dtsch. Chem. Ges* **62,** 3044–3047 (1929).

10. Li, X., Li, Y., Han, H., Miller, D. W. & Wang, G. Solution Structures of Human LL-37 Fragments and NMR-Based Identification of a Minimal Membrane-Targeting Antimicrobial and Anticancer Region. *J. Am. Chem. Soc.* **128,** 5776–5785 (2006).

11. Wang, G. Structures of Human Host Defense Cathelicidin LL-37 and Its Smallest Antimicrobial Peptide KR-12 in Lipid Micelles. *J. Biol. Chem.* **283,** 32637–32643 (2008).

12. Dannehl, C., Gutsmann, T. & Brezesinski, G. Surface activity and structures of two fragments of the human antimicrobial LL-37. *Colloids Surf. B. Biointerfaces* **109,** 129–35 (2013).

13. Leitgeb, B., Szekeres, A., Manczinger, L., Vágvölgyi, C. & Kredics, L. The History of Alamethicin: A Review of the Most Extensively Studied Peptaibol. *Chem. Biodivers.* **4,** 1027–1051 (2007).

14. Pieta, P., Mirza, J. & Lipkowski, J. Direct visualization of the alamethicin pore formed in a planar phospholipid matrix. *Proc. Natl. Acad. Sci. USA* **109,** 21223–21227 (2012).

15. Herzberg, G. *Molecular spectra and molecular structure. Vol.2: Infrared and Raman spectra of polyatomic molecules*. (1945).

16. Siebert, F. & Hildebrandt, P. Vibrational spectroscopy in life science. *Colloid Polym. Sci.* **286,** 487–487 (2008).

17. Herbst, J., Heyne, K. & Diller, R. Femtosecond infrared spectroscopy of bacteriorhodopsin chromophore isomerization. *Science* **297,** 822–5 (2002).

18. Kukura, P., McCamant, D. W., Yoon, S., Wandschneider, D. B. & Mathies, R. A. Structural observation of the primary isomerization in vision with femtosecond-stimulated Raman. *Science* **310,** 1006–9 (2005).

19. Ataka, K. & Heberle, J. Electrochemically induced surface-enhanced infrared difference absorption (SEIDA) spectroscopy of a protein monolayer. *J. Am. Chem. Soc.* **125,** 4986–7 (2003).

20. Murgida, D. H. & Hildebrandt, P. Electron-Transfer Processes of Cytochrome c at Interfaces. New Insights by Surface-Enhanced Resonance Raman Spectroscopy. *Acc. Chem. Res.* **37,** 854–861 (2004).

21. Wilson, E. B., Decius, J. C., Cross, P. C. & Sundheim, B. R. Molecular Vibrations: The Theory of Infrared and Raman Vibrational Spectra. *J. Electrochem. Soc.* **102,** 235C (1955).

22. Goormaghtigh, E., Raussens, V. & Ruysschaert, J.-M. M. Attenuated total reflection infrared spectroscopy of proteins and lipids in biological membranes. *Biochim. Biophys. Acta - Rev. Biomembr.* **1422,** 105–85 (1999).

23. Kóta, Z., Páli, T. & Marsh, D. Orientation and Lipid-Peptide Interactions of Gramicidin A in Lipid Membranes: Polarized Attenuated Total Reflection Infrared Spectroscopy and Spin-Label Electron Spin Resonance. *Biophys. J.* **86,** 1521–1531 (2004).

24. Hartstein, A., Kirtley, J. R. & Tsang, J. C. Enhancement of the Infrared Absorption from Molecular Monolayers with Thin Metal Overlayers. *Phys. Rev. Lett.* **45,** 201–204 (1980).

25. Zaitseva, E., Saavedra, M., Banerjee, S., Sakmar, T. P. & Vogel, R. SEIRA spectroscopy on a membrane receptor monolayer using lipoprotein particles as carriers. *Biophys. J.* **99,** 2327–2335 (2010).

26. Osawa, M. Dynamic Processes in Electrochemical Reactions Studied by Surface-Enhanced Infrared Absorption Spectroscopy (SEIRAS). *Bull. Chem. Soc. Jpn.* **70,** 2861–2880 (1997).

27. Heidary, N., Utesch, T., Zerball M., Horch, M., Millo, D., Fritsch, J., Lenz, O., von Klitzing, R., Hildebrandt, P., Fischer, A., Mroginski, M. A., Zebger, I. Orientation-Controlled Electrocatalytic Efficiency of an Adsorbed Oxygen-Tolerant Hydrogenase. *PLoS One* **10** (11)**,** e0143101 (2015).

28. Ly, H. K., Sezer, M., Wisitruangsakul, N., Feng, J.-J., Kranich, A., Millo, D., Weidinger, I. M., Zebger, I., Murgida, D. H., Hildebrandt, P. Surface-enhanced vibrational spectroscopy for probing transient interactions of proteins with biomimetic interfaces: electric field effects on structure, dynamics and function of cytochrome c. *FEBS J.* **278,** 1382–90 (2011).

29. Kriegel, S., Uchida, T., Osawa, M., Friedrich, T., Hellwig, P. Biomimetic Environment to Study E. coli Complex I through Surface- Enhanced IR Absorption Spectroscopy. *Biochemistry* **53,** 6340–6347 (2014).

30. Jiang, X., Zaitseva, E., Schmidt, M., Siebert, F., Engelhard, M., Ataka, K., Vogel, R., Heberle, J. Resolving voltage-dependent structural changes of a membrane photoreceptor by surface-enhanced IR difference spectroscopy. *Proc. Natl. Acad. Sci.* **105,** 12113–12117 (2008).

31. Kielb, P. *et al.* Spectroscopic Observation of Calcium-Induced Reorientation of Cellobiose Dehydrogenase Immobilized on Electrodes and its Effect on Electrocatalytic Activity. *ChemPhysChem* **16,** 1960–1968 (2015).

32. Yamakata, A., Shimizu, H. & Oiki, S. Surface-enhanced IR absorption spectroscopy of the KcsA potassium channel upon application of an electric field. *Phys. Chem. Chem. Phys.* **17,** 21104–21111 (2015).

33. Jeuken, L. J. C. Electrodes for integral membrane enzymes. *Nat. Prod. Rep.* **26,** 1234 (2009).

34. Kozuch, J., Steinem, C., Hildebrandt, P. & Millo, D. Combined electrochemistry and surface-enhanced infrared absorption spectroscopy of gramicidin A incorporated into tethered bilayer lipid membranes. *Angew. Chem. Int. Ed. Engl.* **51,** 8114–8117 (2012).

35. Kozuch, J., Weichbrodt, C., Millo, D., Giller, K., Becker, S., Hildebrandt, P., Steinem, C. Voltage-dependent structural changes of the membrane-bound anion channel hVDAC1 probed by SEIRA and electrochemical impedance spectroscopy. *Phys. Chem. Chem. Phys.* **16,** 9546–9555 (2014).

36. Osawa, M. Surface-Enhanced Infrared Absorption. in *Topics Appl. Phys.* 163–187 (Springer Berlin Heidelberg, 2001).

37. Aroca, R. F., Ross, D. J. & Domingo, C. Surface-enhanced infrared spectroscopy. *Appl. Spectrosc.* **58,** 324A–338A (2004).

38. Osawa, M., Ataka, K.-I., Yoshii, K. & Nishikawa, Y. Surface-Enhanced Infrared Spectroscopy: The Origin of the Absorption Enhancement and Band Selection Rule in the Infrared Spectra of Molecules Adsorbed on Fine Metal Particles. *Appl. Spectrosc.* **47,** 1497–1502 (1993).

39. Suzuki, Y., Osawa, M., Hatta, A. & Suëtaka, W. Mechanism of absorption enhancement in infrared ATR spectra observed in the Kretschmann configuration. *Appl. Surf. Sci.* **33–34,** 875–881 (1988).

40. Osawa, M. Surface-enhanced Infrared Absorption Spectroscopy. in *Handbook of Vibrational Spectroscopy* 1–15 (2002).

41. Macdonald, J. R. & Barsoukov, E. *Impedance Spectroscopy: Theory, Experiment, and Applications*. (John Wiley & Sons, Inc., 2005).

42. Jahnke, H. G. *et al.* Direct chemosensitivity monitoring ex vivo on undissociated melanoma tumor tissue by impedance spectroscopy. *Cancer Res.* **74,** 6408–6418 (2014).

43. Poenick, S., Jahnke H.-G., Eichler, M., Frost, S., Lilie, H., Robitzki, A. A. Comparative label-free monitoring of immunotoxin efficacy in 2D and 3D mamma carcinoma in vitro models by impedance spectroscopy. *Biosens. Bioelectron.* **53,** 370–6 (2014).

44. Jahnke, H.-G., Braesigk, A., Mack, T. G. A., Poenick, S., Striggow, F., Robitzki, A. A. Impedance spectroscopy based measurement system for quantitative and label-free real-time monitoring of tauopathy in hippocampal slice cultures. *Biosens. Bioelectron.* **32,** 250–258 (2012).

45. Nabae, Y. & Yamanaka, I. Alloying effects of Pd and Ni on the catalysis of the oxidation of dry CH4 in solid oxide fuel cells. *Appl. Catal. A Gen.* **369,** 119–124 (2009).

46. Eicher-Lorka, O., Charkova, T., Matijoska, A., Kuodis, Z., Urbelis G., Penkauskas, T., Mickevicius, M., Bulovas, A., Valincius, G. Cholesterol-based tethers and markers for model membranes investigation. *Chem. Phys. Lipids* **195,** 71–86 (2016).

47. Preta, G., Jankunec, M., Heinrich, F., Griffin, S., Sheldon, I. M., Valincius, G. Tethered bilayer membranes as a complementary tool for functional and structural studies: The pyolysin case. *Biochim. Biophys. Acta* **1858,** 2070–2080 (2016).

48.   Heath, G. R., Li, M., Rong, H., Radu, V., Frielingsdorf, S., Lenz, O., Butt, J. N., Jeuken, L. J. C. Multilayered Lipid Membrane Stacks for Biocatalysis Using Membrane Enzymes. *Adv. Funct. Mater.* **27,** 1606265 (2017).

49.   Kozuch, J., Weichbrodt, C., Millo, D., Giller, K., Becker, S., Hildebrandt, P., Steinem, C. Voltage-dependent structural changes of the membrane-bound anion channel hVDAC1 probed by SEIRA and electrochemical impedance spectroscopy. *Phys. Chem. Chem. Phys.* **16,** 9546–9555 (2014).

50.   Gutiérrez-Sanz, O., Olea, D., Pita, M., Batista, A. P., Alonso, A., Pereira, M. M., Vélez, M., De Lacey, A. L. Reconstitution of respiratory complex I on a biomimetic membrane supported on gold electrodes. *Langmuir* **30,** 9007–15 (2014).

51.   Su, Z., Leitch, J. J., Abbasi, F., Faragher, R. J., Schwan, A. L., Lipkowski, J. EIS and PM-IRRAS studies of alamethicin ion channels in a tethered lipid bilayer. *J. Electroanal. Chem.* 0–1 (2017). doi:10.1016/j.jelechem.2017.12.039

52.   Smith, C. P. & Dwhite, H. S. Theory of the interfacial potential distribution and reversible voltammetric response of electrodes coated with electroactive molecular films. *Anal. Chem.* **64,** 2398–405 (1992).

53.   Becucci, L., Guryanov, I., Maran, F., Scaletti, F. & Guidelli, R. A procedure for estimating the surface dipole potential of monolayers adsorbed on electrodes. *Soft Matter* **8,** 8601 (2012).

54.   Lvovich, V. F. *Impedance spectroscopy: applications to electrochemical and dielectric phenomena.* (John Wiley & Sons, Ltd, 2012).

55.   Valincius, G., Meškauskas, T. & Ivanauskas, F. Electrochemical impedance spectroscopy of tethered bilayer membranes. *Langmuir* **28,** 977–90 (2012).

56.   Gomadam, P. M. & Weidner, J. W. Analysis of electrochemical impedance spectroscopy in proton exchange membrane fuel cells. *Int. J. Energy Res.* **29,** 1133–1151 (2005).

57.   Ohki, S. Properties of lipid bilayer membranes membrane thickness. *J. Theor. Biol.* **26,** 277–287 (1970).

58.   Coster, H. G. L. & Smith, J. R. The molecular organization of bimolecular lipid membranes. A study of the low frequency Maxwell-Wagner impedance dispersion. *BBA - Biomembr.* **373,** 151–164 (1974).

59.   Karplus, M. & McCammon, J. A. Molecular dynamics simulations of biomolecules. *Nat. Struct. Biol.* **9,** 646–652 (2002).

60.   Langham, A. & Kaznessis, Y. N. Molecular Simulations of Antimicrobial Peptides. in 267–285 (2010).

61.   Brooks, B. R., Brooks, C. L., Mackerell, A. D., Nilsson, L., Petrella, R. J., Roux, B., Won, Y., Archontis, G., Bartels, C., Boresch, S., Caflisch, A., Caves, L., Cui, Q., Dinner A. R., Feig, M., Fischer, S., Gao, J., Hodoscek, M., Im, W., Kuczera, K., Lazaridis, T., Ma, J., Ovchinnikov, V., Paci, E., Pastor, R. W., Post, C. B., Pu, J. Z., Schaefer, M., Tidor, B., Venable, R. M., Woodcock, H. L., Wu, X., Yang, W., York, D. M., Karplus M. CHARMM: The biomolecular simulation program. *J. Comput. Chem.* **30,** 1545–1614 (2009).

62.   Phillips, J. C., Braun, R., Wang, W., Gumbart, J., Tajkhorshid E., Villa, E., Chipot, C., Skeel, R. D., Kalé L., Schulten, K. Scalable molecular dynamics with NAMD. *J. Comput. Chem.* **26,** 1781–1802 (2005).

63. RCSB Protein Data Bank - RCSB PDB. (2017). Available at: https://www.rcsb.org.

64. Adelman, S. A. & Brooks, C. L. Generalized Langevin models and condensed-phase chemical reaction dynamics. *J. Phys. Chem.* **86,** 1511–1524 (1982).

65. Uhlenbeck, G. E. & Ornstein, L. S. On the Theory of the Brownian Motion. *Phys. Rev.* **36,** 823–841 (1930).

66. Verlet, L. Computer 'Experiments' on Classical Fluids. I. Thermodynamical Properties of Lennard-Jones Molecules. *Phys. Rev.* **159,** 98–103 (1967).

67. Wang, L. Measurements and Implications of the Membrane Dipole Potential. *Annu. Rev. Biochem.* **81,** 615–635 (2012).

68. Collier, J. H. & Messersmith, P. B. Phospholipid Strategies in Biomineralization and Biomaterials Research. *Annu. Rev. Mater. Res.* **31,** 237–263 (2001).

69. Dowhan, W., Bogdanov, M. & Mileykovskaya, E. Functional roles of lipids in membranes. in *Biochemistry of Lipids, Lipoproteins and Membranes* **9,** 1–37 (Elsevier, 2008).

70. Sud, M. *et al.* LMSD: LIPID MAPS structure database. *Nucleic Acids Res.* **35,** D527-32 (2007).

71. Feigenson, G. W. Phase behavior of lipid mixtures. *Nat. Chem. Biol.* **2,** 560–563 (2006).

72. Jones, M. N. & Chapman, D. *Micelles, monolayers, and biomembranes*. (Wiley, New York, 1995).

73. Tatulian, S. & Cevc, G. *Phospholipids Handbook*. (1993).

74. Epand, R. M. *Lipid Polymorphism and Membrane Properties*. (1997).

75. Meer, G. Van, Voelker, D. R., Feigenson, G. W. Membrane lipids - where they are and how they behave. *Nat. Rev. Mol. Cell Biol.* **9,** 112–124 (2008).

76. Chernomordik, L. Non-bilayer lipids and biological fusion intermediates. *Chem. Phys. Lipids* **81,** 203–213 (1996).

77. Osman, C., Voelker, D. R. & Langer, T. Making heads or tails of phospholipids in mitochondria. *J. Cell Biol.* **192,** 7–16 (2011).

78. van den Brink-van der Laan, E., Killian, J. A. & de Kruijff, B. Nonbilayer lipids affect peripheral and integral membrane proteins via changes in the lateral pressure profile. *Biochim. Biophys. Acta* **1666,** 275–88 (2004).

79. Kooijman, E. E., Chupin, V., Fuller, N. L., Kozlov, M. M., de Kruijff, B., Burger, K. N. J., Rand, P. R. Spontaneous curvature of phosphatidic acid and lysophosphatidic acid. *Biochemistry* **44,** 2097–102 (2005).

80. Singer, S. & Nicolson, G. The fluid Mosaic model. (1972).

81. Stoeckenius, W. & Engelman, D. M. Current models for the structure of biological membranes. *J. Cell Biol.* **42,** 613–46 (1969).

82. Wallach, D. F. & Zahler, P. H. Protein conformations in cellular membranes. *Proc. Natl. Acad. Sci. U. S. A.* **56,** 1552–9 (1966).

83. Lenard, J. & Singer, S. J. Protein conformation in cell membrane preparations as studied by optical rotatory dispersion and circular dichroism. *Proc. Natl. Acad. Sci. U. S. A.* **56,** 1828–1835 (1966).

84. Jacobson, K., Ishihara, A. & Inman, R. Lateral Diffusion of Proteins in Membranes. *Annu. Rev. Physiol.* **49,** 163–175 (1987).

85. Damjanovich, S., Gáspár, R. & Pieri, C. Dynamic receptor superstructures at the plasma membrane. *Q. Rev. Biophys.* **30,** 67–106 (1997).

86. Israelachvili, J. N. Refinement of the fluid-mosaic model of membrane structure. *Biochim. Biophys. Acta - Biomembr.* **469,** 221–225 (1977).

87. Jacobson, K., Sheets, E. D. & Simson, R. Revisiting the fluid mosaic model of membranes. *Science* **268,** 1441–2 (1995).

88. Pralle, A., Keller, P., Florin, E. L., Simons, K. & Hörber, J. K. H. Sphingolipid-cholesterol rafts diffuse as small entities in the plasma membrane of mammalian cells. *J. Cell Biol.* **148,** 997–1008 (2000).

89. Allen, J. A., Halverson-Tamboli, R. A. & Rasenick, M. M. Lipid raft microdomains and neurotransmitter signalling. *Nat. Rev. Neurosci.* **8,** 128–40 (2007).

90. Mongrand, S., Morel J., Laroche, J., Claverol, S., Carde, J.-P., Hartmann, M.-A., Bonneu, M., Simon-Plas, F., Lessire, R., Bessoule, J.-J. Lipid rafts in higher plant cells: purification and characterization of Triton X-100-insoluble microdomains from tobacco plasma membrane. *J. Biol. Chem.* **279,** 36277–86 (2004).

91. Lopez, D. & Kolter, R. Functional microdomains in bacterial membranes. *Genes Dev.* **24,** 1893–1902 (2010).

92. Mileykovskaya, E. & Dowhan, W. Visualization of Phospholipid Domains in Escherichia coli by Using the Cardiolipin-Specific Fluorescent Dye 10- N -Nonyl Acridine Orange. *J Bacteriol* **182,** 1172–1175 (2000).

93. Simons, K. & Toomre, D. Lipid rafts and signal transduction. *Nat. Rev. Mol. Cell Biol.* **1,** 31–9 (2000).

94. Gajate, C. The antitumor ether lipid ET-18-OCH3 induces apoptosis through translocation and capping of Fas/CD95 into membrane rafts in human leukemic cells. *Blood* **98,** 3860–3863 (2001).

95. Lingwood, D. & Simons, K. Lipid rafts as a membrane-organizing principle. *Science* **327,** 46–50 (2010).

96. Pierce, S. K. Lipid rafts and B-cell activation. *Nat. Rev. Immunol.* **2,** 96–105 (2002).

97. Verkleij, A. J., Zwaal, R. F. A., Roelofsen, B., Comfurius, P., Kastelijn, D., van Deenen, L. L. M. The asymmetric distribution of phospholipids in the human red cell membrane. A combined study using phospholipases and freeze-etch electron microscopy. *Biochim. Biophys. Acta* **323,** 178–93 (1973).

98. Voelker, D. R. Lipid assembly into cell membranes. in *Biochemistry of Lipids, Lipoproteins and Membranes* 441–484 (Elsevier, 2008).

99. Hancock, R. E. . & Lehrer, R. Cationic peptides: a new source of antibiotics. *Trends Biotechnol.* **16,** 82–88 (1998).

100. Peschel, A. & Sahl, H. G. The co-evolution of host cationic antimicrobial peptides and microbial resistance. *Nat Rev Microbiol* **4,** 529–536 (2006).

101. Vollmer, W. & Höltje, J. The architecture of the murein (peptidoglycan) in gram-negative bacteria: vertical scaffold or horizontal layer(s)? *J. Bacteriol.* **186,** 5978–87 (2004).

102. Marr, A. G. & Ingraham, J. L. Effect of temperature on the composition of fatty acids in Escherichia coli. *J. Bacteriol.* **84,** 1260–7 (1962).

103. White, D. A., Lennarz, W. J. & Schnaitman, C. A. Distribution of lipids in the wall and cytoplasmic membrane subfractions of the cell envelope of Escherichia coli. *J. Bacteriol.* **109,** 686–90 (1972).

104. Benamara, H., Rihouey, C., Abbes, I., Mlouka, M. A. B., Hardouin, J., Jouenne, T., Alexandre, S. Characterization of membrane lipidome changes in Pseudomonas aeruginosa during biofilm growth on glass wool. *PLoS One* **9,** e108478 (2014).

105. Conrad, R. S. & Gilleland, H. E. Lipid alterations in cell envelopes of polymyxin-resistant Pseudomonas aeruginosa isolates. *J. Bacteriol.* **148,** 487–97 (1981).

106. Hancock, R. E. Alterations in outer membrane permeability. *Annu. Rev. Microbiol.* **38,** 237–64 (1984).

107. Epand, R. M. & Epand, R. F. Lipid domains in bacterial membranes and the action of antimicrobial agents. *Biochim. Biophys. Acta - Biomembr.* **1788,** 289–294 (2009).

108. Malanovic, N. & Lohner, K. Gram-positive bacterial cell envelopes: The impact on the activity of antimicrobial peptides. *Biochim. Biophys. Acta* **1858,** 936–46 (2016). http://dx.doi.org/10.1016/j.bbamem.2015.11.004 (http://creativecommons.org/licenses/by-nc-nd/4.0/)

109. Mishra, N. N. & Bayer, A. S. Correlation of cell membrane lipid profiles with daptomycin resistance in methicillin-resistant Staphylococcus aureus. *Antimicrob. Agents Chemother.* **57,** 1082–5 (2013).

110. White, D. C. & Frerman, F. E. Fatty acid composition of the complex lipids of Staphylococcus aureus during the formation of the membrane-bound electron transport system. *J. Bacteriol.* **95,** 2198–209 (1968).

111. den Kamp, J. A., Redai, I. & van Deenen, L. L. Phospholipid composition of Bacillus subtilis. *J. Bacteriol.* **99,** 298–303 (1969).

112. Bittman, R., Clejan, S., Robinson, B. P. & Witzke, N. M. Kinetics of cholesterol and phospholipid exchange from membranes containing cross-linked proteins or cross-linked phosphatidylethanolamines. *Biochemistry* **24,** 1403–9 (1985).

113. Bishop, D. G., Rutberg, L. & Samuelsson, B. The chemical composition of the cytoplasmic membrane of Bacillus subtilis. *Eur. J. Biochem.* **2,** 448–53 (1967).

114. Lohner, K. Membrane-active Antimicrobial Peptides as Template Structures for Novel Antibiotic Agents. *Curr. Top. Med. Chem.* **17 (5)** 508–519 (2017).

115. Honig, B. H., Hubbell, W. L. & Flewelling, R. F. Electrostatic interactions in membranes and proteins. *Annu. Rev. Biophys. Biophys. Chem.* **15,** 163–93 (1986).

116. Franklin, J. C. & Cafiso, D. S. Internal electrostatic potentials in bilayers: measuring and controlling dipole potentials in lipid vesicles. *Biophys. J.* **65,** 289–299 (1993).

117. Poignard, C., Silve, A., Campion, F., Mir, L. M., Saut, O., Schwartz, L. Ion fluxes, transmembrane potential, and osmotic stabilization: a new dynamic electrophysiological model for eukaryotic cells. *Eur. Biophys. J.* **40,** 235–246 (2011).

118. Kinraide, T. B. Ion fluxes considered in terms of membrane-surface electrical potentials. *Funct. Plant Biol.* **28,** 607 (2001).

119. Shomer, I., Novacky, A. J., Pike, S. M., Yermiyahu, U. & Kinraide, T. B. Electrical potentials of plant cell walls in response to the ionic environment. *Plant Physiol.* **133,** 411–22 (2003).

120. Kinraide, Yermiyahu & Rytwo. Computation of surface electrical potentials of plant cell membranes. Correspondence To published zeta potentials from diverse plant sources. *Plant Physiol.* **118,** 505–12 (1998).

121. Kinraide, T. B. Plasma membrane surface potential (ψPM) as a determinant of ion bioavailability: a critical analysis of new and published toxicological studies and a simplified method for the computation of plant ψPM. *Environ. Toxicol. Chem.* **25,** 3188-3198 (2006).

122. Gawrisch, K., Ruston, D., Zimmerberg, J., Parsegian, V.A., Rand, R. P., Fuller, N. Membrane dipole potentials, hydration forces, and the ordering of water at membrane surfaces. *Biophys. J.* **61,** 1213–23 (1992).

123. Haydon, D. A. & Elliott, J. R. Surface potential changes in lipid monolayers and the 'cut-off' in anaesthetic effects of N-alkanols. *Biochim. Biophys. Acta - Biomembr.* **863,** 337–340 (1986).

124. Wu, Z., Cui, Q. & Yethiraj, A. A New Coarse-Grained Model for Water: The Importance of Electrostatic Interactions. *J. Phys. Chem. B* **114,** 10524–10529 (2010).

125. Shinoda, K., Shinoda, W., Baba, T. & Mikami, M. Comparative molecular dynamics study of ether- and ester-linked phospholipid bilayers. *J. Chem. Phys.* **121,** 9648–9654 (2004).

126. Kendall, J. K. R., Johnson, B. R. G., Symonds, P. H., Imperato, G., Bushby, R. J., Gwyer, J. D., van Berkel, C., Evans, S. D., Jeuken, L. J. C. Effect of the structure of cholesterol-based tethered bilayer lipid membranes on ionophore activity. *Chemphyschem* **11,** 2191–2198 (2010).

127. Su, Z., Shodiev, M., Jay Leitch, J., Abbasi, F. & Lipkowski, J. In situ electrochemical and PM-IRRAS studies of alamethicin ion channel formation in model phospholipid bilayers. *J. Electroanal. Chem.* **819**, 251-259 (2018).

128. Melin, F. & Hellwig, P. Recent advances in the electrochemistry and spectroelectrochemistry of membrane proteins. *Biol. Chem.* **394,** 593–609 (2013).

129. Ataka, K., Giess, F., Knoll, W., Naumann, R., Haber-Pohlmeier, S., Richter, B., Heberle, J. Oriented Attachment and Membrane Reconstitution of His-Tagged Cytochrome c Oxidase to a Gold Electrode: In Situ Monitoring by Surface-Enhanced Infrared Absorption Spectroscopy. *J. Am. Chem. Soc.* **126,** 16199–16206 (2004).

130. Wu, L. & Jiang, X. Infrared Spectroscopy for Studying Plasma Membranes. in *Membrane Biophysics* 319–354 (Springer Singapore, 2018).

131. Ulman, A. Formation and Structure of Self-Assembled Monolayers. *Chem. Rev.* **96,** 1533–1554 (1996).

132. Whitesides, G. M., Kriebel, J. K. & Love, J. C. Molecular engineering of surfaces using self-assembled monolayers. *Sci. Prog.* **88,** 17–48 (2005).

133. Bain, C. D., Evall, J. & Whitesides, G. M. Formation of monolayers by the coadsorption of thiols on gold: variation in the head group, tail group, and solvent. *J. Am. Chem. Soc.* **111,** 7155–7164 (1989).

134. Kozuch, J. A. Structure-Function Relationships of Membrane Proteins - Spectroelectrochemical Investigation of Artificial Membranes vorgelegt von Diplom-Chemiker Jacek Artur Kozuch. (2012). doi:10.14279/depositonce-3486

135. Ataka, K., Stripp, S. T. & Heberle, J. Surface-enhanced infrared absorption spectroscopy (SEIRAS) to probe monolayers of membrane proteins. *Biochim. Biophys. Acta - Biomembr.* **1828,** 2283–2293 (2013).

136. Khurana, R. & Fink, A. L. Do Parallel β-Helix Proteins Have a Unique Fourier Transform Infrared Spectrum? *Biophys. J.* **78,** 994–1000 (2000).

137. Wallace. Recent Advances in the High Resolution Structures of Bacterial Channels: Gramicidin A. *J. Struct. Biol.* **121,** 123–41 (1998).

138. Lin, M. T. & Beal, M. F. Mitochondrial dysfunction and oxidative stress in neurodegenerative diseases. *Nature* **443,** 787–95 (2006).

139. Dobson, C. M. Protein misfolding, evolution and disease. *Trends Biochem. Sci.* **24,** 329–332 (1999).

140. Barth, A. & Zscherp, C. What vibrations tell us about proteins. *Q. Rev. Biophys.* **35,** 369–430 (2002).

141. Barth, A. Infrared spectroscopy of proteins. *Biochim. Biophys. Acta - Bioenerg.* **1767,** 1073–1101 (2007).

142. Steinhoff, H., Mollaaghababa, R., Altenbach, C., Hideg, K., Krebs, M., Khorana, H. G., Hubbell, W. L. Time-resolved detection of structural changes during the photocycle of spin-labeled bacteriorhodopsin. *Science* **266,** 105–107 (1994).

143. Naik, V. M. & Krimm, S. Vibrational analysis of the structure of gramicidin A. I. Normal mode analysis. *Biophys. J.* **49,** 1131–1145 (1986).

144. Naik, V. M. & Krimm, S. Vibrational analysis of the structure of gramicidin A. II. Vibrational spectra. *Biophys. J.* **49,** 1147–1154 (1986).

145. Dwivedi, A. M. & Krimm, S. Dwivedi - 1984 - Vibrational analysis of peptides, polypeptides, and proteins. IXX Force fields for α-helix and β-sheet structures in a side-chain point-mass approximation.pdf. **88(3),** 620 (1984).

146. Marsh, D., Müller, M. & Schmitt, F. J. Orientation of the infrared transition moments for an alpha-helix. *Biophys. J.* **78,** 2499–510 (2000).

147. Schartner, J., Güldenhaupt, J., Mei, B., Rögner, M., Muhler, M., Gerwert, K., Kötting, C. Universal Method for Protein Immobilization on Chemically Functionalized Germanium Investigated by ATR-FTIR Difference Spectroscopy. *J. Am. Chem. Soc.* **135,** 4079–4087 (2013).

148. Wisitruangsakul, N., Lenz, O., Ludwig, M., Friedrich, B., Lendzian, F., Hildebrandt, P., Zebger, I. Monitoring Catalysis of the Membrane Bound Hydrogenase from Ralstonia eutropha H16 by Surface Enhanced IR Absorption Spectroscopy. *Angew. Chem. Int. Ed.* **48,** 611–613 (2009).

149. Aminov, R. I. The role of antibiotics and antibiotic resistance in nature. *Environ. Microbiol.* **11,** 2970–2988 (2009).

150. Fevre, C., Jbel, M., Passet, V., Weill, F.-X., Grimont, P. A. D., Brisse, S. Six Groups of the OXY -Lactamase Evolved over Millions of Years in Klebsiella oxytoca. *Antimicrob. Agents Chemother.* **49,** 3453–3462 (2005).

151. Willyard, C. The drug-resistant bacteria that pose the greatest health threats. *Nature* **543,** 15–15 (2017).

152. Luepke, K. H. *et al.* Past, Present, and Future of Antibacterial Economics: Increasing Bacterial Resistance, Limited Antibiotic Pipeline, and Societal Implications. *Pharmacotherapy* **37,** 71–84 (2017).

153. Livermore, D. M. The need for new antibiotics. *Clin. Microbiol. Infect.* **10 Suppl 4,** 1–9 (2004).

154. Wang, G., Li, X. & Wang, Z. APD3: the antimicrobial peptide database as a tool for research and education. *Nucleic Acids Res.* **44,** D1087–D1093 (2016).

155. Mansour, S. C., Pena, O. M. & Hancock, R. E. W. Host defense peptides: front-line immunomodulators. *Trends Immunol.* **35,** 443–50 (2014).

156. Zasloff, M. Magainins, a class of antimicrobial peptides from Xenopus skin: isolation, characterization of two active forms, and partial cDNA sequence of a precursor. *Proc. Natl. Acad. Sci. U. S. A.* **84,** 5449–53 (1987).

157. Ganz, T. Defensins: antimicrobial peptides of innate immunity. *Nat. Rev. Immunol.* **3,** 710–20 (2003).

158. Boman, H. G. Peptide antibiotics and their role in innate immunity. *Annu. Rev. Immunol.* **13,** 61–92 (1995).

159. Dimarcq, J. L., Bulet, P., Hetru, C. & Hoffmann, J. Cysteine-rich antimicrobial peptides in invertebrates. *Biopolymers* **47,** 465–77 (1998).

160. Gaspar, D., Veiga, A. S. & Castanho, M. A. R. B. From antimicrobial to anticancer peptides. A review. *Front. Microbiol.* **4,** 1–16 (2013).

161. Nguyen, L. T., Haney, E. F. & Vogel, H. J. The expanding scope of antimicrobial peptide structures and their modes of action. *Trends Biotechnol.* **29,** 464–472 (2011).

162. Sani, M.-A. & Separovic, F. How Membrane-Active Peptides Get into Lipid Membranes. *Acc. Chem. Res.* **49,** 1130–8 (2016).

163. Copolovici, D. M., Langel, K., Eriste, E. & Langel, Ü. Cell-penetrating peptides: design, synthesis, and applications. *ACS Nano* **8,** 1972–94 (2014).

164. Madani, F., Lindberg, S., Langel, U., Futaki, S. & Gräslund, A. Mechanisms of cellular uptake of cell-penetrating peptides. *J. Biophys.* **2011,** 414729 (2011).

165. Herce, H. D. & Garcia, A. E. Cell penetrating peptides: how do they do it? *J. Biol. Phys.* **33,** 345–56 (2007).

166. Andreu, D. & Rivas, L. Animal antimicrobial peptides: An overview. *Biopolymers* **47,** 415–433 (1998).

167. Jamasbi, E., Batinovic, S., Sharples, R. A., Sani, M.-A., Robins-Browne, R. M., Wade, J., D., Separovic, F., Hossain, M. A. Melittin peptides exhibit different activity on different cells and model membranes. *Amino Acids* **46,** 2759–66 (2014).

168. Dathe, M., Kaduk, C., Tachikawa, E., Melzig, M. F., Wenschuh, H., Bienert, M. Proline at position 14 of alamethicin is essential for hemolytic activity, catecholamine secretion from chromaffin cells and enhanced metabolic activity in endothelial cells. *Biochim. Biophys. Acta* **1370,** 175–83 (1998).

169. Ageitos, J. M., Sánchez-Pérez, A., Calo-Mata, P. & Villa, T. G. Antimicrobial peptides (AMPs): Ancient compounds that represent novel weapons in the fight against bacteria. *Biochem. Pharmacol.* **133,** 117–138 (2017).

170. Huang, H. W. Molecular mechanism of antimicrobial peptides : The origin of cooperativity. **1758,** 1292–1302 (2006).

171. Matsuzaki, K. Magainins as paradigm for the mode of action of pore forming polypeptides. *Biochim. Biophys. Acta - Rev. Biomembr.* **1376,** 391–400 (1998).

172. Oren, Z. & Shai, Y. Mode of action of linear amphipathic α-helical antimicrobial peptides. *Biopolymers* **47,** 451–463 (1998).

173. Shai, Y. Mechanism of the binding, insertion and destabilization of phospholipid bilayer membranes by alpha-helical antimicrobial and cell non-selective membrane-lytic peptides. *Biochim. Biophys. Acta* **1462,** 55–70 (1999).

174. Zasloff, M. Antimicrobial peptides of multicellular organisms. *Nature* **415,** 389–395 (2002).

175. Pispisa, B., Stella, L., Mazzuca, C. & Venanzi, M. Trichogin Topology and Activity in Model Membranes as Determined by Fluorescence Spectroscopy. in *Reviews in Fluorescence* 47–70 (2006).

176. Neale, C., Hsu, J. C. Y., Yip, C. M. & Pomès, R. Indolicidin Binding Induces Thinning of a Lipid Bilayer. *Biophys. J.* **106,** L29–L31 (2014).

177. Pabst, G., Danner, S., Podgornik, R. & Katsaras, J. Entropy-Driven Softening of Fluid Lipid Bilayers by Alamethicin. *Langmuir* **23,** 11705–11711 (2007).

178. Palm, C., Netzereab, S. & Hällbrink, M. Quantitatively determined uptake of cell-penetrating peptides in non-mammalian cells with an evaluation of degradation and antimicrobial effects. *Peptides* **27,** 1710–1716 (2006).

179. Huang, K. & García, A. E. Free energy of translocating an arginine-rich cell-penetrating peptide across a lipid bilayer suggests pore formation. *Biophys. J.* **104,** 412–420 (2013).

180. Gutsmann, T. Interaction between antimicrobial peptides and mycobacteria. *Biochim. Biophys. Acta - Biomembr.* **1858,** 1034–1043 (2016).

181. Ritonja, a., Kopitar, M., Jerala, R. & Turk, V. Primary structure of a new cysteine proteinase inhibitor from pig leucocytes. *FEBS Lett.* **255,** 211–4 (1989).

182. Gutsmann, T., Hagge, S. O., David, A., Roes, S., Böhling, A., Hammer, M. U., Seydel, U. Lipid-mediated resistance of Gram-negative bacteria against various pore-forming antimicrobial peptides. *J. Endotoxin Res.* **11,** 167–73 (2005).

183. Sørensen, O. E., Follin, P., Johnsen, A. H., Calafat, J., Tjabringa, S., Hiemstra, P. S., Borregaard, N. Human cathelicidin, hCAP-18, is processed to the antimicrobial peptide LL-37 by extracellular cleavage with proteinase 3. *Blood* **97,** 3951–9 (2001).

184. Bals, R., Weiner, D. J., Moscioni, A. D., Meegalla, R. L. & Wilson, J. M. Augmentation of innate host defense by expression of a cathelicidin antimicrobial peptide. *Infect. Immun.* **67,** 6084–9 (1999).

185. Schaller-Bals, S., Schulze, A. & Bals, R. Increased Levels of Antimicrobial Peptides in Tracheal Aspirates of Newborn Infants during Infection. *Am. J. Respir. Crit. Care Med.* **165,** 992–995 (2002).

186. Ong, P. Y., Ohtake, T., Brandt, C., Strickland, I., Boguniewicz, M., Ganz, T., Gallo, R. L., Leung, D. Y. M. Endogenous Antimicrobial Peptides and Skin Infections in Atopic Dermatitis. *N. Engl. J. Med.* **347,** 1151–1160 (2002).

187. Chen, C. I.-U., Schaller-Bals, S., Paul, K. P., Wahn, U. & Bals, R. β-defensins and LL-37 in bronchoalveolar lavage fluid of patients with cystic fibrosis. *J. Cyst. Fibros.* **3,** 45–50 (2004).

188. Overhage, J., Campisano, A., Bains, M., Torfs, E. C. W., Rehm, B. H. A., Hancock, R. E. W. Human host defense peptide LL-37 prevents bacterial biofilm formation. *Infect. Immun.* **76,** 4176–4182 (2008).

189. Dean, S. N., Bishop, B. M. & Hoek, M. L. Van. Natural and synthetic cathelicidin peptides with anti-microbial and anti-biofilm activity against Staphylococcus aureus Natural and synthetic cathelicidin peptides with anti-microbial and anti-biofilm activity against Staphylococcus aureus. *BMC Microbiol.* **11,** 114 (2011).

190. Chennupati, S. K., Chiu, A. G., Tamashiro, E., Banks, C. A., Cohen, M. B., Bleier, B. S., Kofonow, J. M., Tam, E., Cohen, N. A., Effects of an LL-37-derived antimicrobial peptide in an animal model of biofilm Pseudomonas sinusitis. *Am. J. Rhinol. Allergy* **23,** 46–51 (2009).

191. Nijnik, A., Pistolic, J., Filewod, N. C. J. & Hancock, R. E. W. Signaling Pathways Mediating Chemokine Induction in Keratinocytes by Cathelicidin LL-37 and Flagellin. *J. Innate Immun.* **4,** 377–386 (2012).

192. Scott, M. G., Davidson, D. J., Gold, M. R., Bowdish, D., Hancock, R. E. W. The Human Antimicrobial Peptide LL-37 Is a Multifunctional Modulator of Innate Immune Responses. (2016). doi:10.4049/jimmunol.169.7.3883

193. Carretero, M., Escaméz, M. J., García, M., Duarte, B., Holguín, A., Retamosa, L., Jorcano, J. L., del Río M., Larcher, F. In vitro and In vivo Wound Healing-Promoting Activities of Human Cathelicidin LL-37. *J. Invest. Dermatol.* **128,** 223–236 (2008).

194. Braff, M. H., Hawkins, M. A., Di Nardo, A., Lopez-Garcia, B., Howell, M. D., Wong, C., Lin, K., Streib, J. E., Dorschner, R., Leung, D. Y. M., Gallo, R. L. Structure-Function Relationships among Human Cathelicidin Peptides: Dissociation of Antimicrobial Properties from Host Immunostimulatory Activities. *J. Immunol.* **174,** 4271–4278 (2005).

195. Kai-Larsen, Y. & Agerberth, B. The role of the multifunctional peptide LL-37 in host defense. *Frontiers in bioscience : a journal and virtual library* **13,** 3760–3767 (2008).

196. Chamorro, C. I., Weber, G., Grönberg, A., Pivarcsi, A. & Ståhle, M. The Human Antimicrobial Peptide LL-37 Suppresses Apoptosis in Keratinocytes. *J. Invest. Dermatol.* **129,** 937–944 (2009).

197. Barlow, P. G., Li, Y., Wilkinson, T. S., Bowdish, D. M. E., Lau, E., Cosseau, C., Haslett, C., Simpson, A. J., Hancock, R. E. W., Davidson D. J. The human cationic host defense peptide LL-37 mediates contrasting effects on apoptotic pathways in different primary cells of the innate immune system. *J. Leukoc. Biol.* **80,** 509–20 (2006).

198. Barlow, P. G., Beaumont, P. E., Cosseau, C., Mackellar, A., Wilkinson, T. S., Hancock, R. E. W., Haslett, C., Govan, J. R. W., Simpson A. J., Davidson D. J. The human cathelicidin LL-37 preferentially promotes apoptosis of infected airway epithelium. *Am. J. Respir. Cell Mol. Biol.* **43,** 692–702 (2010).

199. Verjans, E., Zels, S., Luyten, W., Landuyt, B. & Schoofs, L. Molecular mechanisms of LL-37-induced receptor activation: An overview. *Peptides* **85,** 16–26 (2016).

200. Sochacki, K. A., Barns, K. J., Bucki, R. & Weisshaar, J. C. Real-time attack on single Escherichia coli cells by the human antimicrobial peptide LL-37. (2011).

201. Kim, E. Y., Rajasekaran, G. & Shin, S. Y. LL-37-derived short antimicrobial peptide KR-12-a5 and its d -amino acid substituted analogs with cell selectivity, anti-biofilm activity, synergistic effect with conventional antibiotics, and anti-inflammatory activity. *Eur. J. Med. Chem.* **136,** 428–441 (2017).

202. Murakami, M., Lopez-Garcia, B., Braff, M., Dorschner, R. A. & Gallo, R. L. Postsecretory Processing Generates Multiple Cathelicidins for Enhanced Topical Antimicrobial Defense. *J. Immunol.* **172,** 3070–3077 (2004).

203. Feng, X., Sambanthamoorthy, K., Palys, T. & Paranavitana, C. The human antimicrobial peptide LL-37 and its fragments possess both antimicrobial and antibiofilm activities against multidrug-resistant Acinetobacter baumannii. *Peptides* **49,** 131–7 (2013).

204. López-García, B., Ubhayasekera, W., Gallo, R. L. & Marcos, J. F. Parallel evaluation of

antimicrobial peptides derived from the synthetic PAF26 and the human LL37. *Biochem. Biophys. Res. Commun.* **356,** 107–113 (2007).

205. Sieprawska-Lupa, M., Mydel, P., Krawczyk, K., Wójcik, K., Puklo, M., Lupa, B., Suder, P., Silberring, J., Reed, M., Pohl, J., Shafer, W., McAleese, F., Foster, T., Travis, J., Potempa, J. Degradation of Human Antimicrobial Peptide LL-37 by Staphylococcus aureus -Derived Proteinases. *Antimicrob. Agents Chemother.* **48,** 4673–4679 (2004).

206. Forbrig, E., Staffa, J. K., Salewski, J., Mroginski, M. A., Hildebrandt, P. Kozuch, J. Monitoring the Orientational Changes of Alamethicin during Incorporation into Bilayer Lipid Membranes. *Langmuir* **34,** 2373–2385 (2018).

207. Meyer, C. E. & Reusser, F. A polypeptide antibacterial agent isolated fromTrichoderma viride. *Experientia* **23,** 85–86 (1967).

208. Cafiso, D. S. Alamethicin: A Peptide Model for Voltage Gating and Protein-Membrane Interactions. *Annu. Rev. Biophys. Biomol. Struct.* **23,** 141–165 (1994).

209. Fox, R. O. & Richards, F. M. A voltage-gated ion channel model inferred from the crystal structure of alamethicin at 1.5-A resolution. *Nature* **300,** 325–30 (1982).

210. Nagao, T., Mishima D., Javkhlantugs, N., Wang, J., Ishioka, D., Yokota, K., Norisada, K., Kawamura, I., Ueda, K., Naito, A. Structure and orientation of antibiotic peptide alamethicin in phospholipid bilayers as revealed by chemical shift oscillation analysis of solid state nuclear magnetic resonance and molecular dynamics simulation. *Biochim. Biophys. Acta - Biomembr.* **1848,** 2789–2798 (2015).

211. Haris, P, Chapman, D. Fourier transform infrared spectra of the polypeptide alamethicin and a possible structural similarity with bactefiorhodopsin. *Biochim. Biophys. Acta* **13,** 375–380 (1988).

212. Bechinger, B. Structure and functions of channel-forming peptides: magainins, cecropins, melittin and alamethicin. *J. Membr. Biol.* **156,** 197–211 (1997).

213. Pieta, P., Mirza, J. & Lipkowski, J. Direct visualization of the alamethicin pore formed in a planar phospholipid matrix. *Proc. Natl. Acad. Sci. U. S. A.* **109,** 21223–7 (2012).

214. Yang, P., Wu, F. G. & Chen, Z. Dependence of alamethicin membrane orientation on the solution concentration. *J. Phys. Chem. C* **117,** 3358–3365 (2013).

215. Tieleman, D. P. P., Berendsen, H. J. C. J. & Sansom, M. S. P. M. S. P. Voltage-Dependent Insertion of Alamethicin at Phospholipid/Water and Octane/Water Interfaces. *Biophys. J.* **80,** 331–346 (2001).

216. Marsh, D. Orientation and peptide-lipid interactions of alamethicin incorporated in phospholipid membranes: polarized infrared and spin-label EPR spectroscopy. *Biochemistry* **48,** 729–37 (2009).

217. Bortolus, M., De Zotti, M., Formaggio, F. & Maniero, A. L. Alamethicin in bicelles: orientation, aggregation, and bilayer modification as a function of peptide concentration. *Biochim. Biophys. Acta* **1828,** 2620–7 (2013).

218. Ye, S., Nguyen, K. T. & Chen, Z. Interactions of alamethicin with model cell membranes investigated using sum frequency generation vibrational spectroscopy in real time in situ. *J. Phys. Chem. B* **114,** 3334–3340 (2010).

219. Yang, P., Wu, F.-G. G. & Chen, Z. Lipid Fluid–Gel Phase Transition Induced Alamethicin Orientational Change Probed by Sum Frequency Generation Vibrational Spectroscopy. *J. Phys. Chem. C* **117,** 17039–17049 (2013).

220. Bechinger, B. The structure, dynamics and orientation of antimicrobial peptides in membranes by multidimensional solid-state NMR spectroscopy. *Biochim. Biophys. Acta* **1462,** 157–83 (1999).

221. Yamaguchi, S., Huster, D., Waring, A., Lehrer, R. I., Kearney, W., Tack, B. F., Hong, M. Orientation and Dynamics of an Antimicrobial Peptide in the Lipid Bilayer by Solid-State NMR Spectroscopy. *Biophys. J.* **81,** 2203–2214 (2001).

222. Ding, B., Soblosky, L., Nguyen, K., Geng, J., Yu, X., Ramamoorthy, A., Chen, Z. Physiologically-Relevant Modes of Membrane Interactions by the Human Antimicrobial Peptide, LL-37, Revealed by SFG Experiments. *Sci. Rep.* **3,** 1854 (2013).

223. Lee, J., Jung, S. W. & Cho, A. E. Molecular Insights into the Adsorption Mechanism of Human β-Defensin-3 on Bacterial Membranes. *Langmuir* **32,** 1782–1790 (2016).

224. Tamm, L. K. & Tatulian, S. A. Infrared spectroscopy of proteins and peptides in lipid bilayers. *Quart. Rev. Biophys.* **30,** 365–429 (1997).

225. Dunkelberger, E. B., Grechko, M. & Zanni, M. T. Transition Dipoles from 1D and 2D Infrared Spectroscopy Help Reveal the Secondary Structures of Proteins: Application to Amyloids. *J. Phys. Chem. B* **119,** 14065–14075 (2015).

226. Nguyen, K. T., Le Clair, S. V, Ye, S. & Chen, Z. Orientation determination of protein helical secondary structures using linear and nonlinear vibrational spectroscopy. *J. Phys. Chem. B* **113,** 12169–80 (2009).

227. Kubelka, J., Silva, R. a G. D. & Keiderling, T. A. Discrimination between Peptide 3 10- and a-Helices. Theoretical Analysis of the Impact of a-Methyl Substitution on Experimental Spectra. *J. Am. Chem. Soc.* **124,** 5325–5332 (2002).

228. Keiderling, T. A. Protein and peptide secondary structure and conformational determination with vibrational circular dichroism. *Curr. Opin. Chem. Biol.* **6,** 682–688 (2002).

229. Myshakina, N. S. & Asher, S. a. Peptide bond vibrational coupling. *J. Phys. Chem. B* **111,** 4271–9 (2007).

230. Karjalainen, E.-L. L. & Barth, A. Vibrational coupling between helices influences the amide i infrared absorption of proteins: Application to bacteriorhodopsin and rhodopsin. *J. Phys. Chem. B* **116,** 4448–4456 (2012).

231. Torii, H., Tasumi, M., Torii, H. & Tasumi, M. Model calculations on the amide-I infrared bands of globular proteins. *J. Chem. Phys.* **96,** 3379–2287 (1992).

232. Osawa, M. Surface-Enhanced Infrared Absorption. *Top. Appl. Phys.* **187,** 785–799 (2002).

233. Krebs, H. A. The Citric Acid Cycle. *J. Sci. Technol. Manag.* **7(1),** (2014).

234. Mitchell, P. Chemiosmotic coupling in oxidative and photosynthetic phosphorylation. 1966. *Biochim. Biophys. Acta* **1807,** 1507–38 (2011).

235. Shepherd, M. & Poole, R. K. Bacterial Respiratory Chains. in *Encyclopedia of Biophysics* **191,** 172–177 (Springer Berlin Heidelberg, 2013).

236. Kriegel, S. Transformation of a membrane protein from the respiratory chain into a sensor for the analysis of its interaction with substrates, inhibitors and lipids. (2013).

237. Weiss, H., Friedrich, T., Hofhaus, G. & Preis, D. The respiratory-chain NADH dehydrogenase (complex 1) of mitochondria. *Eur. J. Biochem.* **197,** 563–576 (1991).

238. Yagi, T. & Matsuno-Yagi, A. The Proton-Translocating NADH−Quinone Oxidoreductase in the Respiratory Chain: The Secret Unlocked. *Biochemistry* **42,** 2266–2274 (2003).

239. Ohnishi, T., Nakamaru-Ogiso, E. & Ohnishi, S. T. A new hypothesis on the simultaneous direct and indirect proton pump mechanisms in NADH-quinone oxidoreductase (complex I). *FEBS Lett.* **584,** 4131–4137 (2010).

240. Friedrich, T., Dekovic, D. K. & Burschel, S. Assembly of the Escherichia coli NADH:ubiquinone oxidoreductase (respiratory complex I). *Biochim. Biophys. Acta* **1857,** 214–23 (2016).

241. Walker, J. E. The NADH:ubiquinone oxidoreductase (complex I) of respiratory chains. *Q. Rev. Biophys.* **25,** 253 (1992).

242. Hirst, J. Mitochondrial Complex I. *Annu. Rev. Biochem.* **82,** 551–575 (2013).

243. Zhu, J., Vinothkumar, K. R. K. K. R. & Hirst, J. Structure of mammalian respiratory complex i. *Nature* **536,** 354–358 (2016).

244. Carroll, J., Fearnley, I. M., Skehel, M., Shannon, R. J., Hirst, J. & Walker, J. E. Bovine complex I is a complex of 45 different subunits. *J. Biol. Chem.* **281,** 32724–7 (2006).

245. Marreiros, B. C., Batista, A. P., Duarte, A. M. S. & Pereira, M. M. A missing link between complex i and group 4 membrane-bound [NiFe] hydrogenases. *Biochim. Biophys. Acta* **1827,** 198–209 (2013).

246. Batista, A. P. & Pereira, M. M. Sodium influence on energy transduction by complexes i from Escherichia coli and Paracoccus denitrificans. *Biochim. Biophys. Acta* **1807,** 286–292 (2011).

247. Roberts, P. G. & Hirst, J. The Deactive Form of Respiratory Complex I from Mammalian Mitochondria Is a Na+/H+ Antiporter. *J. Biol. Chem.* **287,** 34743–34751 (2012).

248. Baradaran, R., Berrisford, J. M., Minhas, G. S. & Sazanov, L. a. Crystal structure of the entire respiratory complex I. *Nature* **494,** 443–8 (2013).

249. Brandt, U. Energy converting NADH:quinone oxidoreductase (complex I). *Annu. Rev. Biochem.* **75,** 69–92 (2006).

250. Fernandes, A. S., Sousa, F. L., Teixeira, M. & Pereira, M. M. Electron paramagnetic resonance studies of the iron-sulfur centers from complex I of Rhodothermus marinus. *Biochemistry* **45,** 1002–1008 (2006).

251. Page, C. C., Moser, C. C., Chen, X. & Dutton, P. L. Natural engineering principles of electron tunnelling in biological oxidation-reduction. *Nature* **402,** 47–52 (1999).

252. Sazanov, L. A. The mechanism of coupling between electron transfer and proton translocation in respiratory complex I. *J. Bioenerg. Biomembr.* **46,** 247–253 (2014).

253. Zickermann, V., Wirth, C., Nasiri, H., Siegmund, K., Schwalbe, H., Hunte, C. & Brandt, U. Mechanistic insight from the crystal structure of mitochondrial complex I. *Science* **347,** 4–9 (2015).

254. Di Luca, A., Gamiz-Hernandez, A. P. & Kaila, V. R. I. Symmetry-related proton transfer pathways in respiratory complex I. *Proc. Natl. Acad. Sci. U. S. A.* **114,** E6314–E6321 (2017).

255. Wirth, C., Brandt, U., Hunte, C. & Zickermann, V. Structure and function of mitochondrial complex I. *Biochim. Biophys. Acta* **1857,** 902–914 (2016).

256. Batista, A. P., Marreiros, B. C. & Pereira, M. M. Decoupling of the catalytic and transport activities of complex I from Rhodothermus marinus by sodium/proton antiporter inhibitor. *ACS Chem. Biol.* **6,** 477–83 (2011).

257. Miyake, H., Ye, S. & Osawa, M. Electroless deposition of gold thin films on silicon for surface-enhanced infrared spectroelectrochemistry. *Electrochem. commun.* **4,** 973–977 (2002).

258. Trasatti, S. & Petrii, O. A. Real surface area measurements in electrochemistry. *Pure Appl. Chem.* **63,** 711–734 (1991).

259. Gutiérrez-Sánchez, C., Olea, D., Marques, M., Fernández, V. M., Pereira, I. A. C., Vélez, M., De Lacey, A. L. Oriented Immobilization of a Membrane-Bound Hydrogenase onto an Electrode for Direct Electron Transfer. *Langmuir* **27,** 6449–6457 (2011).

260. Pereira, M. M., Carita, J. N. & Teixeira, M. Membrane-bound electron transfer chain of the thermohalophilic bacterium Rhodothermus marinus: A novel multihemic cytochrome bc, a new complex III. *Biochemistry* **38,** 1268–1275 (1999).

261. Nunes, O. C., Donato, M. M. & Da Costa, M. S. Isolation and Characterization of Rhodothermus Strains from S. Miguel, Azores. *Syst. Appl. Microbiol.* **15,** 92–97 (1992).

262. Gleißner, M., Kaiser, U., Antonopoulos, E. & Schäfer, G. The Archaeal SoxABCD Complex Is a Proton Pump in Sulfolobus acidocaldarius. *J. Biol. Chem.* **272,** 8417–8426 (1997).

263. Fernandes, A. S., Pereira, M. M. & Teixeira, M. Purification and Characterization of the Complex I from the Respiratory Chain of Rhodothermus marinus. *J. Bioenerg. Biomembr.* **34,** 413–421 (2002).

264. Frisch, M. J., Trucks, G. W., Schlegel, H. B., Scuseria, G. E., Robb, M. A., Cheeseman, J. R., Scalmani, G., Barone, V., Mennucci, B., Petersson G. A. Gaussian 09, Revision D.01. (2013).

265. Perdew, J. P. Density-functional approximation for the correlation energy of the inhomogeneous electron gas. *Phys. Rev. B* **33,** 8822–8824 (1986).

266. Becke, A. D. & Becke. Density-functional exchange-energy approximation with correct asymptotic behavior. *Phys. Rev. A, Gen. Phys.* **38,** 3098–3100 (1988).

267. Kubelka, J., Silva, R. a G. D. & Keiderling, T. A. Discrimination between Peptide 3 10 - and α-Helices. Theoretical Analysis of the Impact of α-Methyl Substitution on Experimental Spectra. *J. Am. Chem. Soc.* **124,** 5325–5332 (2002).

268. Moretto, A., Formaggio, F., Kaptein, B., Broxterman, Q. B., Wu, L., First homo-peptides undergoing a reversible 310-helix/α-helix transition: Critical main-chain length. *Pept. Sci.* **90,** 567–574 (2008).

269. Eaton, J. E., Bateman, D., Hauberg, S. & Wehbring, R. GNU Octave version 4.0.0 manual: a high-level interactive language for numerical computations. (2015).

270. Mroginski, M. A., Mark, F., Thiel, W. & Hildebrandt, P. Quantum mechanics/molecular mechanics calculation of the Raman spectra of the phycocyanobilin chromophore in alpha-C-phycocyanin. *Biophys. J.* **93,** 1885–1894 (2007).

271. Pulay, P., Fogarasi, G., Pang, F. & Boggs, J. E. Systematic ab initio gradient calculation of molecular geometries, force constants, and dipole moment derivatives. *J. Am. Chem. Soc.* **101,** 2550–2560 (1979).

272. Frisch, M. J., Trucks, G. W., Schlegel, H. B., Scuseria, G. E., Robb, M. A., Cheeseman, J. R., Scalmani, G., Barone, V., Mennucci, B., Petersson G. A. Gaussian 09. (2013).

273. Weigend, F. & Ahlrichs, R. Balanced basis sets of split valence, triple zeta valence and quadruple zeta valence quality for H to Rn: Design and assessment of accuracy. *Phys. Chem. Chem. Phys.* **7,** 3297–3305 (2005).

274. Rippers, Y., Utesch, T., Hildebrandt, P., Zebger, I. & Mroginski, M. A. Insights into the structure of the active site of the O2-tolerant membrane bound [NiFe] hydrogenase of R. eutropha H16 by molecular modelling. *Phys. Chem. Chem. Phys.* **13,** 16146–16149 (2011).

275. Nelson, M. T., Humphrey, W., Gursoy, A., Dalke, A., Kalé, L. V., Skeel, R. D., Schulten, K. +NAMD: a Parallel, Object-Oriented Molecular Dynamics Program. *Int. J. Supercomput. Appl. High Perform. Comput.* **10,** 251–268 (1996).

276. Jorgensen, W. L., Chandrasekhar, J., Madura, J. D., Impey, R. W. & Klein, M. L. Comparison of simple potential functions for simulating liquid water. *J. Chem. Phys.* **79,** 926–935 (1983).

277. Feller, S. E., Zhang, Y., Pastor, R. W. & Brooks, B. R. Constant pressure molecular dynamics simulation: The Langevin piston method. *J. Chem. Phys.* **103,** 4613–4621 (1995).

278. Nosé, S. A unified formulation of the constant temperature molecular dynamics methods. *J. Chem. Phys.* **81,** 511–519 (1984).

279. Darden, T., York, D. & Pedersen, L. Particle mesh Ewald: An N ·log(N) method for Ewald sums in large systems. *J. Chem. Phys.* **98,** 10089–10092 (1993).

280. Ryckaert, J.-P., Ciccotti, G. & Berendsen, H. J. . Numerical integration of the cartesian equations of motion of a system with constraints: molecular dynamics of n-alkanes. *J. Comput. Phys.* **23,** 327–341 (1977).

281. Wu, E. L. *et al.* CHARMM-GUI Membrane Builder toward realistic biological membrane simulations. *J. Comput. Chem.* **35,** 1997–2004 (2014).

282. Porcelli, F., Verardi, R., Shi, L., Henzler-wildman, K. A. & Ramamoorthy, A. NMR Structure of the Cathelicidin-Derived Human Antimicrobial Peptide LL-37 in. 5565–5572 (2008).

283. Johansson, J., Gudmundsson, G. H., Rottenberg, M. E., Berndt, K. D. & Agerberth, B. Conformation-dependent Antibacterial Activity of the Naturally Occurring Human Peptide LL-37. *J. Biol. Chem.* **273,** 3718–3724 (1998).

284. Xhindoli, D., Morgera, F., Zinth, U., Rizzo, R., Pacor, S., Tossi, A. New aspects of the structure and mode of action of the human cathelicidin LL-37 revealed by the intrinsic probe p-cyanophenylalanine. *Biochem. J.* **465,** 443–457 (2015).

285. Wang, G., Elliott, M., Cogen, A. L., Ezell, E. L., Gallo, R. L., Hancock, R. E. W. Structure, Dynamics, and Antimicrobial and Immune Modulatory Activities of Human LL-23 and Its Single-Residue Variants Mutated on the Basis of Homologous Primate Cathelicidins. *Biochemistry* **51,** 653–664 (2012).

286. Malmsten, M. Interactions of Antimicrobial Peptides with Bacterial Membranes and Membrane Components. *Curr. Top. Med. Chem.* **16,** 16–24 (2016).

287. de Miguel Catalina, A. Elucidating the Mechanism of Action of Antimicrobial Peptides by means of Computational Approaches. (2017). doi:10.14279/depositonce-6578

288. Henzler-Wildman, K. A., Martinez, G. V, Brown, M. F. & Ramamoorthy, A. Perturbation of the Hydrophobic Core of Lipid Bilayers by the Human Antimicrobial Peptide LL-37 †. *Biochemistry* **43,** 8459–8469 (2004).

289. Dathe, M. & Wieprecht, T. Structural features of helical antimicrobial peptides: their potential to modulate activity on model membranes and biological cells. *Biochim. Biophys. Acta* **1462,** 71–87 (1999).

290. Dathe, M., Nikolenko, H., Meyer, J., Beyermann, M. & Bienert, M. Optimization of the antimicrobial activity of magainin peptides by modification of charge. *FEBS Lett.* **501,** 146–150 (2001).

291. Henzler Wildman, K. A., Lee, D. & Ramamoorthy, A. Mechanism of Lipid Bilayer Disruption by the Human Antimicrobial Peptide, LL-37 †. *Biochemistry* **42,** 6545–6558 (2003).

292. Oren, Z., Lerman, J. C., Gudmundsson, G. H., Agerberth, B. & Shai, Y. Structure and organization of the human antimicrobial peptide LL-37 in phospholipid membranes: relevance to the molecular basis for its non-cell-selective activity. *Biochem. J.* **341,** 501–513 (1999).

293. Wang, G., Mishra, B., Epand, R. F. & Epand, R. M. High-quality 3D structures shine light on antibacterial, anti-biofilm and antiviral activities of human cathelicidin LL-37 and its fragments. *Biochim. Biophys. Acta* **1838,** 2160–72 (2014).

294. Mottamal, M. & Lazaridis, T. Voltage-dependent energetics of alamethicin monomers in the membrane. *Biophys. J.* **122,** 50–7 (2006).

295. Kubelka, J., Kim, J., Bour, P. & Keiderling, T. A. Contribution of transition dipole coupling to amide coupling in IR spectra of peptide secondary structures. *Vib. Spectrosc.* **42,** 63–73 (2006).

296. Boheim, G., Hanke, W. & Jung, G. Alamethicin Pore Formation: Voltage-Dependent Flip-Flop of α-Helix Dipoles. *Biochim. Biophys. Acta* **9,** 181–191 (1983).

297. Stern, H. A. & Feller, S. E. Calculation of the dielectric permittivity profile for a nonuniform system: Application to a lipid bilayer simulation. *J. Chem. Phys.* **118,** 3401–3412 (2003).

298. Schlaich, A., Knapp, E. W. & Netz, R. R. Water Dielectric Effects in Planar Confinement. *Phys. Rev. Lett.* **117,** 48001 (2016).

299. Schwarz, G. & Savko, P. Structural and Dipolar Properties of the Voltage-Dependent Pore Former Alamethicin in Octanol/dioxane. *Biophys. J.* **39,** 211–219 (1982).

300. Banerjee, U., Tsui, F.-P., Balasubramanian, T. N., Marshall, G. R. & Chan, S. I. Structure of Alamethicin in solution. *J. Mol. Biol.* **165,** 757–775 (1983).

301. Guidelli, R. & Becucci, L. Mechanism of voltage-gated channel formation in lipid membranes. *Biochim. Biophys. Acta - Biomembr.* **1858,** 748–755 (2016).

302. Salnikov, E. S., Friedrich, H., Li X., Bertani, P., Reissmann, S., Hertweck, C., O'Neil, J. D. J., Raap, J., Bechinger, B. Structure and alignment of the membrane-associated peptaibols ampullosporin A and alamethicin by oriented 15N and 31P solid-state NMR spectroscopy. *Biophys. J.* **96(1)** 86-100 (2009).

303. Ye, S., Li, H., Wei, F., Jasensky, J., Boughton, A. P., Yang, P., Chen, Z. Observing a model ion channel gating action in model cell membranes in real time in situ: Membrane potential change induced alamethicin orientation change. *J. Am. Chem. Soc.* **134,** 6237-6243 (2012).

304. Su, Z., Leitch, J. J., Abbasi, F., Faragher, R. J. & Schwan, A. L. EIS and PM-IRRAS studies of alamethicin ion channels in a tethered lipid. *J. Electroanal. Chem.* **812,** 213-220 (2018).

305. Saiz, L. & Klein, M. L. Electrostatic interactions in a neutral model phospholipid bilayer by molecular dynamics simulations. *J. Chem. Phys.* **116,** 3052–3057 (2002).

306. Staffa, J. K., Lorenz, L., Stolarski, M., Murgida, D. H., Zebger, I., Utesch, T., Kozuch, J., Hildebrandt, P. Determination of the Local Electric Field at Au/SAM Interfaces Using the Vibrational Stark Effect. *J. Phys. Chem. C* **121,** 22274–22285 (2017).

307. Clarke, R. J. The dipole potential of phospholipid membranes and methods for its detection. *Adv. Colloid Interface Sci.* **89–90,** 263–81 (2001).

308. Jeuken, L. J. C. AFM study on the electric-field effects on supported bilayer lipid membranes. *Biophys. J.* **94,** 4711–7 (2008).

309. Becka, A. M. & Miller, C. J. Electrochemistry at .omega.-hydroxy thiol coated electrodes. 4. Comparison of the double layer at .omega.-hydroxy thiol and alkanethiol monolayer coated Au electrodes. *J. Phys. Chem.* **97,** 6233–6239 (1993).

310. Schkolnik, G., Salewski, J., Millo, D., Zebger, I., Franzen, S., Hildebrandt, P. Vibrational Stark Effect of the Electric-Field Reporter 4-Mercaptobenzonitrile as a Tool for Investigating Electrostatics at Electrode/SAM/Solution Interfaces. *Int. J. Mol. Sci.* **13,** 7466–7482 (2012).

311. Ramírez, P., Andreu, R., Cuesta, Á., Calzado, C. J., Calvente, J. J. Determination of the potential of zero charge of Au(111) modified with thiol monolayers. *Anal. Chem.* **79,** 6473–6479 (2007).

312. Fried, S. D. & Boxer, S. G. Measuring Electric Fields and Noncovalent Interactions Using the Vibrational Stark Effect. *Acc. Chem. Res.* **48,** 998–1006 (2015).

313. Salnikov, E. S., Raya, J., De Zotti, M., Zaitseva, E., Peggion, C., Ballano, G., Toniolo, C., Raap, J., Bechinger, B. Alamethicin Supramolecular Organization in Lipid Membranes from 19 F Solid-State NMR. *Biophys. J.* **111,** 2450–2459 (2016).

314. Rahaman, A. & Lazaridis, T. A thermodynamic approach to alamethicin pore formation. *Biochim. Biophys. Acta* **1838,** 98–105 (2014).

315. Vodyanoy, I., Hall, J. E. & Balasubramanian, T. M. Alamethicin-induced current-voltage curve asymmetry in lipid bilayers. *Biophys. J.* **42,** 71–82 (1983).

316. Heberle, F. A., Marquardt, D., Doktorova, M., Geier, B., Standaert, R. F., Heftberger, P., Kollmitzer, B., Nickels, J. D., Dick, R. A., Feigenson, G. W., Katsaras, J., London, E., Pabst, G. Subnanometer Structure of an Asymmetric Model Membrane: Interleaflet Coupling Influences Domain Properties. *Langmuir* **32,** 5195–5200 (2016).

317. Chen, P., Wang, Z., Zong, S., Chen, H., Zhu, D., Zhong, Y., Cui, Y. A wide range optical pH sensor for living cells using Au@Ag nanoparticles functionalized carbon nanotubes based on SERS signals. *Anal. Bioanal. Chem.* **406,** 6337–46 (2014).

318. Wharton, C. W. Infrared and Raman spectroscopic studies of enzyme structure and function. *Biochem. J.* **233,** 25–36 (1986).

319. Jeuken, L. J. C., Bushby, R. J. & Evans, S. D. Proton transport into a tethered bilayer lipid membrane. *Electrochem. commun.* **9,** 610–614 (2007).

320. Bryant, M. A. & Crooks, R. M. Determination of surface pKa values of surface-confined molecules derivatized with pH-sensitive pendant groups. *Langmuir* **9,** 385–387 (1993).

321. Berrisford, J. M., Baradaran, R. & Sazanov, L. A. Structure of bacterial respiratory complex I. *Biochim. Biophys. Acta* **1857,** 892–901 (2016).

322. Sondag-Huethorst, J. A. M. & Fokkink, L. G. J. Electrochemical Characterization of Functionalized Alkanethiol Monolayers on Gold. *Langmuir* **11,** 2237–2241 (1995).

323. Kozuch, J., Petrusch, N., Gkogkou, D., Gernert, U. & Weidinger, I. M. Calculating average surface enhancement factors of randomly nanostructured electrodes by a combination of SERS and impedance spectroscopy. *Phys. Chem. Chem. Phys.* **17,** 21220–21225 (2015).

324. Cho, S. H., Kim, D. & Park, S.-M. Electrochemistry of conductive polymers: 41. Effects of self-assembled monolayers of aminothiophenols on polyaniline films. *Electrochim. Acta* **53,** 3820–3827 (2008).

325. Wiebalck, S., Kozuch, J., Forbrig, E., Tzschucke C. C., Jeuken L. J. C., Hildebrandt P. Monitoring the Transmembrane Proton Gradient Generated by Cytochrome bo3 in Tethered Bilayer Lipid Membranes Using SEIRA Spectroscopy. *J. Phys. Chem. B* **129,** 2249–2256 (2016).

326. Wirth, C., Brandt, U., Hunte, C. & Zickermann, V. Structure and function of mitochondrial complex I. *Biochim. Biophys. Acta* **1857,** 902–914 (2016).

327. Berrisford, J. M., Baradaran, R. & Sazanov, L. A. Structure of bacterial respiratory complex I. *Biochim. Biophys. Acta* **1857,** 892–901 (2016).

328. Gutiérrez-Sanz, O.; Forbrig, E.; Batista AP.; Pereira MM.; Salewski, J.; Mroginski MA.; Götz, R.; De Lacey, AL.; Kozuch, J.; Zebger, I. Catalytic Activity and Proton Translocation of Reconstituted Respiratory Complex I monitored by Surface-enhanced Infrared Absorption Spectroscopy. *Langmuir* **34** (20), 5703-5711(2016).

329. Gonzalez B. D. Spectroelectrochemical study of biomolecules in artificial membrane systems (2018). doi: 10.14279/depositonce-6921

DANKSAGUNG

SELBSTÄNDIGKEITSERKLÄRUNG

Die selbständige und eigenhändige Anfertigung dieser Arbeit versichere ich Eides statt.

_____

Enrico Forbrig

Berlin, 21.07.2018